NASA Contractor Report 3454



# Shock Associated Noise Reduction From Inverted-Velocity-Profile Coannular Jets

H. K. Tanna, C. K. W. Tam,
and W. H. Brown



CONTRACT NAS1-15971
AUGUST 1981

NASA

NASA Contractor Report 3454

# Shock Associated Noise Reduction From Inverted-Velocity-Profile Coannular Jets

H. K. Tanna, C. K. W. Tam,
and W. H. Brown
*Lockheed-Georgia Company*
*Marietta, Georgia*

Prepared for
Langley Research Center
under Contract NAS1-15971

National Aeronautics
and Space Administration

**Scientific and Technical**
**Information Branch**

1981

# CONTENTS

# CONTENTS (Cont'd)

# SUMMARY

The work described in this report is conducted to quantify and obtain a physical understanding of the noise reduction mechanisms in supersonic inverted-velocity-profile coannular jets, with emphasis on the shock associated noise reduction.

The noise characteristics of coannular jets operated at supercritical pressure ratios are measured in the Lockheed anechoic facility. For all test conditions, corresponding acoustic measurements for the fully-mixed equivalent single jet (defined as having the same thrust, mass flow rate and exit area as the coannular jet) are also obtained so that the noise characteristics from the two types of jets can be compared directly to quantify the noise reductions.

The shock associated noise from the fan or outer stream of the coannular jet is virtually eliminated when the primary or inner stream is operated at a Mach number just above unity, regardless of all the other jet operating parameters. At this optimum condition, the coannular jet provides the maximum noise reduction relative to the equivalent single jet. Furthermore, unlike the reduction of jet mixing noise from a coannular jet, which occurs only at inverted-velocity-profile conditions, the fan-to-primary velocity ratio is not an important parameter in the elimination or reduction of shock noise from a coannular jet. The shock associated noise reduction can be achieved at inverted- as well as normal-velocity-profile conditions, provided the coannular jet is operated with the primary stream just slightly supersonic.

To understand the acoustic results, a simple analytical model for the periodic shock cell structure is first constructed and studied. The model indicates that, as observed in previous optical measurements, a drastic change in the fan stream shock cell structure occurs when the primary stream increases its velocity from subsonic to supersonic. At this point, the almost periodic shock cell structure of the fan stream nearly completely disappears, and hence, the noise radiated is minimum.

In the second part of the theoretical work, a first order shock structure model for the coannular jet is developed. Based on the concept that shock associated noise is generated by the weak interaction between the downstream propagating large scale turbulence structures in the mixing layers of the jet and the repetitive shock cell system, formulae for the peak frequencies and noise intensity scaling are derived. The validity of these formulae is tested by comparison with measured results. Good agreement is found for both subsonic and supersonic primary jet flows.

# 1. INTRODUCTION

In recent years, as a result of the programs sponsored by NASA-Lewis Research Center on model Duct Burning Turbofan (DBTF) engine noise measurements, it has been noted that coaxial or coannular jets with inverted velocity profiles provide a significant noise reduction. The data generated under these programs (refs. 1 and 2) have since been analyzed in detail at the NASA-Langley Research Center (ref. 3), and conclusive evidence is now available to show that a 4-5 dB reduction in sound power levels, without loss of engine performance, can be achieved at certain optimum coannular jet operating conditions. However, the reasons for the observed noise reductions are not clearly and completely understood. If the inverted-profile concept is to be effectively utilized to obtain a wider acoustic margin for the development of the Advanced Supersonic Transport (AST), it is crucial that the noise reduction mechanism be fully understood and that some technological basis be provided for the optimization of coannular jet engine design for minimum noise.

To obtain a fundamental understanding of the noise reduction mechanisms in coannular jets, Lockheed-Georgia conducted a one-year contract study for NASA-Langley, and the results of this investigation were reported fully in Reference 4. During this program, significant progress was made in generating a large amount of aerodynamic and acoustic data on inverted-profile coannular jets, as well as in explaining the noise reductions in such jets. However, the major emphasis in this work was placed on <u>shock-free</u> jet operating conditions, although some work was also conducted on shock-containing conditions. As a result of this effort, the changes in turbulent jet mixing noise characteristics in inverted-profile coannular jets, relative to the equivalent single jet (defined as having the same thrust, mass flow rate, and jet exit area as the coannular jet), have been largely understood and quantified.

The noise benefit from the inverted-profile concept, however, is considered to be maximum in the <u>supersonic</u> regime. At certain supercritical jet operating conditions, large reductions in the shock noise component are believed to occur. This belief was reinforced in the above-mentioned Lockheed study (ref. 4) as a result of extensive optical measurements, which were conducted to observe the variation of shock structure in coannular jets as a function of fan (or outer) and primary (or inner) stream pressure ratio combinations.

In these optical measurements, 42 Schlieren photographs were obtained covering three series of test conditions for the coannular jet. In each series, the primary stream total temperature ($T_{tp}$), the fan stream total temperature ($T_{tf}$), and the fan stream pressure ratio ($\xi_f$) were kept constant, and the primary stream pressure ratio ($\xi_p$) was varied over a large range. The nominal values of the test parameters are given in Table 1.1.

Table 1.1 Test conditions for optical measurements (ref. 4)

| | $T_{tp}$( K) | $T_{tf}$( K) | $\xi_f$ | $\xi_p$ |
|---|---|---|---|---|
| Series 1 | 294 | 728 | 2.93 | 1.00 → 4.49 |
| Series 2 | 728 | 294 | 2.93 | 1.00 → 3.48 |
| Series 3 | 728 | 978 | 2.37 | 1.00 → 3.53 |

In series 1, the fan flow was heated while the primary flow was unheated; in series 2, the primary flow was heated while the fan flow was unheated; finally, in series 3, both streams were heated.

In each test series, the variation in coannular jet shock structure with increasing primary nozzle pressure ratio was qualitatively similar. To illustrate this variation, the Schlieren photographs obtained from series 2 are shown here in Figure 1.1. For $\xi_p = 1$ (Figure 1.1(a)), there is no flow exhausting from the primary nozzle; the annular flow exhausting from the fan nozzle contains a number of clearly identifiable, "donut-shaped" shock cells which rapidly decrease in diameter with downstream distance due to the convergence of the annular flow towards the jet centerline. As soon as the primary flow is turned on, these shock cells remain essentially constant in size, and up to 8 or 10, almost regularly spaced shock cells can now be identified. As $\xi_p$ is increased further, there is not a significant change in the overall "donut-shaped" shock structure, until $\xi_p$ becomes greater than the critical pressure ratio. As soon as $\xi_p$ is increased above approximately 1.9 (Figure 1.1(e)), a drastic change in the shock structure occurs. At this point, the closely-spaced shock cell structure in the fan stream observed in all cases for $\xi_p \leq 1.9$ is largely destroyed, and it is replaced by only one or two shock cells close to the nozzle exits. As $\xi_p$ is now increased to values well in excess of 1.9, the shock cells in the supercritical primary stream become more and more evident, and increase in spacing as $\xi_p$ increases. At the highest value of $\xi_p$ (Figure 1.1($\ell$)), the total shock structure consists of one or two shocks close to the nozzle exit from the fan stream and three or four widely-spaced shock cells in the primary stream.

Although this description of the observed changes in shock structure in inverted-velocity-profile coannular jets is greatly oversimplified, the Schlieren measurements do indicate a sudden change in the shock structure of the outer flow when the inner flow becomes supersonic. Based on these observations, it was postulated that the broadband shock associated noise from coannular jets may be greatly reduced at and near the conditions at which this sudden change in the fan flow shock structure occurs. However, systematic acoustic measurements to support this hypothesis were not available at that time, and one of the primary requirements of the work described in this report was to obtain such acoustic data. In addition, it is vital to understand the associated phenomena so that the noise benefit of coannular jets at supercritical conditions can be exploited.

The overall objective of the present investigation, therefore, is to quantify and obtain a physical understanding of the noise reduction mechanisms in supersonic inverted-velocity-profile coannular jets, with emphasis on the shock associated noise reduction.

This objective was accomplished by (1) conducting extensive acoustic measurements of supersonic coannular jets, and (2) interpreting the measured noise results with the aid of new theoretical models for shock structure and noise characteristics of shock-containing coannular jet flows.

The major findings of this investigation are as follows:

(1) The experimental results obtained in this study show that the shock associated noise from the fan or outer stream of the coannular jet is virtually eliminated when the primary or inner stream is operated at a Mach number just above unity, regardless of all the other jet operating parameters. At this optimum condition, the coannular jet provides the maximum noise reduction relative to the equivalent single jet. Furthermore, unlike the reduction of jet mixing noise from a coannular jet, which occurs only at inverted-velocity-profile conditions, the fan-to-primary velocity ratio is not an important parameter in the elimination or reduction of shock noise from a coannular jet. The shock associated noise reduction can be achieved at inverted- as well as normal-velocity-profile conditions, provided the coannular jet is operated with the primary stream just slightly supersonic.

(2) The theoretical models for shock structure and shock associated noise developed in this program are in complete agreement with the acoustic and optical measurements. The models predict that a drastic change in the fan stream shock cell structure occurs when the primary stream increases its velocity from subsonic to supersonic. At this point, the almost periodic shock cell structure of the fan stream nearly completely disappears, and hence, the noise radiated is minimum.

In this report, the details of the acoustic experiments are given in Section 2, and the measured noise results are presented and discussed fully in Section 3. The next two sections (i.e., Sections 4 and 5) are devoted entirely to theoretical model development and comparison of experimental results with theoretical noise scaling formulae. Finally, the main conclusions of this work are given in Section 6.

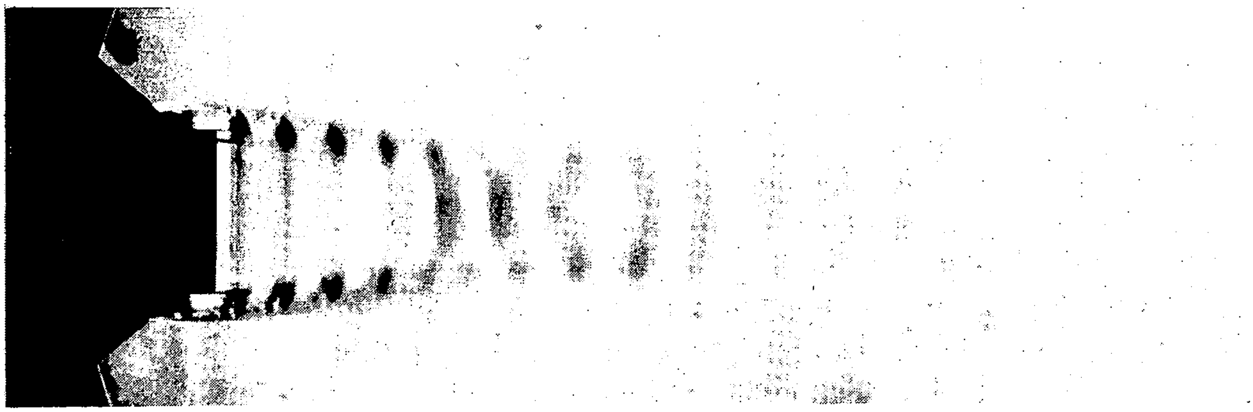

(a) $\xi_p = 1.000$

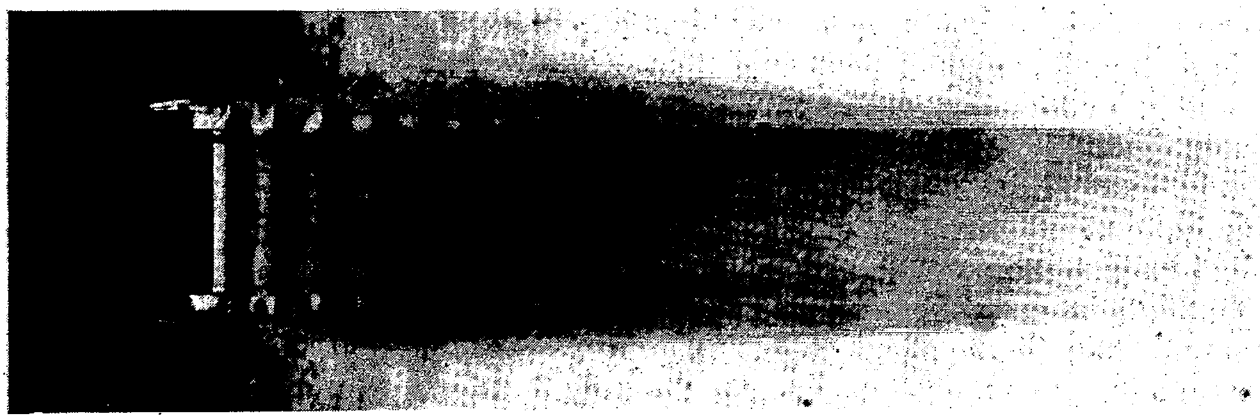

(b) $\xi_p = 1.390$

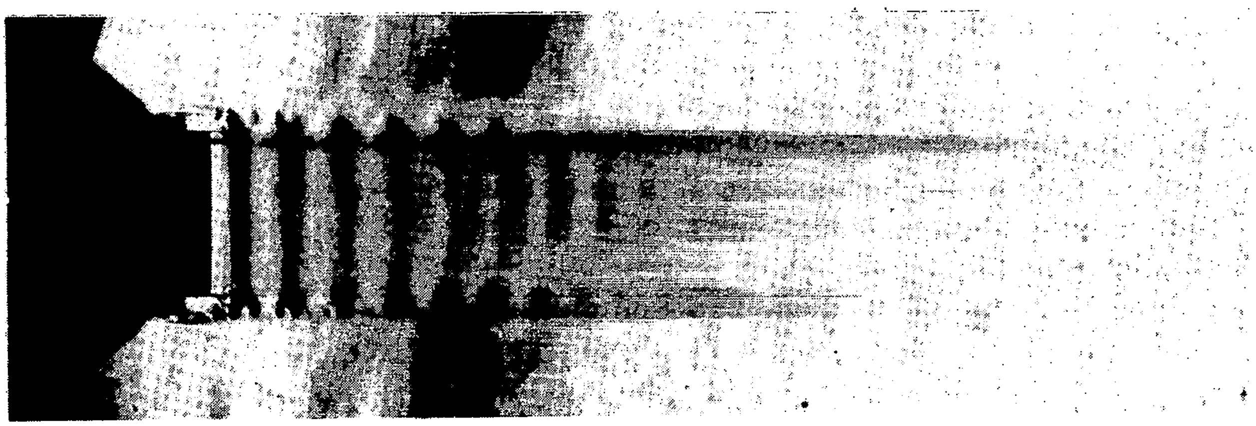

(c) $\xi_p = 1.593$

Figure 1.1 Schlieren photographs showing the variation of shock structure in a coannular jet with increasing $\xi_p$. Fixed $\xi_f = 2.93$, $T_{tp} = 728$ K, $T_{tf} = 294$ K.

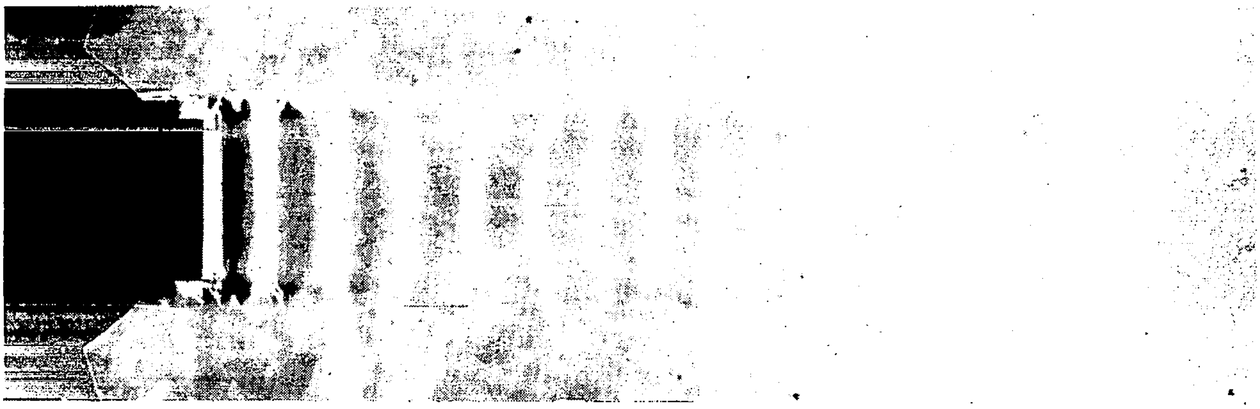

(d) $\xi_p = 1.808$

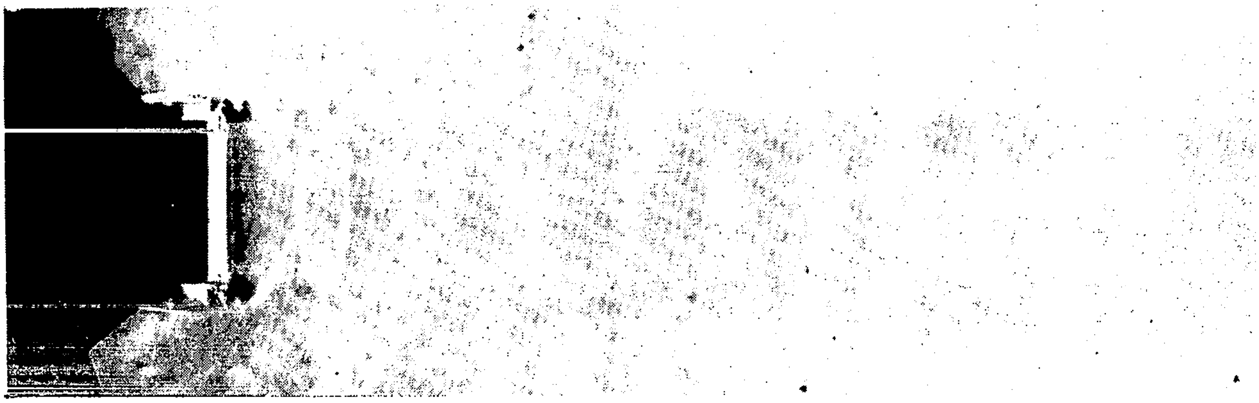

(e) $\xi_p = 1.984$

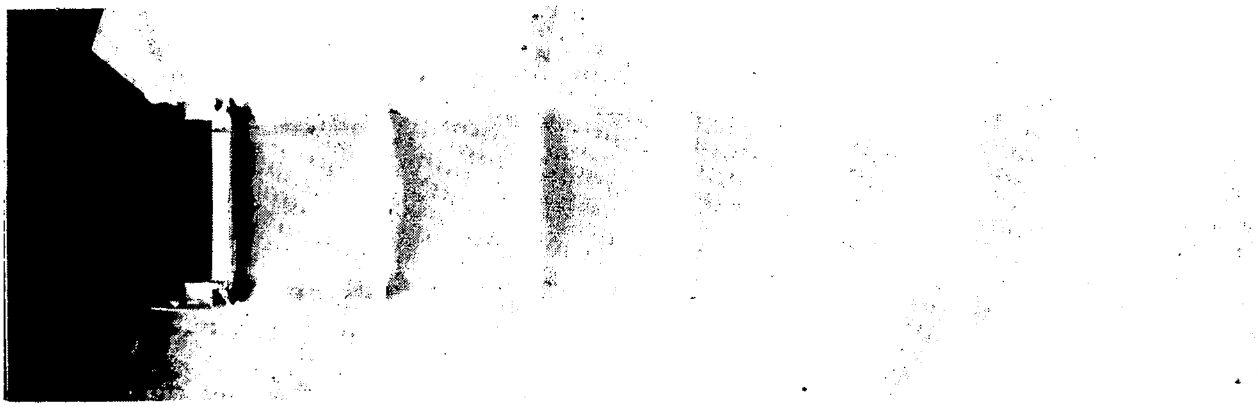

(f) $\xi_p = 2.179$

Figure 1.1 (Continued).

(g) $\xi_p = 2.435$

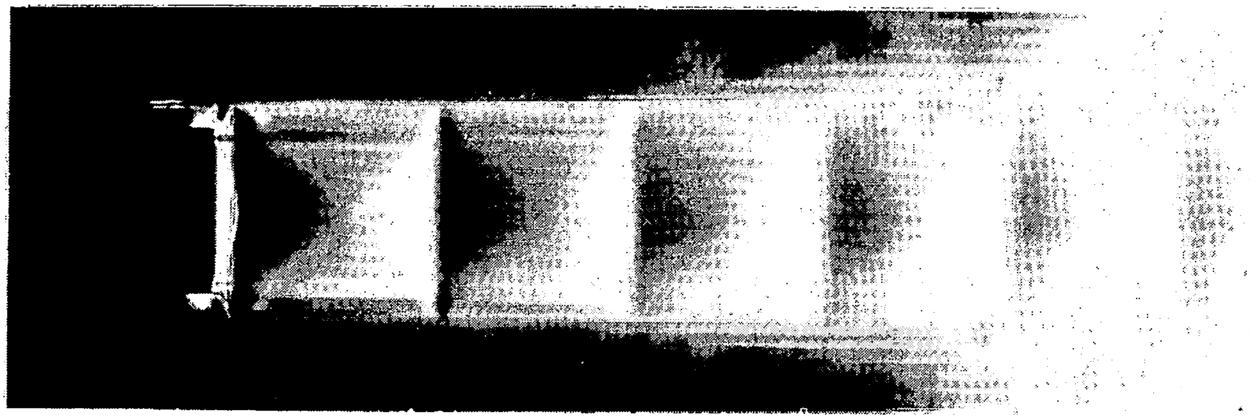

(h) $\xi_p = 2.603$

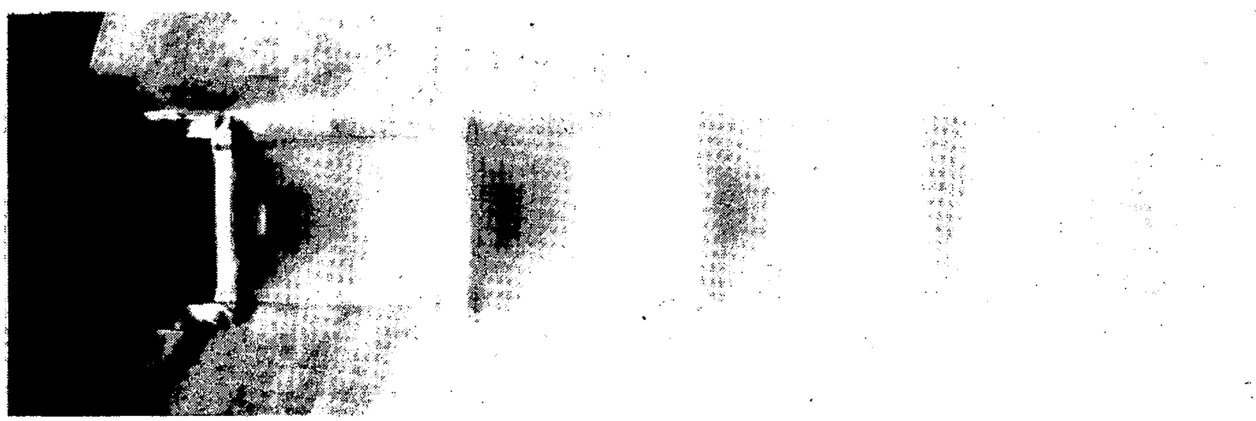

(i) $\xi_p = 2.953$

Figure 1.1 (Continued).

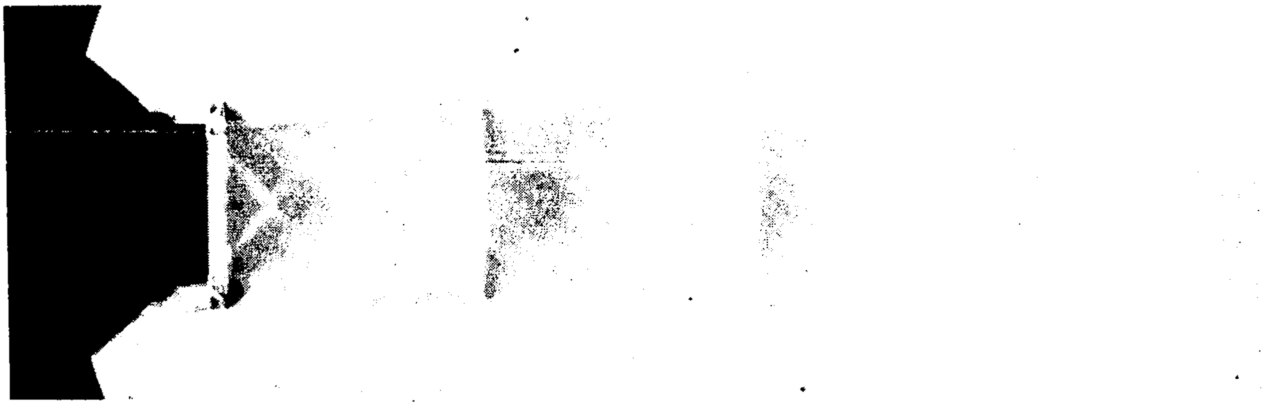

(j) $\xi_p = 3.183$

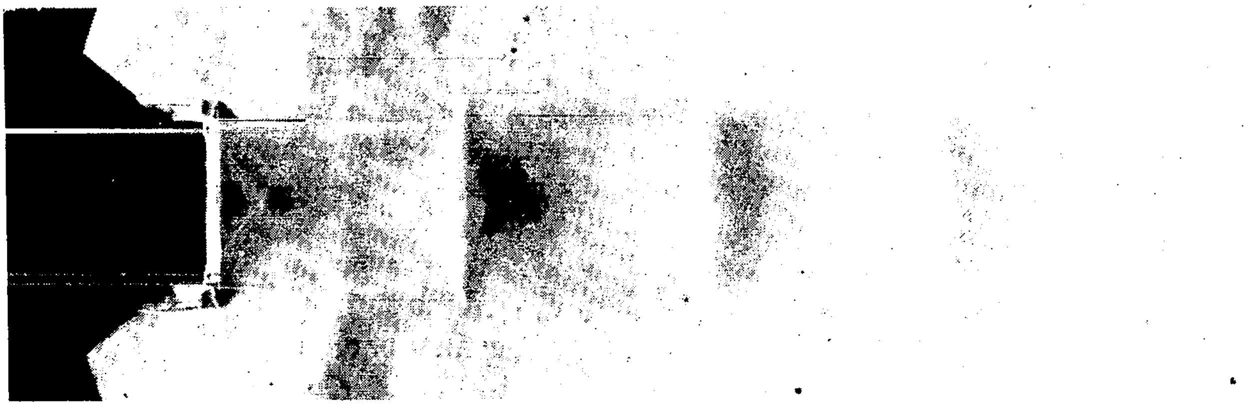

(k) $\xi_p = 3.345$

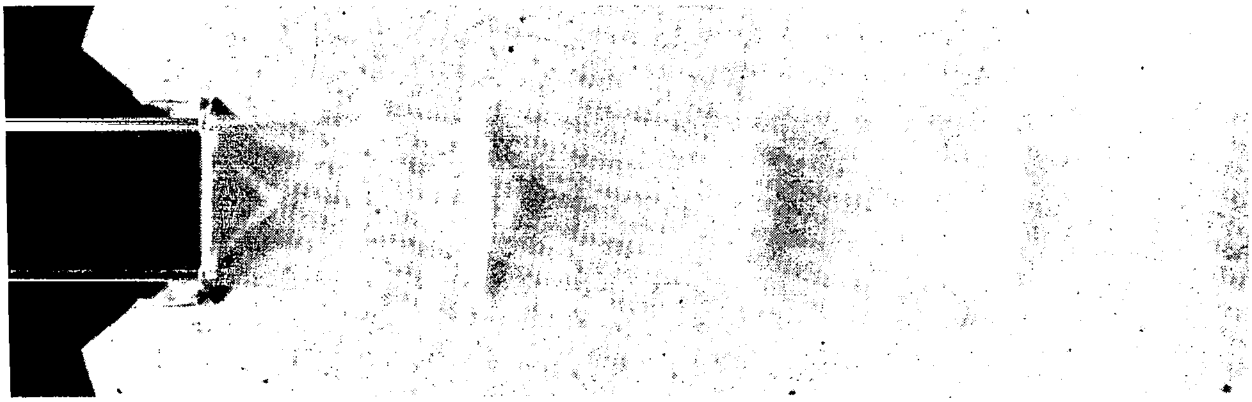

($\ell$) $\xi_p = 3.479$

Figure 1.1 (Concluded).

# 2. ACOUSTIC EXPERIMENTS

The experimental program to obtain the far-field noise characteristics of inverted-velocity-profile coannular jets under supersonic conditions is described in this section in two parts. The first part deals with the facilities and the data acquisition and reduction procedures used in the experiments, while the second part gives the details of the coannular jet test conditions.

## 2.1 FACILITIES AND DATA ACQUISITION

The acoustic experiments were conducted in the Lockheed anechoic facility, which has been used extensively in the past to conduct both single jet and coannular jet noise measurements. A detailed description of this facility is given in Reference 5, and the salient features are summarized below.

The anechoic chamber provides a free-field environment at all frequencies above 200 Hz, and incorporates a specially designed exhaust collector/muffler which (i) provides adequate quantities of jet entrainment air, (ii) distributes this entrainment air symmetrically around the jet axis, and (iii) keeps the airflow circulation velocities in the room to a minimum.

The air supply for the primary and secondary jets originates from the main compressor, which provides up to 9 kg/sec of clean dry air at $2.07 \times 10^6$ N/m$^2$. This air is heated by a propane burner to approximately 1100 K. Downstream of the burner, the primary and secondary air supplies are controlled independently, and each has a hot and a cold valve so that any desired jet operating conditions can be achieved within the pressure and temperature limitations of the system. Each airstream is then directed through a diffuser and a muffler to minimize internal noise levels. The two streams finally enter their respective plenums, which are located upstream of the coannular nozzle section.

Special attention has been paid to flow conditioning. Downstream of the mufflers, the flow area to nozzle exit area is maintained greater than 36:1 up to the nozzle inlet. This ensures that no additional noise or turbulence is generated, since the flow velocities are very low.

To ensure that the relative axial positions of the exit planes of the two nozzles do not vary, a special expansion coupling has been incorporated in the primary ductwork, with a corresponding spacer in the secondary ductwork. This provides for expansion or contraction of the inner duct relative to the outer duct of ±4 mm from center, which is adequate for the thermal expansion associated with the probable temperature differentials between primary and secondary flows.

Finally, to maintain concentricity of the two nozzles at all times, a special spoked nozzle attachment flange is included.

### 2.1.1 Coannular Nozzle Configuration

The coannular nozzle that was used throughout this investigation is shown in Figure 2.1. (The same nozzle was also used for the optical measurements - discussed in Section 1 - during the previous contract study.) The nozzles have been carefully designed to give minimum boundary layer thickness and flow streamlines parallel to the jet axis at the exit. The specifications of the nozzle configuration are as follows:

| | |
|---|---|
| Diameter of primary nozzle | $D_p$ = 4.996 cm |
| Diameter of fan nozzle | $D_f$ = 6.797 cm |
| Primary nozzle lip thickness | $t_p$ = 0.0508 cm |
| Fan nozzle lip thickness | $t_f$ = 0.0508 cm |
| Primary nozzle wall thickness <u>at fan nozzle exit plane</u> | = 0.127 cm |
| Primary nozzle extension beyond fan nozzle exit plane | L = 0.4 $D_p$ |
| Radius ratio | $r_p/r_f$ = 0.735 |
| Primary stream exit area | $A_p$ = 19.604 $cm^2$ |
| Fan stream exit area | $A_f$ = 14.637 $cm^2$ |
| Equivalent (or total) jet exit area | A = 34.241 $cm^2$ |
| Area ratio | $A_f/A_p$ = 0.747 |
| Equivalent nozzle diameter | $D_{eq}$ = 6.603 cm |

To obtain acoustic results for the equivalent single jet corresponding to the coannular jet, measurements were conducted by removing the fan or outer nozzle and operating the primary or inner nozzle alone at the equivalent single jet operating conditions. Since the diameter of this primary nozzle is 4.996 cm, the results were subsequently scaled to an equivalent nozzle diameter of 6.603 cm, using standard size scaling procedures. In this manner, the coannular jet noise data can be compared directly with the equivalent single jet noise data to determine the noise benefit. This point will be elaborated in Section 2.2. Throughout the tests no screech suppression device was used.

### 2.1.2 Data Acquisition

The acoustic measurements were conducted on a polar arc of radius 3.05 m (10 feet). Eleven 6.35 mm ($\frac{1}{4}$-inch) B&K microphones were positioned from 20° to 120° to the downstream jet axis at intervals of 10°. The sound pressure data were recorded on a multi-channel Honeywell tape recorder for subsequent analysis. The recorded data were analyzed on a General Radio one-third octave band analyzer over the frequency range from 200 Hz to 80 KHz, and the results were recorded on a digital tape recorder. The recorded levels were subsequently processed on a digital computer using a data reduction program which applies microphone frequency response corrections and atmospheric attenuation corrections, and computes overall sound pressure levels over the frequency range 200 Hz - 80 KHz.

It should be noted that all sound pressure and sound power results presented in this report are <u>lossless</u> (that is, with zero atmospheric attenuation), and the levels are expressed for a common observer distance of R = 100 $D_{eq}$ (i.e., R = 6.6 m) from the nozzle exit.

## 2.2 TEST PROGRAM

Due to the large number of absolute parameters (e.g., velocity, temperature, area, etc.) as well as parameter ratios involved in characterizing coannular jet noise, the noise reduction can be (and has been) examined and quantified in a number of different ways. In the earlier studies on normal-velocity-profile coannular jets (fan-to-primary velocity ratio $V_f/V_p < 1$), the coannular jet noise levels were almost always compared with the noise levels from the primary jet alone. In many of the initial studies on inverted-velocity-profile coannular jets (i.e., $V_f/V_p > 1$), the noise reduction has been assessed in most part by either (i) comparing coannular jet noise levels with synthesized noise levels, or (ii) comparing coannular jet noise levels to the $V_f/V_p = 1$ case for fixed fan velocity $V_f$. The "synthesized" method has no physical rationale, whereas the other two schemes are at best misleading. It was only relatively recently that some selected results have been re-examined to assess the noise reduction with respect to the corresponding "fully mixed equivalent single jets." But even in those cases where the noise benefit has been evaluated correctly (according to the criteria discussed in the next paragraph), some confusion exists as to whether the net noise reductions are due to reductions in the jet mixing noise component or reductions in the shock noise component, since a clear distinction between shock-free and shock-containing coannular jets has not been made in these evaluations.

In order to evaluate the real noise benefit, it is desirable to have a means of comparing different coannular jet noise levels which takes realistic account of the aircraft propulsion design constraints. Significant parameters in this context include nozzle gross thrust, mass flow rate, total enthalpy change, and exit area. A constant-thrust comparison is obviously essential; which two other parameters should be kept constant is to some extent arbitrary. In the Lockheed work, area and mass flow rate have been chosen for the time being, and it is believed that the final conclusions are not expected to differ significantly if mass flow rate and total energy are kept constant instead (with area as the floating parameter). As a basis for quantifying the noise reductions, therefore, the fully-mixed equivalent single jet, defined as having a uniform exit profile and the same exit area, mass flow rate, and thrust as the actual coannular jets, is used. Comparison on this basis indicates where particular coannular configurations hold promise of useful noise reductions in an actual propulsion application.

In the first Lockheed study on coannular jets (ref. 4), the noise reductions from shock-free coannular jets were quantified and understood on the basis discussed above. The same criteria are now used in the present work where the emphasis is placed on noise reductions from shock-containing coannular jet flows.

As mentioned in Section 1, in the previous contract study (ref. 4), three sets of optical measurements of supercritical inverted-velocity-profile coannular jets were conducted, which revealed that the repetitive shock cell structure in the fan or outer stream can be largely destroyed (or minimized) if the primary or inner nozzle is operated just above the critical pressure ratio. The acoustic test plan presented here is designed to determine whether such a behavior leads to significant reductions in the corresponding shock associated noise (generated in the fan stream) at these "optimum" operating conditions.

Four series of acoustic measurements were conducted as shown in Table 2.1.

Table 2.1 Test conditions for acoustic measurements

| | $T_{tp}$(K) | $T_{tf}$(K) | $p_{tf}/p_a$ | $p_{tp}/p_a$ |
|---|---|---|---|---|
| Series 1 | 300 | 800 | 3.0 | 1.2 → 4.0 |
| Series 2* | 800 | 300 | 3.0 | 1.2 → 4.0 |
| Series 3 | 600 | 800 | 3.0 | 1.2 → 4.0 |
| Series 4 | 300 | 800 | 4.3 | 1.2 → 4.0 |

* Includes cases similar to the schlieren photographs of Section 1.

In the first test series, the primary flow was unheated while the fan flow was heated; in the second test series, the primary flow was heated while the fan flow was unheated; in the third test series, both flows were heated with the fan flow at a higher total temperature ($T_{tf}$) than the primary flow total temperature ($T_{tp}$).

In the first three series, the fan stream pressure ratio ($p_{tf}/p_a$) was maintained constant at 3.0; in series 4, this was increased to 4.3. Within each test series, the primary stream pressure ratio ($p_{tp}/p_a$) was varied from 1.2 to 4.0. Fourteen values of primary pressure ratio were considered in each test series, thus giving a total of 56 coannular jet operating conditions. The values of $p_{tp}/p_a$ were closely spaced around the critical pressure ratio, $p_{tp}/p_a$ = 1.9, so that the noise changes at and around the "optimum" condition can be determined accurately.

As mentioned before, the noise reduction needs to be assessed by comparing the coannular jet noise levels with the corresponding equivalent single jet noise levels. The equivalent single jet is defined here as having the same exit area, mass flow rate, and thrust as the coannular jet. In principle, although the noise characteristics at the fully-mixed equivalent conditions can be obtained by using the existing noise prediction capability, it was felt that in certain cases the inaccuracies in the noise predictions, especially at supersonic conditions, may be of the same order of magnitude as the real noise reductions. Hence, in this basic research program, it was decided that conclusions based in part on noise predictions be avoided. Therefore, measurements at 56 equivalent jet conditions were also conducted in this program using a convergent nozzle.

An outline of the procedure used to calculate the equivalent single jet operating conditions corresponding to the coannular jet operating conditions is given in a block diagram form in Figure 2.2. A computer program based on this procedure was written, and the output from this program, presented here as Tables 2.2, 2.3, 2.4 and 2.5, gives all the information relevant to the test plan for this investigation. In this test plan, the ambient pressure ($p_a$) and the ambient temperature ($T_a$) were taken to be 98.25 KN/m$^2$ (14.25 psi) and 300K (80°F), respectively. In the tables, the pressure ratio, total temperature, mass flow rate, thrust, and the fully-expanded jet velocity for the coannular jets (i.e., primary and fan streams) and the equivalent single jet are given for each test point (TP). In addition, for each test series, the fully-expanded fan-to-primary velocity ratio, $V_f/V_p$, is listed in the last column of each table.

Finally, the test plan is also illustrated graphically in Figures 2.3 and 2.4, where the 56 coannular jet test points are indicated by the circles — the full circles representing series 1, 2 and 3 with fan stream pressure ratio of 3.0, and the open circles representing series 4 with $p_{tf}/p_a$ = 4.3. The total experimental program spans a wide range of fully-expanded fan-to-primary velocity ratios ($V_f/V_p$) from 0.55 to 4.27. The fully-expanded equivalent jet velocity varies from approximately 380 to 650 m/s. Within each series, the test point at which the primary stream pressure ratio becomes critical (i.e. $p_{tp}/p_a$ = 1.9) is shown by the dashed lines in both figures. At these conditions, the values of $V_f/V_p$ are 0.77, 1.47, 2.08 and 2.35 for series 2, series 3, series 1 and series 4 tests, respectively. Hence, in this experimental program, if the current postulations regarding the maximum reductions in the shock noise component are valid, then we can expect to see large reductions in coannular jet noise levels (relative to the equivalent single jet noise levels) at these four velocity ratios.

In the next section, se will see if this is indeed true.

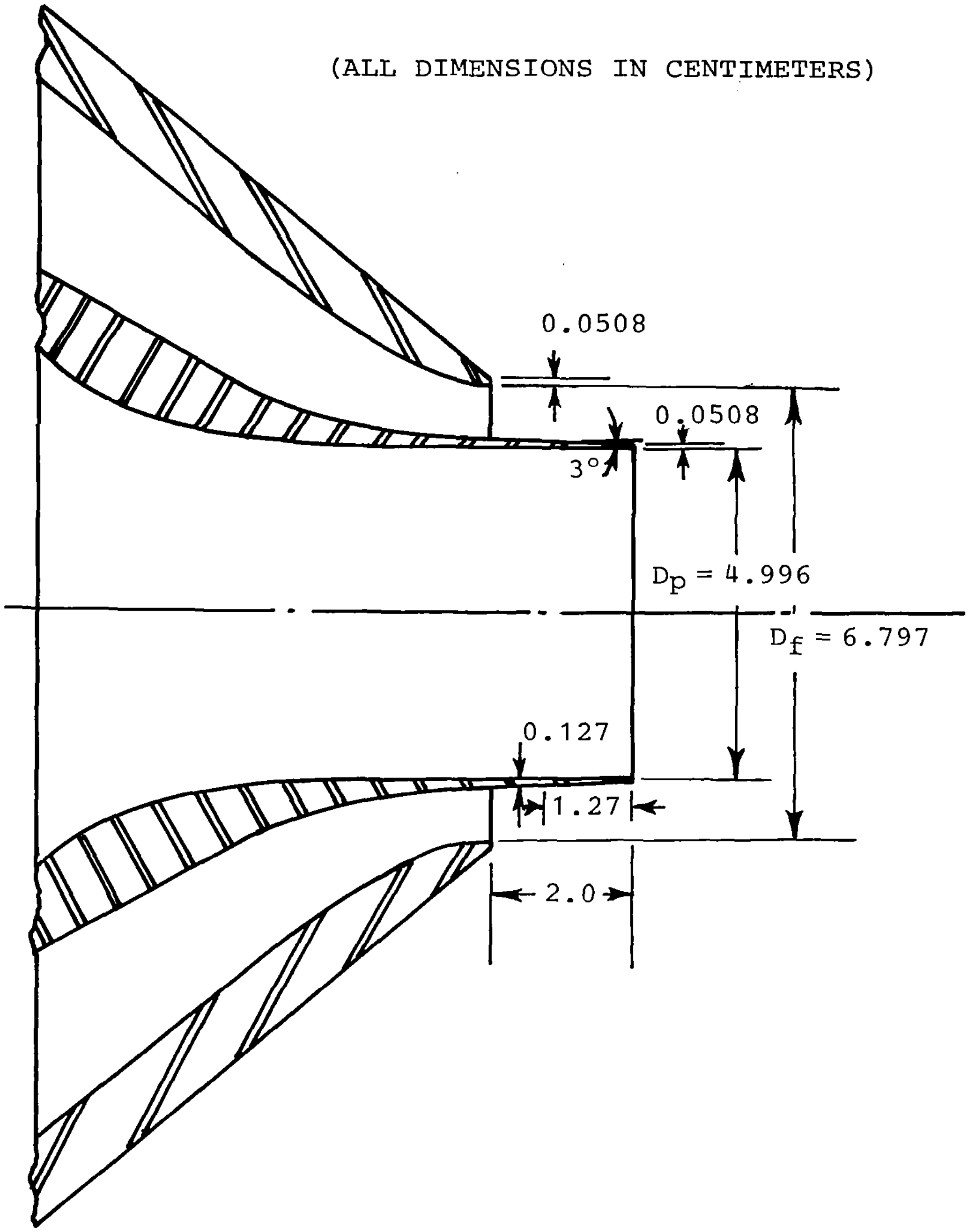


Figure 2.1 Coannular nozzle configuration.

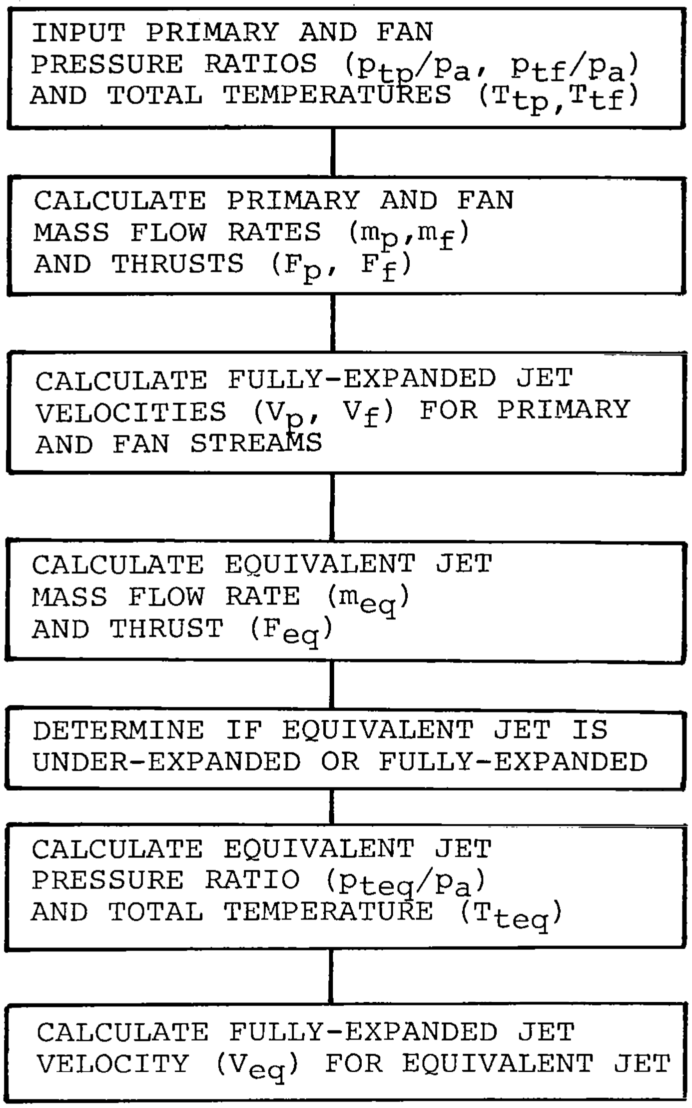


Figure 2.2 Procedure to calculate equivalent single jet operating conditions using coannular jet operating conditions.

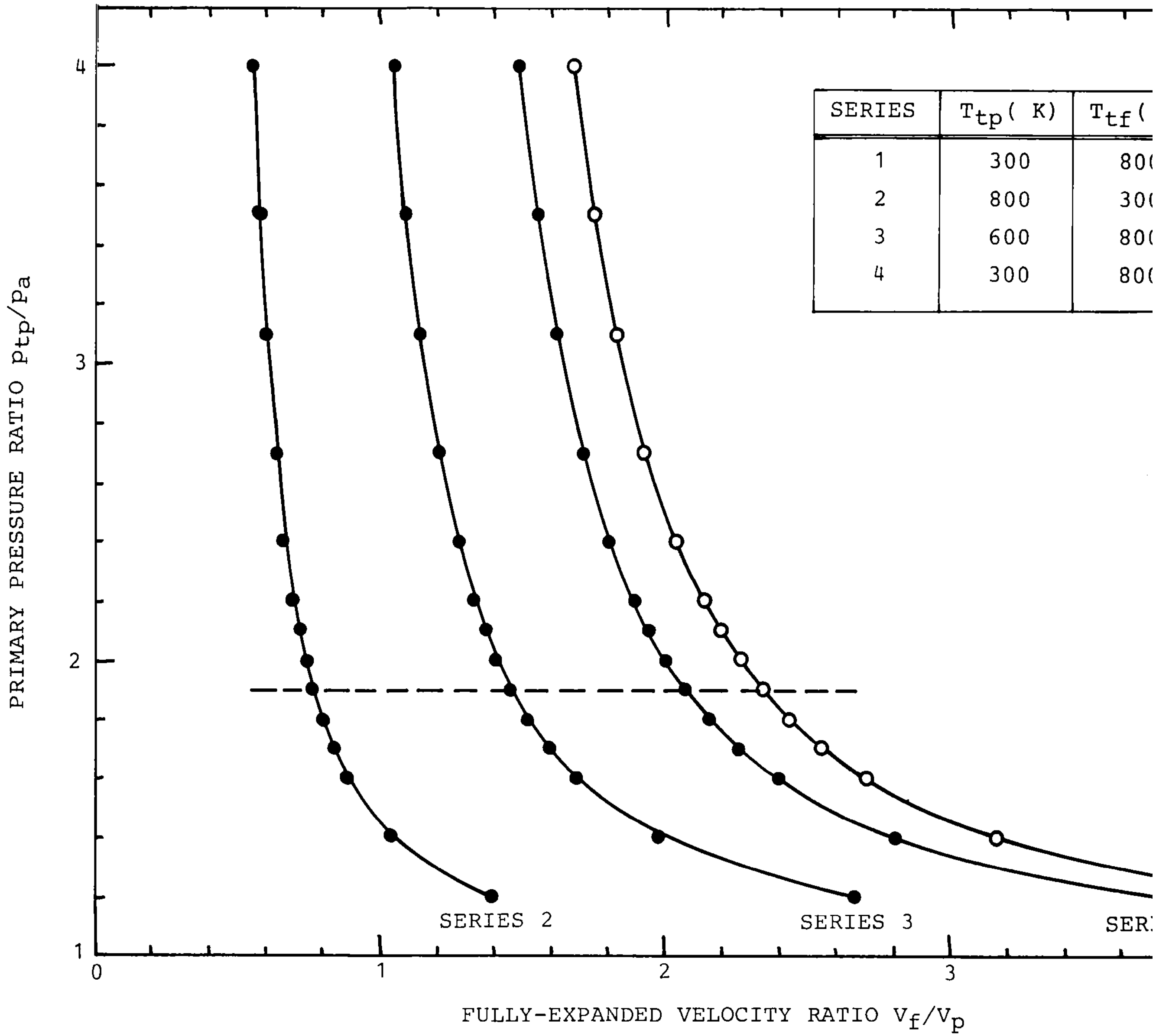


Figure 2.3 Experimental program chart showing coannular jet operating conditions

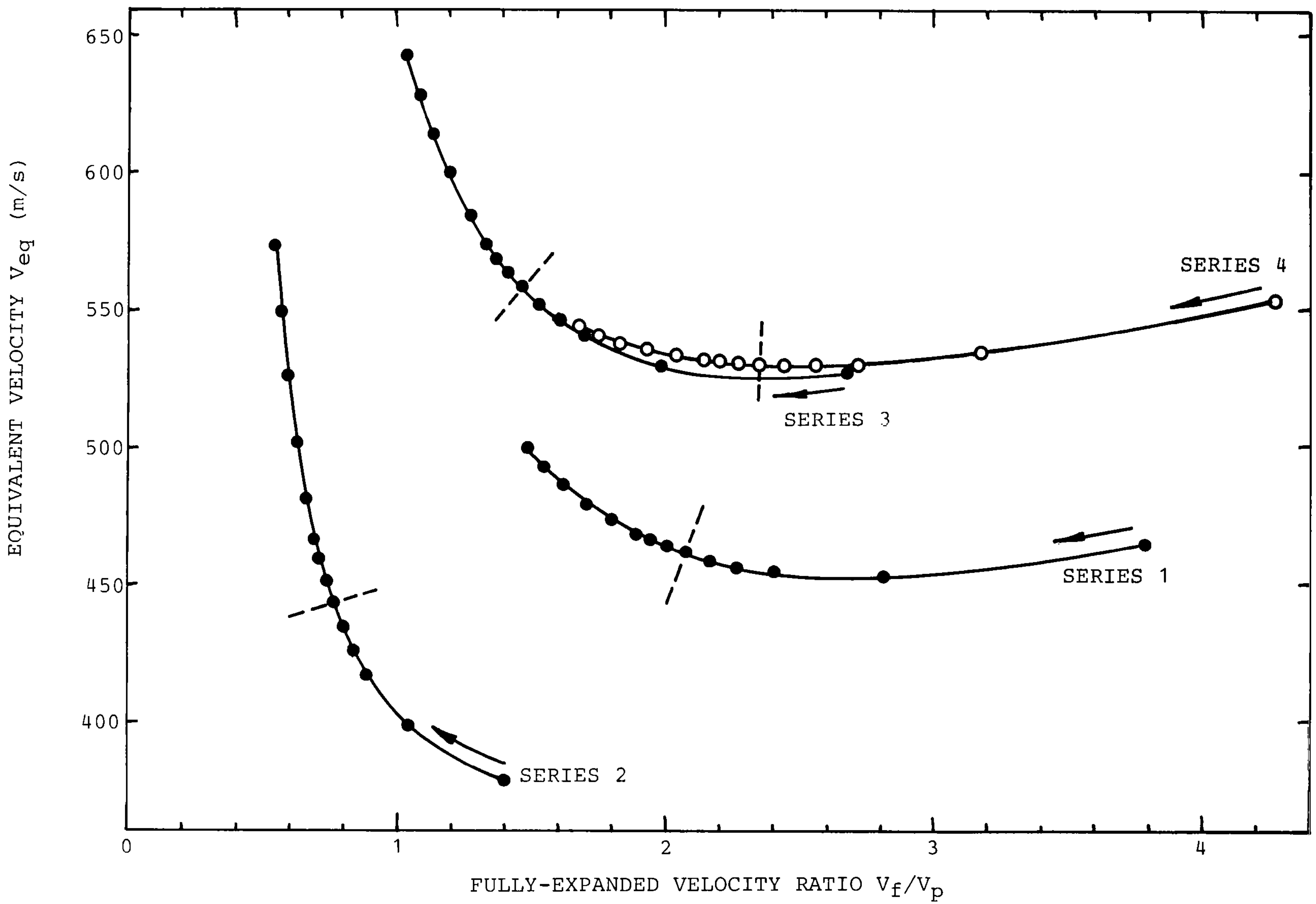


Figure 2.4 Values of equivalent single jet velocity ($V_{eq}$) in the experimental program.

Table 2.2 Test conditions for Series 1.

| TP | JET | PRESSURE RATIO PT/PA | TOTAL TEMPERATURE DEG K | MASS FLOW RATE KG/S | THRUST NEWTONS | VELOCITY M/S | VELOCITY RATIO VF/VP |
|---|---|---|---|---|---|---|---|
| 1 | PRIMARY | 1.200 | 300.0 | 0.4121 | 72.1 | 174.9 | 3.79 |
| | FAN | 3.000 | 800.0 | 0.6094 | 400.7 | 662.3 | |
| | EQUIVALENT | 1.897 | 637.8 | 1.0214 | 472.8 | 464.1 | |
| 2 | PRIMARY | 1.400 | 300.0 | 0.5786 | 136.0 | 235.1 | 2.82 |
| | FAN | 3.000 | 800.0 | 0.6094 | 400.7 | 662.3 | |
| | EQUIVALENT | 2.047 | 549.0 | 1.1879 | 536.7 | 452.8 | |
| 3 | PRIMARY | 1.600 | 300.0 | 0.7036 | 193.7 | 275.3 | 2.41 |
| | FAN | 3.000 | 800.0 | 0.6094 | 400.7 | 662.3 | |
| | EQUIVALENT | 2.182 | 510.7 | 1.3130 | 594.4 | 453.8 | |
| 4 | PRIMARY | 1.700 | 300.0 | 0.7574 | 220.6 | 291.3 | 2.27 |
| | FAN | 3.000 | 800.0 | 0.6094 | 400.7 | 662.3 | |
| | EQUIVALENT | 2.245 | 499.0 | 1.3668 | 621.3 | 455.7 | |
| 5 | PRIMARY | 1.800 | 300.0 | 0.8070 | 246.4 | 305.3 | 2.17 |
| | FAN | 3.000 | 800.0 | 0.6094 | 400.7 | 662.3 | |
| | EQUIVALENT | 2.306 | 490.0 | 1.4164 | 647.1 | 458.2 | |
| 6 | PRIMARY | 1.900 | 300.0 | 0.8532 | 271.2 | 317.9 | 2.08 |
| | FAN | 3.000 | 800.0 | 0.6094 | 400.7 | 662.3 | |
| | EQUIVALENT | 2.364 | 483.1 | 1.4625 | 671.9 | 460.8 | |
| 7 | PRIMARY | 2.000 | 300.0 | 0.8981 | 295.6 | 329.2 | 2.01 |
| | FAN | 3.000 | 800.0 | 0.6094 | 400.7 | 662.3 | |
| | EQUIVALENT | 2.421 | 477.0 | 1.5075 | 696.3 | 463.5 | |
| 8 | PRIMARY | 2.100 | 300.0 | 0.9430 | 320.0 | 339.4 | 1.95 |
| | FAN | 3.000 | 800.0 | 0.6094 | 400.7 | 662.3 | |
| | EQUIVALENT | 2.478 | 471.3 | 1.5524 | 720.7 | 466.0 | |
| 9 | PRIMARY | 2.200 | 300.0 | 0.9879 | 344.4 | 348.8 | 1.90 |
| | FAN | 3.000 | 800.0 | 0.6094 | 400.7 | 662.3 | |
| | EQUIVALENT | 2.536 | 466.0 | 1.5973 | 745.1 | 468.4 | |
| 10 | PRIMARY | 2.400 | 300.0 | 1.0777 | 393.3 | 365.4 | 1.81 |
| | FAN | 3.000 | 800.0 | 0.6094 | 400.7 | 662.3 | |
| | EQUIVALENT | 2.650 | 456.2 | 1.6871 | 793.9 | 472.9 | |
| 11 | PRIMARY | 2.700 | 300.0 | 1.2124 | 466.5 | 386.1 | 1.72 |
| | FAN | 3.000 | 800.0 | 0.6094 | 400.7 | 662.3 | |
| | EQUIVALENT | 2.822 | 443.6 | 1.8218 | 867.2 | 479.1 | |
| 12 | PRIMARY | 3.100 | 300.0 | 1.3921 | 564.1 | 408.2 | 1.62 |
| | FAN | 3.000 | 800.0 | 0.6094 | 400.7 | 662.3 | |
| | EQUIVALENT | 3.051 | 429.6 | 2.0014 | 964.8 | 486.3 | |
| 13 | PRIMARY | 3.500 | 300.0 | 1.5717 | 661.8 | 426.1 | 1.55 |
| | FAN | 3.000 | 800.0 | 0.6094 | 400.7 | 662.3 | |
| | EQUIVALENT | 3.280 | 418.1 | 2.1810 | 1062.5 | 492.6 | |
| 14 | PRIMARY | 4.000 | 300.0 | 1.7962 | 783.8 | 444.3 | 1.49 |
| | FAN | 3.000 | 800.0 | 0.6094 | 400.7 | 662.3 | |
| | EQUIVALENT | 3.566 | 406.3 | 2.4056 | 1184.5 | 499.6 | |

TP TEST POINT

Table 2.3 Test conditions for Series 2.

| TP | JET | PRESSURE RATIO PT/PA | TOTAL TEMPERATURE DEG K | MASS FLOW RATE KG/S | THRUST NEWTONS | VELOCITY M/S | VELOCITY RATIO VF/VP |
|---|---|---|---|---|---|---|---|
| 15 | PRIMARY | 1.200 | 800.0 | 0.2516 | 71.9 | 286.0 | 1.41 |
| | FAN | 3.000 | 300.0 | 1.0059 | 403.0 | 403.2 | |
| | EQUIVALENT | 1.902 | 423.1 | 1.2574 | 474.9 | 378.1 | |
| 16 | PRIMARY | 1.400 | 800.0 | 0.3523 | 135.5 | 384.6 | 1.05 |
| | FAN | 3.000 | 300.0 | 1.0059 | 403.0 | 403.2 | |
| | EQUIVALENT | 2.051 | 421.7 | 1.3581 | 538.5 | 397.0 | |
| 17 | PRIMARY | 1.600 | 800.0 | 0.4274 | 192.6 | 450.7 | 0.89 |
| | FAN | 3.000 | 300.0 | 1.0059 | 403.0 | 403.2 | |
| | EQUIVALENT | 2.185 | 429.8 | 1.4333 | 595.6 | 416.3 | |
| 18 | PRIMARY | 1.700 | 800.0 | 0.4596 | 219.2 | 477.0 | 0.85 |
| | FAN | 3.000 | 300.0 | 1.0059 | 403.0 | 403.2 | |
| | EQUIVALENT | 2.248 | 434.9 | 1.4655 | 622.2 | 425.5 | |
| 19 | PRIMARY | 1.800 | 800.0 | 0.4893 | 244.7 | 500.2 | 0.81 |
| | FAN | 3.000 | 300.0 | 1.0059 | 403.0 | 403.2 | |
| | EQUIVALENT | 2.307 | 440.3 | 1.4951 | 647.7 | 434.3 | |
| 20 | PRIMARY | 1.900 | 800.0 | 0.5169 | 269.2 | 520.9 | 0.77 |
| | FAN | 3.000 | 300.0 | 1.0059 | 403.0 | 403.2 | |
| | EQUIVALENT | 2.365 | 445.9 | 1.5227 | 672.2 | 442.7 | |
| 21 | PRIMARY | 2.000 | 800.0 | 0.5441 | 293.5 | 539.6 | 0.75 |
| | FAN | 3.000 | 300.0 | 1.0059 | 403.0 | 403.2 | |
| | EQUIVALENT | 2.422 | 451.4 | 1.5499 | 696.5 | 450.8 | |
| 22 | PRIMARY | 2.100 | 800.0 | 0.5713 | 317.9 | 556.6 | 0.72 |
| | FAN | 3.000 | 300.0 | 1.0059 | 403.0 | 403.2 | |
| | EQUIVALENT | 2.479 | 456.7 | 1.5771 | 720.8 | 456.7 | |
| 23 | PRIMARY | 2.200 | 800.0 | 0.5985 | 342.2 | 572.1 | 0.70 |
| | FAN | 3.000 | 300.0 | 1.0059 | 403.0 | 403.2 | |
| | EQUIVALENT | 2.536 | 461.9 | 1.6043 | 745.2 | 466.4 | |
| 24 | PRIMARY | 2.400 | 800.0 | 0.6529 | 390.8 | 599.5 | 0.67 |
| | FAN | 3.000 | 300.0 | 1.0059 | 403.0 | 403.2 | |
| | EQUIVALENT | 2.650 | 471.8 | 1.6587 | 793.8 | 481.0 | |
| 25 | PRIMARY | 2.700 | 800.0 | 0.7345 | 463.7 | 633.9 | 0.64 |
| | FAN | 3.000 | 300.0 | 1.0059 | 403.0 | 403.2 | |
| | EQUIVALENT | 2.821 | 485.7 | 1.7404 | 866.7 | 501.4 | |
| 26 | PRIMARY | 3.100 | 800.0 | 0.8433 | 560.9 | 670.7 | 0.60 |
| | FAN | 3.000 | 300.0 | 1.0059 | 403.0 | 403.2 | |
| | EQUIVALENT | 3.049 | 502.6 | 1.8492 | 963.9 | 526.3 | |
| 27 | PRIMARY | 3.500 | 800.0 | 0.9521 | 658.2 | 700.5 | 0.58 |
| | FAN | 3.000 | 300.0 | 1.0059 | 403.0 | 403.2 | |
| | EQUIVALENT | 3.277 | 517.8 | 1.9580 | 1061.2 | 548.7 | |
| 28 | PRIMARY | 4.000 | 800.0 | 1.0881 | 779.7 | 730.9 | 0.55 |
| | FAN | 3.000 | 300.0 | 1.0059 | 403.0 | 403.2 | |
| | EQUIVALENT | 3.561 | 534.9 | 2.0940 | 1182.7 | 574.0 | |

TP TEST POINT

Table 2.4 Test conditions for Series 3.

| TP | JET | PRESSURE RATIO PT/PA | TOTAL TEMPERATURE DEG K | MASS FLOW RATE KG/S | THRUST NEWTONS | VELOCITY M/S | VELOCITY RATIO VF/VP |
|---|---|---|---|---|---|---|---|
| 29 | PRIMARY | 1.200 | 600.0 | 0.2909 | 72.0 | 247.5 | 2.68 |
| | FAN | 3.000 | 800.0 | 0.6094 | 400.7 | 662.3 | |
| | EQUIVALENT | 1.897 | 621.0 | 0.9002 | 472.7 | 527.2 | |
| 30 | PRIMARY | 1.400 | 600.0 | 0.4077 | 135.7 | 332.8 | 1.99 |
| | FAN | 3.000 | 800.0 | 0.6094 | 400.7 | 662.3 | |
| | EQUIVALENT | 2.046 | 748.4 | 1.0171 | 536.4 | 529.5 | |
| 31 | PRIMARY | 1.600 | 600.0 | 0.4952 | 193.1 | 389.9 | 1.70 |
| | FAN | 3.000 | 800.0 | 0.6094 | 400.7 | 662.3 | |
| | EQUIVALENT | 2.181 | 720.7 | 1.1046 | 593.7 | 539.9 | |
| 32 | PRIMARY | 1.700 | 600.0 | 0.5327 | 219.8 | 412.6 | 1.61 |
| | FAN | 3.000 | 800.0 | 0.6094 | 400.7 | 662.3 | |
| | EQUIVALENT | 2.243 | 713.4 | 1.1421 | 620.5 | 545.8 | |
| 33 | PRIMARY | 1.800 | 600.0 | 0.5673 | 245.4 | 432.6 | 1.53 |
| | FAN | 3.000 | 800.0 | 0.6094 | 400.7 | 662.3 | |
| | EQUIVALENT | 2.303 | 708.6 | 1.1766 | 646.1 | 551.8 | |
| 34 | PRIMARY | 1.900 | 600.0 | 0.5995 | 270.0 | 450.5 | 1.47 |
| | FAN | 3.000 | 800.0 | 0.6094 | 400.7 | 662.3 | |
| | EQUIVALENT | 2.361 | 705.5 | 1.2088 | 670.7 | 557.8 | |
| 35 | PRIMARY | 2.000 | 600.0 | 0.6310 | 294.4 | 466.6 | 1.42 |
| | FAN | 3.000 | 800.0 | 0.6094 | 400.7 | 662.3 | |
| | EQUIVALENT | 2.418 | 702.8 | 1.2404 | 695.1 | 563.5 | |
| 36 | PRIMARY | 2.100 | 600.0 | 0.6626 | 318.7 | 481.2 | 1.38 |
| | FAN | 3.000 | 800.0 | 0.6094 | 400.7 | 662.3 | |
| | EQUIVALENT | 2.475 | 700.3 | 1.2719 | 719.4 | 569.1 | |
| 37 | PRIMARY | 2.200 | 600.0 | 0.6941 | 343.1 | 494.5 | 1.34 |
| | FAN | 3.000 | 800.0 | 0.6094 | 400.7 | 662.3 | |
| | EQUIVALENT | 2.532 | 697.9 | 1.3035 | 743.8 | 574.3 | |
| 38 | PRIMARY | 2.400 | 600.0 | 0.7572 | 391.8 | 518.2 | 1.28 |
| | FAN | 3.000 | 800.0 | 0.6094 | 400.7 | 662.3 | |
| | EQUIVALENT | 2.647 | 693.5 | 1.3666 | 792.5 | 584.3 | |
| 39 | PRIMARY | 2.700 | 600.0 | 0.8519 | 464.8 | 547.7 | 1.21 |
| | FAN | 3.000 | 800.0 | 0.6094 | 400.7 | 662.3 | |
| | EQUIVALENT | 2.818 | 687.6 | 1.4612 | 865.5 | 597.8 | |
| 40 | PRIMARY | 3.100 | 600.0 | 0.9781 | 562.2 | 579.4 | 1.14 |
| | FAN | 3.000 | 800.0 | 0.6094 | 400.7 | 662.3 | |
| | EQUIVALENT | 3.046 | 680.9 | 1.5874 | 962.9 | 613.7 | |
| 41 | PRIMARY | 3.500 | 600.0 | 1.1043 | 659.6 | 605.0 | 1.09 |
| | FAN | 3.000 | 800.0 | 0.6094 | 400.7 | 662.3 | |
| | EQUIVALENT | 3.275 | 675.2 | 1.7136 | 1060.3 | 627.8 | |
| 42 | PRIMARY | 4.000 | 600.0 | 1.2620 | 781.4 | 631.0 | 1.05 |
| | FAN | 3.000 | 800.0 | 0.6094 | 400.7 | 662.3 | |
| | EQUIVALENT | 3.560 | 669.1 | 1.8714 | 1182.1 | 643.1 | |

TP TEST POINT

Table 2.5 Test conditions for Series 4.

| TP | JET | PRESSURE RATIO PT/PA | TOTAL TEMPERATURE DEG K | MASS FLOW RATE KG/S | THRUST NEWTONS | VELOCITY M/S | VELOCITY RATIO VF/VP |
|---|---|---|---|---|---|---|---|
| 43 | PRIMARY | 1.200 | 300.0 | 0.4121 | 72.1 | 174.9 | 4.27 |
| | FAN | 4.300 | 800.0 | 0.8734 | 636.6 | 746.4 | |
| | EQUIVALENT | 2.450 | 671.8 | 1.2855 | 708.7 | 554.4 | |
| 44 | PRIMARY | 1.400 | 300.0 | 0.5786 | 136.0 | 235.1 | 3.17 |
| | FAN | 4.300 | 800.0 | 0.8734 | 636.6 | 746.4 | |
| | EQUIVALENT | 2.600 | 592.9 | 1.4520 | 772.6 | 535.3 | |
| 45 | PRIMARY | 1.600 | 300.0 | 0.7036 | 193.7 | 275.3 | 2.71 |
| | FAN | 4.300 | 800.0 | 0.8734 | 636.6 | 746.4 | |
| | EQUIVALENT | 2.735 | 556.3 | 1.5770 | 830.3 | 530.1 | |
| 46 | PRIMARY | 1.700 | 300.0 | 0.7574 | 220.6 | 291.3 | 2.56 |
| | FAN | 4.300 | 800.0 | 0.8734 | 636.6 | 746.4 | |
| | EQUIVALENT | 2.798 | 544.4 | 1.6308 | 857.2 | 529.5 | |
| 47 | PRIMARY | 1.800 | 300.0 | 0.8070 | 246.4 | 305.3 | 2.44 |
| | FAN | 4.300 | 800.0 | 0.8734 | 636.6 | 746.4 | |
| | EQUIVALENT | 2.859 | 535.2 | 1.6804 | 883.0 | 529.6 | |
| 48 | PRIMARY | 1.900 | 300.0 | 0.8532 | 271.2 | 317.9 | 2.35 |
| | FAN | 4.300 | 800.0 | 0.8734 | 636.6 | 746.4 | |
| | EQUIVALENT | 2.917 | 527.8 | 1.7266 | 907.8 | 530.2 | |
| 49 | PRIMARY | 2.000 | 300.0 | 0.8981 | 295.6 | 329.2 | 2.27 |
| | FAN | 4.300 | 800.0 | 0.8734 | 636.6 | 746.4 | |
| | EQUIVALENT | 2.974 | 521.2 | 1.7715 | 932.2 | 531.0 | |
| 50 | PRIMARY | 2.100 | 300.0 | 0.9430 | 320.0 | 339.4 | 2.20 |
| | FAN | 4.300 | 800.0 | 0.8734 | 636.6 | 746.4 | |
| | EQUIVALENT | 3.032 | 515.0 | 1.8164 | 956.6 | 531.7 | |
| 51 | PRIMARY | 2.200 | 300.0 | 0.9879 | 344.4 | 348.8 | 2.14 |
| | FAN | 4.300 | 800.0 | 0.8734 | 636.6 | 746.4 | |
| | EQUIVALENT | 3.089 | 509.2 | 1.8613 | 981.1 | 532.4 | |
| 52 | PRIMARY | 2.400 | 300.0 | 1.0777 | 393.3 | 365.4 | 2.04 |
| | FAN | 4.300 | 800.0 | 0.8734 | 636.6 | 746.4 | |
| | EQUIVALENT | 3.203 | 498.4 | 1.9511 | 1029.9 | 533.8 | |
| 53 | PRIMARY | 2.700 | 300.0 | 1.2124 | 466.5 | 386.1 | 1.93 |
| | FAN | 4.300 | 800.0 | 0.8734 | 636.6 | 746.4 | |
| | EQUIVALENT | 3.375 | 484.1 | 2.0858 | 1103.1 | 535.9 | |
| 54 | PRIMARY | 3.100 | 300.0 | 1.3921 | 564.1 | 408.2 | 1.83 |
| | FAN | 4.300 | 800.0 | 0.8734 | 636.6 | 746.4 | |
| | EQUIVALENT | 3.604 | 467.9 | 2.2655 | 1200.8 | 538.4 | |
| 55 | PRIMARY | 3.500 | 300.0 | 1.5717 | 661.8 | 426.1 | 1.75 |
| | FAN | 4.300 | 800.0 | 0.8734 | 636.6 | 746.4 | |
| | EQUIVALENT | 3.833 | 454.3 | 2.4451 | 1298.4 | 540.9 | |
| 56 | PRIMARY | 4.000 | 300.0 | 1.7962 | 783.8 | 444.3 | 1.68 |
| | FAN | 4.300 | 800.0 | 0.8734 | 636.6 | 746.4 | |
| | EQUIVALENT | 4.119 | 440.2 | 2.6696 | 1420.5 | 543.8 | |

TP TEST POINT

# 3. MEASURED RESULTS

The results from the acoustic experiments conducted in this program are presented in this section in sufficient detail to show the major features of shock associated noise and its reduction in inverted-velocity-profile coannular jets. The data are plotted and discussed to cover three specific aspects: (1) the variation of coannular jet noise levels with primary stream Mach number, (2) the comparison of noise characteristics of coannular jets and equivalent single jets on an absolute basis, and (3) the differences in noise levels between the coannular jet and the equivalent single jet (on a relative basis) to quantify the noise reductions. In addition to the results presented in this section, a comprehensive set of sound pressure level data in the form of one-third octave band spectra is given in Appendix 1 of this report.

## 3.1 OVERALL SOUND PRESSURE LEVEL RESULTS

The overall sound pressure levels as a function of observer angle $\theta$ (relative to the jet exhaust) are plotted in Figure 3.1 for five values of the primary stream Mach number ($M_p$) to cover the entire range of coannular jet operating conditions within test series 1. The two lowest values of $M_p$ are subsonic, the third value ($M_p = 1.05$) is slightly supersonic, and the remaining two values of $M_p$ are supersonic. Also shown in the same figure are the corresponding overall sound pressure levels for the equivalent single jet. These are indicated by the square symbols. For both types of jets (i.e., coannular jet and equivalent single jet) operated at supersonic conditions, the noise radiated at small angles to the jet exhaust is normally dominated by the turbulent jet mixing noise component, while the noise radiated at large angles is primarily controlled by the shock noise component. Since the main objective in this program is to study the reduction of shock associated noise in inverted-velocity-profile coannular jets, we will restrict the discussion that follows mainly to the OASPL results in the forward arc of the jet.

Figure 3.1 shows that at the lowest primary stream Mach number, $M_p = 0.52$, the coannular jet is much noisier than the equivalent single jet in the forward arc. This is because the shock associated noise from the fan stream of the coannular jet is very high. As the value of $M_p$ is increased to 1.05, a dramatic reversal in trend occurs, and the coannular jet is now much quieter than the equivalent single jet in the forward arc. Finally, as the primary flow becomes more and more supersonic, the shock structure in this stream gains strength, and the resulting shock associated noise becomes more and more important. The net result is that in this test series, even though the coannular jet at $M_p = 1.38$ is still quieter than the equivalent single jet in the forward arc, the effective noise reduction is not as large as that in the $M_p = 1.05$ case. That is, it appears that the reduction in shock associated noise from the coannular jet is maximum when the primary stream is operated at a Mach number just above unity. This observation will be reinforced further when we will present the results in a different form as well as when we will examine the detailed spectral results.

So far we have discussed the variation of OASPL results with $\theta$ and $M_p$ for test series 1. For completeness, the corresponding results obtained from test series 2, 3 and 4 are presented in the same fashion in Figures 3.2, 3.3, and 3.4, respectively. An examination of these figures reveals that even though minor variations exist in the results, the overall features discussed above are evident in all cases. On the whole, a coannular jet, which is approximately 8 - 10 dB noisier than the equivalent single jet in the forward arc when the primary stream is subsonic, becomes approximately 3 - 7 dB quieter when the primary stream becomes slightly supersonic. The exact noise benefit varies from one test series to another, and it is governed by the basic jet mixing noise component of the coannular jet at the optimum condition, whose level undoubtedly varies from one test series to another. We will return to this point later.

To make the above observations clearer, the overall sound pressure level results for all four test series are cross-plotted in Figures 3.5 through 3.8. Here, the results at $\theta = 120°$ only are considered (where shock noise dominates), and the OASPL values of the coannular jet (circles) and the equivalent single jet (squares) are compared as a function of the primary stream Mach number, $M_p$. Each of these four figures reveal two important features. First, when the variation of coannular jet noise levels with $M_p$ is examined on its own, it is absolutely clear that the noise level reaches a minimum within each test series, and this "optimum" condition is obtained when the primary stream Mach number becomes slightly greater than one. The second feature arises when the coannular jet noise levels are compared with the corresponding equivalent single jet noise levels. Here, as observed earlier in the directivity plots (Figures 3.1 through 3.4), it is quite clear that within each test series, the coannular jet, which starts off by being noisier than the equivalent single jet when $M_p$ is in the low subsonic range, becomes quieter as $M_p$ is increased, especially when $M_p$ is supersonic. Furthermore, as before, the <u>maximum</u> noise reduction appears to occur when the primary stream Mach number is just slightly supersonic.

Finally, the reduction of shock associated noise from coannular jets can be examined even more explicitly by plotting the <u>differences</u> in overall sound pressure levels, $\Delta$OASPL, between the coannular jet and the equivalent single jet. These results are shown in Figures 3.9 through 3.12 for test series 1 through 4, respectively. Once again, the noise benefit is examined as a function of the primary stream Mach number, $M_p$. However, in these four figures, the results at $\theta = 90°$ are also included together with the results at $\theta = 120°$ which we have been concentrating on so far. The figures really speak for themselves. Noting that the coannular jet is quieter than the equivalent single jet when $\Delta$OASPL is negative, and vice versa, each one of these four figures shows that at both $\theta = 90°$ and $\theta = 120°$, the noise reduction is maximum when the primary stream is operated just above the critical pressure ratio (i.e., when $M_p$ is greater than approximately 1.0). The maximum noise reduction at $\theta = 90°$ is slightly lower than the maximum noise reduction at $\theta = 120°$. As mentioned earlier, since this is governed by the basic level of the jet mixing noise component of the coannular jet at the "optimum" or "minimum noise" condition, the results are simply telling us that the jet mixing noise level at $\theta = 90°$ is higher than the jet mixing noise level at $\theta = 120°$. This is entirely consistent with the existing knowledge of shock-free coannular jet noise, in particular the variation of jet mixing noise level with observer angle θ.

This last aspect is very important from the standpoint of practical application of the results of these experiments. There is no doubt that the shock associated noise from a coannular jet is virtually eliminated when the primary jet is operated at a slightly supersonic Mach number. However, the maximum noise reduction at this "optimum" condition varies from one test series to another, it being the highest for test series 2 and the lowest for test series 3 in the present experiments. This implies that at the "optimum" condition, the noise level of the coannular jet is governed or set by the residual jet mixing noise. Therefore, in order to obtain the maximum noise reduction relative to the equivalent single jet, the basic jet mixing noise at the optimum condition of the coannular jet must also be reduced relative to the jet mixing noise level of the equivalent single jet. In principle, this can be achieved by a judicious selection of the engine cycle for a particular application. That is, to obtain the maximum noise reduction from an inverted-velocity-profile coannular jet relative to the equivalent single jet, two criteria must be kept in mind. First, the pressure ratio of the primary flow must be kept slightly greater than the critical value to eliminate (or at least minimize) the shock associated noise, and second, the combination of fan nozzle pressure ratio and primary and fan flow total temperatures must be selected carefully to minimize the jet mixing noise component.

Another important finding which emerges from these results, and which must not be overlooked, is that in test series 2, even though the coannular jet is operated at normal-velocity-profile conditions (i.e., with fan-to-primary velocity ratio $V_f/V_p < 1$ — see Table 2.3), large reductions in noise are still obtained. In fact, in the present experiments, the reductions in the OASPLs are the largest for test series 2. Hence, it is apparent that a coannular jet need not be necessarily operated at inverted-velocity-profile conditions to reduce the shock associated noise component. Provided that the coannular jet is operated with the primary stream slightly supersonic, the shock associated noise is virtually eliminated (or at least minimized) regardless of whether the velocity ratio $V_f/V_p$ is less than or greater than unity.

So far we have discussed the OASPL results only in the forward arc of the jet, which is of primary interest as far as the objective of this program is concerned. However, to verify that the results from these experiments are consistent with past observations on jet mixing noise from coannular jets, it is worthwhile to at least look at some results in the rear arc where the noise is dominated by the jet mixing noise component. Figures 3.13 and 3.14 show the variation of ΔOASPL with primary stream Mach number ($M_p$) at $\theta = 30°$ for test series 1 and 2. In both the figures, the values of velocity ratio $V_f/V_p$ are also indicated. In Figure 3.13, the coannular jet is operated at inverted-velocity-profile conditions, and the noise reductions at $\theta = 30°$ are essentially due to the reduction in the jet mixing noise relative to that of the equivalent single jet. In contrast, the coannular jet is operated at normal-velocity-profile conditions in Figure 3.14. As a result, the jet mixing noise levels at $\theta = 30°$ are higher than those for the equivalent single jet. These findings are entirely in agreement with the results of previous studies on coannular jet noise under shock-free conditions, as described in Reference 6.

## 3.2 ONE-THIRD OCTAVE BAND SPL SPECTRA

In the preceding subsection dealing with overall sound pressure level results, it was assumed throughout that the noise levels in the forward arc of the jet are dominated by shock associated noise, and therefore, the reductions in OASPLs in the forward arc reflect the reductions in shock associated noise. We can now proceed to substantiate this general assumption by presenting detailed spectral results for the sound pressure.

Figures 3.15 through 3.18 show the comparison between SPL spectra of the coannular jet and the equivalent single jet at $\theta = 120°$ for the four series of experiments. Within each test series, five values of the primary stream Mach number ($M_p$) are chosen to be consistent with the OASPL comparisons presented earlier in Figures 3.1 through 3.4. In general, as is usually the case, the low frequency parts of the spectra are smoothly varying, which is a well-established characteristic of the jet mixing noise component. On the other hand, the middle and high frequency parts of the spectra display the peaky shapes associated with the shock associated noise component, except, of course, when the shock noise is eliminated or is not dominant.

On the whole, the low frequency noise levels from the coannular jet are about the same as the corresponding low frequency noise levels from the equivalent single jet. Hence, it can be concluded that in the forward arc the jet mixing noise levels for the coannular jet and the equivalent single jet are roughly the same. It is the difference in noise levels at the high frequencies, however, that is of major interest in the present work. In this regard, each of the four figures essentially displays a similar trend, which is as follows. At the lowest value of $M_p$, the shock noise from the coannular jet is much higher than the equivalent single jet noise level. This shock noise is generated in the fan stream of the coannular jet since the primary stream is subsonic, and hence shock-free. As $M_p$ is increased, the shock noise in the equivalent single jet increases in level, while the shock noise in the coannular jet decreases. At $M_p = 1.05$, there is little indication of any shock noise in the coannular jet (exept in Figure 3.18), and the entire spectrum is broad and smooth. This is the so-called "optimum" condition, where the coannular jet gives the maximum noise reduction relative to the equivalent single jet. Beyond this optimum condition, when $M_p$ is increased in the supersonic range, a shock associated noise peak in the coannular jet noise spectrum reappears. However, the shock associated noise in this regime is generated by the supersonic primary stream, and its strength increases as the Mach number $M_p$ increases. At the highest value of $M_p$ in each figure, the shock noise from the coannular jet is almost the same as the shock noise from the equivalent single jet.

To emphasize the elimination or reduction of shock associated noise in a coannular jet at the optimum condition even further, the SPL spectra at $\theta = 120°$ from all the test points are presented in Figures 3.19 through 3.22. The four figures refer to the four series of experiments. Within each test series, the results at all values of the primary stream Mach number ($M_p$), covering a wide range from 0.52 to 1.56, are included for completeness. As each figure is glanced over from top to bottom, it becomes absolutely clear that the shock associated noise from the coannular jet is eliminated (or at least minimized) when the primary flow Mach number is slightly greater than one. The spectrum at this condition is indicated by the thicker line in each figure. On either side of this minimum noise condition, shock associated noise is clearly present. For $M_p \lesssim 1$, it is generated in the fan stream of the coannular jet, while for $M_p \gtrsim 1$, it is generated in the supersonic primary stream of the coannular jet.

Finally, to conclude this presentation of the spectral results, it is worthwhile to touch upon the jet mixing noise aspect, just as it was done in the case of the OASPL results. Figures 3.23 and 3.24 show the comparison of SPL spectra from the coannular jet and the equivalent single jet at $\theta = 30^\circ$, where the jet mixing noise predominates.

In Figure 3.23, the fan-to-primary velocity ratio ($V_f/V_p$) is 2.27. At this inverted-profile condition, the coannular jet exhibits a double-peaked spectrum shape, where the second peak is the result of the turbulent mixing noise generated in the outer or fan stream shear layer. The comparison with the equivalent single jet noise spectrum is qualitatively identical to similar comparisons seen in the previous studies (for example, ref. 6). That is, the coannular jet is quieter than the equivalent single jet at middle frequencies and noisier at the high frequencies. The physical reasons for these effects have also been fully understood in the previous contract study (ref. 4).

In contrast, the comparison shown in Figure 3.24 refers to a case where the coannular jet is operated at normal-velocity-profile conditions, the value of $V_f/V_p$ being 0.81. In this case, the coannular jet is no longer quieter than the equivalent single jet in the middle frequency range. Again, this is entirely consistent with previous observations (ref. 6) on the noise characteristics of uninverted- or normal-velocity-profile coannular jets under shock-free conditions.

## 3.3 OVERALL SOUND POWER LEVEL RESULTS

The polar sound pressure level results (lossless data) obtained from the present experiments were used to compute the corresponding sound power levels for all test points, using conventional procedures. The overall sound power levels (OAPWL) for all coannular jet and equivalent single jet test conditions were calculated by adding the one-third octave band sound power levels.

The results from the entire test program are presented on a relative basis in Figure 3.25, where the values of ΔOAPWL (defined as OAPWL for the coannular jet minus OAPWL for the equivalent single jet) for each test series are plotted against the fan-to-primary velocity ratio, $V_f/V_p$. The figure is a remarkable demonstration of the "minimum noise condition" in coannular jets. For each test series, a condition exists at which the acoustic energy radiated by the coannular jet, compared to that radiated from the equivalent single jet (at identical thrust, mass flow rate and exit area), attains a minimum value. Also shown in Figure 3.25 are vertical arrows which indicate the values of $V_f/V_p$ for each test series where the primary stream Mach number $M_p$ is approximately 1.0. These values of $V_f/V_p$ agree remarkably well with the minimum points in the ΔOAPWL curves. Therefore, it can be concluded that the reduction in the total acoustic power of a coannular jet due to the elimination (or reduction) of the shock associated noise component is maximum when the primary flow is slightly supersonic. Furthermore, unlike the reduction of jet mixing noise from a coannular jet, which occurs only at inverted-velocity-profile conditions, velocity ratio ($V_f/V_p$) is not an important parameter in the elimination or reduction of shock associated noise from a coannular jet. The shock associated noise reduction can be achieved at normal- as well as inverted-velocity-profile conditions, provided $M_p$ is maintained greater than approximately 1.0.

## 3.4 PERCEIVED NOISE LEVEL RESULTS

The model-scale acoustic data presented above were finally transformed to typical full-scale conditions using standard scaling procedures for jet noise. A scale factor of twenty was used for this purpose, and this resulted into an equivalent nozzle diameter of 1.32 meters for the larger-scale configuration. The lossless larger-scale data were then subjected to atmospheric attenuation corrections for standard FAA day (25° C, 70% relative humidity), and static perceived noise levels (PNL's) in PNdB were calculated for several sideline distances including 305 m (1000 ft) and 649 m (2128 ft).

As in the case of the overall sound power level results, the (static) peak PNL values for the coannular jet and the equivalent single jet were used to calculate the difference between the two (called ΔPEAK PNL) at all test conditions. The variation of ΔPEAK PNL with fan-to-primary velocity ratio ($V_f/V_p$) for each test series is shown in Figures 3.26 and 3.27 for the two sideline distances of 305 m and 649 m, respectively. The results are quite similar to the ΔOAPWL plot of Figure 3.25, and hence, the same observations and conclusions made earlier in Section 3.3 apply here as well. Briefly speaking, at both sideline distances considered here, the (static) peak PNL's from the coannular jet, relative to the peak PNL's of the equivalent single jet, reach a minimum value when the primary stream of the coannular jet is operated just above $M_p = 1$. This minimum noise condition is a direct result of the reduction (or elimination) of shock associated noise from coannular jets, and depending upon the test series, it occurs at inverted- as well as normal-velocity-profile conditions.

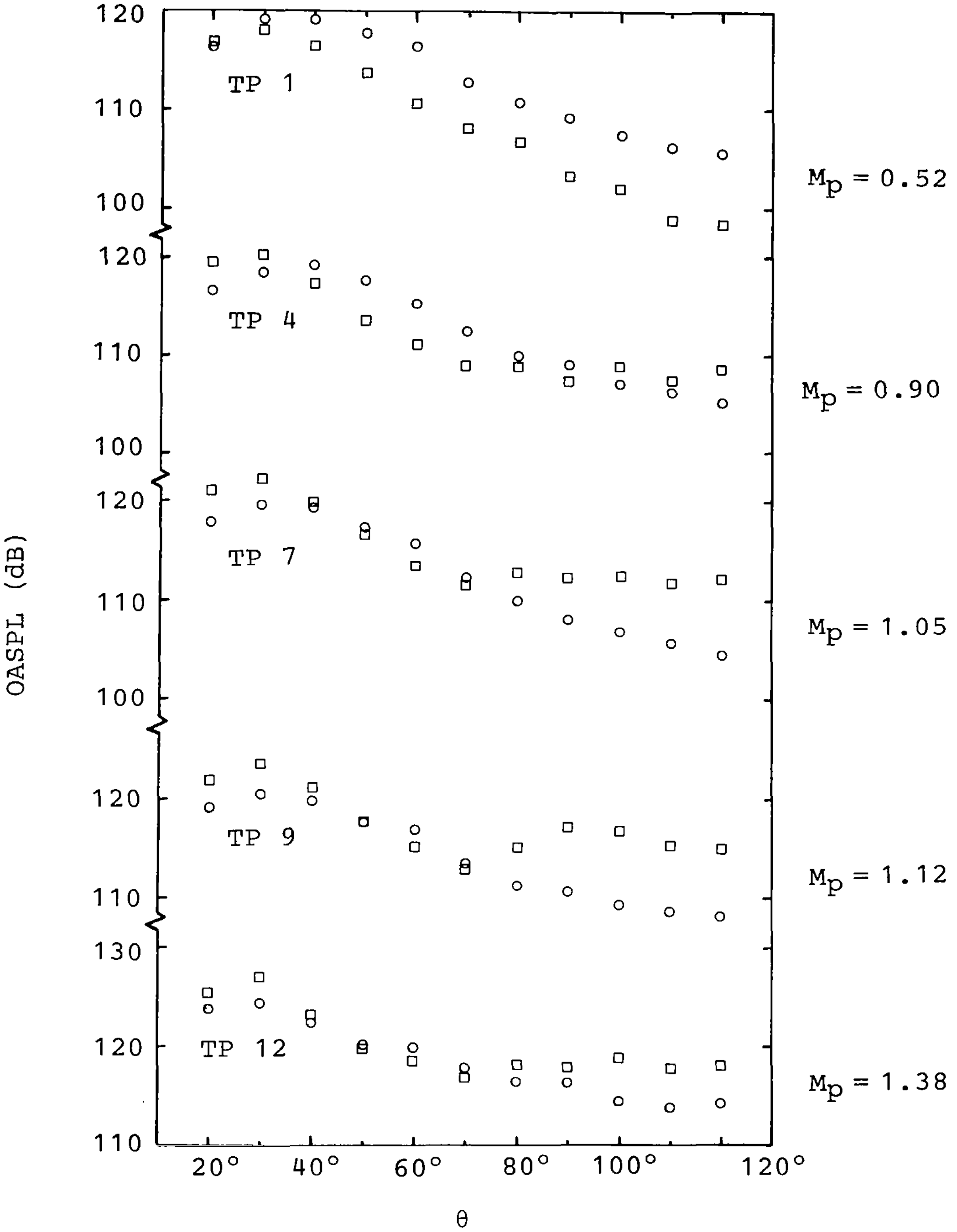


Figure 3.1 Variation of OASPL directivity with primary stream Mach number ($M_p$): Test Series 1.
○ Coannular Jet, □ Equivalent Single Jet

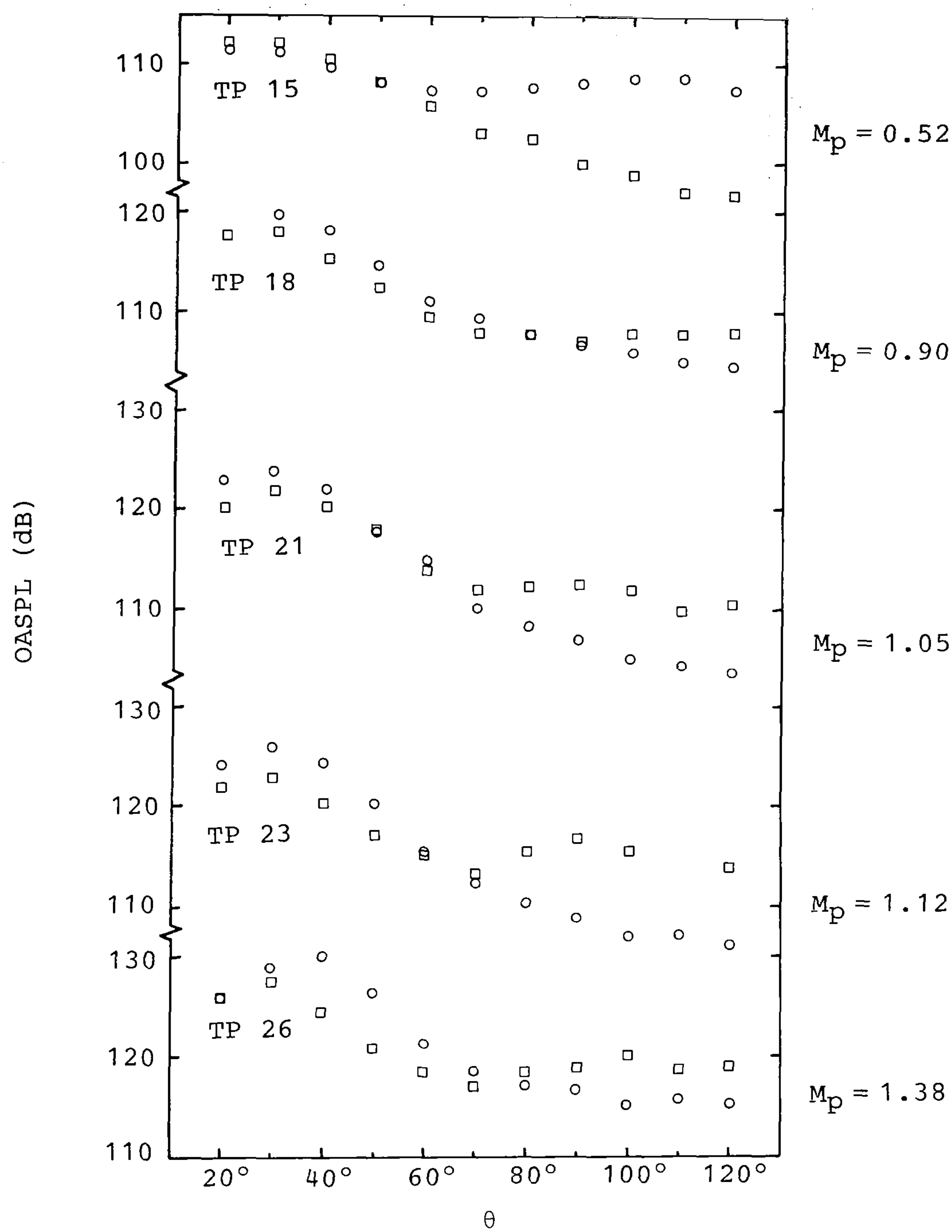


Figure 3.2 Variation of OASPL directivity with primary stream Mach number ($M_p$): Test Series 2.
O Coannular Jet, □ Equivalent Single Jet

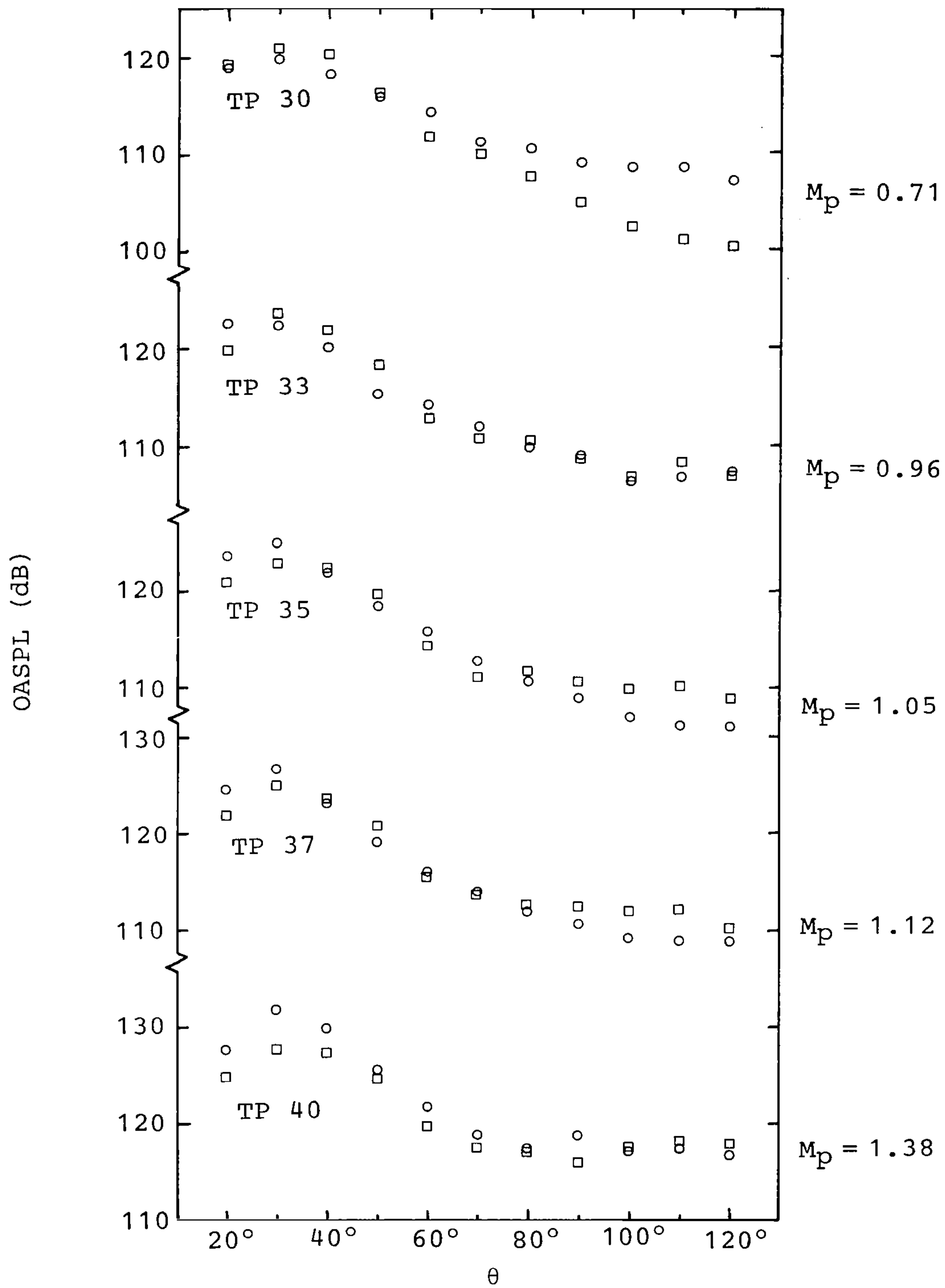


Figure 3.3 Variation of OASPL directivity with primary stream Mach number ($M_p$): Test Series 3.
○ Coannular Jet, □ Equivalent Single Jet

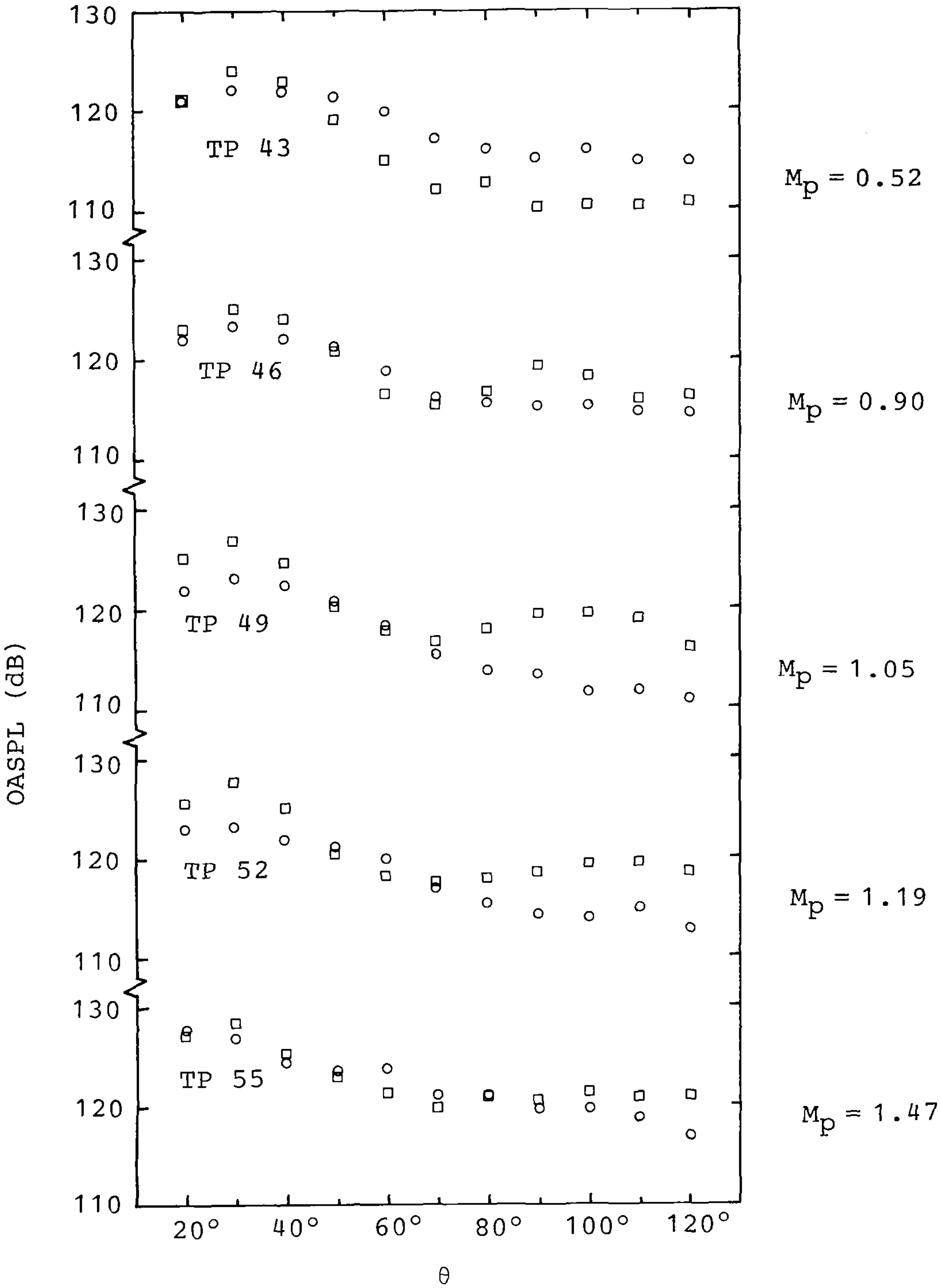


Figure 3.4 Variation of OASPL directivity with primary stream Mach number ($M_p$): Test Series 4.
O Coannular Jet, □ Equivalent Single Jet

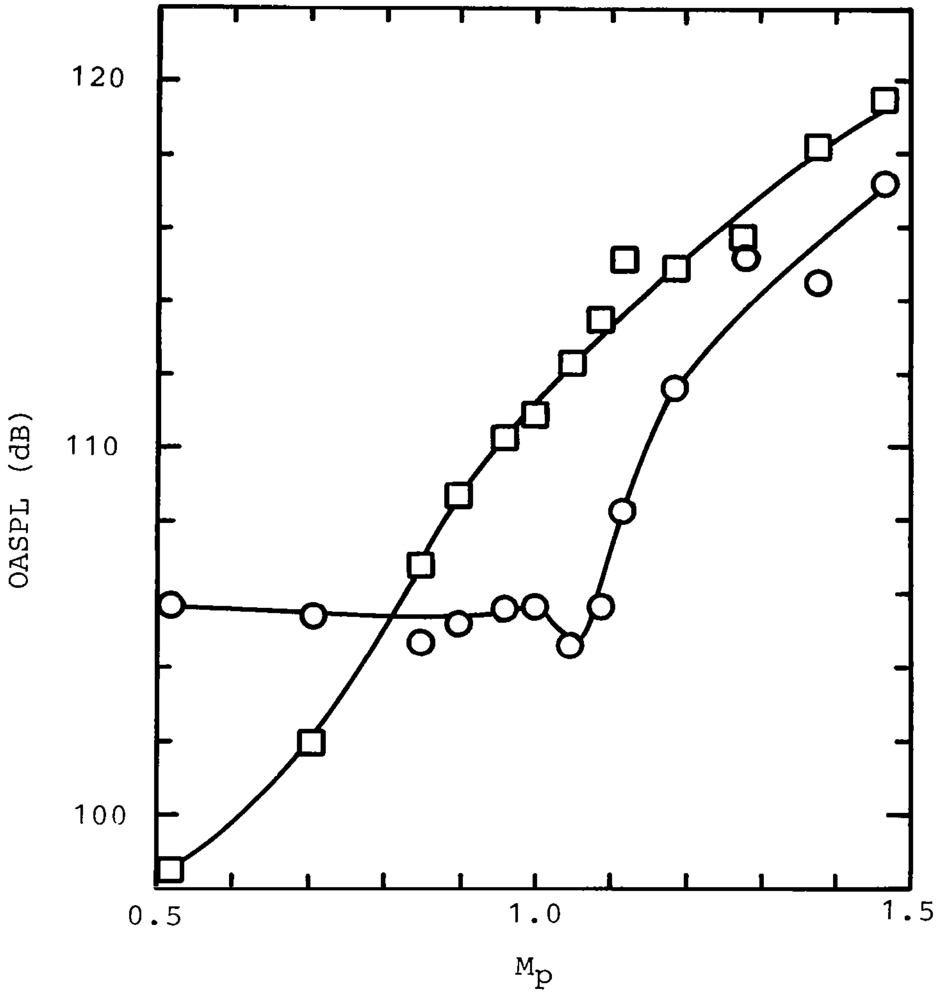


Figure 3.5 Comparison of noise levels from coannular jet and equivalent single jet: Test Series 1; $\theta = 120°$.
○ Coannular Jet, □ Equivalent Single Jet

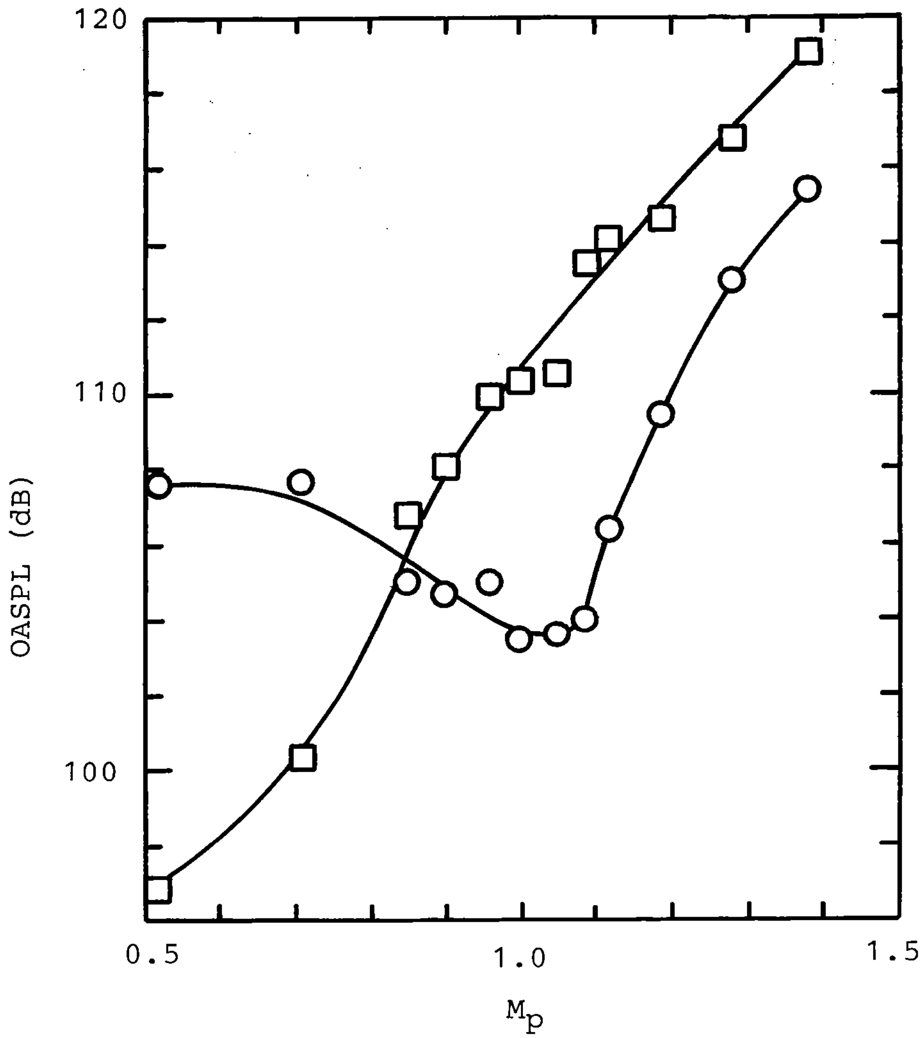


Figure 3.6 Comparison of noise levels from coannular jet and equivalent single jet: Test Series 2; $\theta = 120°$. ○ Coannular Jet, □ Equivalent Single Jet

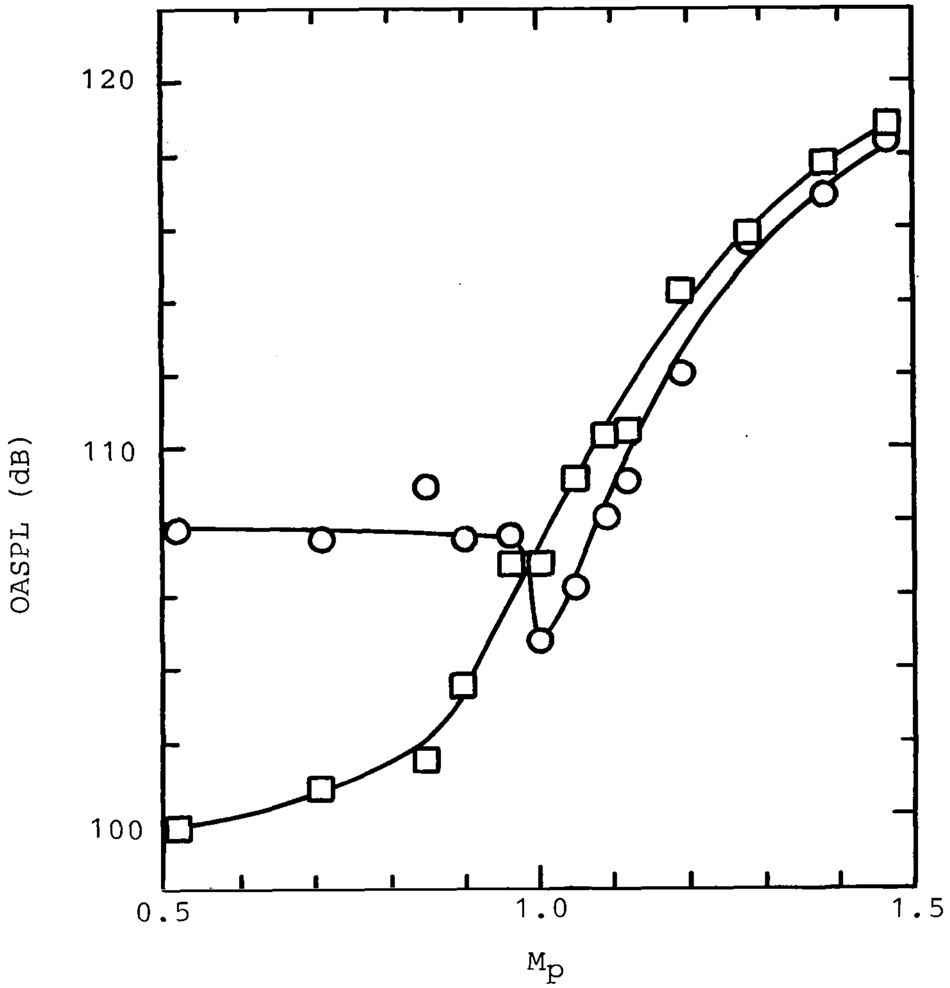


Figure 3.7 Comparison of noise levels from coannular jet and equivalent single jet: Test Series 3; $\theta = 120°$. ○ Coannular Jet, □ Equivalent Single Jet

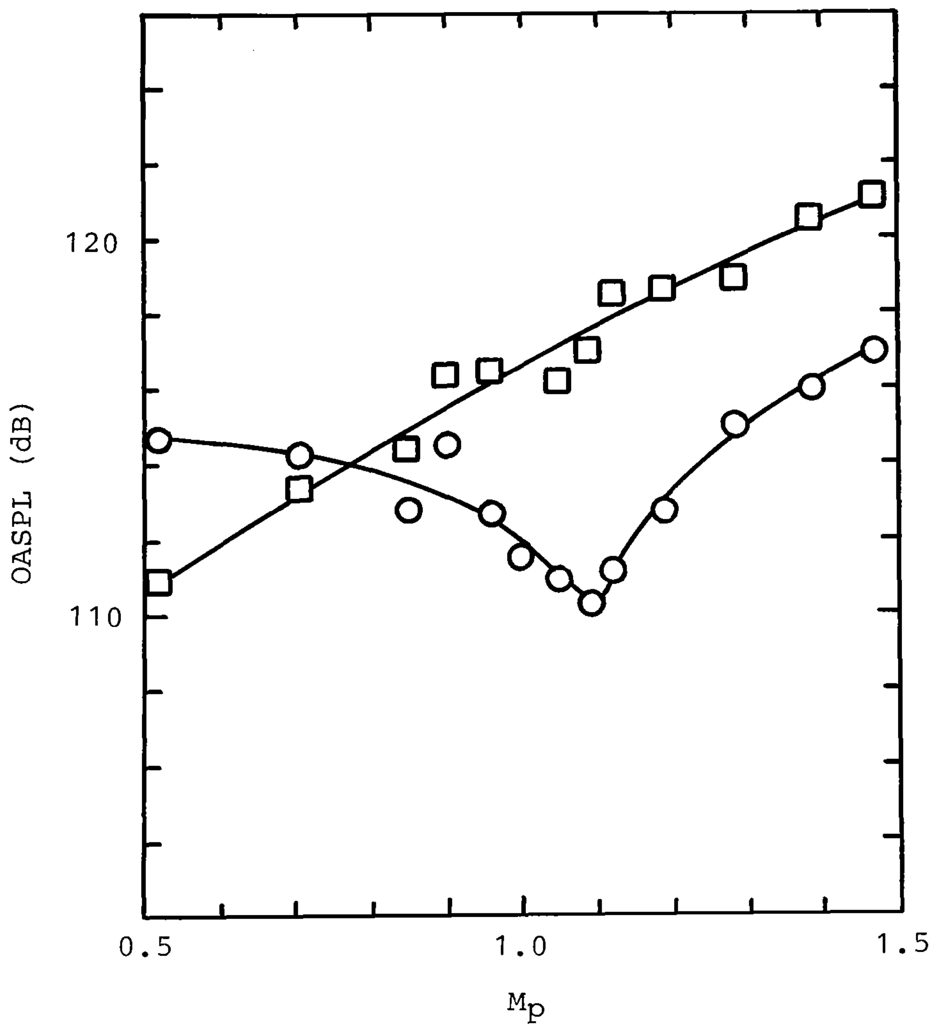


Figure 3.8 Comparison of noise levels from coannular jet and equivalent single jet: Test Series 4; $\theta = 120°$.
○ Coannular Jet, □ Equivalent Single Jet

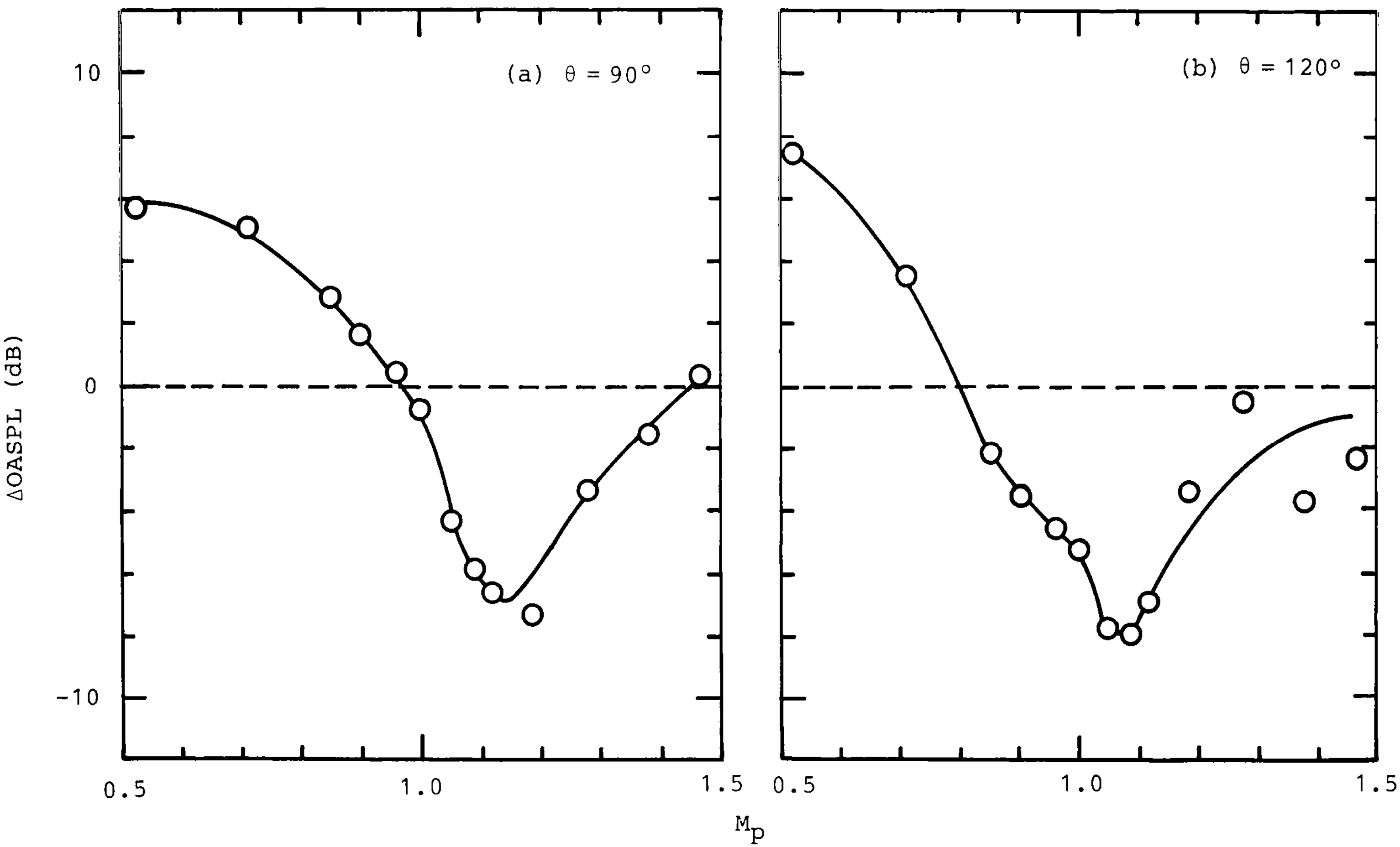


ΔOASPL = OASPL (Coannular Jet) - OASPL (Equivalent Single Jet)

Figure 3.9 Variation of ΔOASPL with $M_p$: Test Series 1.

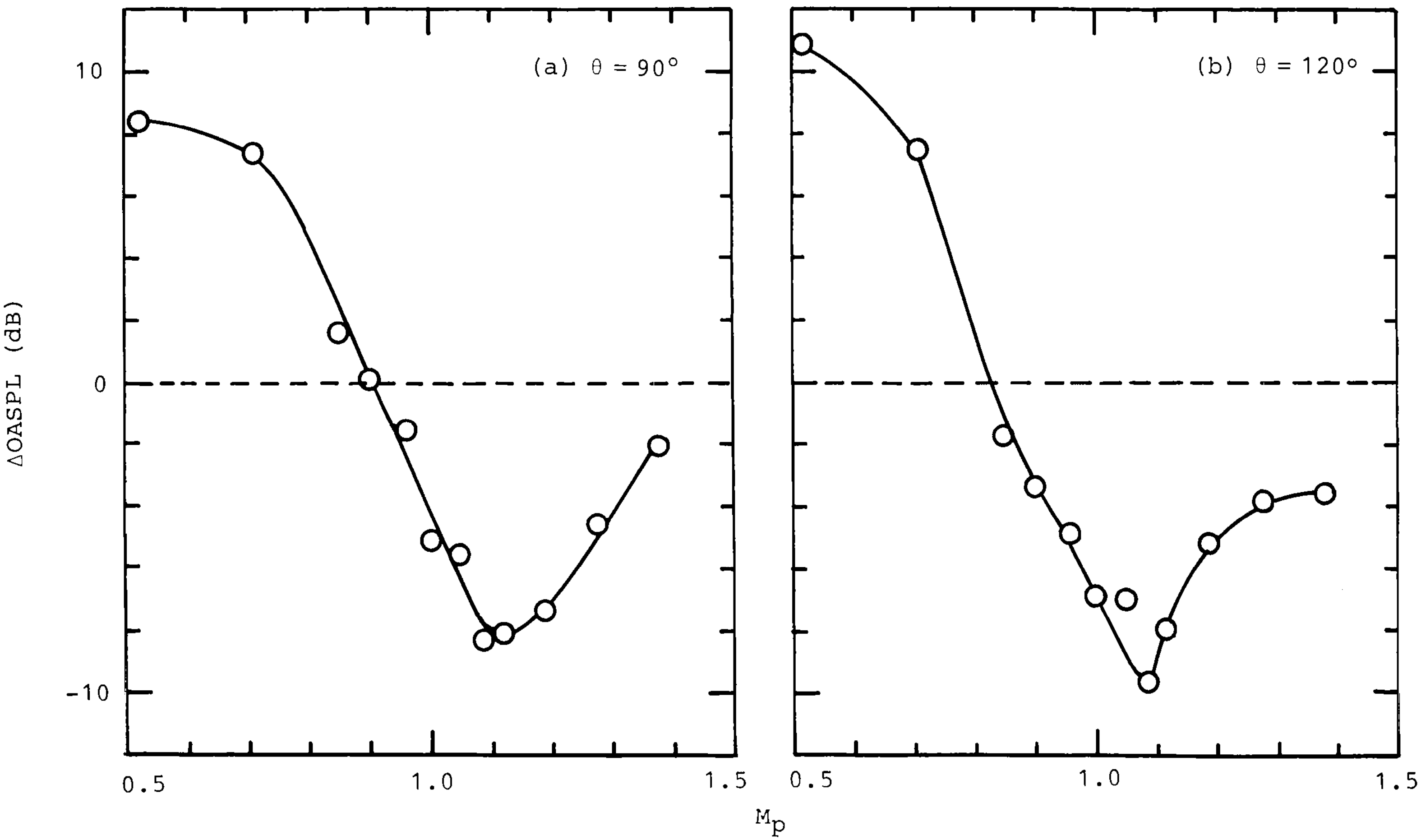


$\Delta OASPL = OASPL$ (Coannular Jet) - $OASPL$ (Equivalent Single Jet)

Figure 3.10 Variation of ΔOASPL with $M_p$: Test Series 2.

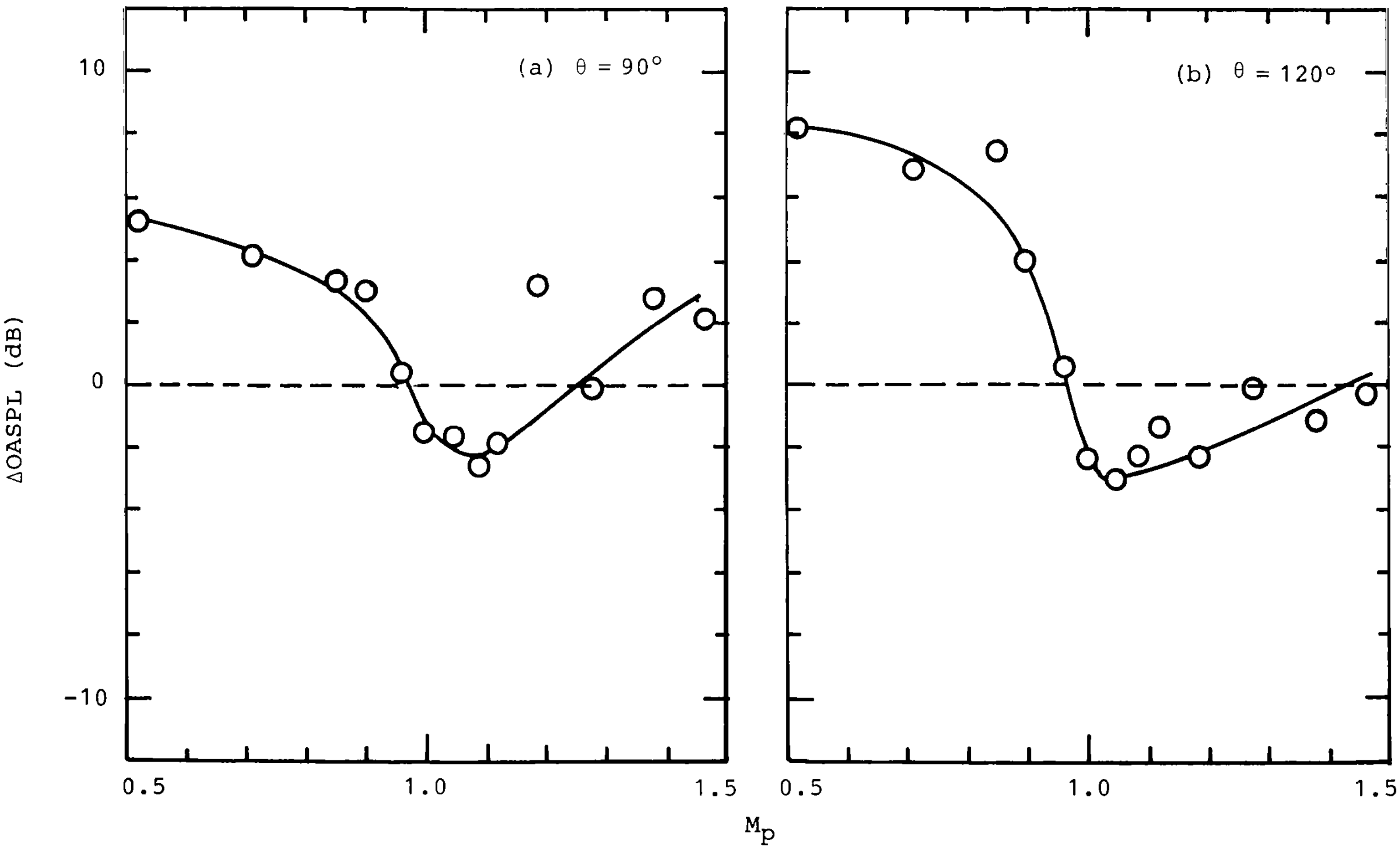


ΔOASPL = OASPL (Coannular Jet) - OASPL (Equivalent Single Jet)

Figure 3.11 Variation of ΔOASPL with $M_p$: Test Series 3.

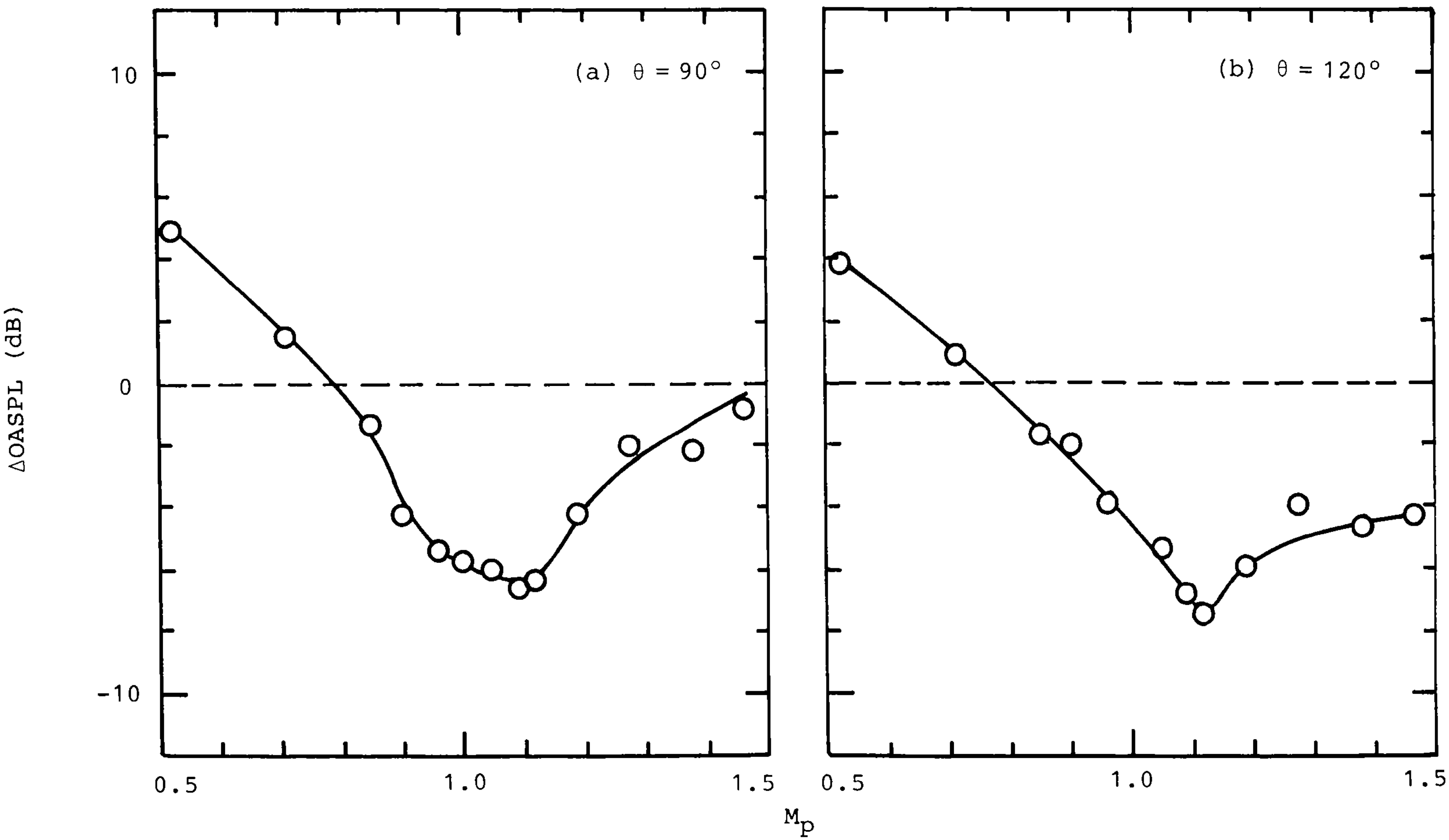


ΔOASPL = OASPL (Coannular Jet) - OASPL (Equivalent Single Jet)

Figure 3.12 Variation of ΔOASPL with $M_p$: Test Series 4.

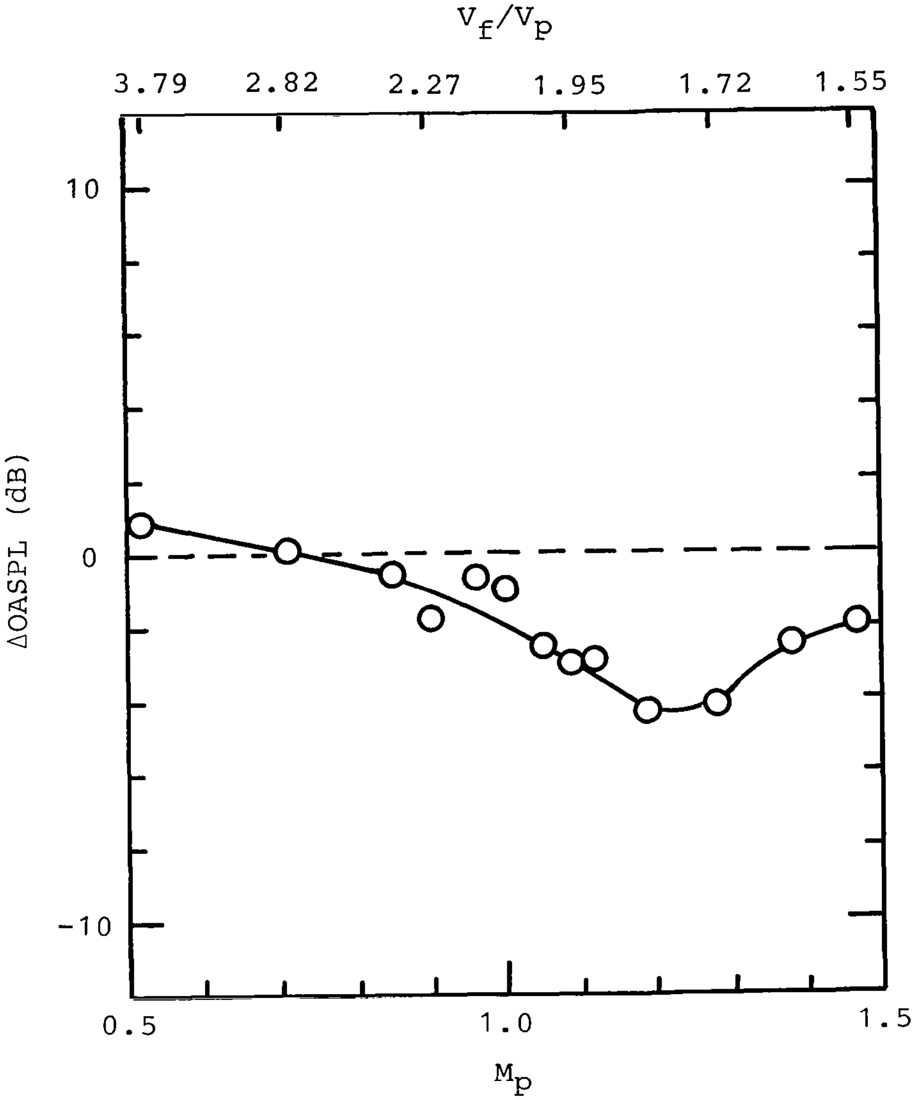

Vf/Vp
3.79
2.82
2.27
1.95
1.72
1.55
10
0
-10
ΔOASPL (dB)
0.5
1.0
1.5
Mp

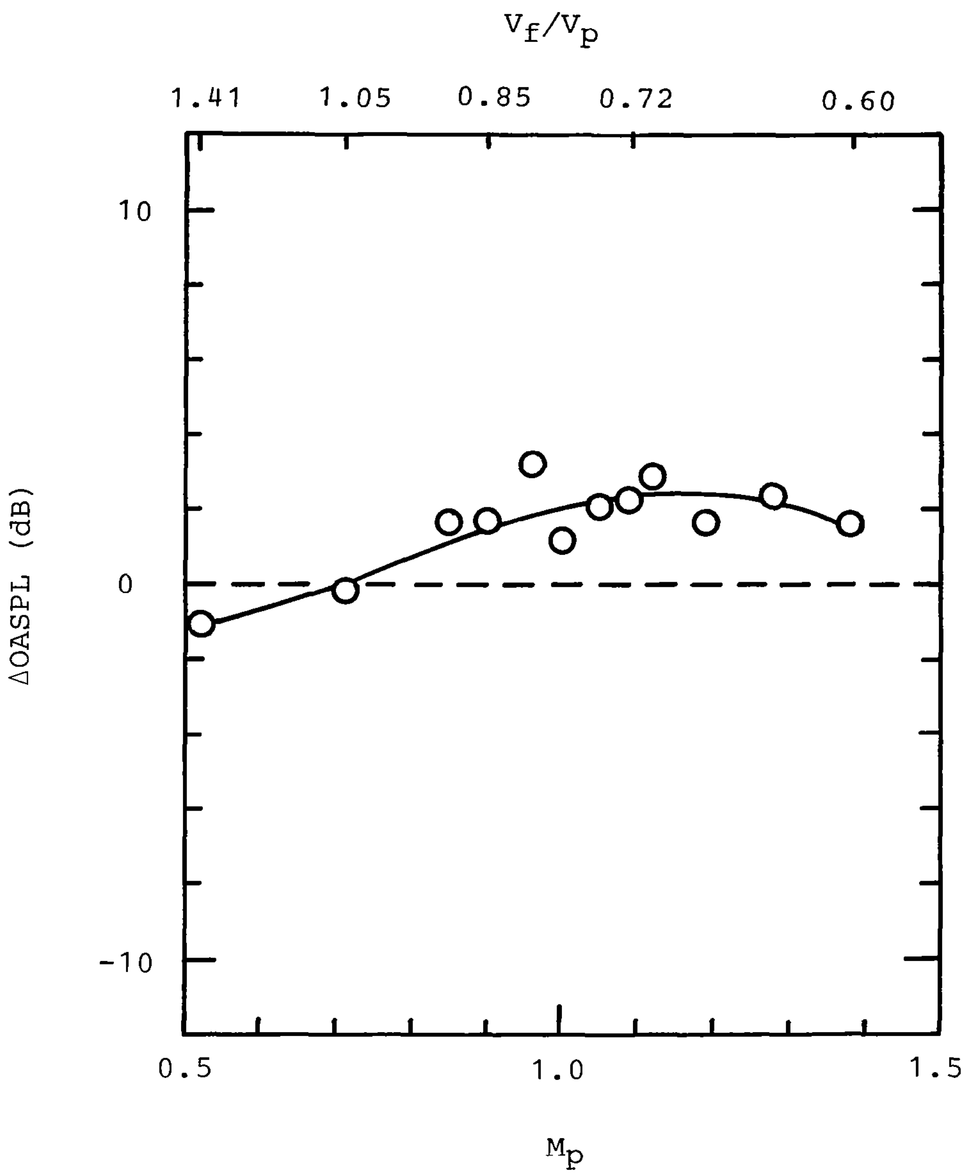


ΔOASPL = OASPL (Coannular Jet) - OASPL (Equivalent Single Jet)

Figure 3.14 Variation of ΔOASPL with $M_p$: Test Series 2; $\theta = 30°$.

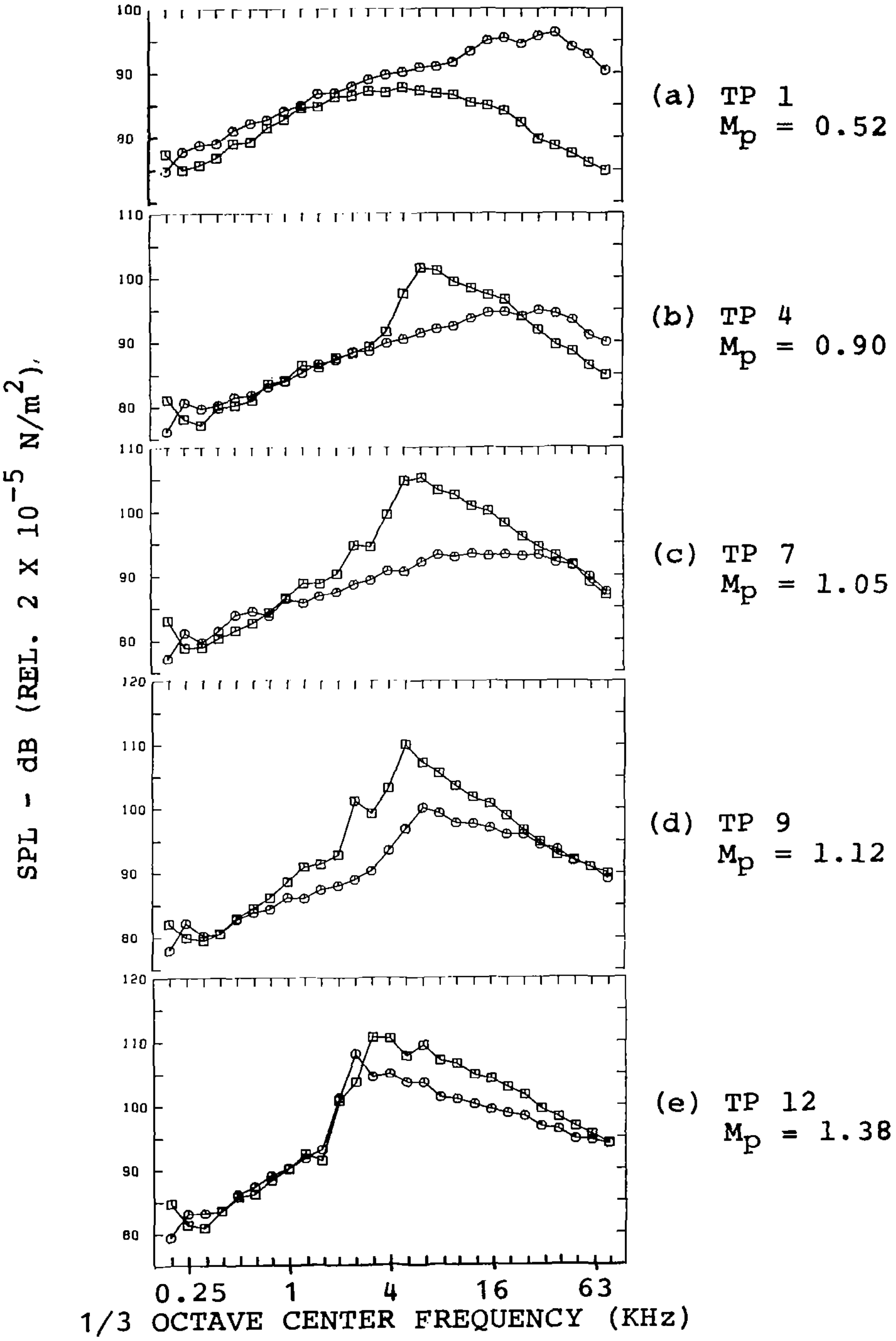


Figure 3.15 Comparison between SPL spectra of coannular jet (o) and equivalent single jet (□) at $\theta = 120°$ as a function of $M_p$: Test Series 1.

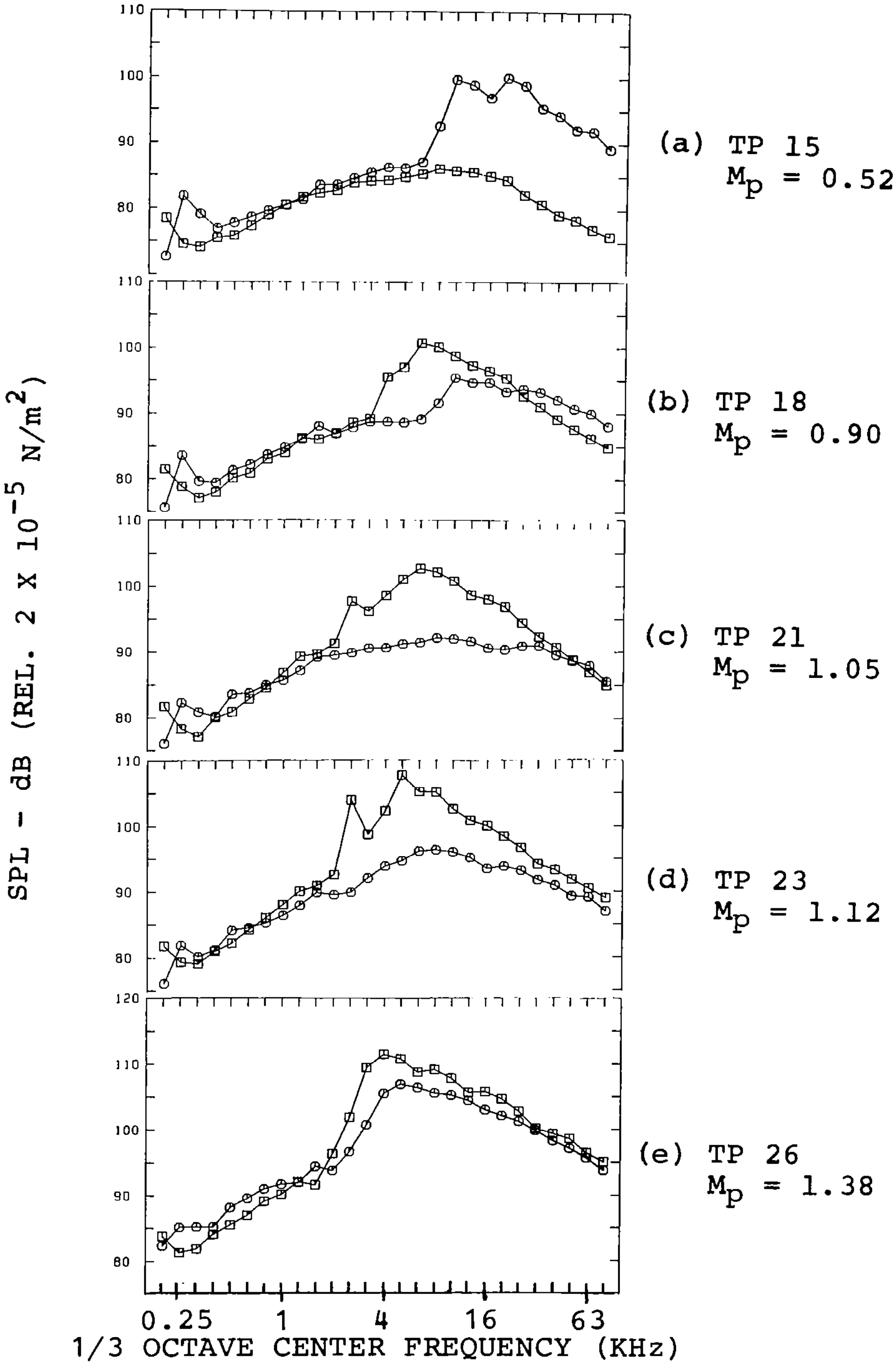


Figure 3.16 Comparison between SPL spectra of coannular jet (o) and equivalent single jet (□) at $\theta = 120°$ as a function of $M_p$: Test Series 2.

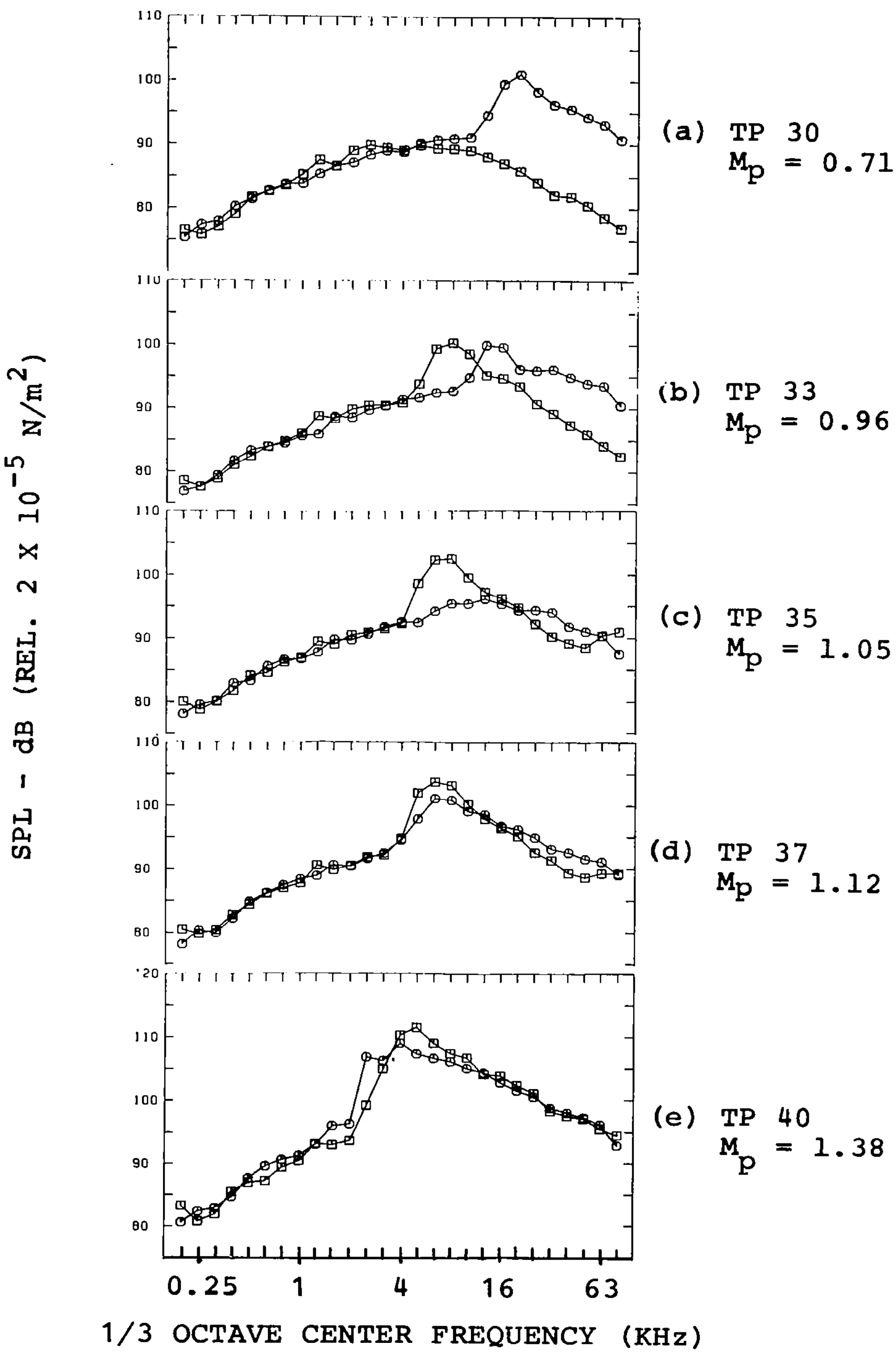


Figure 3.17 Comparison between SPL spectra of coannular jet (o) and equivalent single jet (□) at $\theta = 120°$ as a function of $M_p$: Test Series 3.

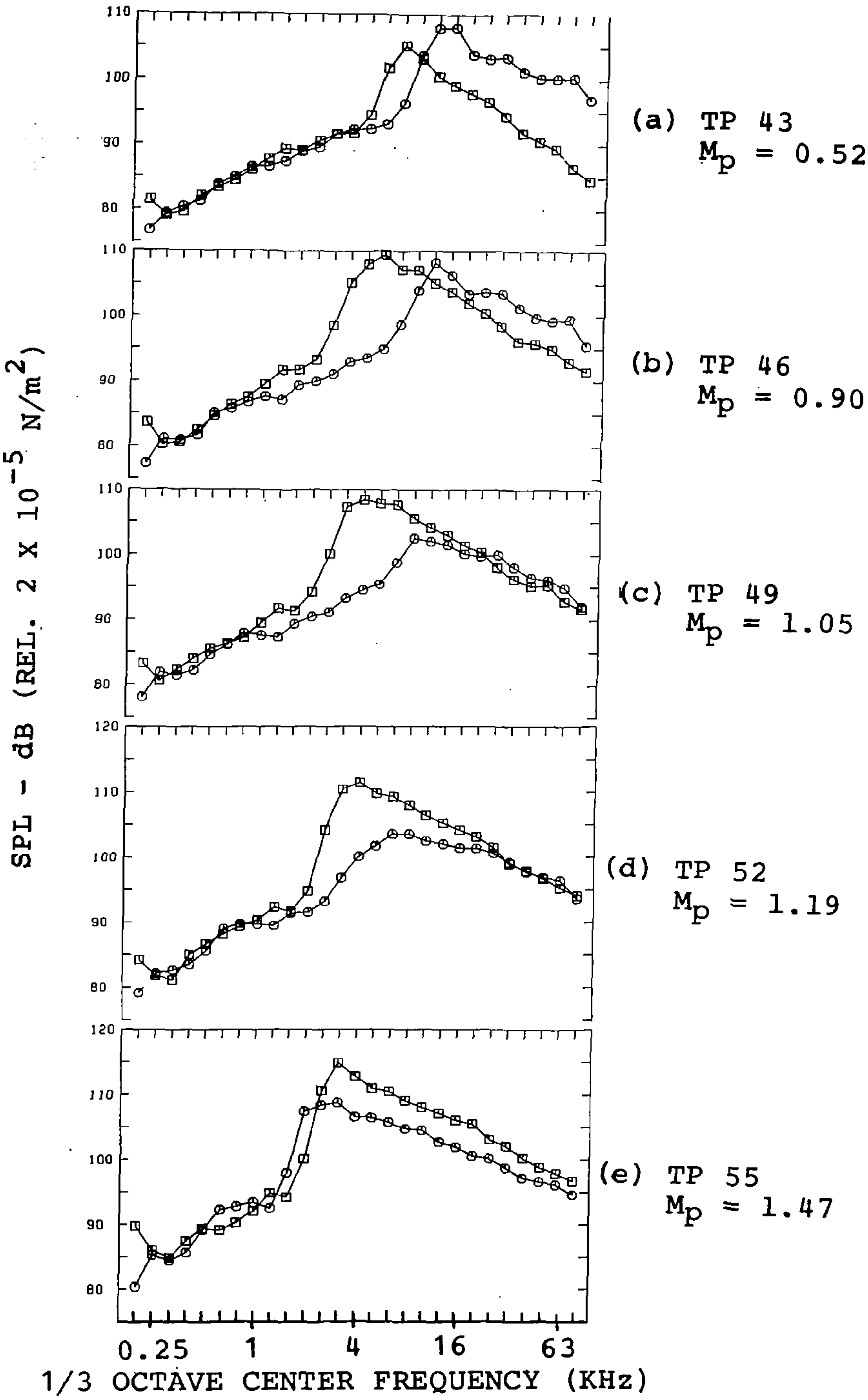


Figure 3.18 Comparison between SPL spectra of coannular jet (o) and equivalent single jet (□) at $\theta$ = 120° as a function of $M_p$: Test Series 4.

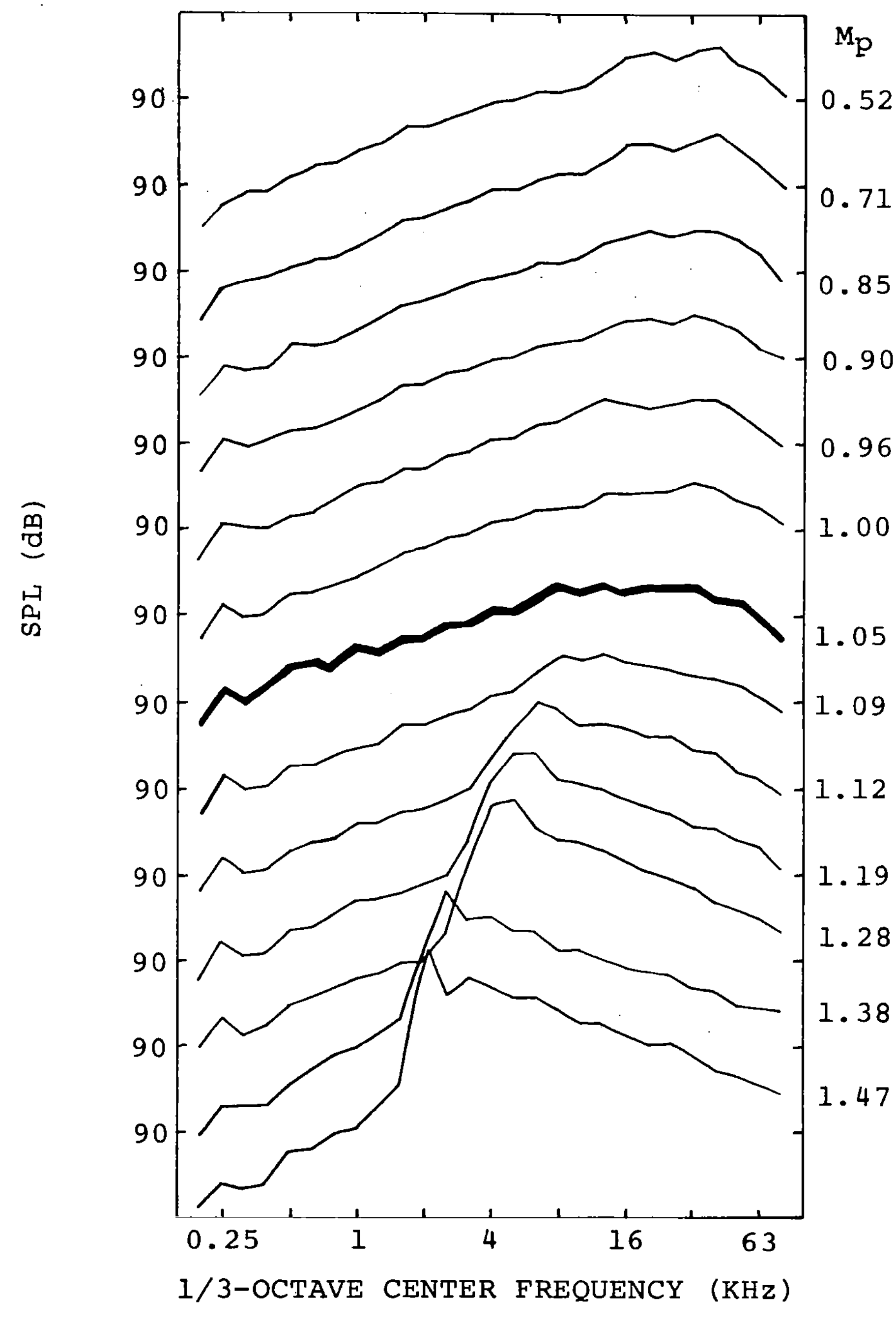


Figure 3.19 Variation of SPL spectrum at $\theta = 120°$ with primary stream Mach number $(M_p)$: Test Series 1.

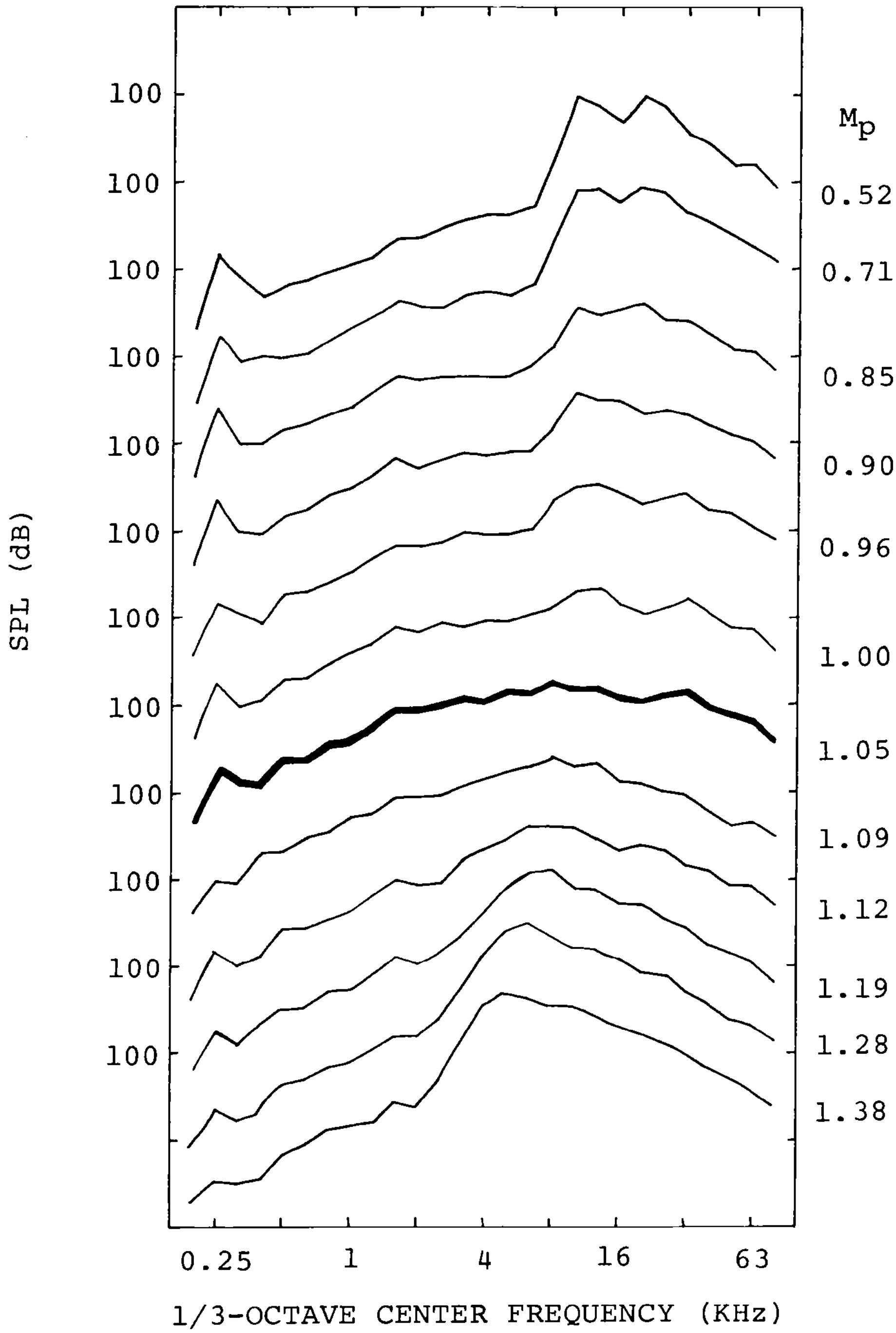


Figure 3.20 Variation of SPL spectrum at $\theta = 120°$ with primary stream Mach number ($M_p$): Test Series 2.

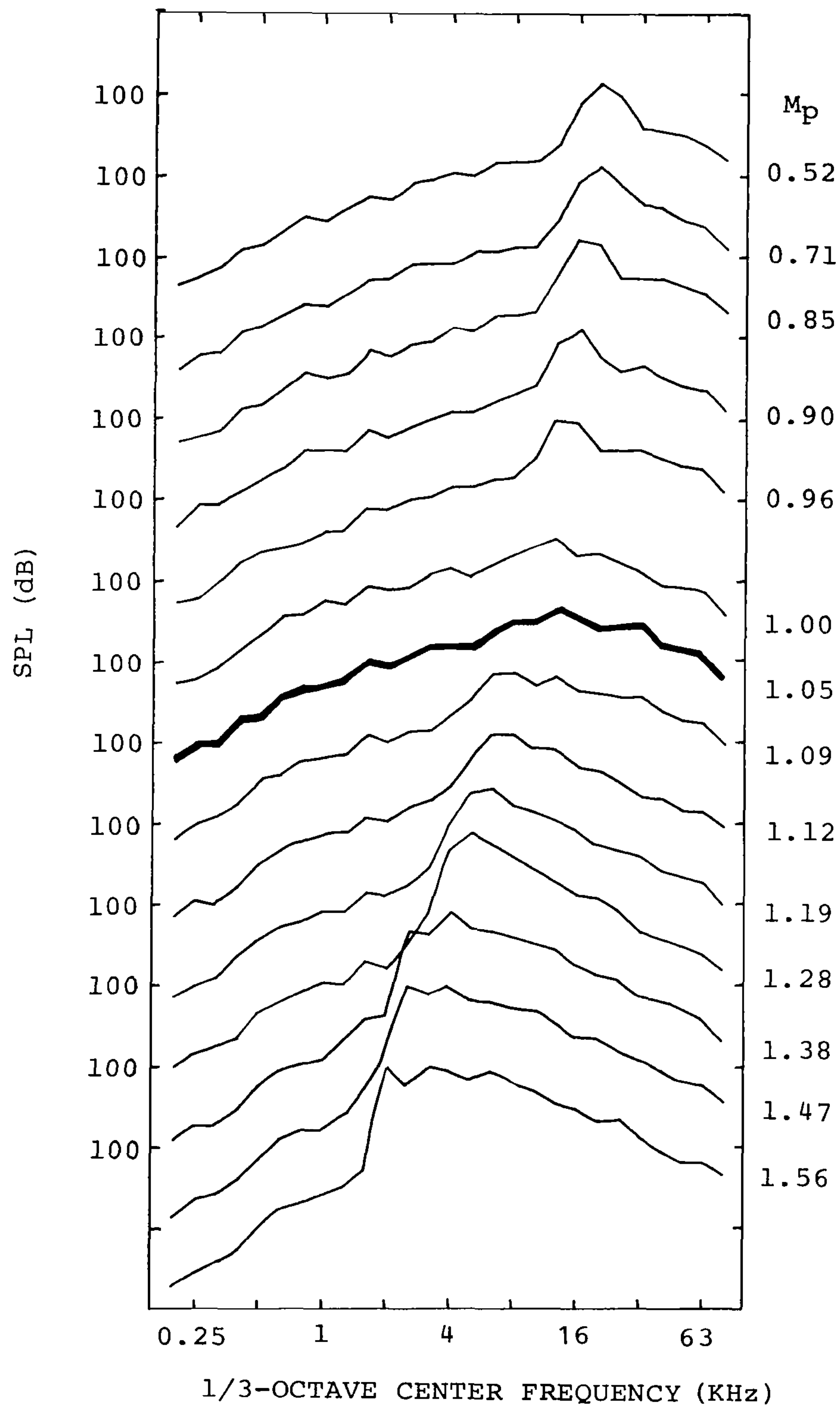


Figure 3.21 Variation of SPL spectrum at $\theta = 120^\circ$ with primary stream Mach number ($M_p$): Test Series 3.

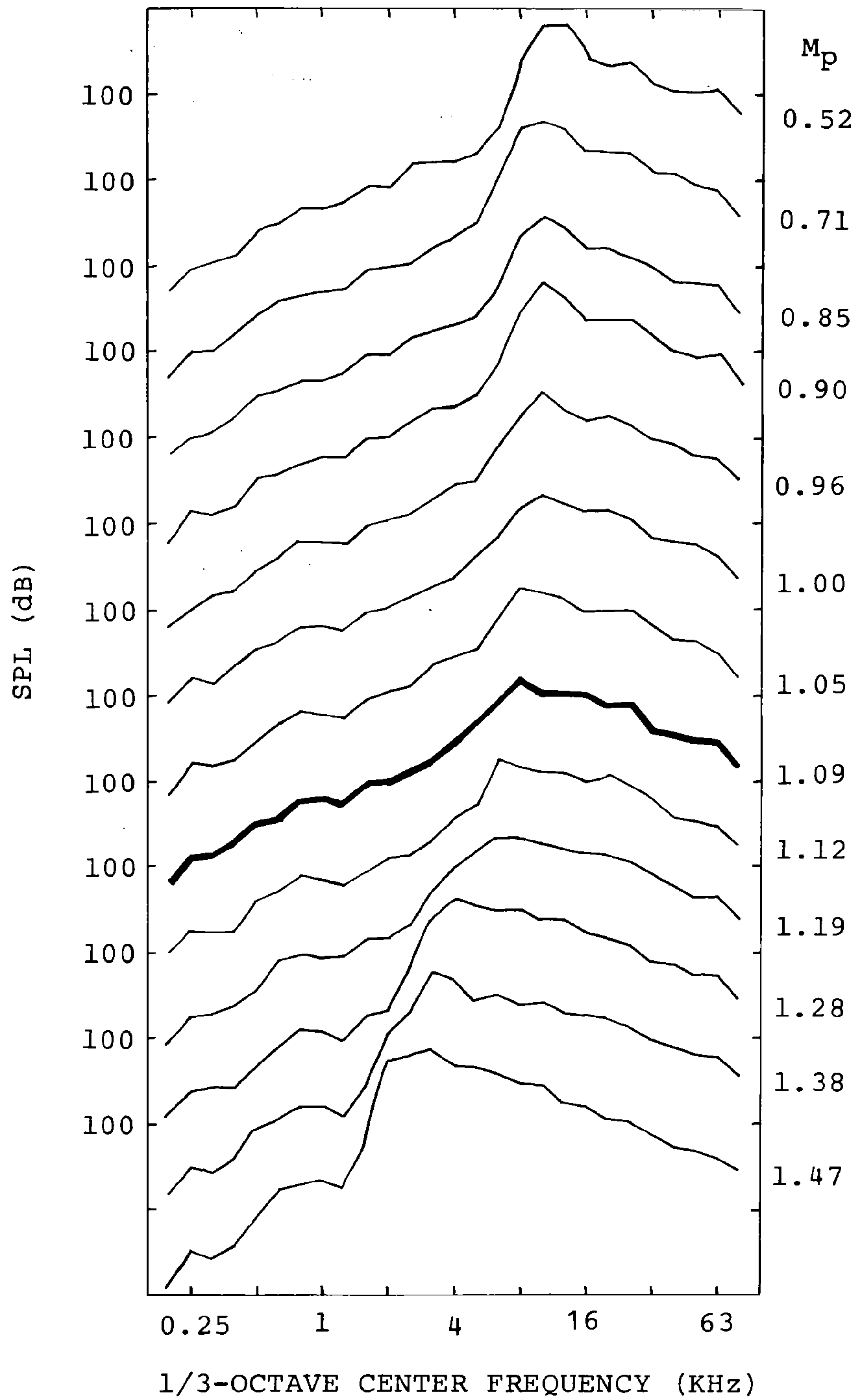


Figure 3.22 Variation of SPL spectrum at $\theta$ = 120° with primary stream Mach number ($M_p$): Test Series 4.

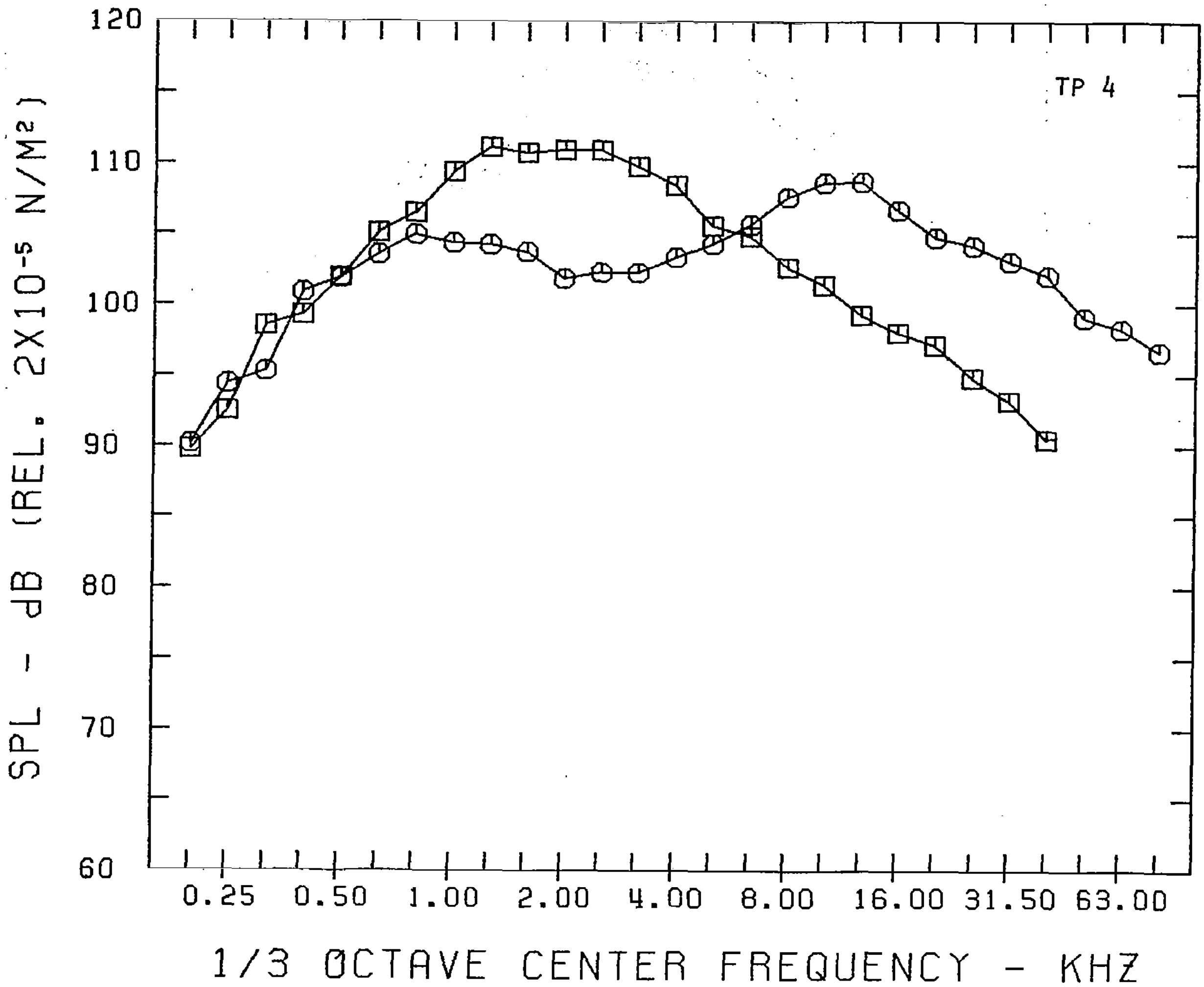


Figure 3.23 Comparison of SPL spectra at $\theta = 30^{\circ}$: $V_f/V_p = 2.27$.
—○— Coannular Jet; —□— Equivalent Single Jet

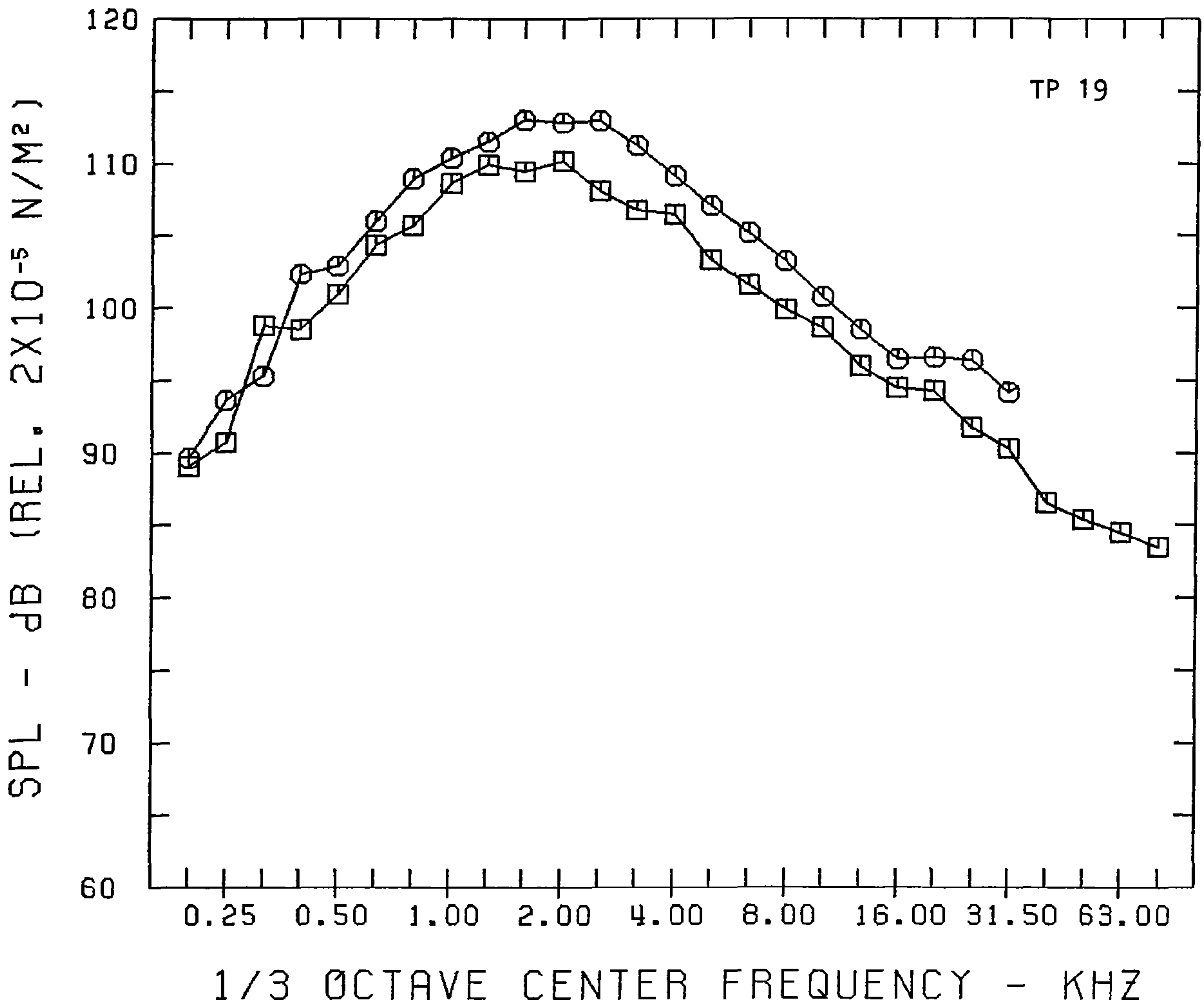


Figure 3.24 Comparison of SPL spectra at $\theta$ = 30°: $V_f/V_p$ = 0.81.
—○— Coannular Jet; —□— Equivalent Single Jet

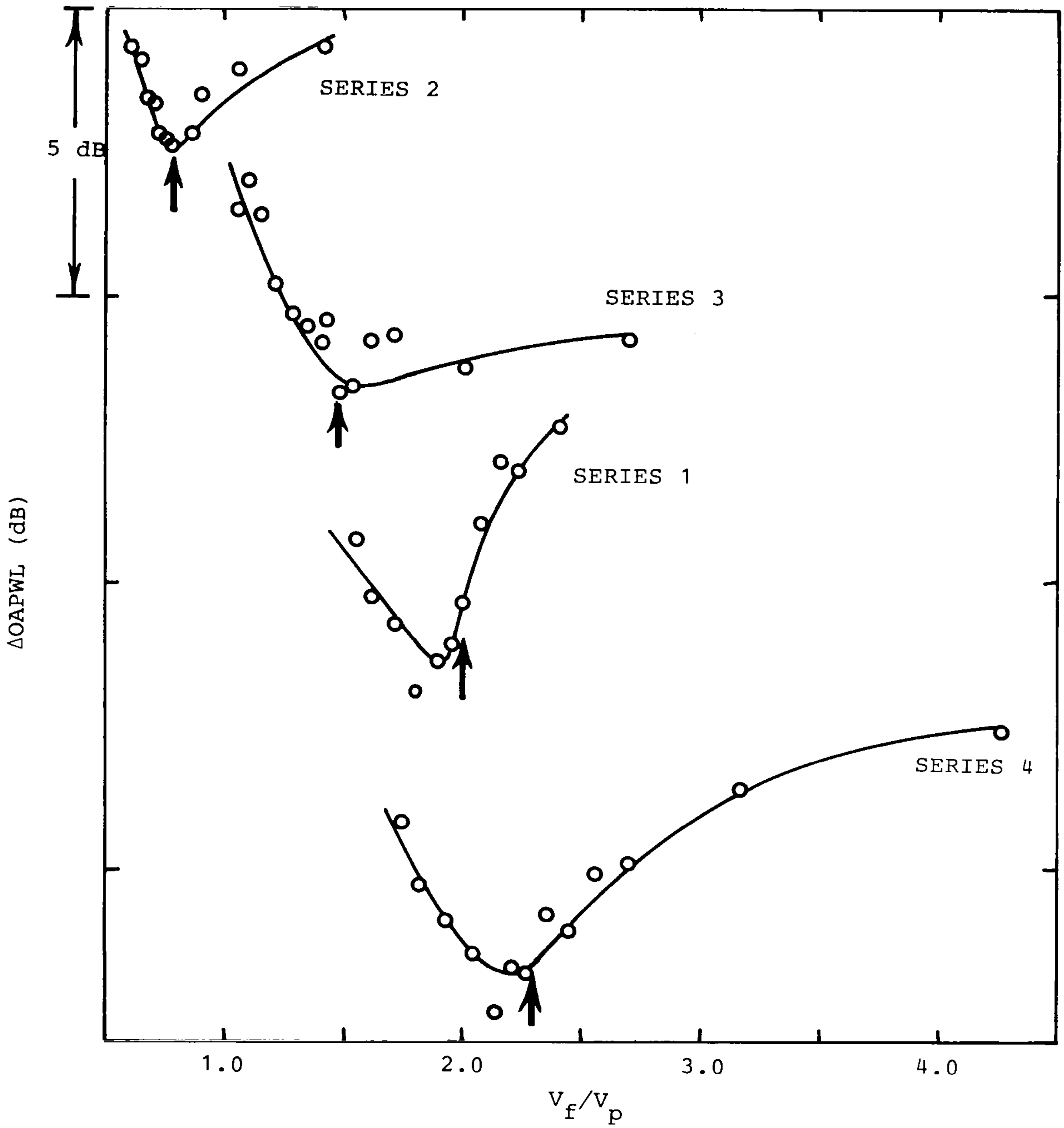


ΔOAPWL = OAPWL (Coannular Jet) - OAPWL (Equivalent Single Jet)

↑ Indicates value of $V_f/V_p$ when $M_p \doteq 1$

Figure 3.25 Variation of ΔOAPWL with coannular jet velocity ratio $V_f/V_p$.

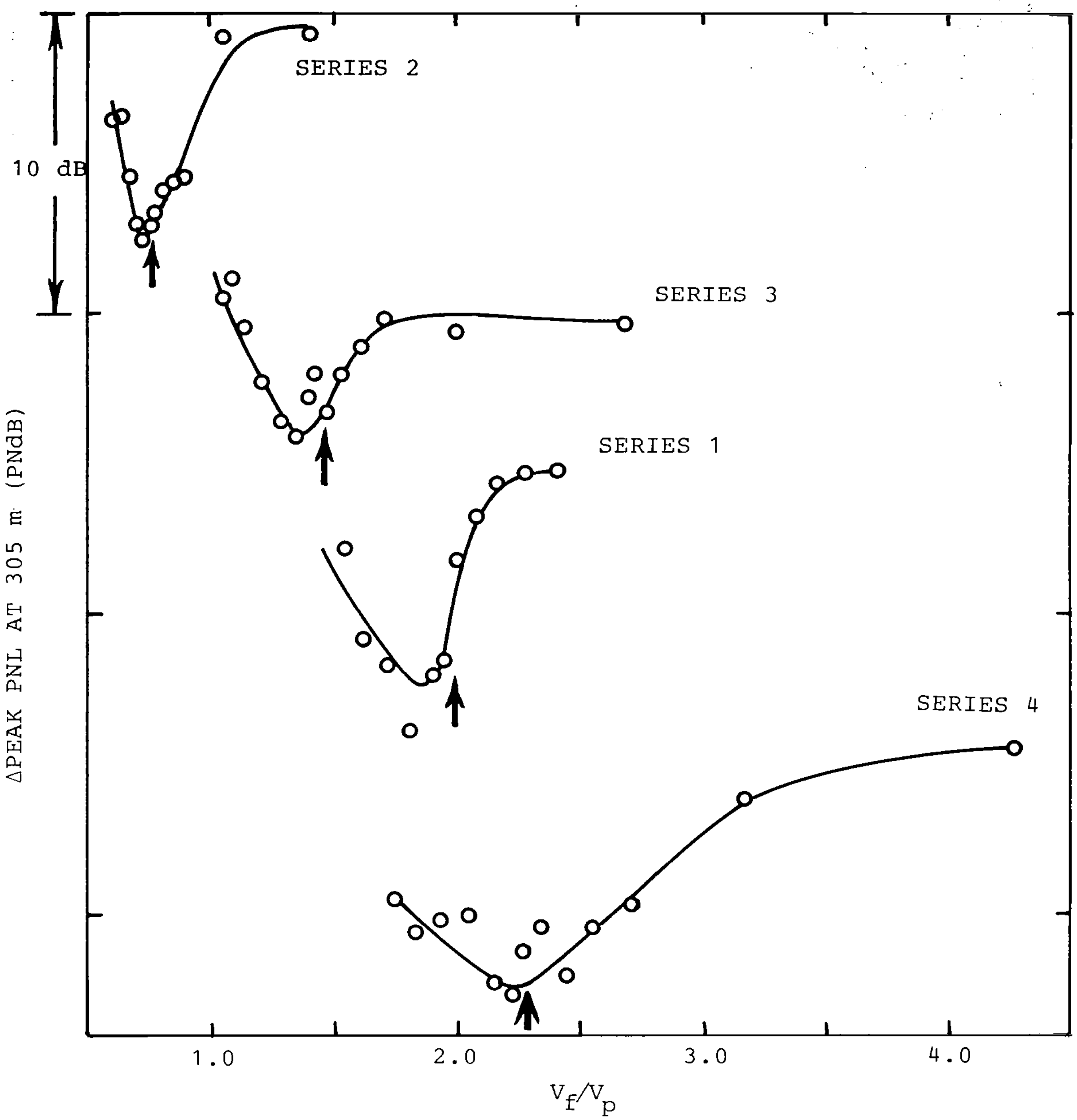


ΔPEAK PNL = PEAK PNL (Coannular Jet) - PEAK PNL (Equivalent Single Jet)

↑ Indicates value of $V_f/V_p$ when $M_p \doteq 1$

Figure 3.26 Variation of ΔPEAK PNL at 305 m with coannular jet velocity ratio $V_f/V_p$.

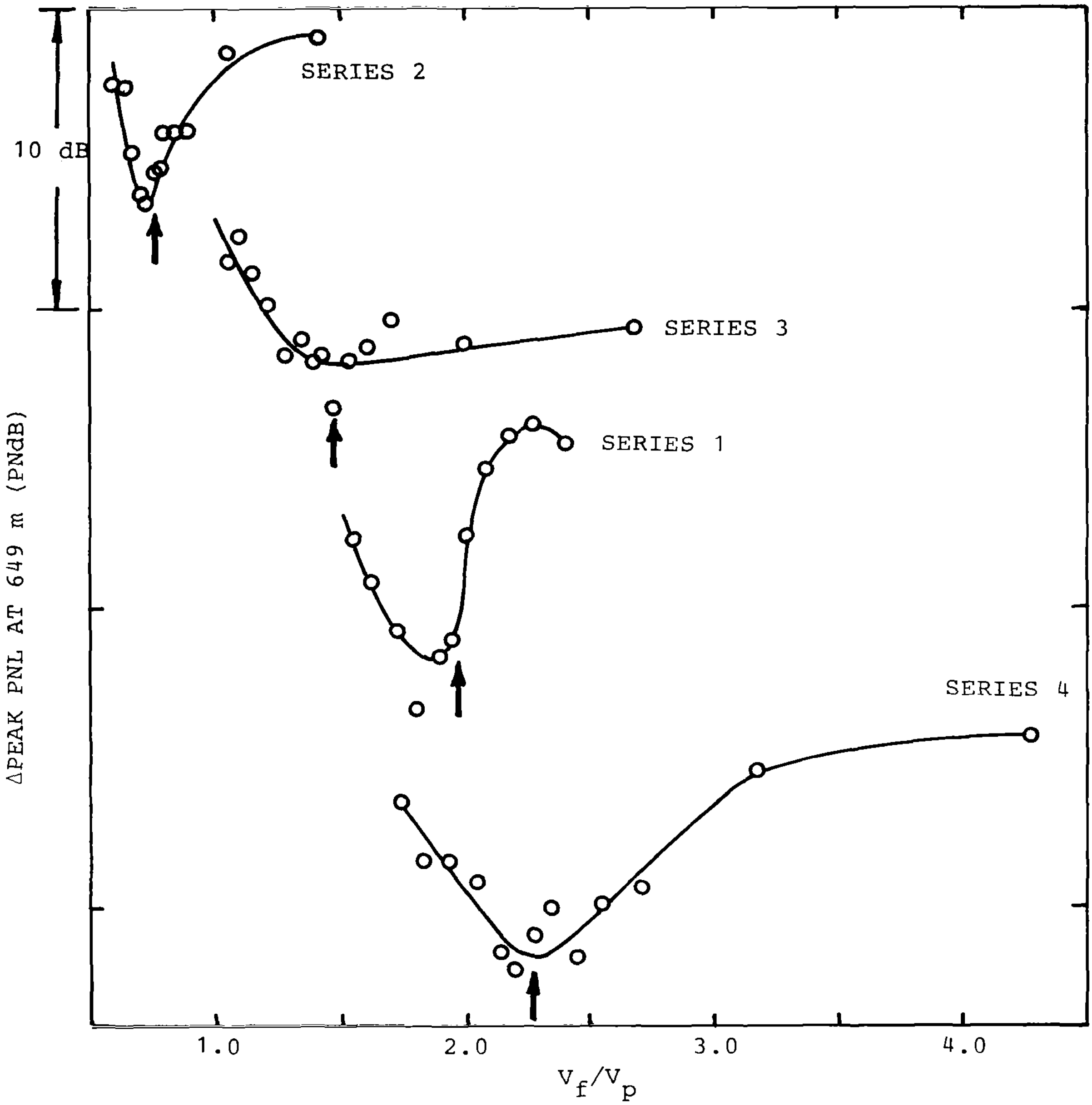


ΔPEAK PNL = PEAK PNL (Coannular Jet) - Peak PNL (Equivalent Single Jet)

↑ Indicates value of $V_f/V_p$ when $M_p \doteq 1$

Figure 3.27 Variation of ΔPEAK PNL at 649 m with coannular jet velocity ratio $V_f/V_p$.

# 4. MINIMUM SHOCK ASSOCIATED NOISE CONDITION

So far in this report, experimental results on coannular jet noise have been presented which show that for a fixed supersonic fan stream Mach number, the shock associated noise drops suddenly to a minimum as the reservoir pressure of the primary jet increases. When this happens, the almost periodic shock cell structure of the fan stream is found to nearly completely disappear. In the present section, an analytical model of this phenomenon is constructed and studied. It is theoretically established that this sudden change in the shock structure and hence the decrease in shock associated noise would occur when the primary jet flow is just slightly supersonic regardless of the Mach number and temperature of the fan stream.

## 4.1 INTRODUCTION

In recent years it is generally recognized that shock associated noise is an important noise component of imperfectly expanded supersonic jets. This noise component possesses certain special characteristics which make it distinctly different from jet mixing noise. Experimentally, shock associated noise has been found to be fairly omnidirectional. It can, therefore, be easily observable in the forward arc where jet mixing noise is less predominant. Although shock associated noise is broadband in nature, it's bandwidth is relatively narrow in comparison with jet mixing noise. Within its somewhat narrow bandwidth the spectrum is dominated by a characteristic peak. It is quite well established that in the case of a single imperfectly expanded supersonic jet (refs. 7, 8 and 9) the frequency of this spectral peak bears a simple relationship to the direction of radiation. This simple relationship led to the recognition that the sources of shock associated noise could be spatially coherent over several shock cells. Presently, we believe that shock associated noise is generated by the weak interaction between the downstream propagating large scale turbulent structures in the mixing layer of the jet and the periodic shock cell system. The noise is a form of Mach wave radiation produced by the supersonic phase components of the coherent shock-turbulence interaction. It is important to emphasize here that the periodicity of the shock cells is crucial to the generation of these supersonic phase components. If the periodicity of the shock cell structure is destroyed then constructive interference of the noise sources would be prevented. This, in turn, will result in the elimination of the supersonic source components and hence the observed shock associated noise.

The flow field and shock structure of an inverted-profile jet could be very complicated depending on the geometry of the nozzle exit and the primary nozzle lip thickness. To avoid having to consider this complex flow field which is highly sensitive to the particular nozzle design, this investigation will be confined to inverted-profile coannular jets with nozzle exit velocity aligned in the direction of the jet axis. Further, the primary nozzle lip is to be very thin compared to the thickness of the fan stream or the primary jet radius. Figure 2.1 shows the configuration of the coannular nozzle used throughout the experimental program of this study. To obtain an understanding of the shock structure in an inverted-profile coannular jet, extensive Schlieren observations were made. These results have previously been reported (ref. 4). Three series of optical measurements were conducted. In each test series the fan (or outer) stream pressure ratio ($\xi_f$), the fan stream total temperature ($T_{tf}$), and the primary stream total temperature ($T_{tp}$) were kept constant. The primary stream pressure ratio ($\xi_p$) was varied over an extensive range. Figure 1.1 illustrates the change in the shock structure as the primary flow Mach number increases. At subsonic primary flow Mach number, a repetitive shock cell system exists in the outer fan stream. As the Mach number increases there is a gradual increase in the length of the shock cells until the primary flow becomes supersonic. At a slightly supersonic Mach number an abrupt change takes place, resulting in the more or less complete disappearance of the shock cells in the fan stream. Further increase in the primary flow Mach number gives rise to the development of a new shock system principally in the primary stream. The strength of this new shock structure seems to increase with further increase in the primary stream pressure ratio.

The optical observations described above clearly indicate that the shock associated noise of an inverted-profile coannular jet can be generated by shock-turbulence interaction with the shock cells either in the fan stream or in the primary stream, depending on the primary flow Mach number. Since the shock structures are very different in these two cases, the shock associated noise characteristics will, therefore, be very different. The experimentally observed noise characteristics and the theoretical development of formulae for peak frequency and intensity scaling will be reported in Section 5 of this report. When the primary flow is just slightly supersonic, the Schlieren pictures reveal that the periodic shock structure is the weakest. Thus, as shown in Section 3, the shock associated noise of an inverted-profile jet attains a minimum at this operating condition. The objectives of this section are to provide a theoretical basis for this phenomenon and to demonstrate using experimental results that the shock associated noise, indeed, is a minimum at this condition. It will be shown that this is true regardless of the fan stream Mach number, temperature and all other operating parameters. The extent of noise reduction by operating a jet at this minimum shock associated noise condition will be briefly investigated. Relationship between the present results and other works on this phenomenon using more complicated nozzle geometry will be discussed at the end of this section.

## 4.2 CONDITION FOR MINIMUM SHOCK ASSOCIATED NOISE

We will now investigate the conditions under which the periodic shock structure in the outer fan stream would disappear. For this purpose we will assume that the thickness of the fan stream is small compared with the radius of the primary jet so that the flow in the fan stream can effectively be considered two-dimensional as shown in Figure 4.1(a). To simplify the model, the flow in the fan and primary streams will be regarded as uniform, separated and bounded by vortex sheets. In order that periodic shock cells can exist in the fan stream, the flow there must be supersonic. However, the flow in the primary stream can be either subsonic or supersonic. These two cases will be analyzed separately below. Now the question of whether periodic shock cells would disappear in the fan stream is the same mathematically as under what condition can the fan stream support a solution of the governing equations of motion which is periodic in the mean flow direction. If no such solution is possible then periodic shock cells would unlikely be found. In other words the present problem is one involving the search for possible eigenfunctions which are periodic in the flow direction. Here, we will first formulate and then solve this eigenvalue problem. In the next subsection, the predicted results of the solution will be compared with experimental results.

### 4.2.1 Subsonic Primary Flow ($M_p < 1$)

Let $M_f$ and $M_p$ denote the flow Mach numbers of the fan and the primary streams, respectively, as shown in Figure 4.1(a). The thickness of the fan stream will be taken to be d. We will first consider the possible existence of a weak shock system in the fan stream in the case $M_f > 1$ and $M_p < 1$. Such a shock structure can to a first approximation be represented by a linear solution of the equations of motion. The equations of motion are the time independent continuity, momentum and energy equations. We will use (u,v) to denote the velocity components associated with the periodic shock cell solution in the x and y directions, and p and $\rho$ to denote the corresponding change in pressure and density. To avoid confusion, subscripts f and p will be used to designate physical quantities which are in the fan and the primary stream, respectively. The formation of a periodic shock structure will inevitably cause a periodic displacement of the top and bottom vortex sheets bounding the fan stream. These displacements will be denoted by $\zeta(x)$ and $\eta(x)$ as indicated in Figure 4.1(b).

The linearized governing equations are:

$0 \leq y \leq d$:

$$\bar{\rho}_f \, \nabla \cdot \vec{v}_f + \bar{u}_f \frac{\partial \rho_f}{\partial x} = 0 \qquad (4\text{-}1)$$

$$\bar{\rho}_f \, \bar{u}_f \frac{\partial \vec{v}_f}{\partial x} = -\nabla p_f \qquad (4\text{-}2)$$

$$p_f = \bar{a}_f^{\,2}\, \rho_f \tag{4-3}$$

$y \leq 0$:

$$\bar{\rho}_p\, \nabla \cdot \vec{v}_p + \bar{u}_p \frac{\partial \rho_p}{\partial x} = 0 \tag{4-4}$$

$$\bar{\rho}_p\, \bar{u}_p \frac{\partial \vec{v}_p}{\partial x} = -\nabla p_p \tag{4-5}$$

$$p_p = \bar{a}_p^{\,2}\, \rho_p \tag{4-6}$$

where the mean flow quantities are indicated by a bar and $\bar{a}_f$ and $\bar{a}_p$ are the speeds of sound in the fan and the primary stream. The boundary conditions at $y = 0$ and $y = d$ are the continuity of pressure and vortex sheet displacements, namely,

at $y = 0$:

$$p_p = p_f \tag{4-7}$$

$$\bar{u}_f \frac{\partial \eta}{\partial x} = v_f \tag{4-8}$$

$$\bar{u}_p \frac{\partial \eta}{\partial x} = v_p \tag{4-9}$$

at $y = d$:

$$p_f = 0 \tag{4-10}$$

In addition, far away from the fan stream it is expected that the disturbances associated with the shock structure be bounded. Thus

$$y \to -\infty, \quad \text{solution must be bounded.} \tag{4-11}$$

By eliminating all the other variables in favor of pressure p, the above problem can be greatly simplified mathematically to

$0 \leq y \leq d$:

$$\frac{\partial^2 p_f}{\partial y^2} - (M_f^{\,2} - 1) \frac{\partial^2 p_f}{\partial x^2} = 0 \tag{4-12}$$

$y \leq 0$:

$$\frac{\partial^2 p_p}{\partial y^2} + (1 - M_p^2) \frac{\partial^2 p_p}{\partial x^2} = 0 \qquad (4\text{-}13)$$

at $y = 0$: $\qquad p_f = p_p \qquad (4\text{-}14)$

$$\frac{1}{M_f^2} \frac{\partial p_f}{\partial y} = \frac{1}{M_p^2} \frac{\partial p_p}{\partial y} \qquad (4\text{-}15)$$

at $y = d$: $\qquad p_f = 0 \qquad (4\text{-}16)$

$y \to -\infty$: $\qquad p_p$ is bounded $\qquad (4\text{-}17)$

In deriving equation (4-15) the condition of static pressure balance, i. e., $\bar{\rho}_f \bar{a}_f^2 = \bar{\rho}_p \bar{a}_p^2$, has been used. Without loss of generality we will look for periodic solution of (4-12) to (4-17) in the form

$$\left.\begin{aligned} p_f(x, y) &= \mathrm{Re}\,[\hat{p}_f(y)\, e^{ikx}] \\ p_p(x, y) &= \mathrm{Re}\,[\hat{p}_p(y)\, e^{ikx}] \end{aligned}\right\} \qquad (4\text{-}18)$$

where $R_e$ [ ] denotes "the real part of." In (4-18) k is as yet an unknown constant to be determined later. Substitution of (4-18) into equations (4-12) to (4-16) leads to the following eigenvalue problem.

$0 \leq y \leq d$:

$$\frac{d^2 \hat{p}_f}{dy^2} + k^2 (M_f^2 - 1) \hat{p}_f = 0 \qquad (4\text{-}19)$$

$y \leq 0$:

$$\frac{d^2\hat{p}_p}{dy^2} - k^2 (1 - M_p^2)\, \hat{p}_p = 0 \tag{4-20}$$

at $y = 0$:

$$\hat{p}_p = \hat{p}_f \tag{4-21}$$

$$\frac{1}{M_f^2} \frac{d\hat{p}_f}{dy} = \frac{1}{M_p^2} \frac{d\hat{p}_p}{dy} \tag{4-22}$$

at $y = d$:

$$\hat{p}_f = 0 \tag{4-23}$$

The solution of (4-19) which satisfies (4-23) is

$$\hat{p}_f = A \sin \left(k \sqrt{M_f^2 - 1}\, (d - y)\right). \tag{4-24}$$

The solution of (4-20) which is bounded as $y \to -\infty$ is

$$\hat{p}_p = B \exp \left(k \sqrt{1 - M_p^2}\, y\right) \; ; \; \mathrm{Re}\,(k) > 0. \tag{4-25}$$

Straightforward substitution of (4-24) and (4-25) into (4-21) and (4-22) yields two linear homogeneous algebraic equations for A and B. The condition for non-trivial solution gives the following eigenvalue equation

$$\tan \left(\sqrt{M_f^2 - 1}\, kd\right) = - \frac{M_p^2}{M_f^2} \sqrt{\frac{M_f^2 - 1}{1 - M_p^2}} \; . \tag{4-26}$$

There are infinitely many solutions to (4-26). They are

$$k_n = \frac{1}{\sqrt{M_f^2 - 1}\, d} \left\{ (2n - 1)\pi - \tan^{-1}\left[\frac{M_p^2}{M_f^2}\sqrt{\frac{M_f^2 - 1}{1 - M_p^2}}\right]\right\} \tag{4-27}$$

where $n = 1, 2, 3, \ldots\ldots$

Corresponding to each value of k in (4-27) is a distinct eigenfunction of a form given by (4-24) and (4-25). The significance of these eigenfunctions is that any periodic solution in the fan stream can be constructed by using a linear combination of them. Thus we may conclude that if the flow in the primary stream is subsonic, it is possible to have a periodic shock cell structure in the fan stream. The length of the shock cells, L, is equal to the longest wave length of the eigenfunctions, that is,

$$\frac{L}{d} = \frac{2\pi}{k_1 d} = \frac{2\pi\sqrt{M_f^2 - 1}}{\pi - \tan^{-1}\left[\frac{M_p^2}{M_f^2}\sqrt{\frac{M_f^2 - 1}{1 - M_p^2}}\right]} \,. \tag{4-28}$$

This result will be compared with experimental results later.

### 4.2.2 Supersonic Primary Flow ($M_p > 1$)

When the primary flow is supersonic, i.e. $M_p > 1$, equations (4-19) to (4-23) are still valid. The solution of (4-19) which satisfies (4-23) is still given by (4-24). However the solution of (4-20) which is bounded and satisfies the outgoing wave condition is

$$\hat{P}_p = D \exp\left[ik\sqrt{M_p^2 - 1}\, y\right]; \qquad \mathrm{Im}(k) < 0. \tag{4-29}$$

By substitution of (4-24) and (4-29) into boundary conditions (4-21) and (4-22) one finds that the eigenvalue equation for k is

$$\tan\left(\sqrt{M_f^2 - 1}\ kd\right) = i\sqrt{\frac{M_f^2 - 1}{M_p^2 - 1}}\ \frac{M_p^2}{M_f^2} \,. \tag{4-30}$$

The roots of (4-30) are either purely imaginary or complex. There is no real value of k which satisfies this equation. When k is complex or purely imaginary, solution (4-18) will decay exponentially in the flow direction. Therefore, in this case spatially periodic solutions are not possible. In other words, when the primary stream is supersonic, periodic shock cells cannot be maintained in the fan stream.

### 4.2.3 A Physical Explanation

The simple model described above indicates clearly that a drastic change in the fan stream shock cell structure would take place when the primary stream increases its velocity from subsonic to supersonic. Physically, this abrupt change in the shock cell system arises principally because a subsonic flow cannot transmit flow discontinuities such as shocks and expansion fans but a supersonic flow can. When the primary flow is subsonic, an incident oblique shock in the supersonic fan stream is reflected as an expansion fan with pressure jump across the fan and the shock being equal as illustrated in Figure 4.2. The expansion fan propagates upward. Upon reflection from the upper shear layer another shock wave of the same strength is formed. This process is repated over and over again spatially. In this way a periodic shock cell structure is formed. On the other hand, if the primary stream is supersonic, it can sustain flow discontinuities. In this case an incident shock wave will be partly transmitted. The reflected expansion wave thus would have a much smaller pressure jump across it than that across the incident shock. This is shown schematically in Figure 4.3. Therefore, after one or two reflections the shock becomes one of negligible strength. Because of this a shock cell pattern of longer than one or two periods cannot be maintained. In the case of coaxial jets, the primary jet is of finite radius. As a result the transmitted waves will be reflected by the outer boundary of the jet on the opposite side. But unless an extremely unusual situation occurs these reflected waves will not fit the periodicity of the original trapped waves in the fan stream (because of the difference in the radii of the coaxial streams). Thus the amplitude of the periodic shock cells in the fan stream, again, must decay in the axial direction just as depicted by the simple model above.

In summary, we see that when the primary flow stream Mach number is slightly supersonic no periodic shock cell pattern can form in the outer fan stream. Also, at just slightly supersonic Mach number, the shock cell structure of the primary stream is extremely weak. Thus under this condition the coherent interaction between turbulence in the mixing layers of the jet and the shock cell structure is most ineffective. As a result the corresponding shock associated noise must be the least intense, as has been shown in Section 3.

## 4.3 COMPARISON WITH SCHLIEREN OBSERVATIONS

The mathematical model of the periodic shock cell structure in the fan stream developed in section 4.2 predicts the length of the shock cells as given by equation (4-28). This theoretical result will now be compared with the Schlieren observations of reference 4. The optical measurements were conducted at three series of test conditions. In each series, the primary stream total temperature ($T_{tp}$), the fan stream total temperature ($T_{tf}$) and the fan stream pressure ratio ($\xi_f$) were kept constant, and the primary stream pressure ratio ($\xi_p$) was varied over an extensive range. The values of these parameters in the three test series are shown in Table 4.1.

Table 4.1 Coannular jet test conditions in the optical measurements (ref. 4)

| | $T_{tp}$(K) | $T_{tf}$(K) | $\xi_f$ | $\xi_p$ |
|---|---|---|---|---|
| Series 1 | 294 | 728 | 2.93 | 1.00 → 4.49 |
| Series 2 | 728 | 294 | 2.93 | 1.00 → 3.48 |
| Series 3 | 728 | 978 | 2.37 | 1.00 → 3.53 |

In series 1, the fan flow is heated while the primary flow is unheated. In series 2, it is the other way around. In series 3, both streams are heated.

The values of L/d for all the test points with subsonic primary flow were measured from the Schlieren photographs given in reference 4. The sample photographs shown earlier in Figure 1.1 refer to test series 2. The measured values of L/d as a function of $M_p$ are plotted in Figures 4.4 and 4.5. The theoretical curves of equation (4-28) are also shown. As can be seen there is a very favorable agreement between the calculated and the measured results. Considering the simplicity of the mathematical model, the degree of agreement obtained must be regarded as quite impressive. Here the good agreement found not only provides strong support for the validity of the model presented, but also suggests that a linear shock structure model does offer a reasonable first estimate of the crucial features of a shock system. Of course, one would expect more accurate agreement using an annular model to derive the shock cell spacing. In section 5, a linear shock cell model will, therefore, again be used in our discussion of the characteristics of shock associated noise of inverted-profile coannular jets.

## 4.4 DISCUSSION

Prior to the work of Tanna et al (ref. 4), Dosanjh and his coworkers (ref. 10) at the Syracuse University had conducted optical studies of cold inverted-profile coaxial jets for several years. They reported the observation of the phenomenon of 'sudden' disappearance of the shock structure in the fan stream and the accompanied reduction in jet noise. They attributed the occurence of this phenomenon to the formation of a complex shock structure slightly downstream of the nozzle exit. However, exactly why such a shock structure would form and in what way this structure eliminated the repetitive shock pattern were not elaborated. A closer examination of their work reveals that there are, at least, two major differences between their results and the present findings. First of all, to obtain the minimum noise condition using their nozzle configuration, the pressure ratio of the primary stream, $\xi_p$, must be set at a specific value which depends on the pressure ratio of the fan stream, $\xi_f$, whereas in the present experiments the optimum condition is simply $\xi_p \simeq 1.9$. Secondly, in the present investigation, the noise reduction is brought about mainly by the elimination of shock associated noise. Thus the observed noise reduction is effective only in the high frequency part of the noise spectrum and in the forward arc region. The measurements of Dosanjh et al., on the other hand, indicate a uniform noise reduction across a very broad frequency band and in nearly all directions. These distinct differences clearly imply that the minimum noise condition of their jet was achieved by a reduction not only in shock associated noise but in jet mixing noise as well.

What causes these profound differences? We believe that the basic reason lies in the nozzle geometry. Unlike our nozzle configuration, Dosanjh et al used an unusually thick lip primary nozzle (the thickness of the lip was larger than the thickness of the fan stream). In addition, at their nozzle exit the flow was not aligned in the direction of the jet axis. Instead the fan stream impinged radially on the primary stream. This caused the development of an extremely complex flow field and shock structure. The radial impingement arrangement inevitably greatly increased violent turbulent mixing and thus the basic jet noise. We speculate that under the optimum operating condition of their jet, the inner and outer streams were able to mix somewhat more smoothly and that the outer part of the inner stream became supersonic and hence helped to eliminate the repetitive shock pattern in the fan stream. This led to a reduction in mixing as well as shock associated noise as was observed. Because of the strong radial flow we believe their findings are not applicable to other nozzle designs and that the larger noise reduction they found might simply be the consequence of their jet being noisier to start with.

Subsequent works at the Syracuse University by Dosanjh et al. (refs. 11, 12 and 13) using cold and hot jets appeared to arrive at a somewhat different criterion for the minimum noise condition. In these later investigations a new nozzle with a basic design similar to that of Figure 2.1 was used. These authors carried out overall jet noise measurements under a fixed fan stream operating pressure. The minimum noise condition was obtained by varying the primary stream pressure ratio until the so called "jet acoustic efficiency," a term defined by them, was the smallest. When both the primary and fan streams were unheated they found that the minimum noise condition was achieved when $\xi_p \simeq 2.02$. This value is consistent with the present finding but differs from that of reference 10. However, when the primary stream was unheated and the fan stream was heated, they stated that they were unable to observe a definitive minimum under their definition of minimum jet acoustic efficiency. This appears to be somewhat misleading, for in Figure 3.9(b) under the same conditions, our data clearly shows a distinct shock associated noise minimum at a slightly supersonic primary jet Mach number.

To conclude, we want to emphasize that there are some major differences between the results and conclusions of the present work and those of the Syracuse University carried out over a number of years. The contributing factors to these differences appear to be in the nozzle design, the definition of minimum noise condition, and most importantly, the way by which the observed phenomenon is interpreted and understood.

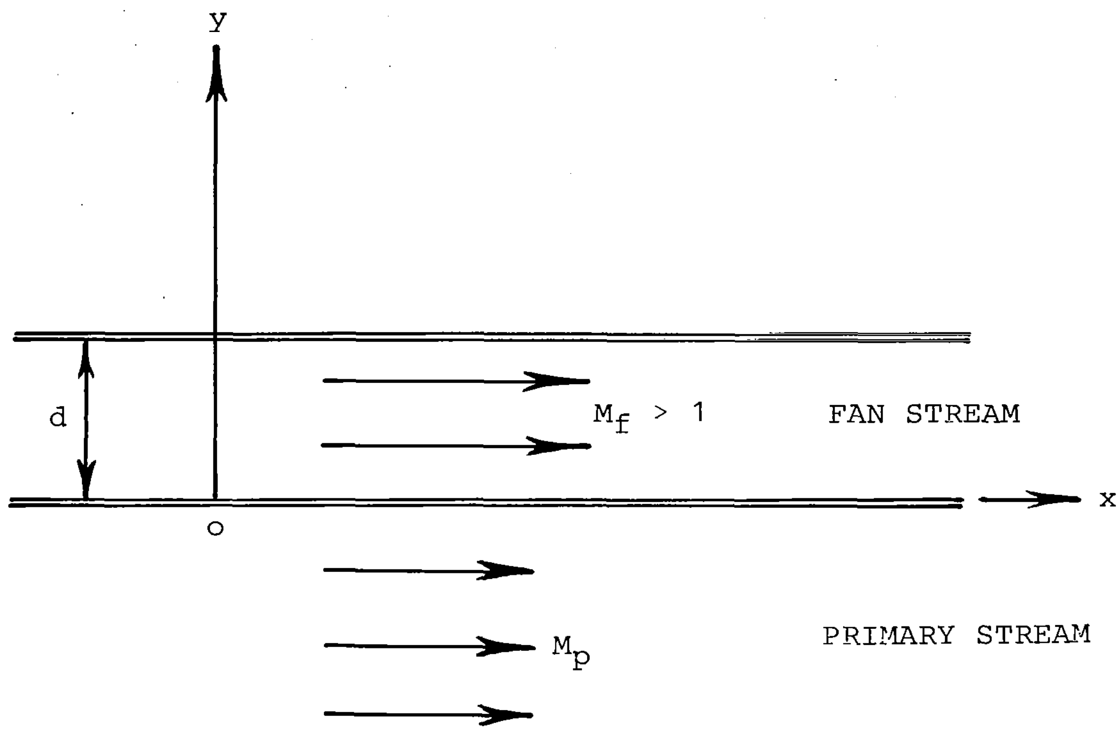


Figure 4.1(a) Model of fan stream and primary stream flow.

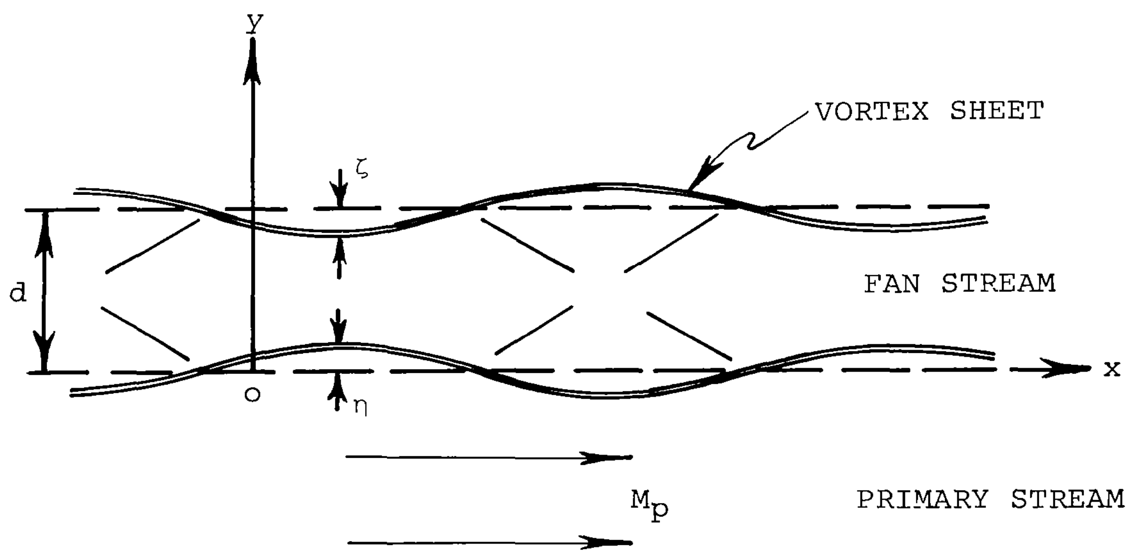


Figure 4.1(b) First order shock structure in the fan stream.

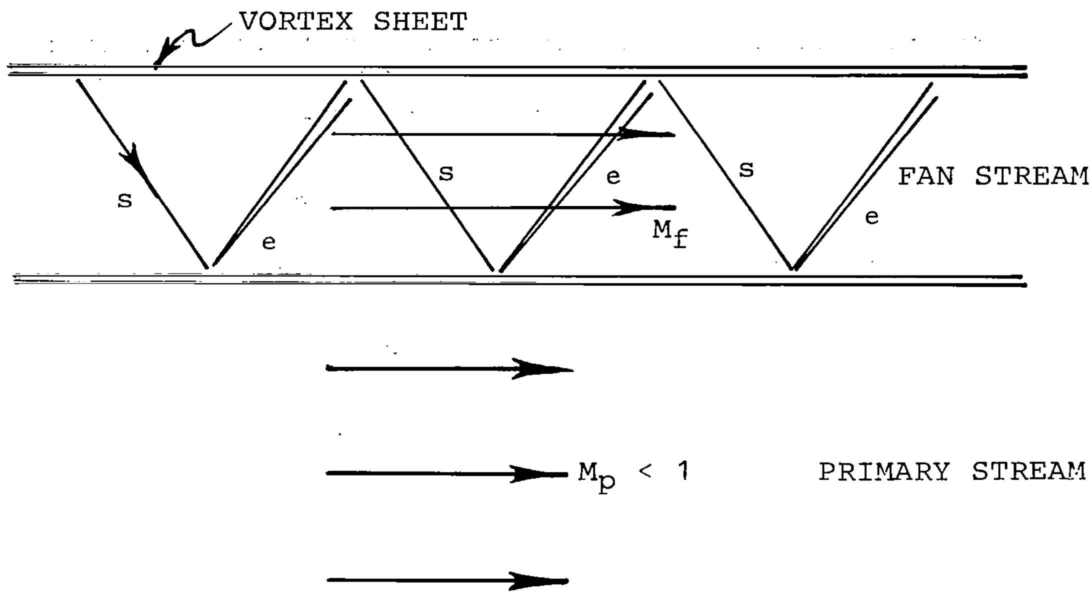


Figure 4.2 Schematic diagram illustrating the reflection of shocks and expansion fans in the fan stream when the primary flow is subsonic. s = shock, e = expansion fan.

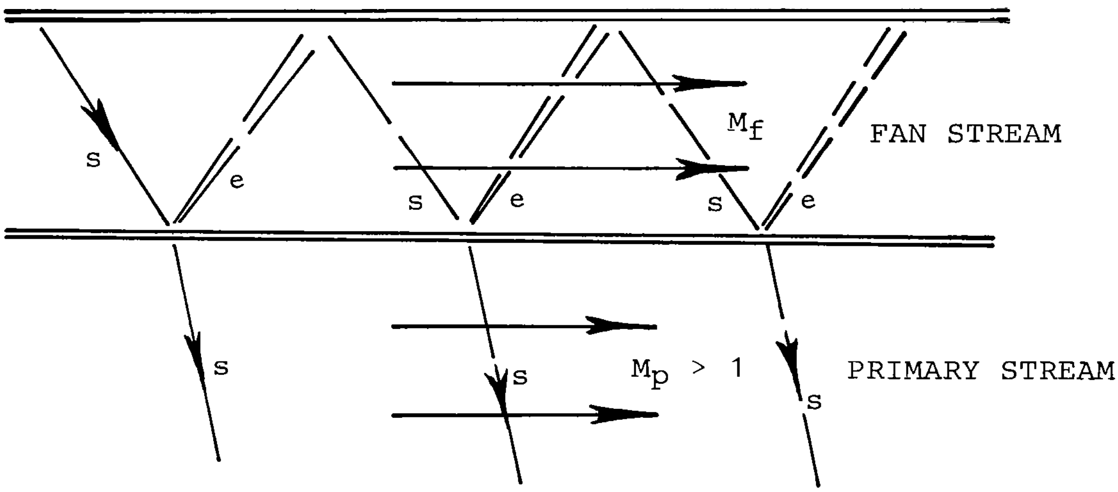


Figure 4.3 Schematic diagram illustrating the reflection of shocks and expansion fans in the fan stream when the primary flow is supersonic. s = shock, e = expansion fan.

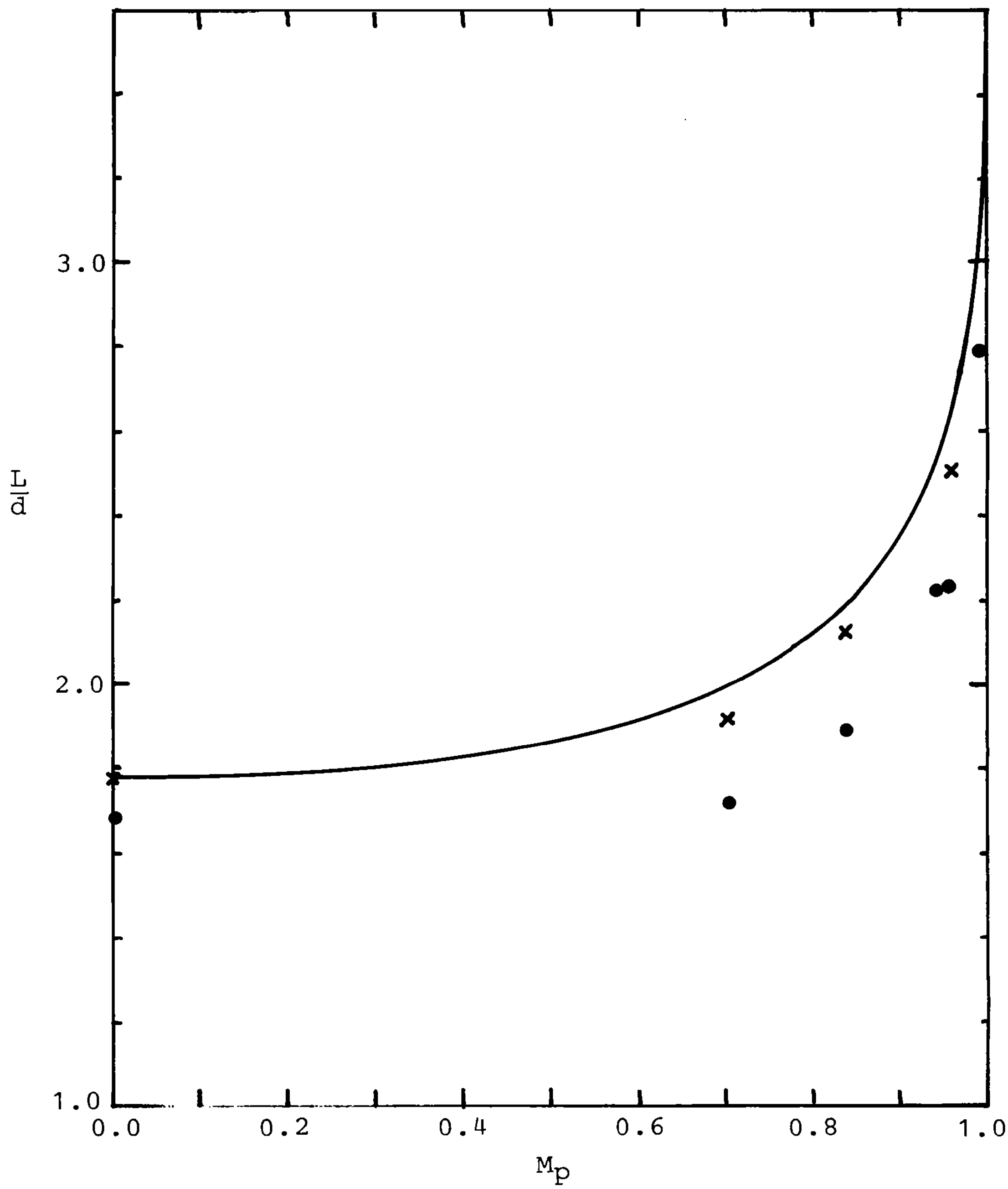


Figure 4.4 Length of shock cell in the fan stream. $M_f = 1.341$, Data from NASA CR-158995.
● Test Series 1; x Test Series 2
——— Equation (4-28)

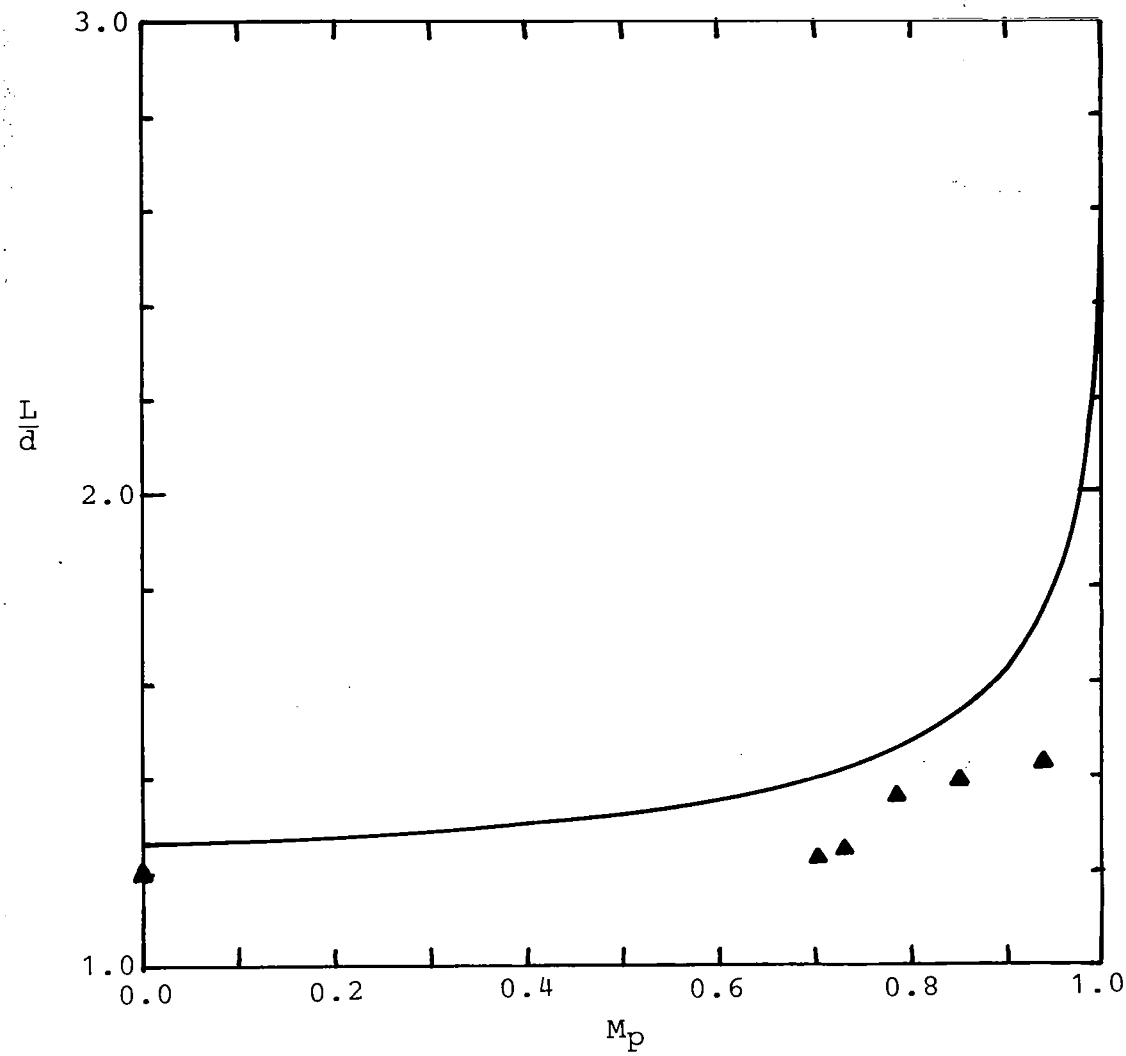


Figure 4.5 Length of shock cell in the fan stream. $M_f = 1.182$, Data from NASA CR-158995.
▲ Test Series 2
——— Equation (4-28)

# 5. SHOCK STRUCTURE AND NOISE CHARACTERISTICS

The basic objective of the work described in this section is to obtain an understanding of the characteristics of shock associated noise from inverted-profile coannular jets in terms of the properties of the shock cell structure and the jet flow. To achieve this, a first order shock cell model is developed. Based on the concept that shock associated noise is generated by the weak interaction between the large scale turbulent structures in the mixing layers of the jet and the repetitive shock cell system, formulae for the peak frequencies as well as noise intensity scaling are derived. The calculated results of these formulae agree very favorably with experimental results.

## 5.1 INTRODUCTION

In Section 4 some of the observed features of shock associated noise were briefly discussed. It was pointed out that depending on the jet operating conditions, a repetitive shock structure can exist either in the fan stream or in the primary jet stream. The shock structure in these two cases can be very different. Hence the characteristics of the noise generated by these shock cell systems would also be very different. In the following, they will, therefore, be investigated separately.

Shock associated noise is generated by sources which are coherent spatially over several shock cell spacings. This was first recognized by Harper-Bourne & Fisher (ref. 7) who studied the noise of choked jets. They proposed a simple model consisting of an array of well correlated point sources to describe the noise generation process. In a more recent paper, the present authors (ref. 9) investigated the shock associated noise of imperfectly-expanded supersonic jets from convergent-divergent nozzles. An alternative noise generation mechanism, based on the proposition that this noise is produced by the weak interaction between the downstream propagating large scale turbulent structures in the mixing layer of the jet and the periodic shock structure in the jet plume, was suggested. A simple analytical model of this noise generation process was developed from which a peak frequency formula and a noise intensity scaling formula were derived. It turned out that these formulae contained the theoretical results of Harper-Bourne & Fisher (ref. 7) as a special case. Further, it was shown that these analytical results agreed very favorably with experimental results for underexpanded as well as overexpanded jet operating conditions, and for hot as well as cold jets.

In this section the general approach and concept developed in reference 9 will be extended to the case of inverted-profile coannular jets. A first order shock structure model for the inverted-velocity-profile jet will be constructed. Based on this mathematical model, peak frequency formulae and noise intensity scaling formulae are derived. The validity of these formulae is tested by comparing the predicted results with measured results. It will be shown that good agreement is found both for subsonic as well as supersonic primary jet flow.

## 5.2 JETS WITH SUPERSONIC PRIMARY FLOW

The flow field near the nozzle exit of an inverted-profile jet is strongly influenced by the nozzle configuration and the thickness of the primary nozzle lip. The present work is confined to jets with negligibly thin primary nozzle lip and with exit velocity vector aligned in the direction of the jet axis. A schematic diagram of the nozzle configuration and the flow is shown in Figure 5.1. The exact dimensions of the jet nozzle used in the present experimental program can be found in Figure 2.1.

When the flow in the primary stream is supersonic a repetitive shock structure would form principally in the primary stream. However, the influence of this shock system would also extend into the fan stream. For a slightly underexpanded jet the shock cells are formed by weak oblique shock waves. A first order model of such a weak shock structure can be obtained by solving the appropriate boundary value problem associated with the linearized equations of motion. For a single jet this type of model had previously been considered by Prandtl (ref. 14) and Pack (ref. 15), and has been found to be useful for estimating the peak frequency and intensity of shock associated noise (ref. 9). Here we will extend these earlier works to the case of supersonic coannular jets.

### 5.2.1 A First Order Shock Structure Model

Consider the jet flow as shown in Figure 5.1. For simplicity we will assume that the mean flow in each region is uniform and that the fan stream and the primary stream are bounded and separated by vortex sheets. We will use $M_f$ and $M_p$ to denote the Mach numbers in the fan and primary streams, respectively. The inner and outer radii of the coannular jet are taken to be a and b. The ambient pressure is denoted by $p_a$ and the pressure at the exit of the primary nozzle is assumed to be $p_a + \Delta p$. The time independent linearized equations of motion governing the flow quantities of the shock structure have been given in full in Section 4 and hence will not be repeated here. In terms of the pressure perturbations in the fan and primary streams, $p_f$ and and $p_p$ respectively, the boundary value problem for the shock cell structure can be written out as,

$r \leq a$:

$$\frac{\partial^2 p_p}{\partial r^2} + \frac{1}{r}\frac{\partial p_p}{\partial r} - (M_p^2 - 1)\frac{\partial^2 p_p}{\partial x^2} = 0 \tag{5-1}$$

$a \leq r \leq b$:

$$\frac{\partial^2 p_f}{\partial r^2} + \frac{1}{r}\frac{\partial p_f}{\partial r} - (M_f^2 - 1)\frac{\partial^2 p_f}{\partial x^2} = 0 \tag{5-2}$$

at $r = 0$: $\quad p_p$ is bounded (5-3)

at $r = a$:

$$\left\{\begin{array}{ll} p_p = p_f & (5\text{-}4) \\ \dfrac{1}{M_p^2}\dfrac{\partial p_p}{\partial r} = \dfrac{1}{M_f^2}\dfrac{\partial p_f}{\partial r} & (5\text{-}5) \end{array}\right.$$

at $r = b$: $\quad p_f = 0$ (5-6)

at $x = 0$:

$$\left\{\begin{array}{lll} p_f = 0 & ;\ a \leq r \leq b & (5\text{-}7) \\ p_p = \Delta p & ;\ r \leq a & (5\text{-}8) \\ \dfrac{\partial p_p}{\partial x} = 0 & & (5\text{-}9) \end{array}\right.$$

$x \to \infty$ : $\quad$ solution is bounded (5-10)

where $(r,x,\theta)$ are the variables of a cylindrical coordinate system centered at the nozzle exit as shown in Figure 5.1. Here the fan stream is assumed to be perfectly expanded.

The solution of (5-1) to (5-10) can be constructed by the method of eigenfunction expansion (ref. 16). Following this method we will first assume that the solution can be represented by a linear combination of separable solutions. It is straightforward to find in this case that these separable solutions are of the form,

$$\left.\begin{array}{l} p_f\ (r,x) = \hat{p}_f(r)\cos kx \\ p_p\ (r,x) = \hat{p}_p(r)\cos kx \end{array}\right\} \tag{5-11}$$

Substitution of (5-11) into (5-1) to (5-6) leads to the following eigenvalue problem:

$r \leq a$:

$$\frac{d^2\hat{p}_p}{dr^2} + \frac{1}{r}\frac{d\hat{p}_p}{dr} + k^2 (M_p^2 - 1)\ \hat{p}_p = 0 \tag{5-12}$$

$a \leq r \leq b$:

$$\frac{d^2\hat{p}_f}{dr^2} + \frac{1}{r}\frac{d\hat{p}_f}{dr} + k^2 (M_f^2 - 1)\ \hat{p}_f = 0 \tag{5-13}$$

at $r = 0$:

$$\hat{p}_p \text{ is bounded} \tag{5-14}$$

at $r = a$:

$$\hat{p}_p = \hat{p}_f \tag{5-15}$$

$$\frac{1}{M_p^2}\frac{d\hat{p}_p}{dr} = \frac{1}{M_f^2}\frac{d\hat{p}_f}{dr} \tag{5-16}$$

at $r = b$:

$$\hat{p}_f = 0 \tag{5-17}$$

where k is the eigenvalue.

The solution of (5-12) which satisfies (5-14) is

$$\hat{p}_p = A\, J_o\, (k \sqrt{M_p^2 - 1}\ r). \tag{5-18}$$

The solution of (5-13) which satisfies (5-17)and (5-15) is

$$\hat{p}_f = A \left[ \frac{J_o(k\sqrt{M_p^2 - 1}\ a)\left[J_o(k\sqrt{M_f^2 - 1}\ r)\ Y_o(k\sqrt{M_f^2 - 1}\ b) - J_o(k\sqrt{M_f^2 - 1}\ b)\ Y_o(k\sqrt{M_f^2 - 1}\ r)\right]}{\left[J_o(k\sqrt{M_f^2 - 1}\ a)\ Y_o(k\sqrt{M_f^2 - 1}\ b) - J_o(k\sqrt{M_f^2 - 1}\ b)\ Y_o(k\sqrt{M_f^2 - 1}\ a)\right]} \right] \tag{5-19}$$

where $J_o(z)$ and $Y_o(z)$ are Bessel and Neumann functions of zeroth order, respectively. A is an arbitrary constant. Substitution of (5-18) and (5-19) into (5-16) leads to the following eigenvalue equations for k:

$$\frac{J_o\left(k\sqrt{M_p^2-1}\,a\right)}{J_1\left(k\sqrt{M_p^2-1}\,a\right)}\;\frac{\sqrt{M_f^2-1}}{\sqrt{M_p^2-1}}\;\frac{M_p^2}{M_f^2}=\left[\frac{\left[J_o\left(k\sqrt{M_f^2-1}\,a\right)Y_o\left(k\sqrt{M_f^2-1}\,b\right)-J_o\left(k\sqrt{M_f^2-1}\,b\right)Y_o\left(k\sqrt{M_f^2-1}\,a\right)\right]}{\left[J_1\left(k\sqrt{M_f^2-1}\,a\right)Y_o\left(k\sqrt{M_f^2-1}\,b\right)-J_o\left(k\sqrt{M_f^2-1}\,b\right)Y_1\left(k\sqrt{M_f^2-1}\,a\right)\right]}\right] \tag{5-20}$$

Equation (5-20) has infinitely many roots. In Appendix 3 it is shown that all these roots are real. For convenience we will denote them as $k_i$, $i = 1, 2, 3$ ..... and assume that they are arranged in an ascending order or magnitude. A discussion of the positions of these roots is given in Appendix 4. To compute $k_i$ numerically one can make use of the limit $(b-a)/a \ll 1$ which is the case of a single jet to provide a starting value for an iterative scheme. In this limit which is discussed in reference 9, $k_i\sqrt{M_p^2-1}\,a$ is approximately equal to the $i^{th}$ root of the zeroth order Bessel function. Corresponding to each root $k_i$ of (5-20) is an eigenfunction given by (5-18) and (5-19). In Appendix 2 it is proved that these eigenfunctions form an orthogonal set. If $(\hat{p}_{fi}, \hat{p}_{pi})$ is the $i^{th}$ eigenfunction then the orthogonality condition is,

$$\frac{M_f^2-1}{M_f^2}\int_a^b \hat{p}_{fi}\,\hat{p}_{fj}\,r\,dr+\frac{M_p^2-1}{M_p^2}\int_0^a \hat{p}_{pi}\,\hat{p}_{pj}\,r\,dr=0\;;\; i\neq j. \tag{5-21}$$

We will now make use of this orthogonality property of the eigenfunctions to construct the shock cell solution to the boundary value problem of (5-1) to (5-10). To do this we will let,

$$\left.\begin{aligned} p_p(r,x) &= \sum_{i=1}^{\infty} A_i\,\hat{p}_{pi}(r)\cos(k_i x) \quad ; r \le a \\ p_f(r,x) &= \sum_{i=1}^{\infty} A_i\,\hat{p}_{fi}(r)\cos(k_i x) \quad ; a \le r \le b \end{aligned}\right\} \tag{5-22}$$

where $A_i$ are arbitrary constants. It is easy to see that as it is with the exception of conditions (5-7) and (5-8), solution (5-22) satisfies the boundary value problem of (5-1) to (5-10). Substitution of (5-22) into (5-7) and (5-8) yields

$$\sum_{i=1}^{\infty} A_i \hat{p}_{fi} (r) = 0 \quad ; a \leq r \leq b \tag{5-23}$$

$$\sum_{i=1}^{\infty} A_i \hat{p}_{pi} (r) = \Delta p \; ; r \leq a \tag{5-24}$$

Equations (5-23) and (5-24) are to hold simultaneously in their respective range of r. To find amplitude $A_i$, multiply (5-23) by

$$\frac{M_f^2 - 1}{M_f^2} \hat{p}_{fj} (r) \, r$$

and integrate over r from r=a to r=b. Also multiply (5-24) by

$$\frac{M_p^2 - 1}{M_p^2} \hat{p}_{pj} (r) \, r$$

and integrate over r from r = 0 to r = a. The sum of these two equations, after making use of the orthogonality condition (5-21), gives

$$A_j = \frac{\dfrac{M_p^2 - 1}{M_p^2} \Delta p \displaystyle\int_0^a \hat{p}_{pj}(r) \, r dr}{\dfrac{M_f^2 - 1}{M_f^2} \displaystyle\int_a^b \hat{p}_{fj}^2 (r) \, r dr + \dfrac{M_p^2 - 1}{M_p^2} \displaystyle\int_0^a \hat{p}_{pj}^2 (r) \, r dr} . \tag{5-25}$$

Thus the first order shock solution corresponding to a nozzle exit pressure difference $\Delta p$ is found. It is given by (5-22) and (5-25).

### 5.2.2 Peak Frequency and Noise Intensity Scaling Formulae

In reference 9 it was suggested that the shock associated noise is generated by the weak but coherent interaction between the downstream propagating large scale turbulent structures in the mixing layer of the jet and its repetitive shock cell system. For inverted profile coannular jets with supersonic primary flows, a similar situation arises so that these jets would also radiate intense shock associated noise. As was discussed in reference 9 the source of this type of noise radiation can be pictured as a superposition of travelling waves. The noise is a form of Mach waves produced by the supersonic phase velocity components. On following the analysis of reference 9 and using the first order shock structure of (5-22), it is easy to show that the frequency, $f_p$, of the spectral peak of shock associated noise is given approximately by

$$f_p = \frac{u_c}{\frac{2\pi}{k_1}\ (1 - M_c \cos\theta)} \tag{5-26}$$

where $u_c$ is the convection velocity of the large scale turbulent structures, $k_1$ is the smallest eigenvalue of (5-20), $\theta$ is the direction of noise radiation and $M_c$ denotes $u_c/c_a$ with $c_a$ being the ambient speed of sound. Equation (5-26) is formally the same as that of a single jet issued from a convergent-divergent nozzle. The principal difference lies in what $k_1$ is and its dependence on the flow configuration. In other words, the accuracy of (5-26) reflects the accuracy of estimating the wave length of the shock cell structure. Thus by comparing (5-26) with experiments, we are actually also testing the validity of the first order shock structure developed above.

Now let us consider a series of experiments in which the outer fan stream Mach number is kept constant while the Mach number of the primary stream, $M_p$, increases gradually. As $M_p$ increases the intensity of shock associated noise, I, also increases. Now to find the dependence of I on $M_p$, we can follow the argument presented in reference 9 and derive that

$$I \propto \text{(Variation of noise source strength as measured from perfectly expanded jet condition)}^2. \tag{5-27}$$

For weak shock-turbulence interaction it was pointed out in reference 9 that the turbulence can be considered more or less constant and the dominant source strength variation comes from the change in the strength of shocks. From the first order shock solutions of (5-22) we see that the change in the strength of the shocks is affected by the change in $M_p$ in a very complicated way. The explicit dependence of this solution is shown in (5-22) and (5-25). However, the change in $M_p$ will also affect $\Delta p$ through which the strength of the shock is changed. Now regardless of the value of $M_p$ shown explicitly in (5-22), (5-25), (5-18) and (5-19) the shock is of zero strength if $\Delta p$ is zero. Thus to the lowest order, the change in the shock strength measured from the perfectly-expanded condition is proportional to the change in $\Delta p$ of (5-25).

With this understanding, (5-27) can be rewritten as,

$$I_{\text{shock associated noise}} \propto \left(\frac{\Delta p}{p_a}\right)^2 . \tag{5-28}$$

It was shown in reference 9 that for a convergent-divergent nozzle of design Mach number $M_d$, $\Delta p/p_a$ is proportional to $(M_p^2 - M_d^2)$. Hence (5-28) becomes

$$I_{\text{shock associated noise}} \propto (M_p^2 - M_d^2)^2 . \tag{5-29}$$

For a choked nozzle, $M_d$ is equal to unity. Thus for such a jet the intensity of shock associated noise would vary as

$$I_{\text{shock associated noise}} \propto (M_p^2 - 1)^2 \tag{5-30}$$

under a constant fan stream operating condition. The validity of scaling formula (5-30) will be tested by comparing with experimental results below.

### 5.2.3 Comparison with Experiment

An extensive experimental study of shock associated noise from inverted-profile coannular jets was conducted in this program. Full details are given in Section 2, and the salient features are as follows: The experimental program consisted of four series of tests. The coannular nozzle used in these tests is shown in Figure 2.1. In each series of tests all the basic jet parameters except the pressure ratio of the primary stream ($\xi_p$) were held constant. These parameters included the primary stream total temperature ($T_{tp}$), the fan stream total temperature ($T_{tf}$) and the fan stream pressure ratio ($\xi_f$). The primary stream pressure ratio and hence the Mach number was increased by a small increment at a time until the Mach number range of 0.52 to 1.56 was covered during each test series. The values of the various jet operating parameters in the experimental program are shown in Table 5.1.

Table 5.1 Coannular jet operating conditions in the acoustic experiments.

| | $T_{tp}$( K) | $T_{tf}$ ( K) | $\xi_f$ | $\xi_p$ |
|---|---|---|---|---|
| Series 1 | 300 | 800 | 3.0 | 1.2 → 4.0 |
| Series 2 | 800 | 300 | 3.0 | 1.2 → 4.0 |
| Series 3 | 600 | 800 | 3.0 | 1.2 → 4.0 |
| Series 4 | 300 | 800 | 4.3 | 1.2 → 4.0 |

Eleven microphones were used to provide intensity and spectral data of the total jet noise over the angular range from 20° to 120° relative to the jet axis. To examine the shock associated noise component alone it is necessary to subtract the contribution of jet mixing noise from these data. In the rear arc of the jet, turbulent mixing noise predominates. Hence in this section, only those data measured in the forward arc of the jet where shock associated noise is important will be analyzed in detail.

According to the first order shock structure model developed above, the shock associated noise for supersonic primary flow will peak at a frequency, $f_p$, given approximately by equation (5-26). In the present inverted-velocity-profile flow configuration, shock associated noise is considered to be generated principally by the weak interaction between the large scale turbulent structures in the mixing layer separating the fan and primary streams and the repetitive shock cell system of the primary stream. The mean velocity of the mixing layer varies from $\bar{u}_p$ (the primary stream velocity) to $\bar{u}_f$ (the fan stream velocity) with an average velocity, $\bar{u}_a$, equal to $0.5\ (\bar{u}_p + \bar{u}_f)$. In the absence of extensive flow and turbulence measurements we will take $u_c$, the convective velocity of the large turbulent structures in equation (5-26), to be equal to $0.7 u_a$ in analogy to that of a single jet. Thus (5-26) becomes

$$f_p = \frac{k_1\ u_a}{2\pi\ (1 - M_a \cos\theta)} \tag{5-31}$$

where $u_a = 0.5\ (\bar{u}_f + \bar{u}_p)$ and $M_a = u_a/c_a$.

To test the accuracy of (5-31) the calculated peak frequencies will now be compared with experimental results. Figures 5.2 and 5.3 show the measured noise spectra at $M_p = 1.28$ and $M_p = 1.47$ of test series 1. The noise spectra at $\theta = 90°$ and $\theta = 120°$ are dominated by a single peak of relatively narrow bandwidth which is one of the characteristics of shock associated noise. As can be seen the calculated peak frequency values match quite closely with the measured peak frequencies. The dependence of $f_p$ on the observation angle $\theta$ is accurately predicted in both cases. Figures 5.4 through 5.9 are representative data taken from test series 2, 3 and 4. The calculated peak frequencies of (5-31) are also shown. The agreement between measurements and predictions is extremely good in all the cases. In the four test series of the present experimental program, the primary and fan stream temperatures were varied from cold to hot and vice versa. The Mach number range covered was quite extensive. In all the test points examined, there is always a favorable agreement between the calculated values of (5-31) and experimental results. Based on this it is possible to state confidently that equation (5-31) can indeed provide an accurate first estimate of the peak frequency of shock associated noise from inverted-profile coannular jets with supersonic primary flow.

The variation of the measured noise intensity at $\theta = 120°$ for each test series as a function of the primary flow Mach number was studied in Section 3 (see Figures 3.5 to 3.8). These noise intensity curves drop to a minimum at a slightly supersonic primary flow Mach number. It was pointed out there that at this minimum noise condition the noise is essentially turbulent mixing noise alone. As the primary flow Mach number increases there is a rapid rise in the noise intensity. This rapid increase in noise level over a relatively small Mach number range is the result of the large contribution of shock associated noise. Thus as a first estimate of the shock associated noise intensity, we will assume that the turbulent mixing noise is fairly constant relative to shock noise and is equal to the noise intensity at the minimum noise condition of each test series. That is,

$$I_{\text{shock associated noise}} = I_{\text{measured}} - I_{\text{turbulent mixing noise}}$$

$$\simeq I_{\text{measured}} - I_{\text{measured at minimum noise condition}} \qquad (5\text{-}32)$$

By means of (5-32) the shock associated noise intensity as a function of primary flow Mach number can be calculated. These values can now be used to test the accuracy of the shock associated noise intensity scaling formula (5-30). Figures 5.10, 5.11, 5.12 and 5.13 show the intensity of shock associated noise (computed according to equation (5-32)) as $\beta = \sqrt{M_p^2 - 1}$ varies for each test series. The solid straight line in each of these figures represents the expected noise intensity as given by formula (5-30). It is evident from these figures that the agreement between measured data and (5-30) is quite good. By comparing the four figures it is easy to see that the proportionality factor of (5-30) is not a universal constant. Test series 1 and 3 have the same fan stream Mach number, fan stream total temperature and similar primary stream total temperature. The proportionality constants are practically equal in these two cases. Test series 2, on the other hand, has a normal instead of an inverted temperature profile. Although the fan stream Mach number is the same as in test series 1 and 3, the shock associated noise intensity is less. This reflects the fact that the large scale turbulent structures in the jet mixing layer are influenced by the velocity and temperature gradients of the shear layer.

## 5.3 JETS WITH SUBSONIC PRIMARY FLOW

When the primary flow is subsonic, a repetitive shock cell structure can exist in the supersonic fan stream. Although the gross features of the shock cells such as the length of each cell are controlled by the mean velocity profile, the strength of the shocks and other details are very much influenced by the nozzle design. If the fan stream nozzle exit is recessed back relative to the primary nozzle, then the ratio of the length of this recess to the fan stream nozzle height (annulus) is an important parameter in determining the internal structure of the shock cells. In addition, the thickness of the primary nozzle lip does exert an important influence on the flow field in its vicinity and hence the repetitive shock system downstream. Through their influence on the shock cell system, all these factors are, therefore, important in the subsequent generation of shock associated noise. The nozzle used in the present experimental work (see Figure 2.1) has a very thin primary nozzle lip but a rather large recess ratio of 2.23. Thus the measured data would in some aspects be reflecting the nozzle configuration and the particular recess ratio used. The basic objective of this investigation is to obtain an understanding of the shock associated noise of inverted-profile coannular jets that are not too dependent on the particular nozzle configuration. It is beyond the scope of this work to study the influence of the primary nozzle lip thickness, fan stream nozzle recess ratio and other nozzle configuration variables on shock associated noise. We will confine our investigation only to the effects of the flow variables such as the fan and primary stream Mach numbers and the speed of sound, etc.

### 5.3.1 A First Order Shock Structure Model

The strength of the shock cell system in the fan stream is obviously controlled by the mismatch of pressure at the nozzle exit and the ambient pressure and other configuration details of the coannular nozzle. Beyond the primary nozzle exit (see Figure 2.1), the spacings of shock cells are, however, completely determined by the jet flow. Within the restricted objective of this work as stated above, we will now develop a first order shock structure model to estimate the size of the shock cells as a function of the flow parameters. This information will be used later to determine the peak frequencies of the shock associated noise.

Consider the flow configuration as shown in Figure 5.14. Because the flow in the primary jet is subsonic, the influence of the shock structure in the supersonic fan stream will extend upstream into the primary nozzle. In terms of pressure perturbations in the fan stream, $p_f$, and the primary stream, $p_p$, the boundary value problem for the first order shock structure is,

$r \leq a$ ; $-\infty < x < \infty$:

$$\frac{\partial^2 p_p}{\partial r^2} + \frac{1}{r} \frac{\partial p_p}{\partial r} + (1 - M_p^2) \frac{\partial^2 p_p}{\partial x^2} = 0 \tag{5-33}$$

$a \leq r \leq b$ ; $x \geq 0$:

$$\frac{\partial^2 p_f}{\partial r^2} + \frac{1}{r} \frac{\partial p_f}{\partial r} - (M_f^2 - 1) \frac{\partial^2 p_f}{\partial x^2} = 0 \tag{5-34}$$

$r = b$:

$$p_f = 0 \tag{5-35}$$

$r = a$; $x > 0$:

$$p_f = p_p \tag{5-36}$$

$$\frac{1}{M_f^2}\frac{\partial p_f}{\partial r} = \frac{1}{M_p^2}\frac{\partial p_p}{\partial r} \tag{5-37}$$

as $x \to \pm\infty$, $\quad p_p$ is bounded (5-38)

at $x = 0$:

$$\left.\begin{aligned} p_f &= \Delta p && (5\text{-}39)\\ \frac{\partial p_f}{\partial x} &= 0 && (5\text{-}40)\end{aligned}\right\} \quad a \le r \le b$$

$$\left.\begin{aligned} &r = 0: && p_p \text{ is bounded}\\ &r = a,\ x < 0: && \frac{\partial p_p}{\partial r} = 0\end{aligned}\right\} \tag{5-41}$$

As before this boundary value problem can be solved by the method of eigenfunction expansion. However, because of the upstream influence inside the primary nozzle, two sets of eigenfunction expansion are necessary, one for $x \ge 0$ and the other for $x \le 0$. For $x \le 0$, it is straightforward to show that the appropriate expansion which satisfies (5-33), (5-38) and (5-41) is

$r \le a$:

$$p_p\ (r, x) = \sum_{m=1}^{\infty} C_m\ J_o\ (\mu_m \frac{r}{a})\exp\left[\frac{\mu_m\ x}{a\sqrt{1 - M_p^2}}\right] \tag{5-42}$$

where $\mu_m$ are the zeros of the first order Bessel function and $C_m$ is a set of arbitrary constants. For $x \ge 0$, the appropriate eigenfunction expansion can be found by using separable solutions as in section 5.2. Let

$$\left.\begin{aligned} p_f\ (r, x) &= \mathrm{Re}\ [\hat{p}_f\ (r)\ \cos kx]\\ p_p\ (r, x) &= \mathrm{Re}\ [\hat{p}_p\ (r)\ \cos kx]\end{aligned}\right\} \tag{5-43}$$

where k is an arbitrary constant and Re [ ] = real part of. Substitution of (5-43) into (5-33) to (5-37) leads to the following eigenvalue problem:

$a \le r \le b$:

$$\frac{d^2\hat{p}_f}{dr^2} + \frac{1}{r}\frac{d\hat{p}_f}{dr} + k^2\ (M_f^2 - 1)\ \hat{p}_f = 0 \tag{5-44}$$

$r \leq a$:

$$\frac{d^2\hat{p}_p}{dr^2} + \frac{1}{r}\frac{d\hat{p}_p}{dr} - k^2 \, (1 - M_p{}^2) \, \hat{p}_p = 0 \tag{5-45}$$

$r = b$: $\quad \hat{p}_f = 0 \qquad (5\text{-}46)$

$$r = a: \begin{cases} \hat{p}_f = \hat{p}_p & (5\text{-}47) \\ \dfrac{1}{M_f{}^2}\dfrac{d\hat{p}_f}{dr} = \dfrac{1}{M_p{}^2}\dfrac{d\hat{p}_p}{dr} & (5\text{-}48) \end{cases}$$

The general solution of (5-44) which satisfies (5-46) is

$$\hat{p}_f = D \, \frac{I_o(k\sqrt{1 - M_p{}^2}\, a)[J_o(k\sqrt{M_f{}^2 - 1}\, r)\, Y_o(k\sqrt{M_f{}^2 - 1}\, b)}{[\, J_o(k\sqrt{M_f{}^2 - 1}\, a)\, Y_o(k\sqrt{M_f{}^2 - 1}\, b)} \tag{5-49}$$

$$\frac{- J_o\,(k\sqrt{M_f{}^2 - 1}\, b)\, Y_o\,(k\sqrt{M_f{}^2 - 1}\, r)]}{- J_o\,(k\sqrt{M_f{}^2 - 1}\, b)\, Y_o\,(k\sqrt{M_f{}^2 - 1}\, a)]}$$

The general solution of (5-45) which is bounded at $r = 0$ and satisfies (5-47) is

$$\hat{p}_p = D\, I_o\,(k\sqrt{1 - M_p{}^2}\, r) \tag{5-50}$$

where $I_o(z)$ is the zeroth order modified Bessel function. To satisfy the last condition of the eigenvalue problem (5-48), the eigenvalue k must be a root of the following equation:

$$- \frac{I_o\,(k\sqrt{1 - M_p{}^2}\, a)}{I_1\,(k\sqrt{1 - M_p{}^2}\, a)} \sqrt{\frac{M_f{}^2 - 1}{1 - M_p{}^2}} \; \frac{M_p{}^2}{M_f{}^2} =$$

$$\left[\frac{J_o\,(k\sqrt{M_f{}^2 - 1}a)\; Y_o\,(k\sqrt{M_f{}^2 - 1}b) - J_o\,(k\sqrt{M_f{}^2 - 1}b)\; Y_o\,(k\sqrt{M_f{}^2 - 1}a)}{J_1\,(k\sqrt{M_f{}^2 - 1}a)\; Y_o\,(k\sqrt{M_f{}^2 - 1}b) - J_o\,(k\sqrt{M_f{}^2 - 1}b)\; Y_1\,(k\sqrt{M_f{}^2 - 1}a)}\right] \tag{5-51}$$

The roots of (5-51) are either real or purely imaginary. This can be shown by noting that equation (A3-1) of Appendix 3 is also applicable to the present problem. Since $M_p^2$ is less than unity, the right hand side of (A3-1) is either positive or negative. k being the square root of the right hand side must, therefore, be either real or purely imaginary. The real roots represent periodic solutions in the flow direction. These are solutions of special interest to the shock associated noise problem. A discussion of the locations of these roots is given in Appendix 4. If k is purely imaginary (5-43) will give unbounded solution as $x \to \infty$. These roots are to be discarded. Corresponding to each real root of (5-51) the eigenfunction $(\hat{p}_{fi}, \hat{p}_{pi})$ is given in the form of (5-49) and (5-50) so that the full solution for $x \geq 0$ is

$$p_f(r, x) = \sum_{i=1}^{\infty} D_i \hat{p}_{fi}(r) \cos(k_i x) \tag{5-52}$$

$$p_p(r, x) = \sum_{i=1}^{\infty} D_i \hat{p}_{pi}(r) \cos(k_i x) \tag{5-53}$$

where $D_i$ ($i = 1, 2, 3 \ldots$) are arbitrary constants. The last step in finding the first order shock structure solution is to impose the boundary and joining conditions on (5-42), (5-52) and (5-53) at $x = 0$. Here, however, we will not pursue this point any further as the fan nozzle exit geometry used in our experiment is quite different from the simple model of Figure 5.14. The difference will manifest itself in the values of $C_m$ and $D_m$ of (5-42), (5-52) and (5-53) only. It will not affect the eigenfunctions ($\hat{p}_{fi}(r) \cos k_i x$, $\hat{p}_{pi}(r) \cos k_i x$). We will not make use of these coefficients to study the effect of Mach number on the intensity of shock associated noise.

### 5.3.2 Peak Frequency Formulae

In reference 9 it was shown that for a supersonic jet from a convergent-divergent nozzle, the shock associated noise was concentrated around a single peak. This noise was generated by the interaction of downstream propagating large scale turbulent structures and the lowest mode of periodic shock cell solution. It was found that the higher order modes could also give rise to supersonic source component and hence shock associated noise. However, for the single jet case the amplitudes of higher order modes were so much smaller than the fundamental that their associated noise would be difficult to observe. For the inverted-profile coannular jet, the amplitudes $D_i$ in (5-52) of the various periodic modes are highly dependent on the nozzle configuration. Schlieren photographs of the jet flow taken in an earlier experiment (ref. 4) clearly indicated that a highly complicated internal structure existed inside the basic shock pattern. This strongly suggested that, at least, several higher order modes were present in the fan stream shock cell structure. Thus the resulting shock associated noise spectrum might not consist of just the usual single characteristic peak. Instead it could be dominated by a sequence of peaks with overlapping half-widths.

To estimate these peak frequencies, one can simply make use of the first order shock cell solution given by equation (5-52). By following the analysis of reference 9 it is straightforward to find that the $i^{th}$ peak frequency is given approximately by

$$f_{pi} = \frac{u_c\ k_i}{2\pi\ (1 - M_c \cos\theta)} \tag{5-54}$$

where $k_i$ is the $i^{th}$ smallest real root of the eigenvalue equation (5-51). The quantity $u_c$ is the convection velocity of the large scale turbulent structures in the outer fan stream mixing layer. According to the single jet turbulence data $u_c$ is nearly equal to 0.7 $u_f$ where $u_f$ is the fan stream velocity. Incorporating this into (5-54) one finds

$$f_{pi} = \frac{0.7\ u_f\ k_i}{2\pi\ (1 - 0.7\ M_f \cos\theta)} \tag{5-55}$$

$$(i = 1, 2, 3 \ldots\ldots).$$

To compare (5-55) with measurements, the values of $k_i$ have to be found by solving (5-51) numerically. It turns out that this can be accomplished relatively easily by using an iterative root finding procedure such as Newton's method. As first guess values, the wave numbers given by formula (4-27) of Section 4 have been found to be extremely helpful.

### 5.3.3 Comparison with Experiment

We will now compare the calculated peak frequencies of (5-55) with experimental data. Figures 5.15 and 5.16 show the measured noise spectra at two experimental conditions of test series 1 (see Table 5.1). In Figure 5.15 with $M_p$ = 0.52, the spectrum clearly exhibits twin peaks at both $\theta$ = 90° and $\theta$ = 120°. The calculated peak frequencies corresponding to the first two shock cell modes are also shown. As can be seen, there is good agreement between calculated results and measured peak frequencies. Figure 5.16 shows similar results at a high subsonic primary flow Mach number of 0.90. In this case the upper frequency limit of the measured spectrum at $\theta$= 60° is high enough to include the peak frequency of the noise generated by the first shock cell mode. At $\theta$ = 120° the calculated peak frequencies of the first four modes are included. The data shows two well defined peaks near the first two calculated peak values. For the third and fourth peaks, the measured data points are too far apart to establish whether these peaks do exist or not. That is, the spectral analysis in one-third octave bands does not provide adequate resolution, and narrowband frequency analysis is required to distinguish these peaks.

Figures 5.17 to 5.22 show similar data for test series 2, 3 and 4. A closer examination of all the data (including those not given in this report) and calculated peak frequency values reveals that the shock associated noise consists of at least two or more peaks. Strong indications are found in test series 2 that as many as four to five modes are contributing to the far field shock associated noise. The lack of resolution in the data, however, prohibits a clear identification of the higher order modes. When the peak frequencies are sufficiently close to each other the overlapping of contributions from adjacent modes causes the spectrum to look like a smooth continuous curve with occasional irregularities. Great care must, therefore, be exercised in interpreting the high frequency end of the shock associated noise spectra.

In formula (5-55) the value of $k_i$ is not a function of the fan stream Mach number ($M_f$) alone. As can be seen in (5-51) it depends on the primary flow Mach number ($M_p$) also. To illustrate this dependence, we will examine the noise spectra at $\theta = 120^{\circ}$ for different values of $M_p$ but at a constant $M_f$. Figures 5.23 to 5.26 give the measured spectra and calculated peak frequencies for the four test series. It is easy to see that as the primary flow Mach number increases the measured as well as the calculated peak frequencies decrease. The change in the lowest peak frequency is the largest and is most noticeable in the test series 3 data. The decrease in the observed peak frequency when $M_p$ increases from 0.52 to 0.96 is as large as one-third of the original peak frequency value. This is reproduced by the calculated results, although the calculated results appear to somewhat overpredict the change in peak frequency with changing $M_p$ in some other cases.

The intensity of shock associated noise, I, does not appear to be much influenced by the subsonic primary flow Mach number. This can be seen from Figures 3.5 to 3.8 of Section 3. In each of these figures the measured noise intensity is practically constant over the range $M_p < 1$. Thus I is a function of the fan stream Mach number, $M_f$, alone. By following the arguments of section 5.2, it is straightforward to derive the scaling formula $I \propto (M_f^2 - M_d^2)^2$ where $M_d$ is the fan stream nozzle design Mach number. Here we will, however, not pursue this point further as there are not enough data points to verify this formula.

To sum up, an exceedingly favorable overall agreement is found when comparing all the spectral data, including those not shown in this report, with equation (5-55). The dependence of $f_{pi}$ in (5-55) on the variables $\theta$, $M_f$ and $M_p$ are all confirmed by experimental results. The good agreement between theory and experiment obtained here provides further validation of the shock associated noise generation mechanism proposed in reference 9.

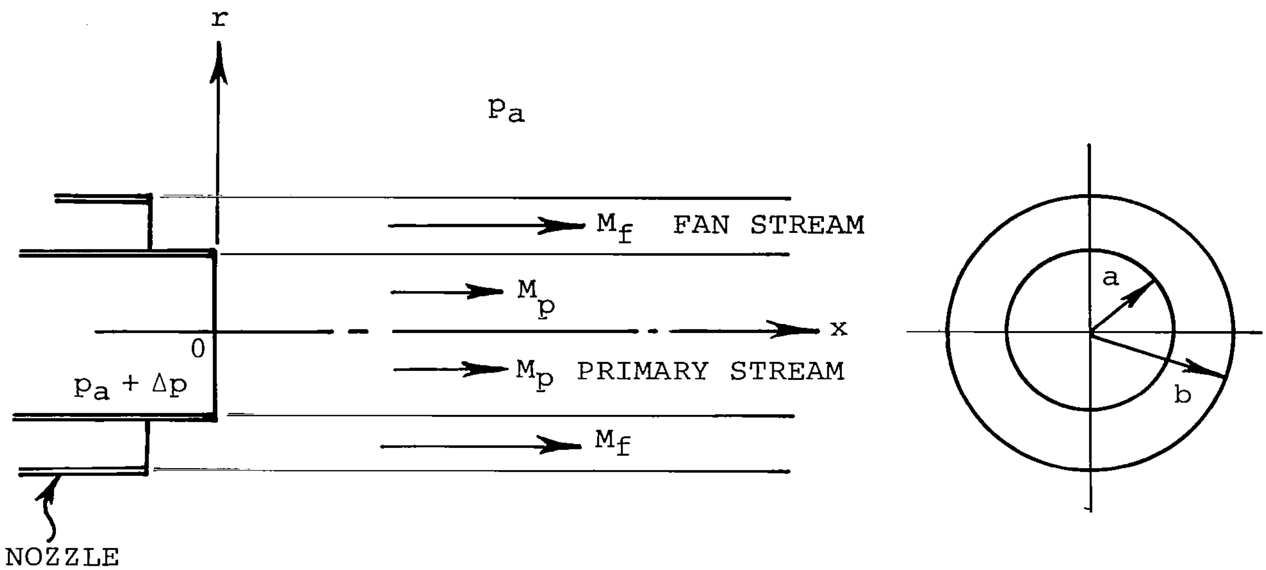


Figure 5.1 Schematic diagram of nozzle geometry and vortex sheet bounded inverted-profile coannular jet.

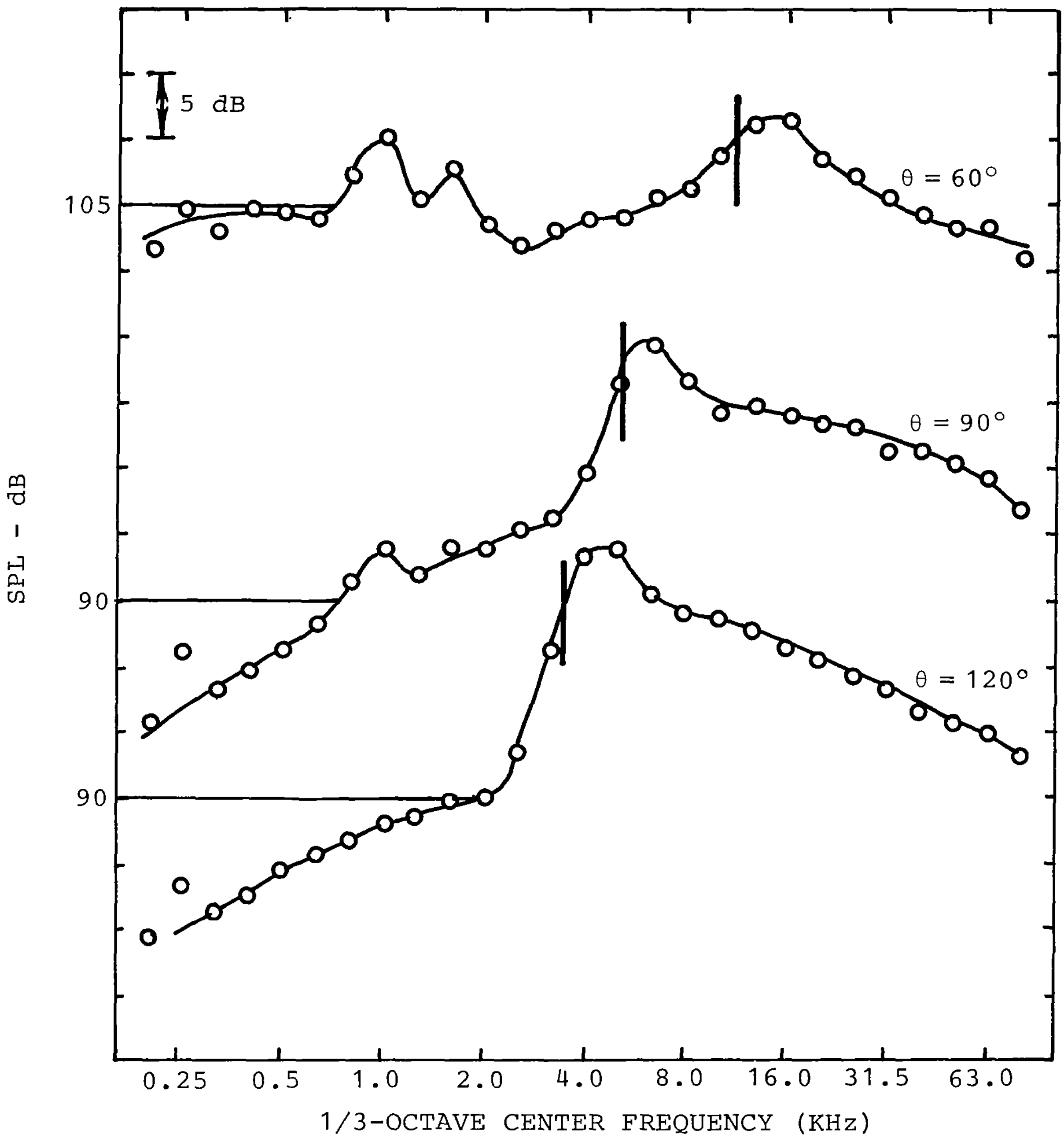


Figure 5.2 Noise spectra at $M_p = 1.28$: Series 1.
▬▬ Calculated peak frequency.

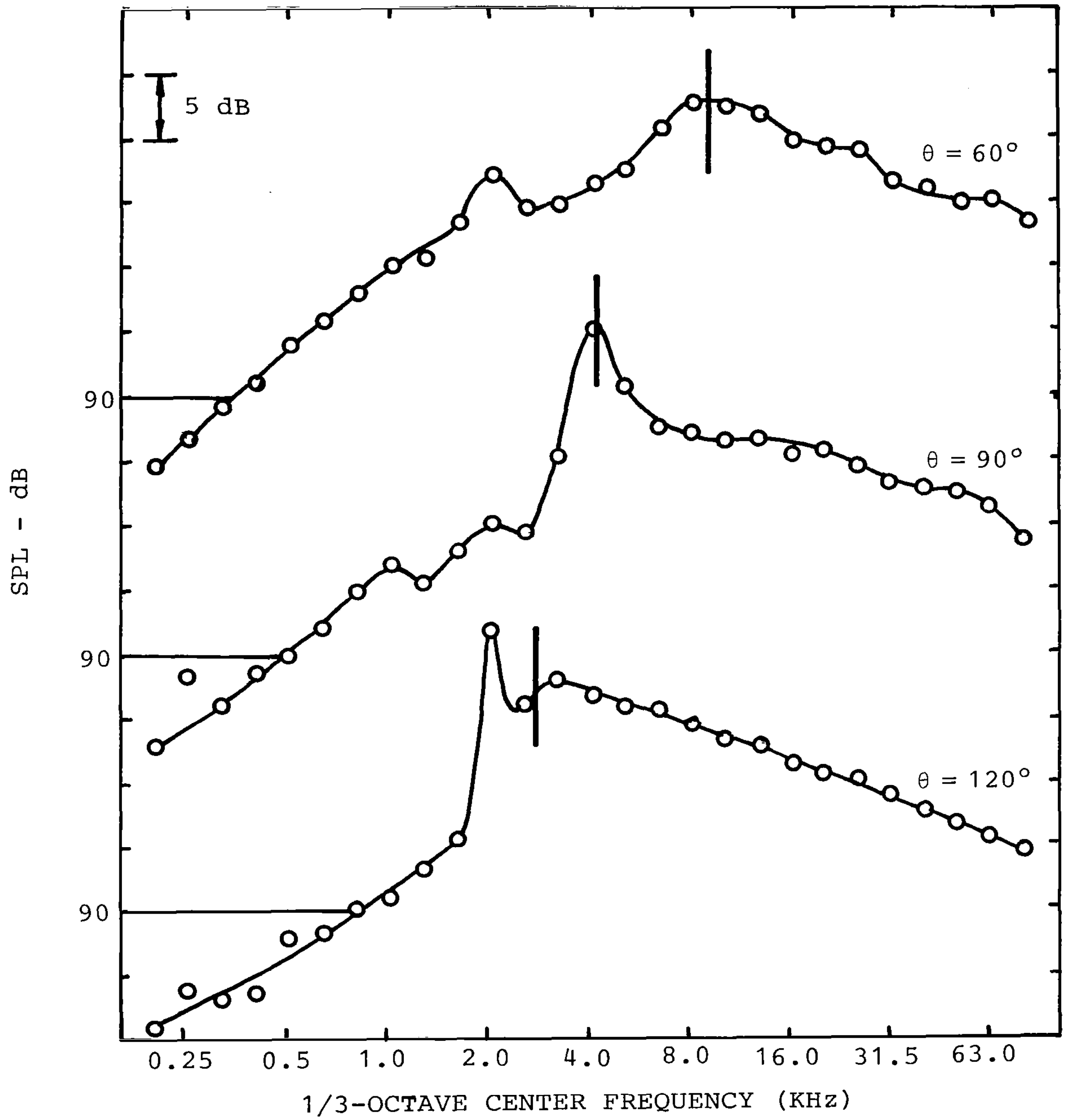


Figure 5.3 Noise spectra at $M_p = 1.47$: Series 1.
——— Calculated peak frequency

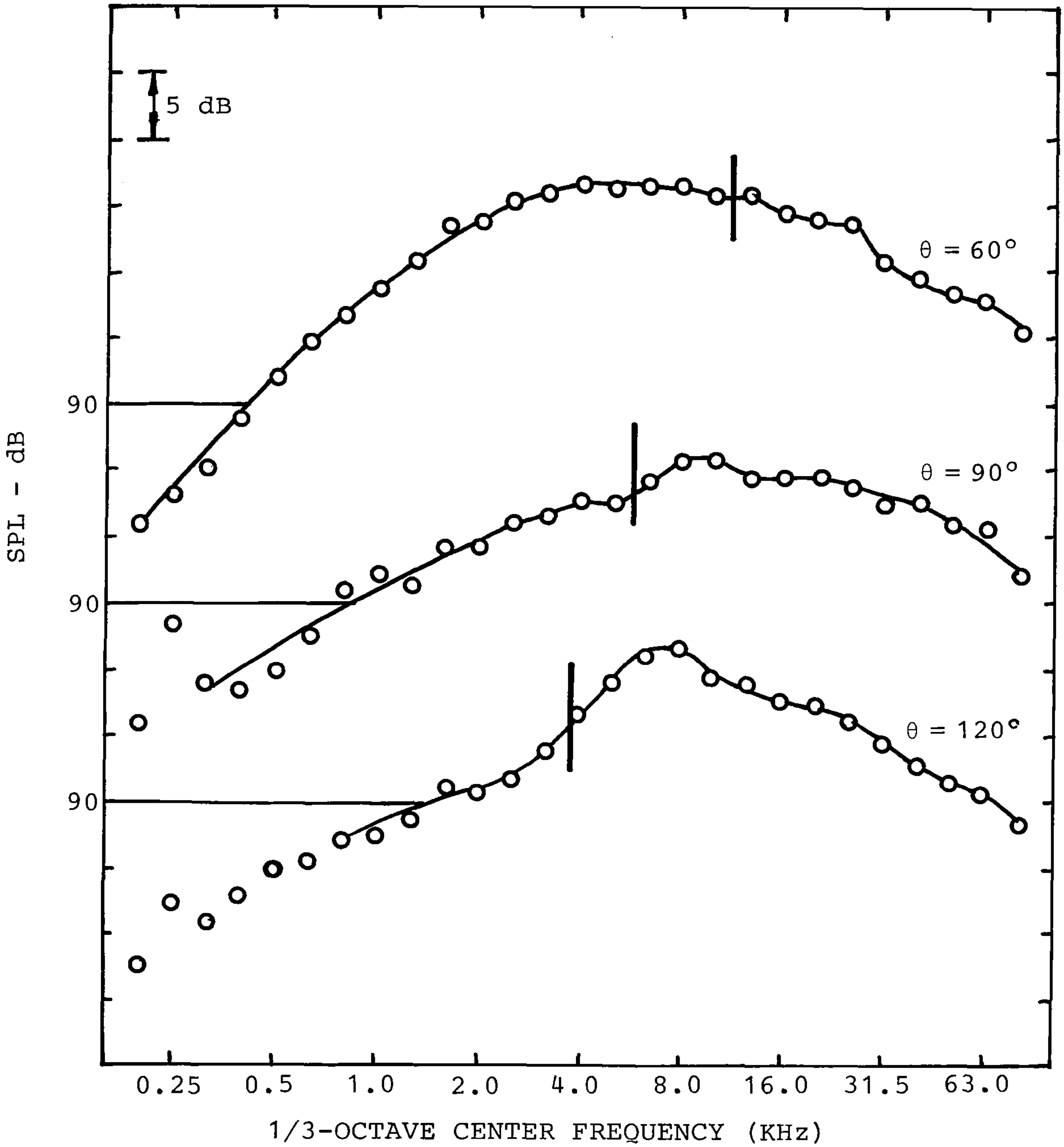


Figure 5.4 Noise spectra at $M_p = 1.19$: Series 2.
——— Calculated peak frequency.

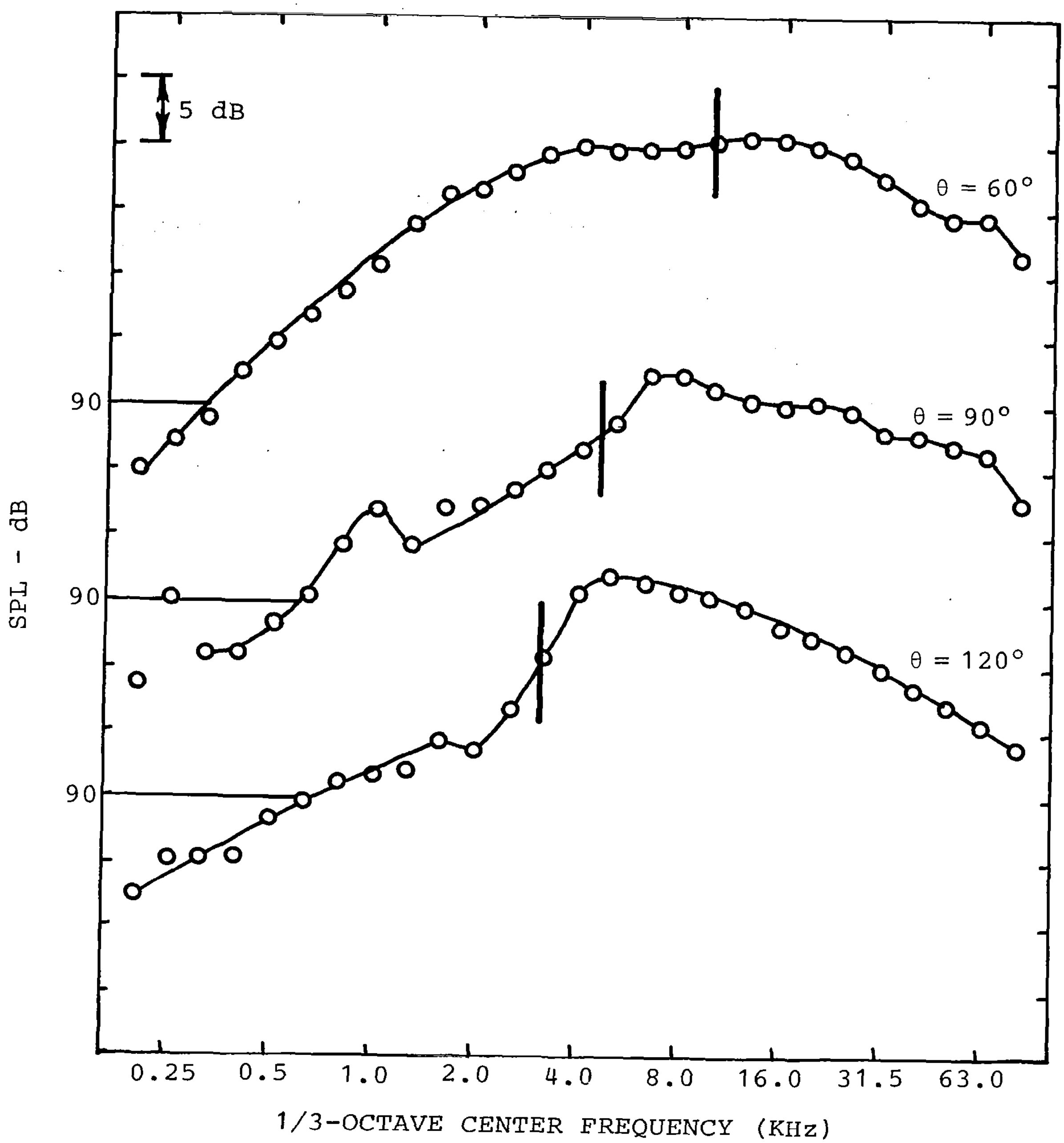


Figure 5.5 Noise spectra at $M_p = 1.38$: Series 2.
——— Calculated peak frequency.

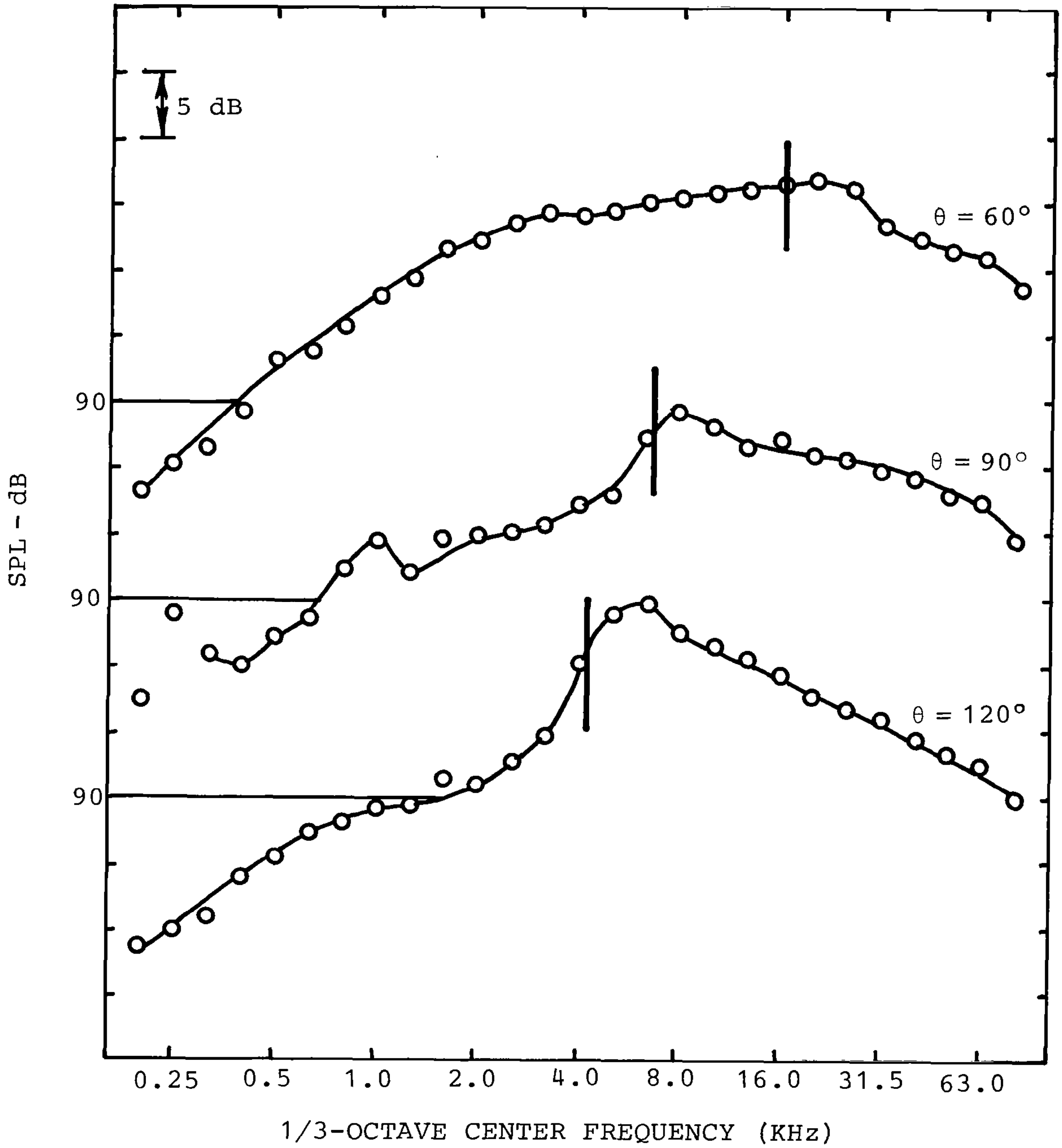


Figure 5.6 Noise spectra at $M_p = 1.19$: Series 3.
——— Calculated peak frequency.

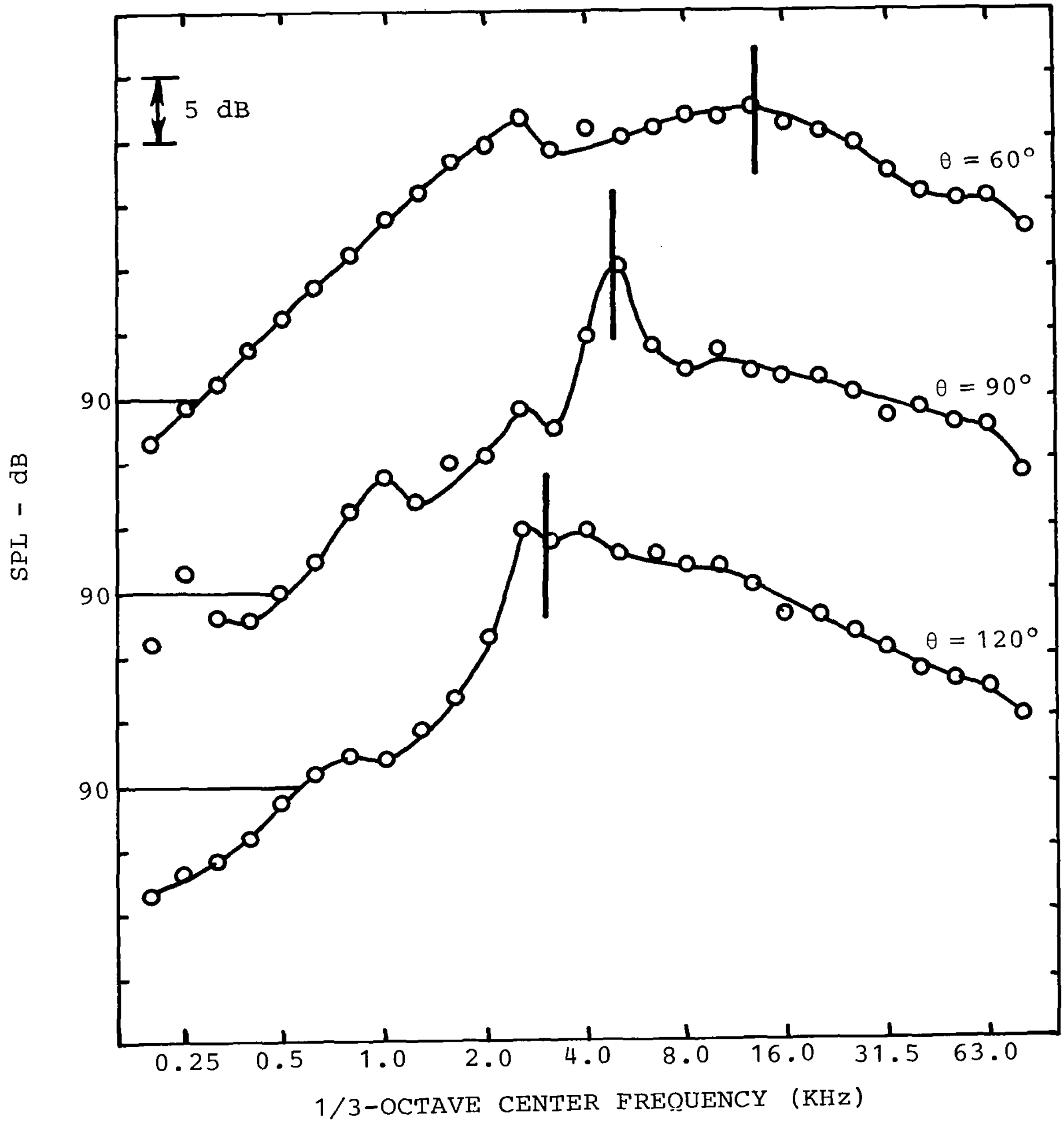


Figure 5.7 Noise spectra at $M_p = 1.47$: Series 3.
——— Calculated peak frequency.

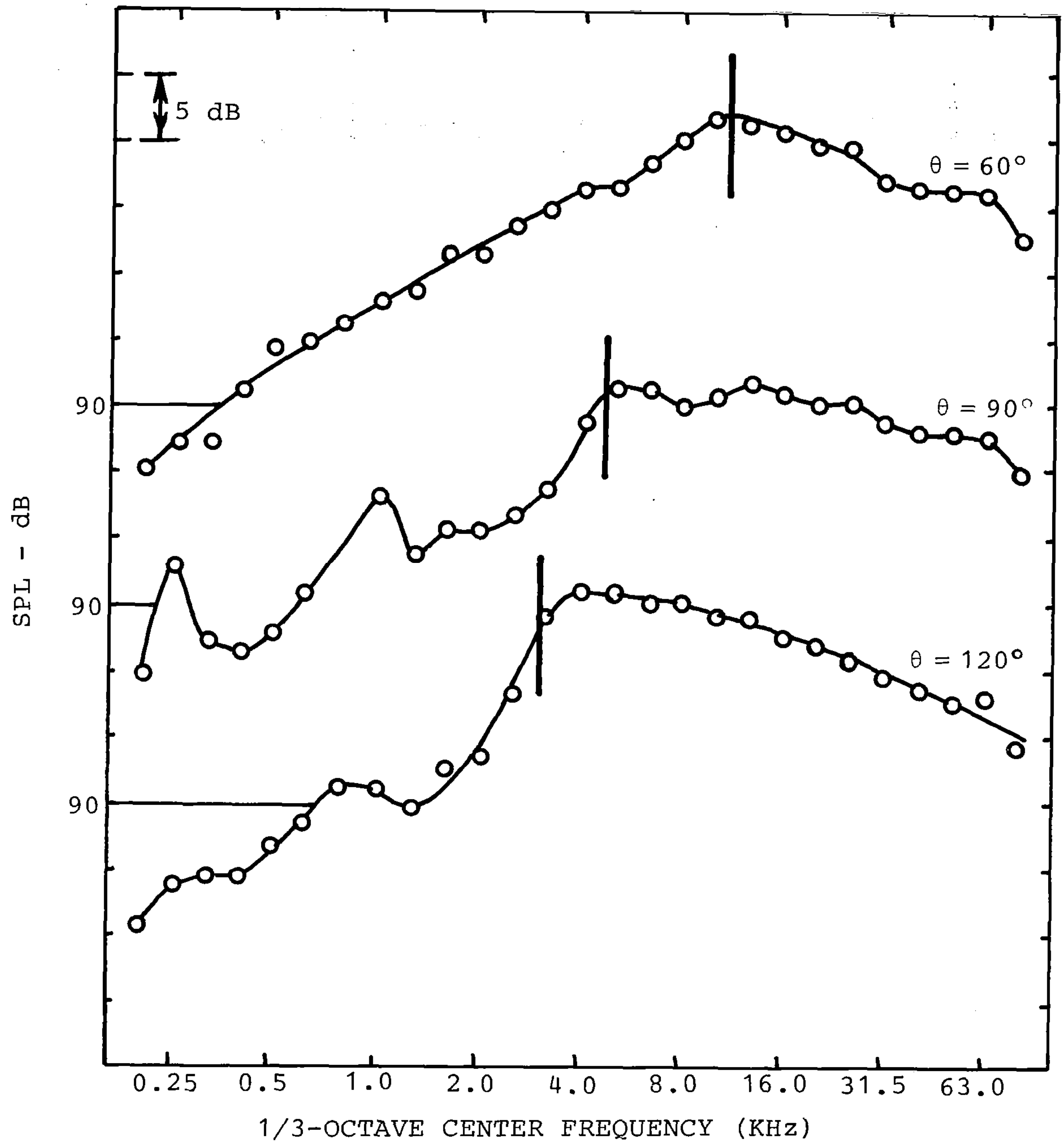


Figure 5.8 Noise spectra at $M_p = 1.28$: Series 4.
——— Calculated peak frequency.

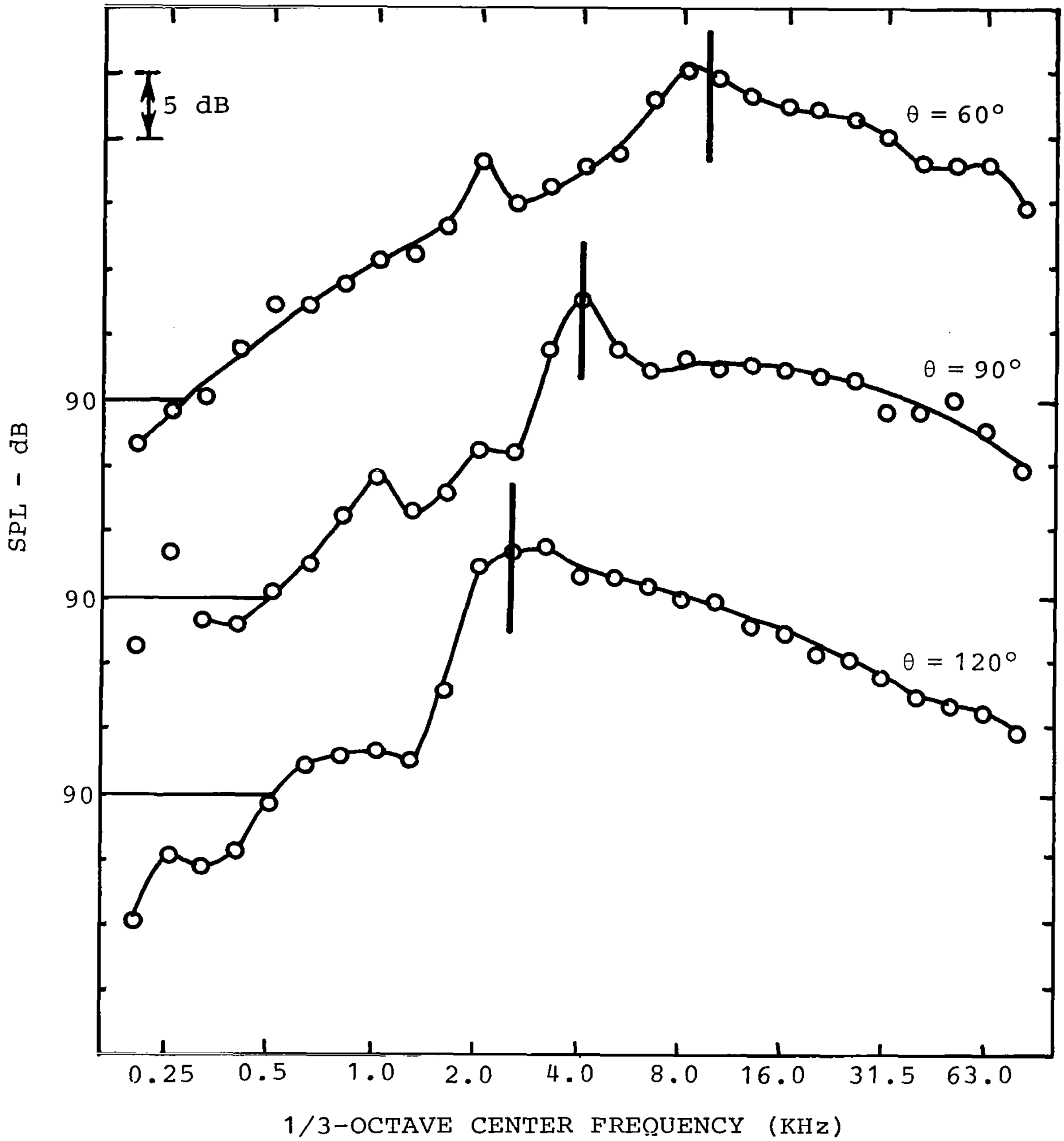


Figure 5.9 Noise spectra at $M_p = 1.47$: Series 4.
——— Calculated peak frequency.

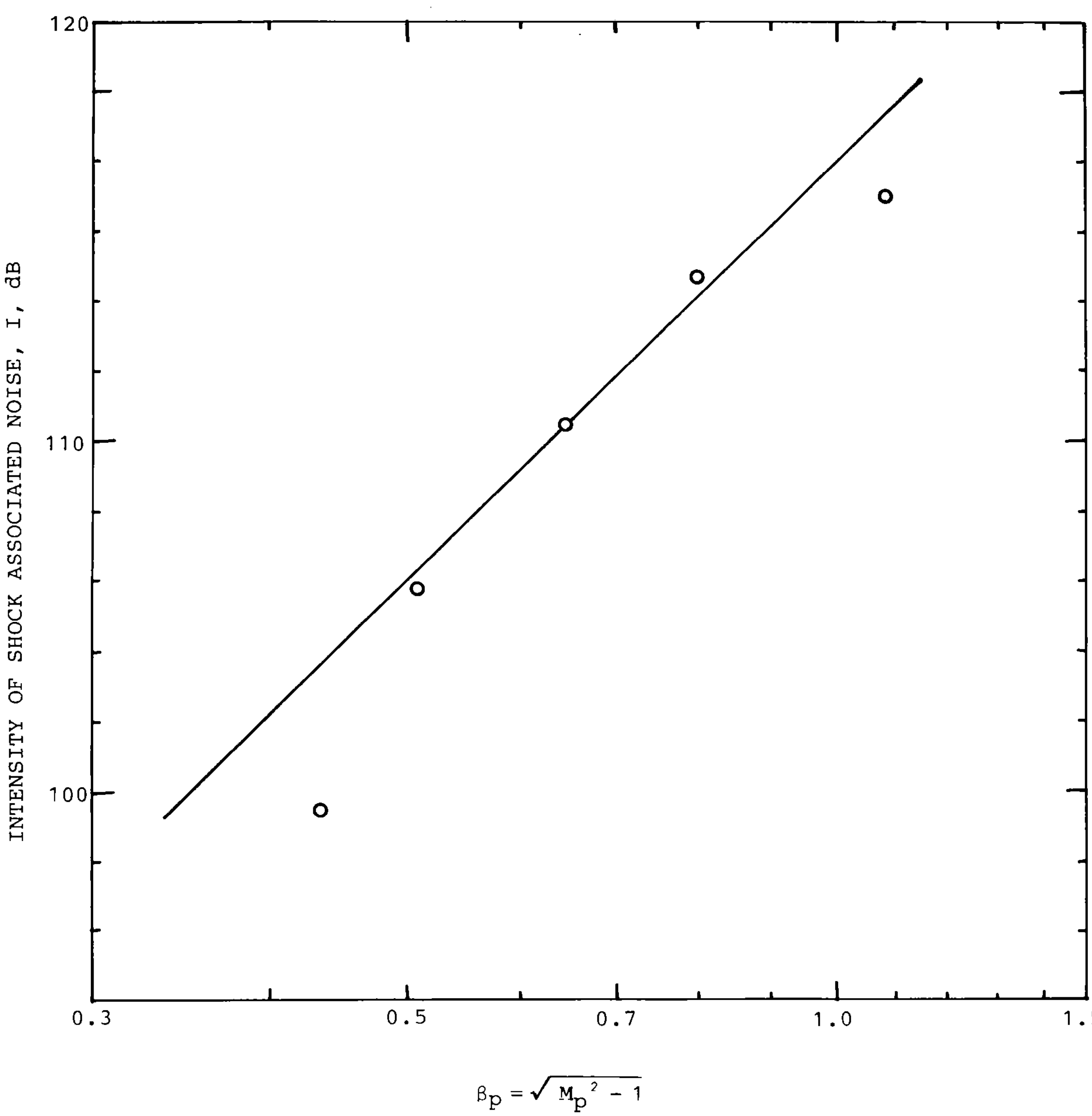


Figure 5.10 Intensity of shock associated noise as a function of $\beta_p$: Series 1, $\theta = 120°$.
o Experiment; ——— $I \propto \beta_p^4$.

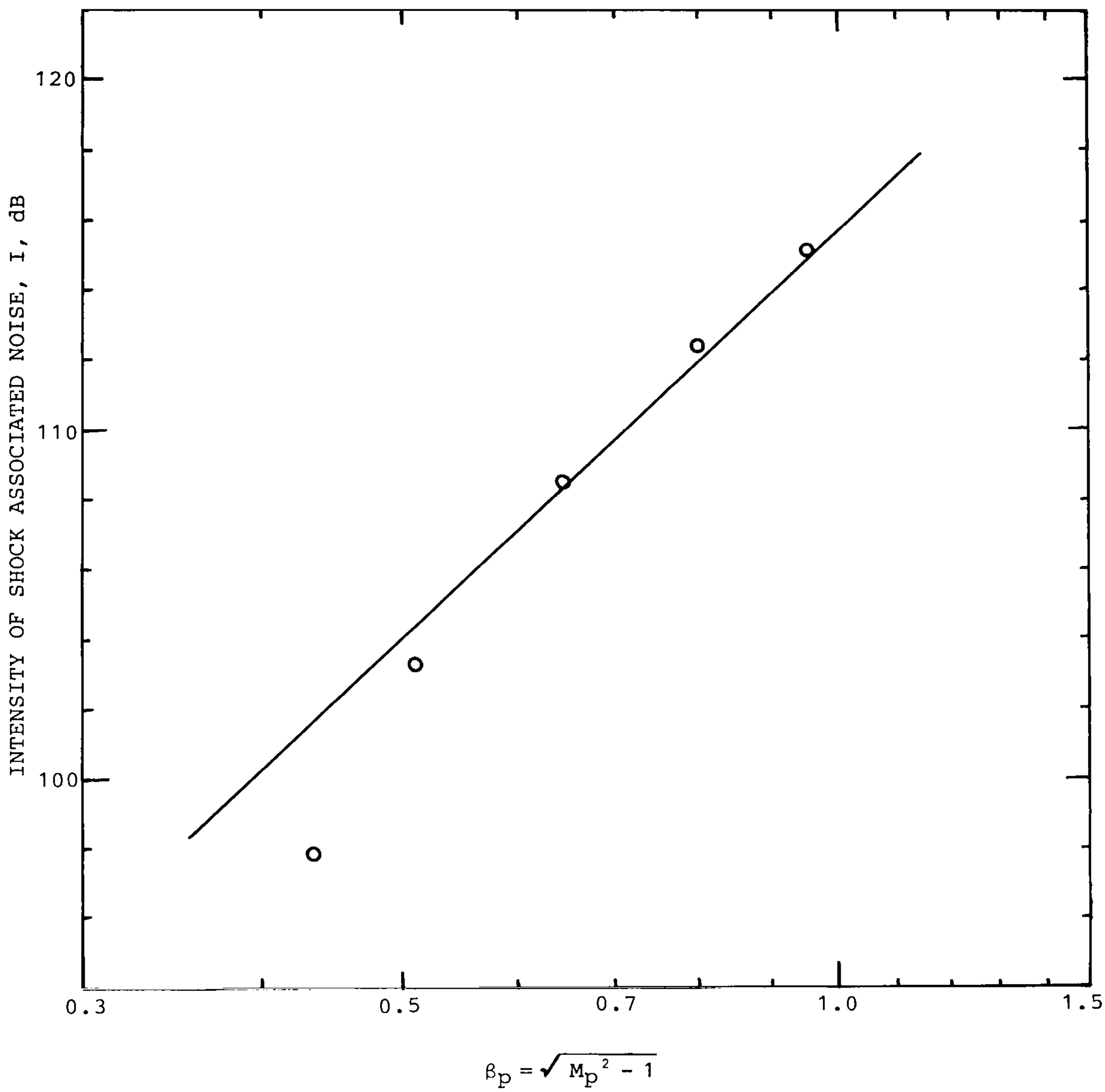


Figure 5.11 Intensity of shock associated noise as a function of $\beta_p$: Series 2, $\theta = 120°$.
o Experiment; ——— $I \propto \beta_p^4$.

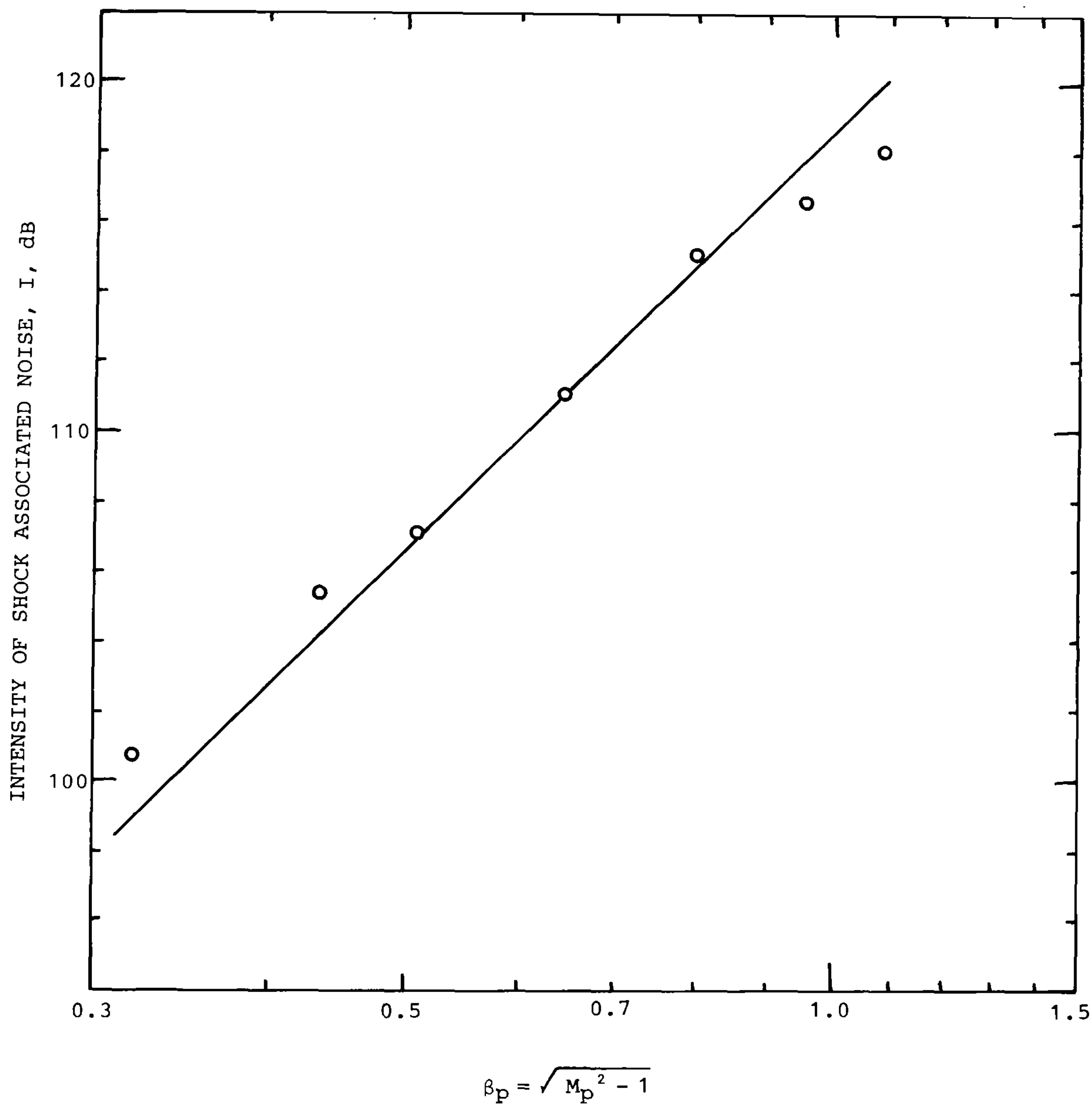


Figure 5.12 Intensity of shock associated noise as a function of $\beta_p$: Series 3, $\theta$ = 120°.
o Experiment; ——— $I \propto \beta_p^4$.

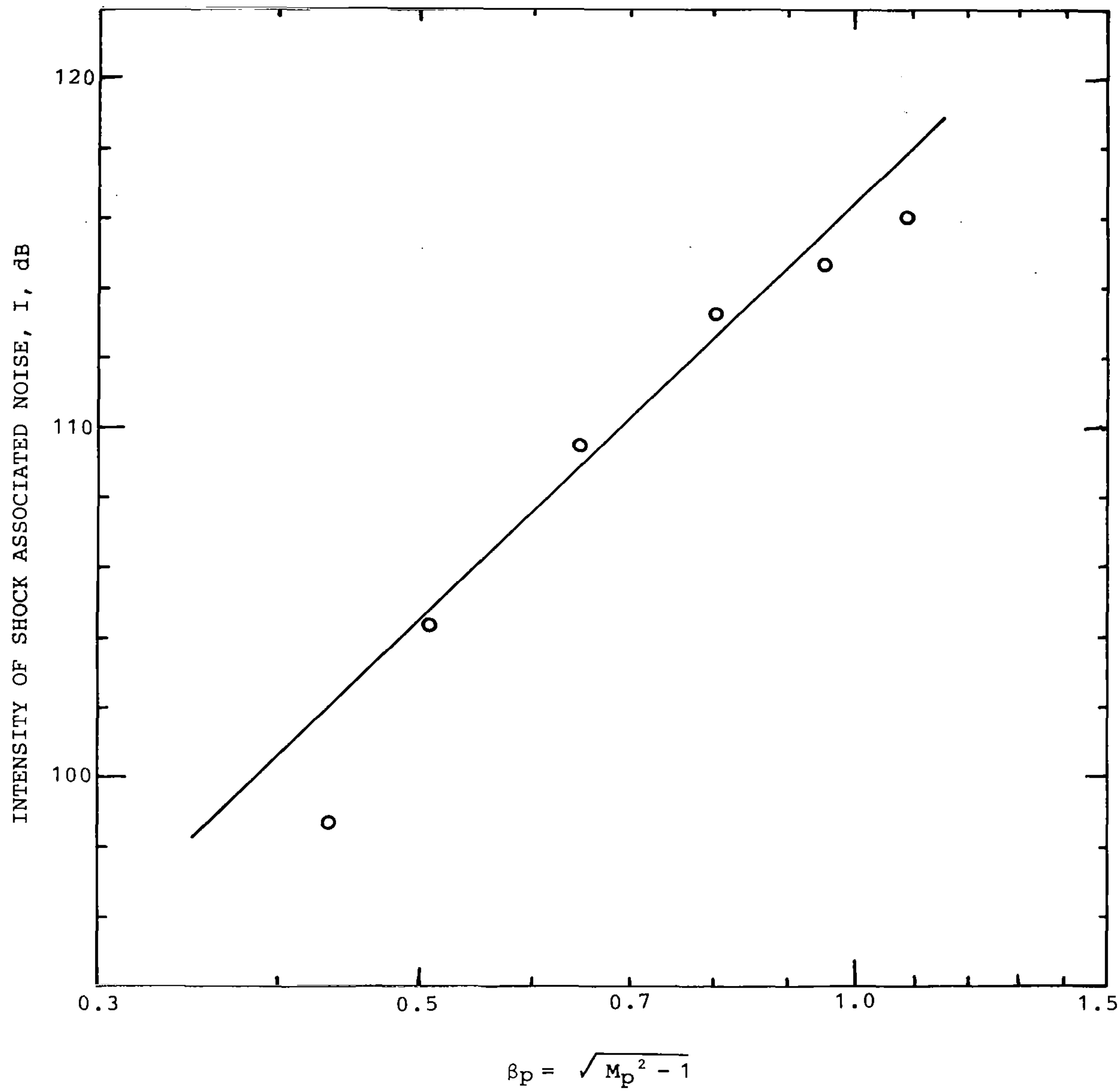


Figure 5.13 Intensity of shock associated noise as a function of $\beta_p$: Series 4, $\theta = 120°$. o Experiment; ——— $I \propto \beta_p^4$.

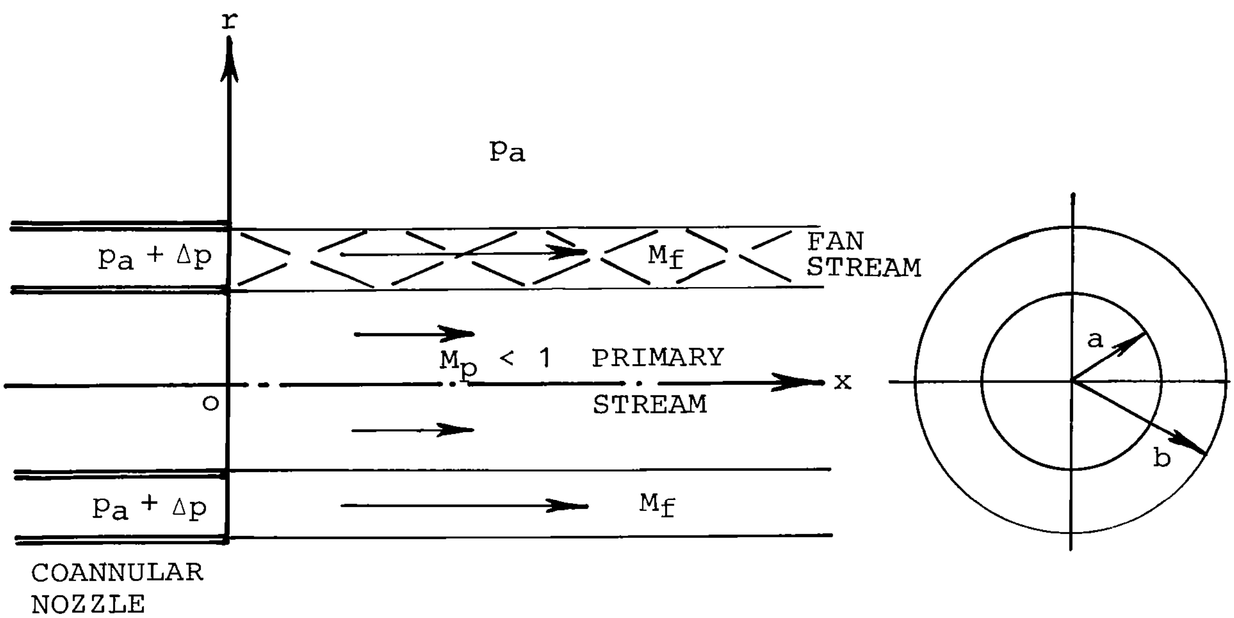


Figure 5.14 Schematic diagram of coannular jet flow bounded by vortex sheet.

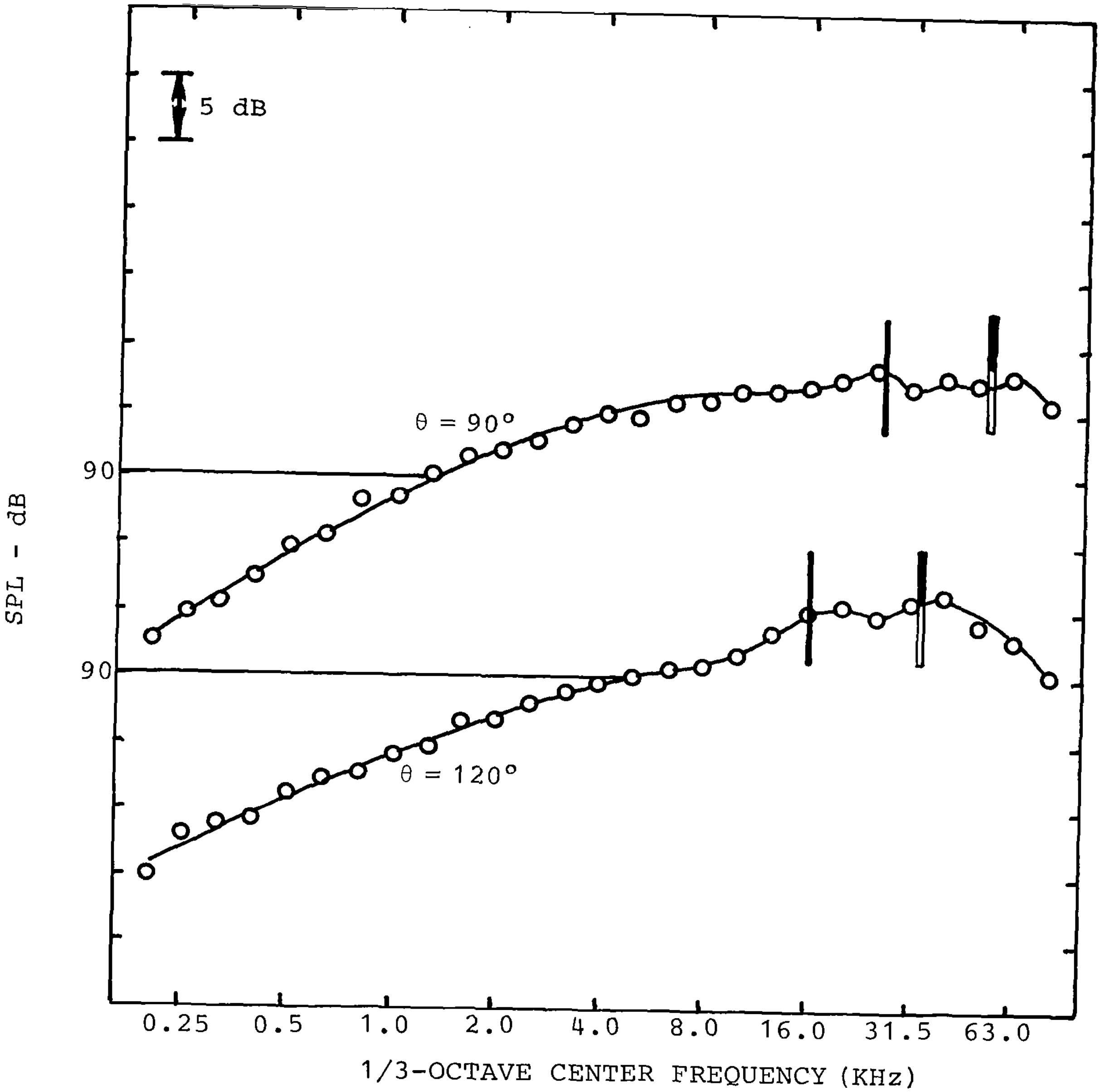


Figure 5.15 Noise spectra at $M_p = 0.52$: Series 1.

Mode 1 } Calculated peak frequency
Mode 2

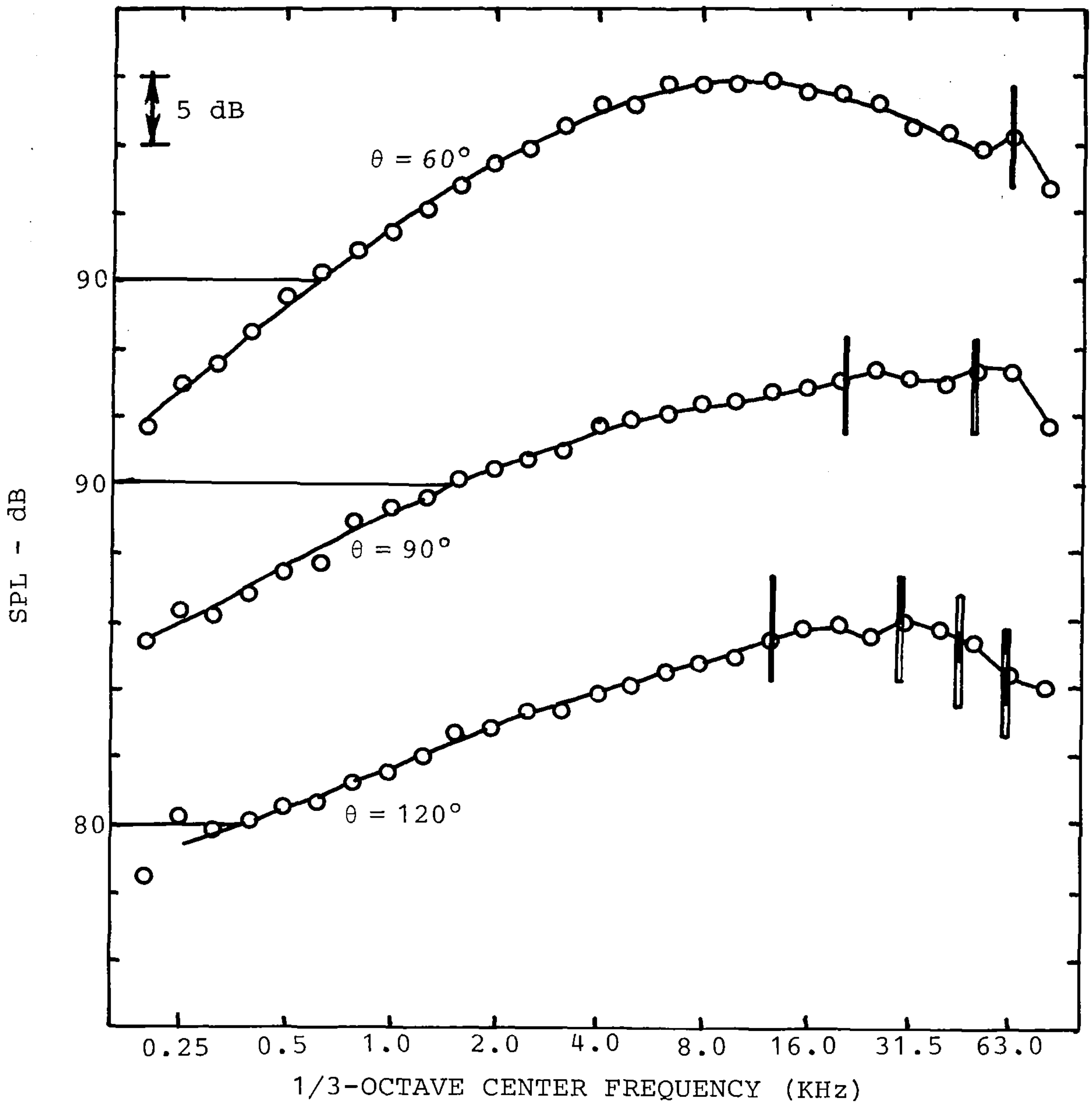


Figure 5.16 Noise spectra at $M_p = 0.90$: Series 1.

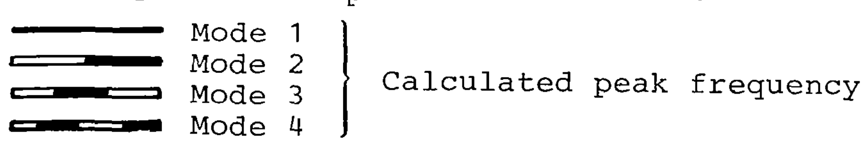

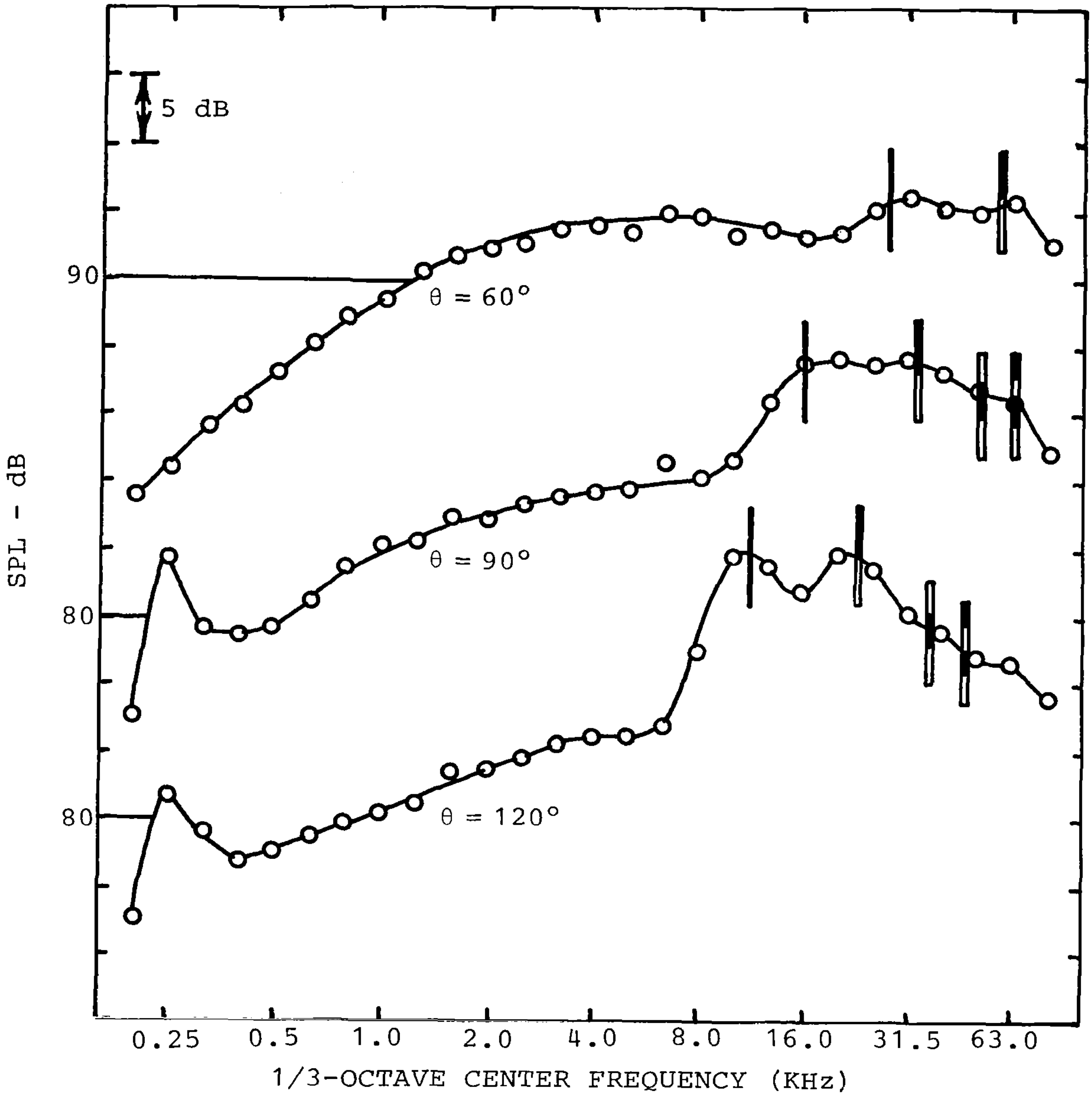


Figure 5.17 Noise spectra at $M_p = 0.52$: Series 2.

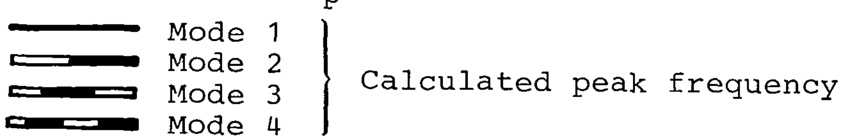

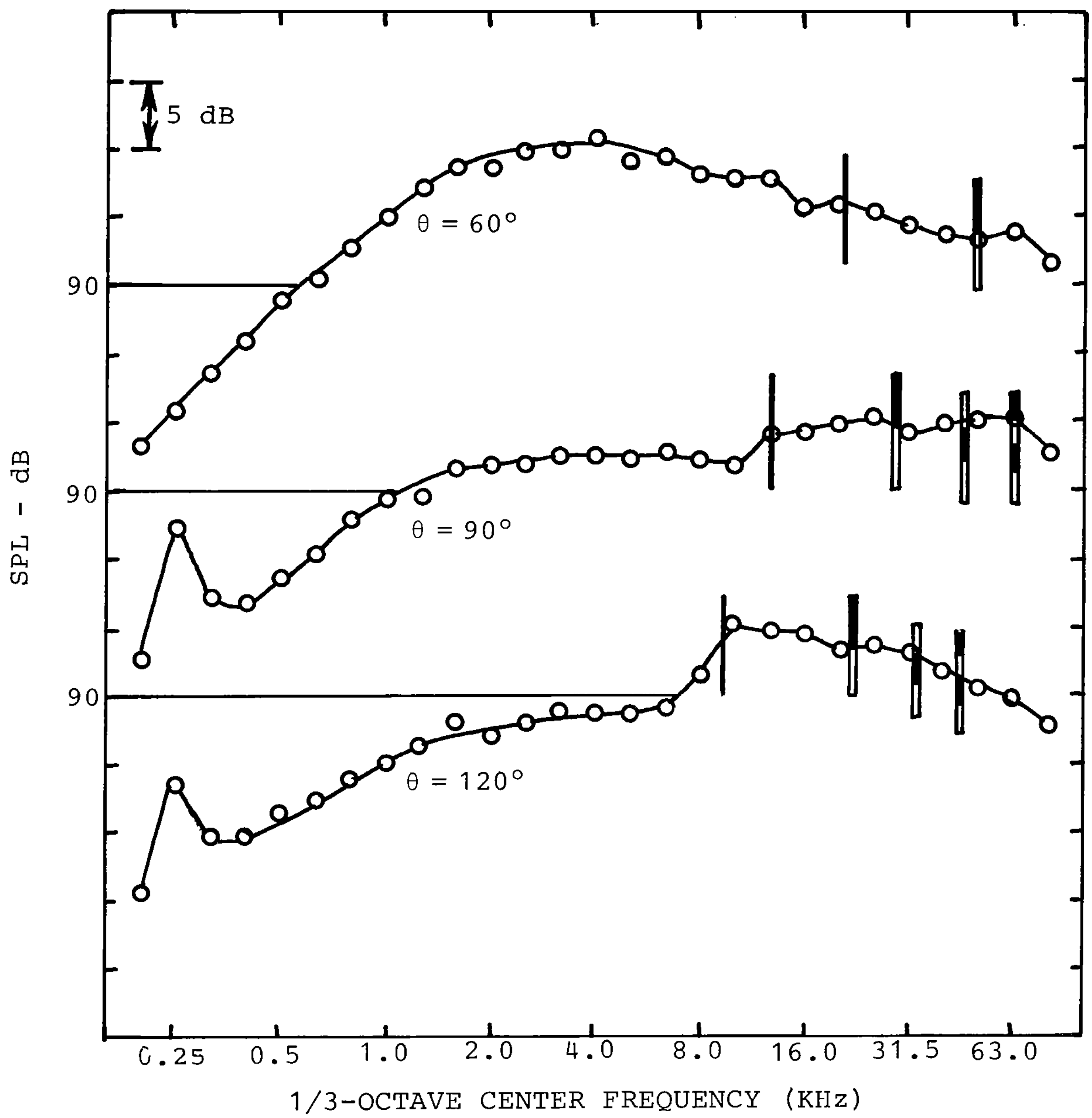


Figure 5.18 Noise spectra at $M_p = 0.90$: Series 2.

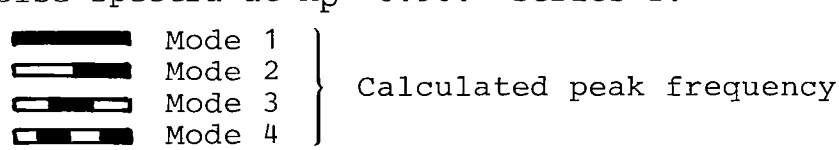

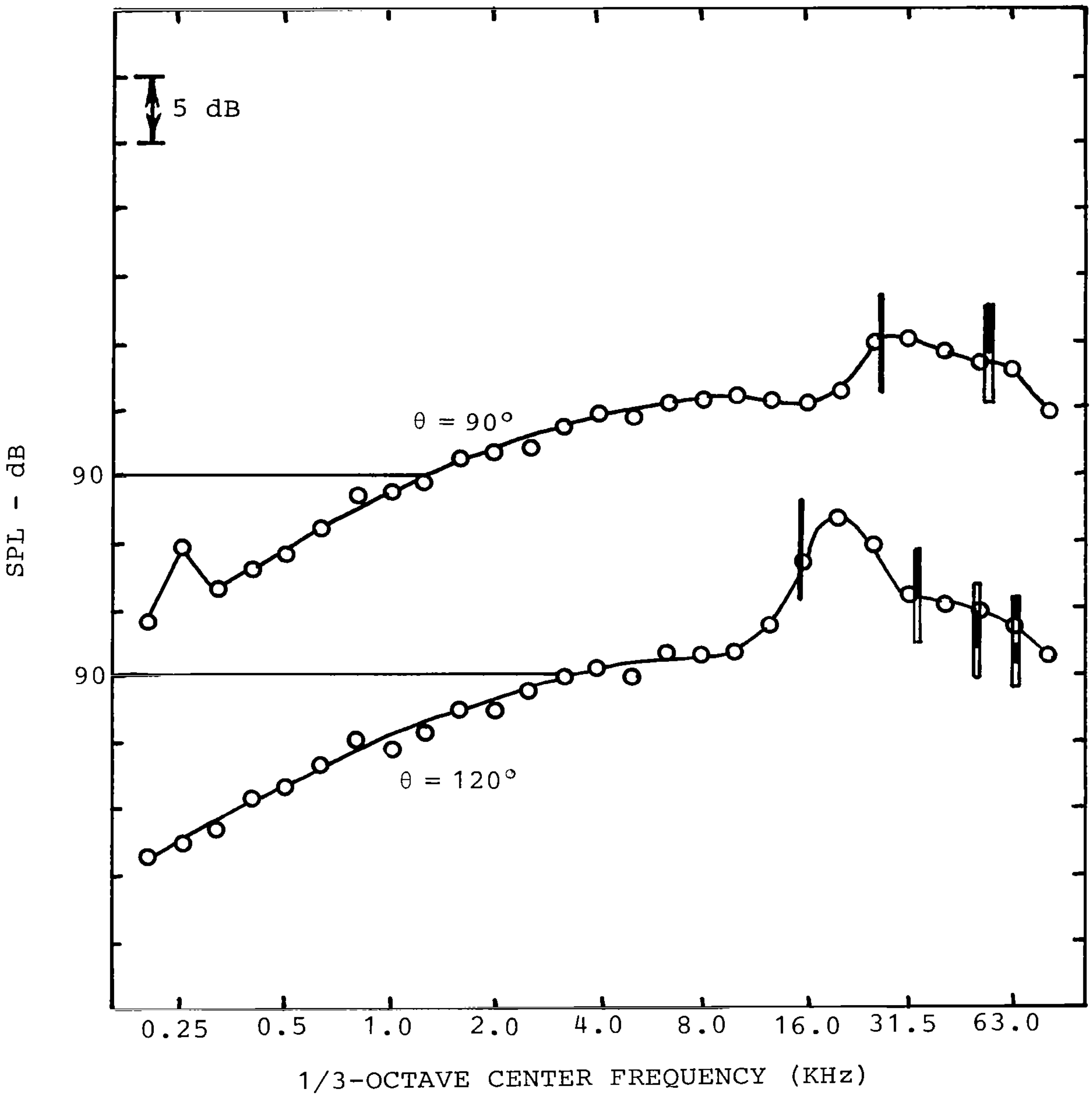


Figure 5.19 Noise spectra at $M_p = 0.52$: Series 3.

Mode 1
Mode 2
Mode 3
Mode 4
} Calculated peak frequency

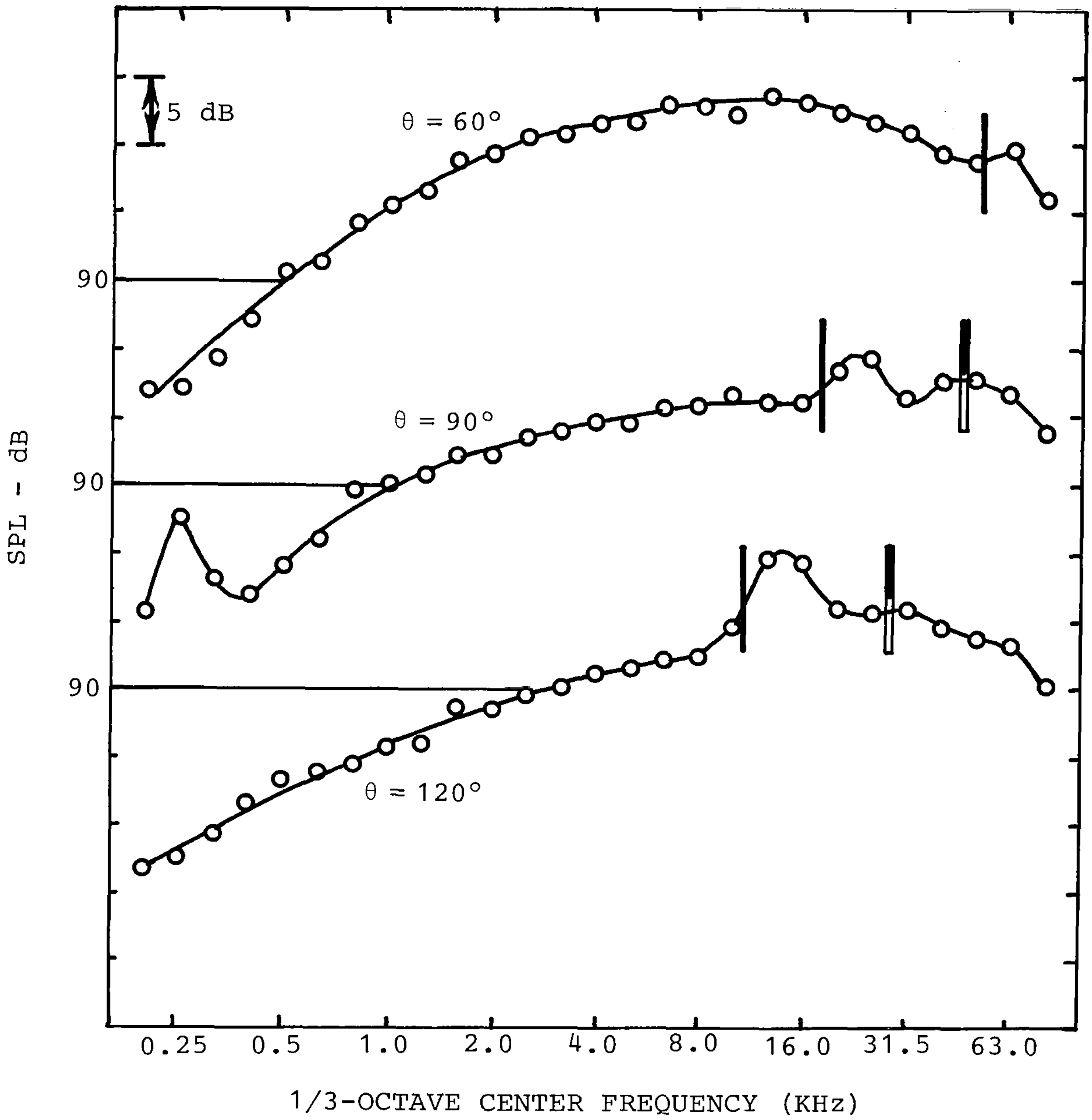


Figure 5.20 Noise spectra at $M_p = 0.96$: Series 3.

Mode 1 } Calculated peak frequency
Mode 2

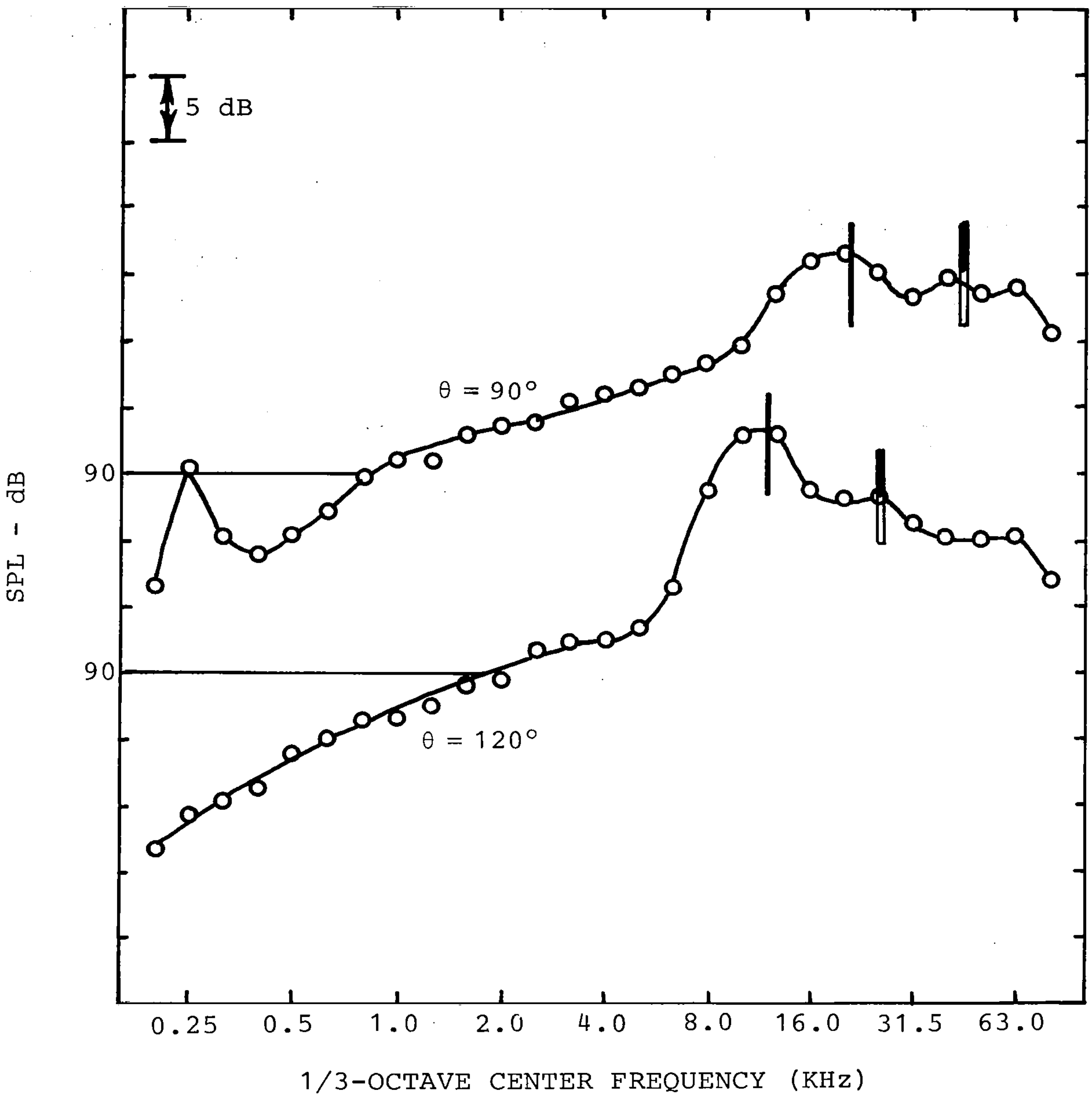


Figure 5.21 Noise spectra at $M_p = 0.52$: Series 4.

Mode 1 | Calculated peak frequency
Mode 2 |

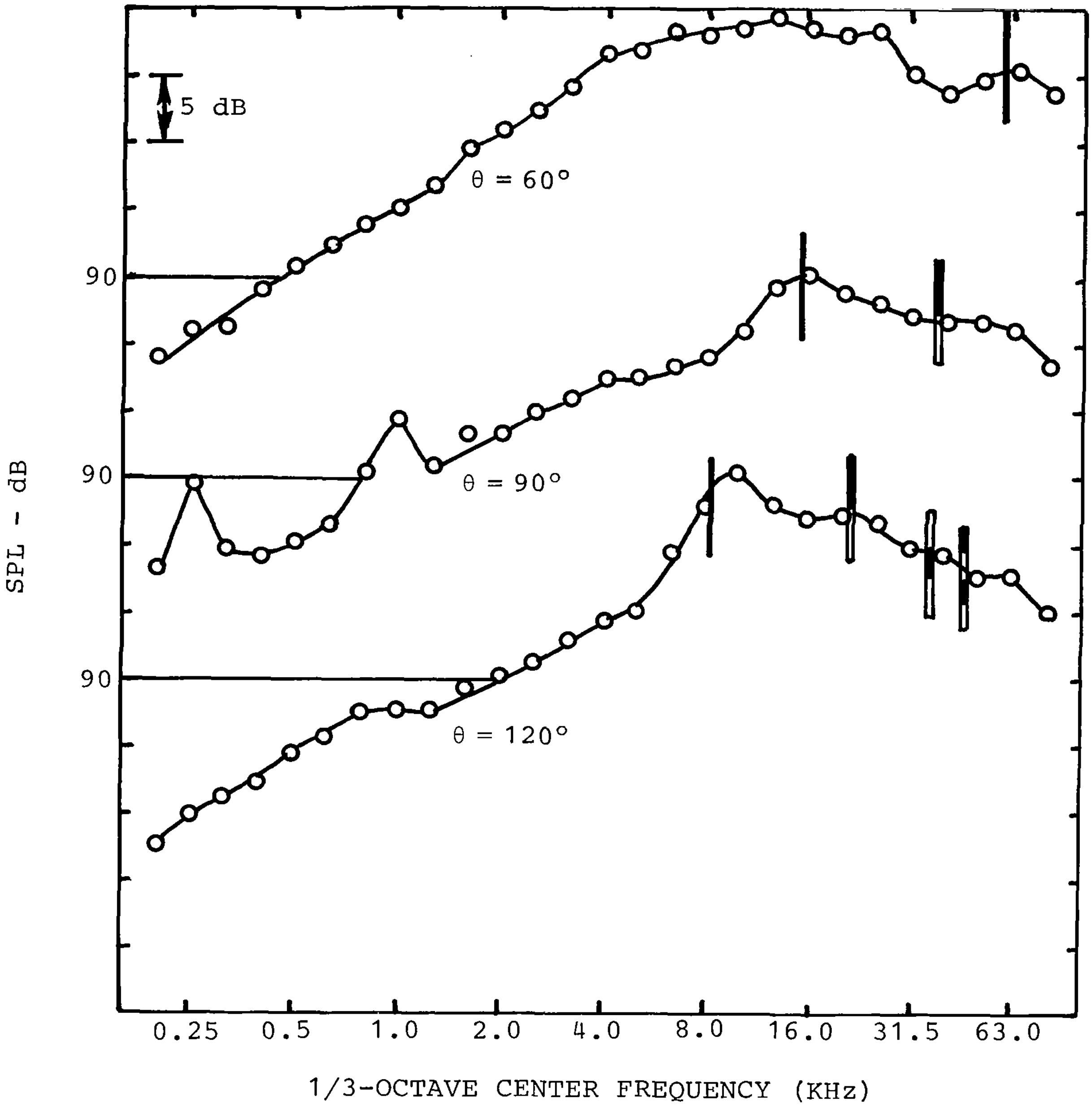


Figure 5.22 Noise spectra at $M_p = 0.96$: Series 4.

Mode 1
Mode 2
Mode 3
Mode 4
} Calculated peak frequency

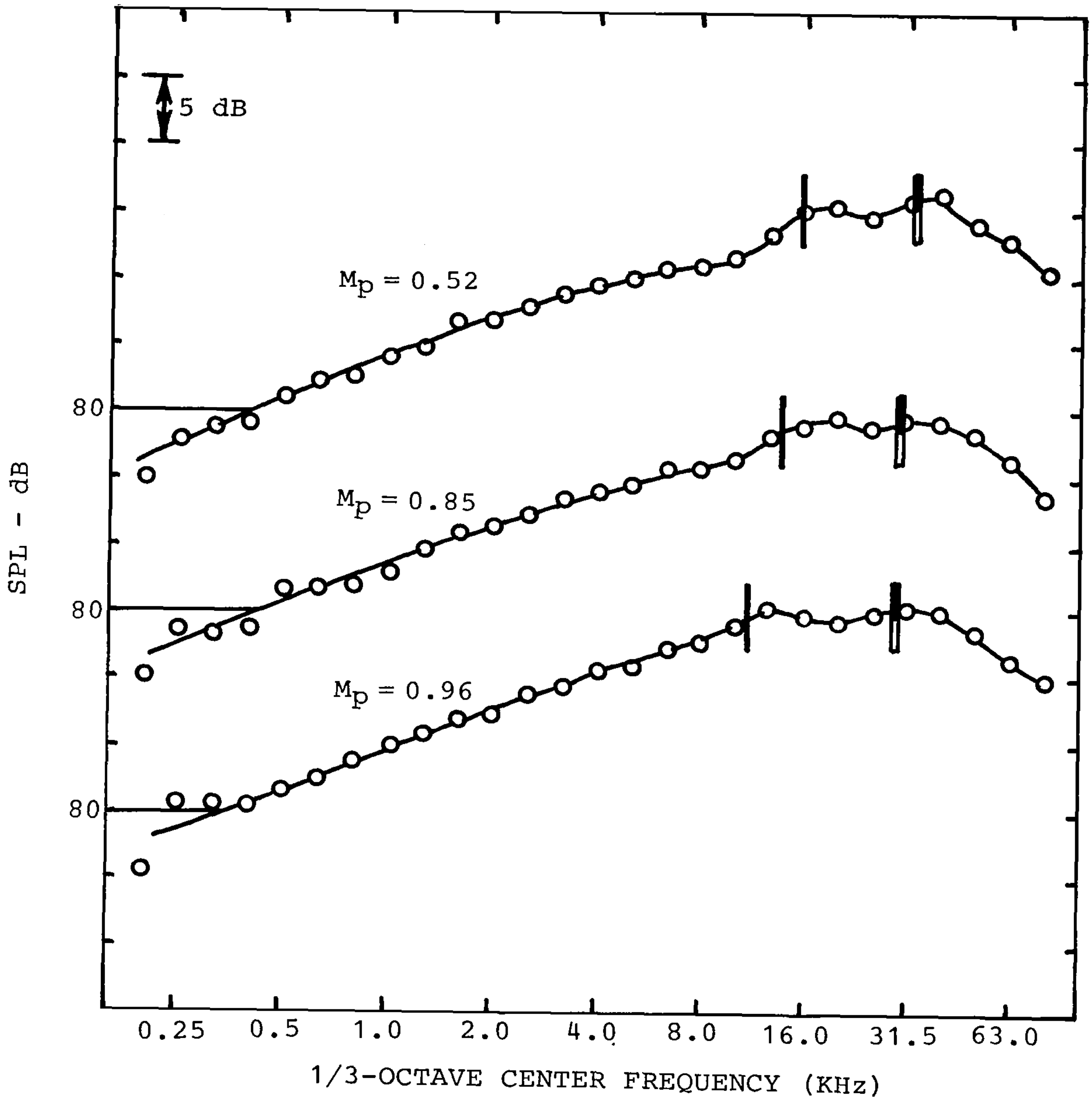


Figure 5.23 Noise spectra at $\theta = 120°$: Series 1.

Mode 1 } Calculated peak frequency
Mode 2

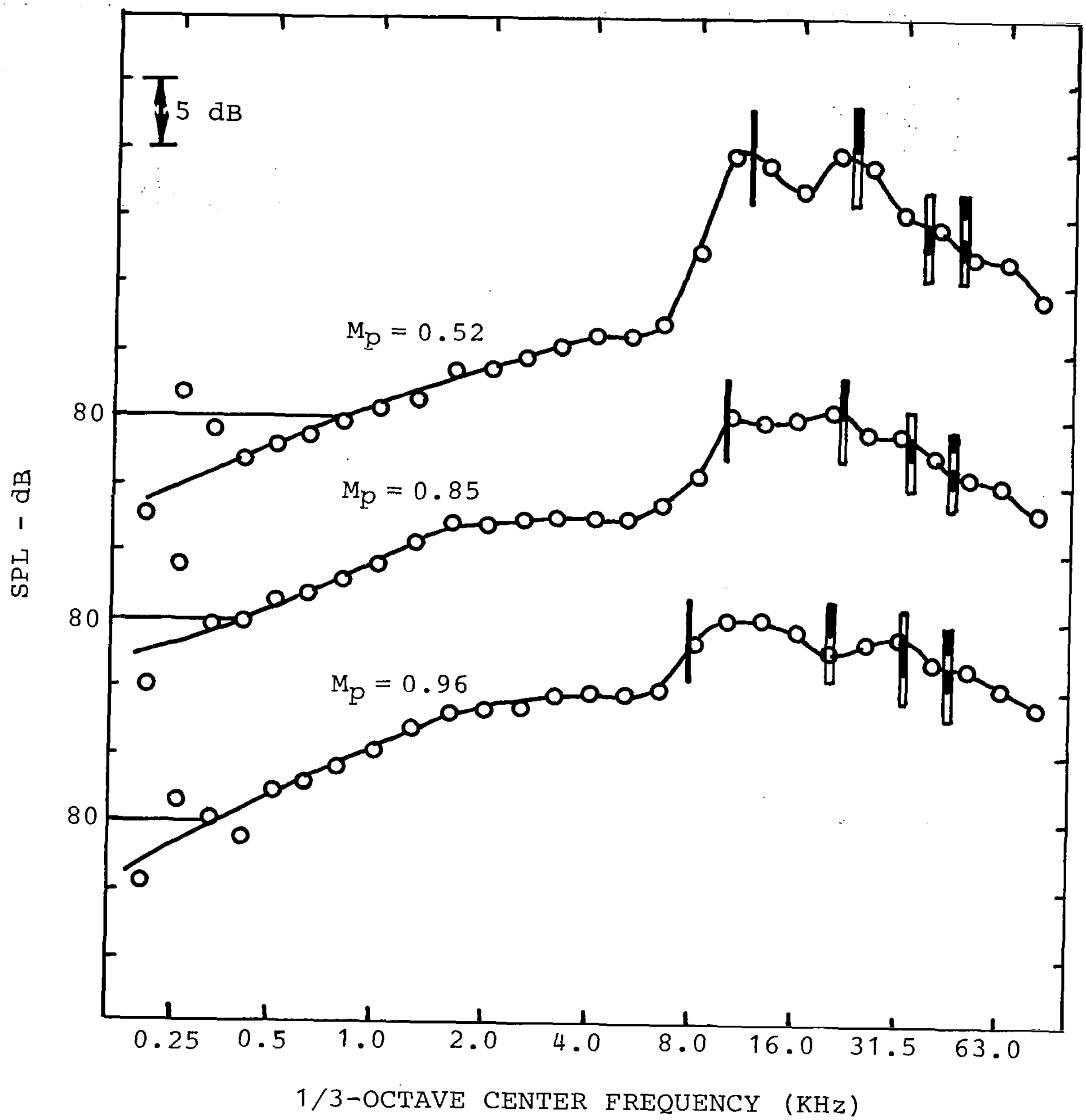


Figure 5.24 Noise spectra at $\theta = 120°$: Series 2.

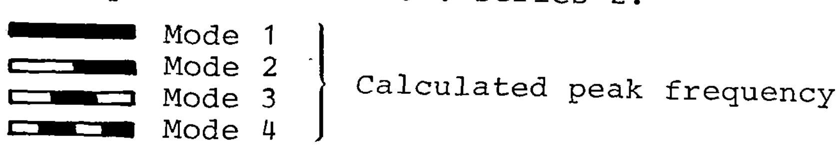

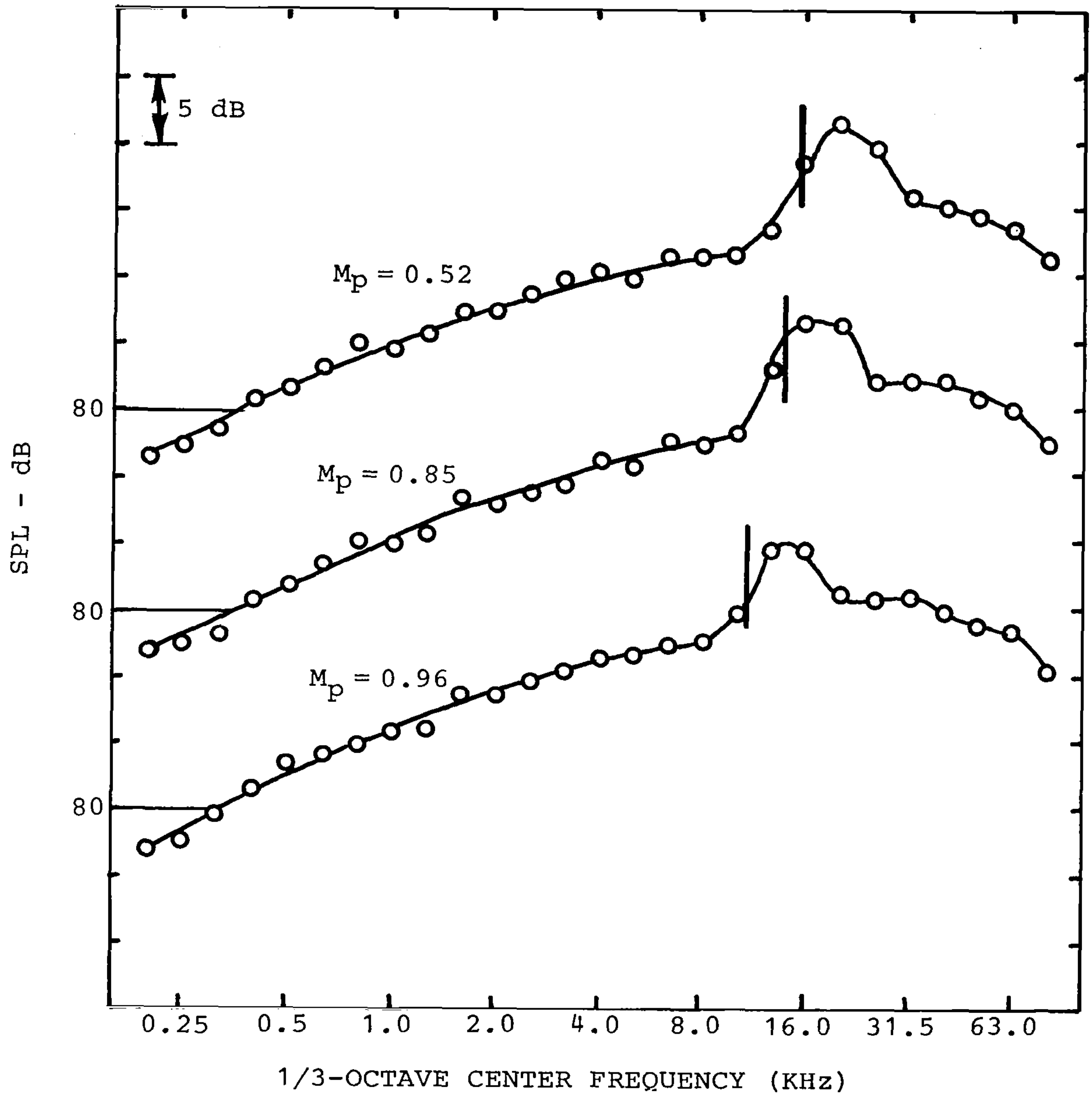


Figure 5.25 Noise spectra at $\theta = 120°$: Series 3.
▬ Mode 1 Calculated peak frequency

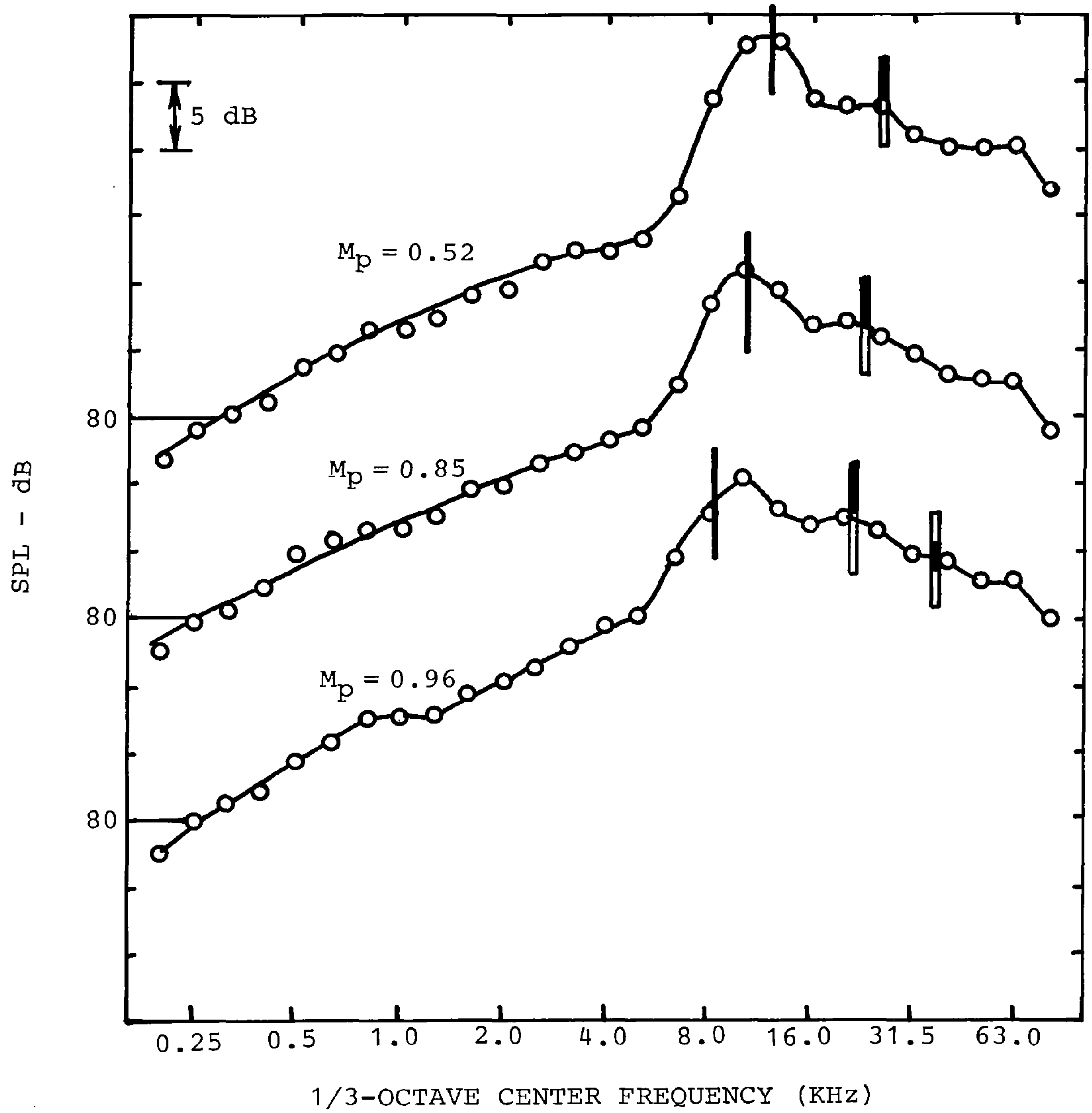


Figure 5.26 Noise spectra at $\theta = 120°$: Series 4.

Mode 1
Mode 2
Mode 3
} Calculated peak frequency

# 6. CONCLUSIONS

The research activity associated with coaxial or coannular jet noise has intensified in recent years as a result of the NASA-Lewis funded programs on model duct-burning turbofan engine noise measurements, in which it has been observed that coannular jets with "inverted" velocity profiles provide significant noise reductions. To obtain a fundamental understanding of the noise reduction mechanisms in coannular jets, Lockheed-Georgia first conducted a one-year contract study for NASA-Langley in which the major emphasis was placed on shock-free jet operating conditions. As a result of this effort, the changes in turbulent jet mixing noise characteristics in inverted-profile coannular jets, relative to the fully-mixed equivalent single jet (defined as having the same thrust, mass flow rate, and exit area as the coannular jet), have been largely quantified and understood.

In the same Lockheed study, extensive optical measurements were also conducted to observe the variation of shock structure in coannular jets as a function of fan (or outer) and primary (or inner) stream pressure ratio combinations. These optical measurements indicated that for a fixed supercritical fan pressure ratio, the shock structure of the outer flow undergoes a sudden change when the primary pressure ratio becomes just supercritical. Although similar observations were also reported by Dosanjh and his coworkers at Syracuse University, any noise benefit which might be associated with these "sudden" changes in the shock structure was neither quantified nor understood prior to the present program. One of the primary requirements of the work described in this report was to obtain systematic acoustic data to support the postulation, based on the optical measurements mentioned above, that the broadband shock associated noise from coannular jets may be greatly reduced at and near the conditions at which this sudden change in the fan flow shock structure occurs. In addition, it was necessary to obtain a fundamental understanding of the associated phenomena, so that the noise benefit of coannular jets at supersonic conditions can be scientifically optimized.

The overall objective of the present investigation, therefore, was to quantify and obtain a physical understanding of the noise reduction mechanisms in supersonic inverted-velocity-profile coannular jets, with emphasis on the shock associated noise reduction.

A summary of the work conducted to achieve this objective and the main conclusions are given below.

## Experimental Work

The noise characteristics of coannular jets operated at supercritical pressure ratios have been measured in the Lockheed anechoic facility using a "primary-extended" coannular nozzle configuration of fan-to-primary area ratio $A_f/A_p = 0.747$ and equivalent nozzle diameter $D_{eq} = 6.6$ cm. Four series of acoustic measurements were conducted. Within each test series, the fan stream pressure ratio and the total temperatures of the primary and fan flows were kept fixed, while the primary stream pressure ratio was varied from 1.2 to 4.0. For all coannular jet test conditions, corresponding acoustic measurements for the equivalent single jet were also obtained so that the noise characteristics from the two types of jet can be compared directly. The total experimental program covered a wide range of fully-expanded fan-to-primary velocity ratios ($V_f/V_p$) from 0.55 to 4.27. The fully-expanded equivalent jet velocity was varied from 380 to 650 m/s.

The results from the acoustic experiments have been analyzed (1) to show the variation of coannular jet noise levels with primary stream Mach number, and (2) to quantify the noise reductions in terms of the differences in noise levels between the coannular jet and the equivalent single jet.

In the forward arc of the jet, where shock associated noise predominates, the acoustic results have conclusively proven the hypothesis, made at the beginning of this program and based on earlier optical measurements, that the shock associated noise from the fan stream of a coannular jet is indeed virtually eliminated (or at least minimized) when the primary flow is operated at a Mach number ($M_p$) just above unity. Furthermore, this "optimum" condition occurs at all values of (supercritical) fan stream pressure ratio and primary and fan flow total temperatures considered in the present experiments. At this optimum condition, the coannular jet provides the maximum noise reduction relative to the equivalent single jet. Since shock noise is practically eliminated at this condition, the actual magnitude of this maximum noise reduction is simply governed by the basic jet mixing noise level of the coannular jet when $M_p$ is slightly greater than 1.0.

The second most important finding from the acoustic experiments is that, unlike the reduction of jet mixing noise from a coannular jet, which occurs only at inverted-velocity-profile conditions, velocity ratio $V_f/V_p$ is not an important parameter in the elimination or reduction of shock associated noise from a coannular jet. The shock associated noise reduction can be achieved at inverted- as well as normal-velocity-profile conditions, provided the coannular jet is operated with the primary stream just slightly supersonic.

## Theoretical Work

To understand the experimental results on shock associated noise reduction from coannular jets at the "optimum" condition (when the almost periodic shock cell structure of the fan stream nearly completely disappears), an analytical model for the periodic shock cell structure has been constructed and studied first. It has been established that this abrupt change in the shock structure, and hence the decrease in shock associated noise, would occur when the primary jet flow is just slightly supersonic regardless of the Mach number and temperature of the fan stream.

The simple model indicates that a drastic change in the fan stream shock cell structure takes place when the primary stream increases its velocity from subsonic to supersonic. Physically, this abrupt change in the shock cell system arises principally because a subsonic flow cannot transmit flow discontinuities such as shocks and expansion fans but a supersonic flow can. Hence, when the primary stream Mach number is slightly supersonic, no periodic shock cell pattern can form in the outer fan stream. Also, at Mach number just above one, the shock cell structure of the primary stream is extremely weak. Thus under this condition, the coherent interaction between the turbulence in the mixing layers of the jet and the periodic shock cell system is most ineffective. As a result, the corresponding shock associated noise is the least intense.

In the second part of the theoretical work, a first order shock structure model for the inverted-profile coannular jet has been developed. Based on the concept that shock associated noise is generated by the weak interaction between the downstream propagating large scale turbulence structures in the mixing layers of the jet and the repetitive shock cell system, formulae for the peak frequencies as well as noise intensity scaling have been derived. The validity of these formulae was tested by comparing the predicted results with measured results. Good agreement was found both for subsonic as well as supersonic primary jet flows.

When the primary flow is highly supersonic ($M_p > 1$), the shock structure extends from the primary stream to the entire fan stream. The resulting shock associated noise is generated mainly by the interaction of turbulence and the shock cell structure in the primary stream, and it exhibits characteristics which are similar to those of a single jet. The noise spectrum consists mainly of a single characteristic peak. The noise intensity varies approximately as $(M_p^2 - M_d^2)^2$, where $M_d$ is the nozzle design Mach number. For a choked nozzle, its intensity scales as $(M_p^2 - 1)^2$ under a fixed fan stream operating condition.

When the primary flow is subsonic ($M_p < 1$), the shock structure exists only in the fan stream. In this case, the primary flow Mach number does not seem to have a significant influence on the radiated noise intensity. However, it does affect the values of the peak frequency of the noise spectrum. Aside from the basic periodicity of the shock structure in the fan stream, the shock cells tend to have a more complex internal structure. It is believed that the formation of this internal structure is strongly influenced by the geometrical configuration of the coannular nozzle design. Because of this additional internal shock pattern the shock cell system can be considered as made up of more than one periodic component. The shock associated noise in this case, therefore, consists of a sequence of spectral peaks. At the high frequency end of the spectrum these peaks tend to merge together to form a broadband spectral curve. The observation of this multi-peak shock associated noise spectrum shape is new and does not seem to have been reported by other investigators before. The measured frequencies of these peaks agreed quite well with theoretical values calculated according to a linear shock cell model.

Finally, the good agreement between theory and experiment obtained in this work provides further validation of the shock associated noise generation mechanism proposed recently by the authors (ref. 9). In addition, it strongly indicates that a linear shock cell model is useful not only for correlating shock associated noise, but, perhaps, even in the development of a comprehensive shock associated noise theory.

# APPENDIX 1

# ACOUSTIC DATA

This appendix contains the acoustic data acquired under this contract. To keep the appendix to a reasonable size, only one-sixth of the total data generated from the experimental program are included. However, these data have been carefully selected and organized such that for each test series, the variation of the noise characteristics with primary stream Mach number and observer angle can be systematically seen in sufficient detail.

A figure index describing the various plots (27 x 4 = 104 in all) is given in Table A1.1. For each of the four test series, the results are given for every other test point. Also, out of the eleven values of observer angle $\theta$ considered in the experimental program, the data in this appendix are presented at four values of $\theta$, namely, (a) $\theta = 30°$, (b) $\theta = 60°$, (c) $\theta = 90°$, and (d) $\theta = 120°$.

The results are plotted in the form of one-third octave band sound pressure level spectra. The spectra are "lossless" (i.e., with zero atmospheric attenuation), and the levels are expressed for a common observer distance of 100 equivalent nozzle diameters ($R = 100\ D_{eq}$) from the nozzle exit plane.

Each plot shows a comparison between two spectra, the coannular jet noise spectrum and the corresponding equivalent single jet noise spectrum. The following symbols are used throughout the appendix:

○ Coannular Jet

□ Equivalent Single Jet

Table A1.1 Figure index for acoustic data

| Figure Number | Test Series | Test Point | $p_{tf}/p_a$ | $T_{tf}$( K) | $T_{tp}$( K) | $p_{tp}/p_a$ |
|---|---|---|---|---|---|---|
| A1.1 | 1 | 1 | 3.0 | 800 | 300 | 1.2 |
| A1.2 | | 3 | | | | 1.6 |
| A1.3 | | 5 | | | | 1.8 |
| A1.4 | | 7 | | | | 2.0 |
| A1.5 | | 9 | | | | 2.2 |
| A1.6 | | 11 | | | | 2.7 |
| A1.7 | | 13 | | | | 3.5 |
| A1.8 | 2 | 15 | 3.0 | 300 | 800 | 1.2 |
| A1.9 | | 17 | | | | 1.6 |
| A1.10 | | 19 | | | | 1.8 |
| A1.11 | | 21 | | | | 2.0 |
| A1.12 | | 23 | | | | 2.2 |
| A1.13 | | 25 | | | | 2.7 |
| A1.14 | 3 | 29 | 3.0 | 800 | 600 | 1.2 |
| A1.15 | | 31 | | | | 1.6 |
| A1.16 | | 33 | | | | 1.8 |
| A1.17 | | 35 | | | | 2.0 |
| A1.18 | | 37 | | | | 2.2 |
| A1.19 | | 39 | | | | 2.7 |
| A1.20 | | 41 | | | | 3.5 |
| A1.21 | 4 | 43 | 4.3 | 800 | 300 | 1.2 |
| A1.22 | | 45 | | | | 1.6 |
| A1.23 | | 47 | | | | 1.8 |
| A1.24 | | 49 | | | | 2.0 |
| A1.25 | | 51 | | | | 2.2 |
| A1.26 | | 53 | | | | 2.7 |
| A1.27 | | 55 | | | | 3.5 |

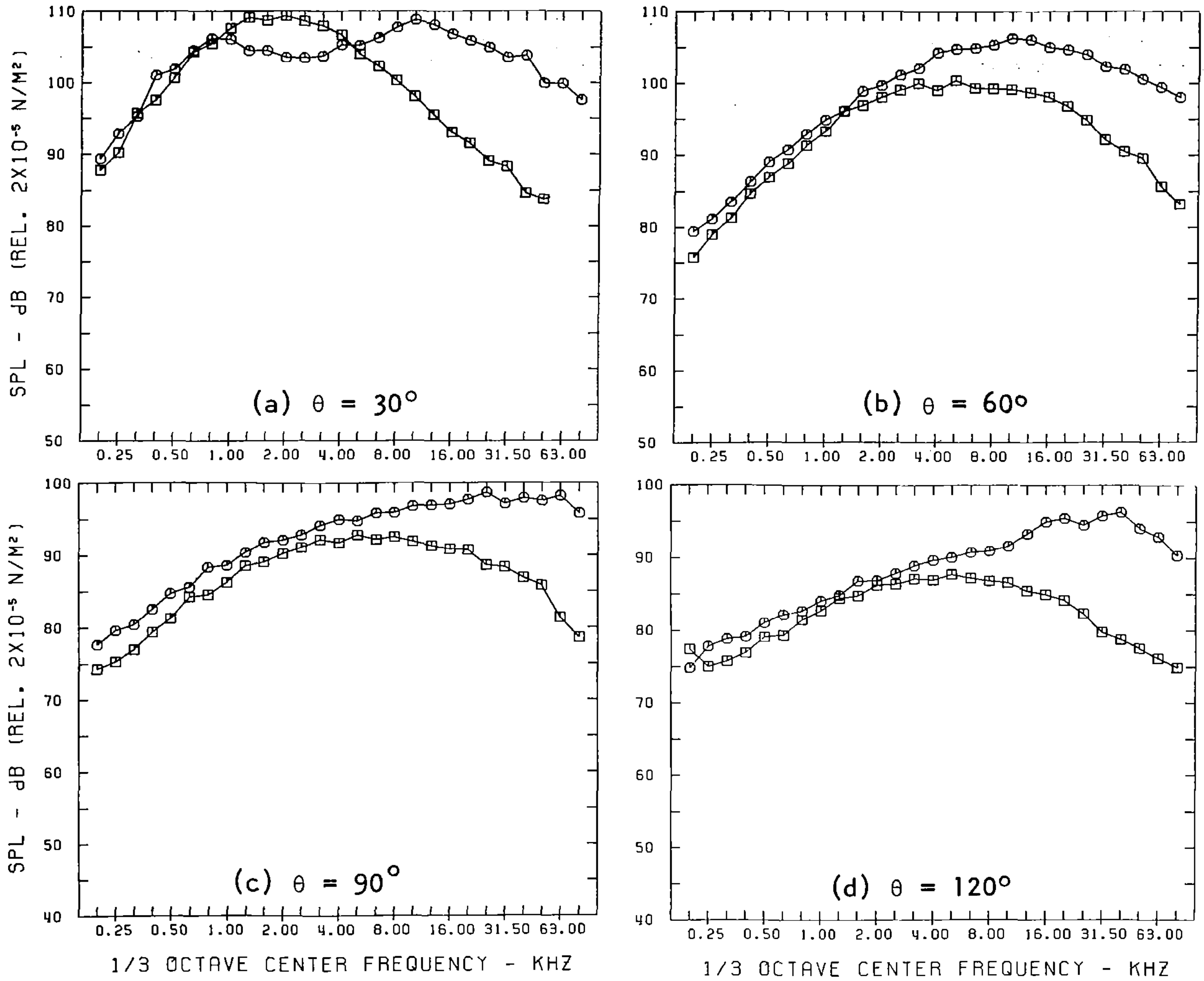
SPL - dB (REL. 2X10⁻⁵ N/M²)
(a) θ = 30°
(b) θ = 60°
(c) θ = 90°
(d) θ = 120°
1/3 OCTAVE CENTER FREQUENCY - KHZ
0.25 0.50 1.00 2.00 4.00 8.00 16.00 31.50 63.00
110
100
90
80
70
60
50
40

Figure A1.1

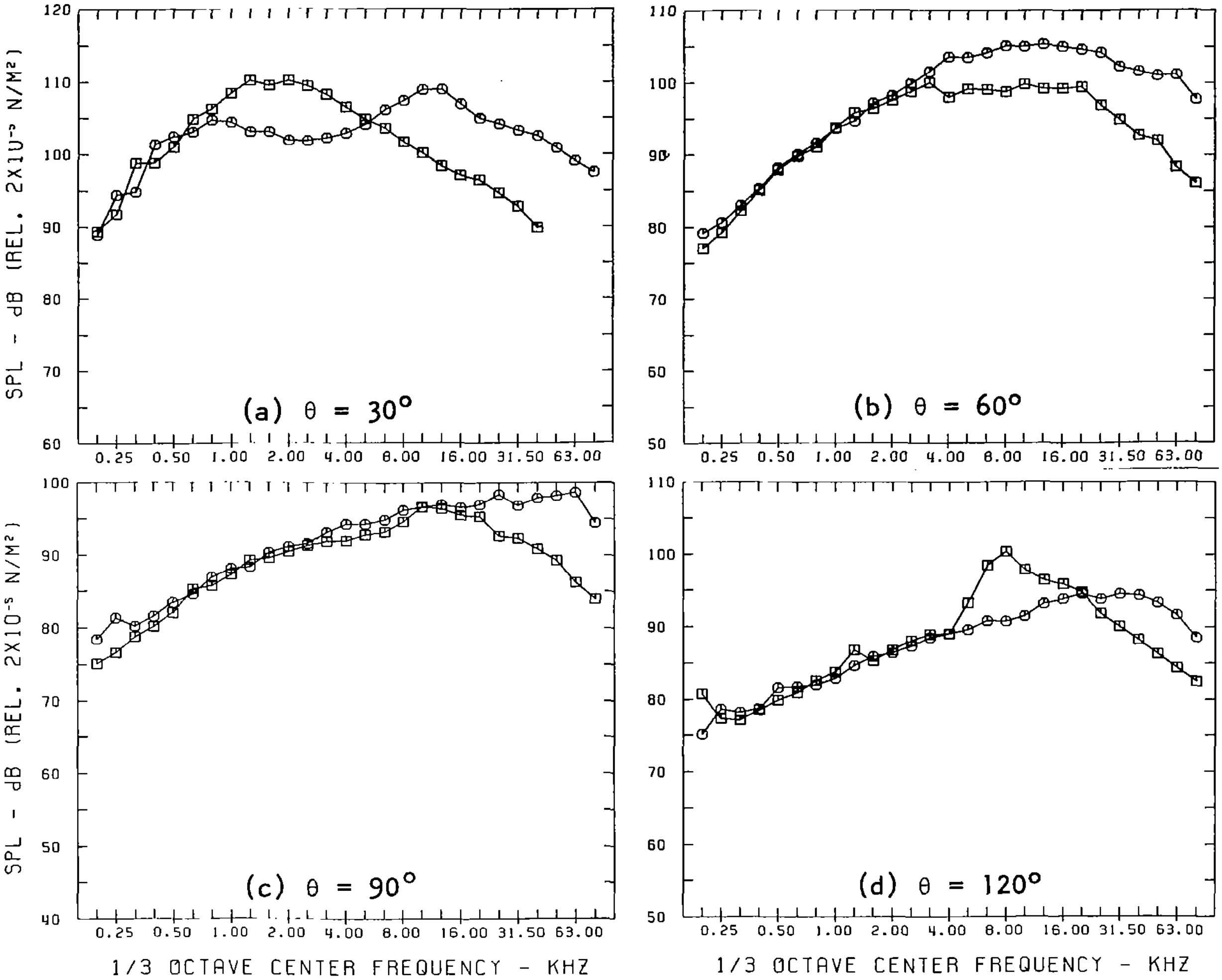
SPL - dB (REL. 2X10⁻⁵ N/M²)
(a) θ = 30°
(b) θ = 60°
(c) θ = 90°
(d) θ = 120°
0.25 0.50 1.00 2.00 4.00 8.00 16.00 31.50 63.00
1/3 OCTAVE CENTER FREQUENCY - KHZ
1/3 OCTAVE CENTER FREQUENCY - KHZ

Figure A1.2

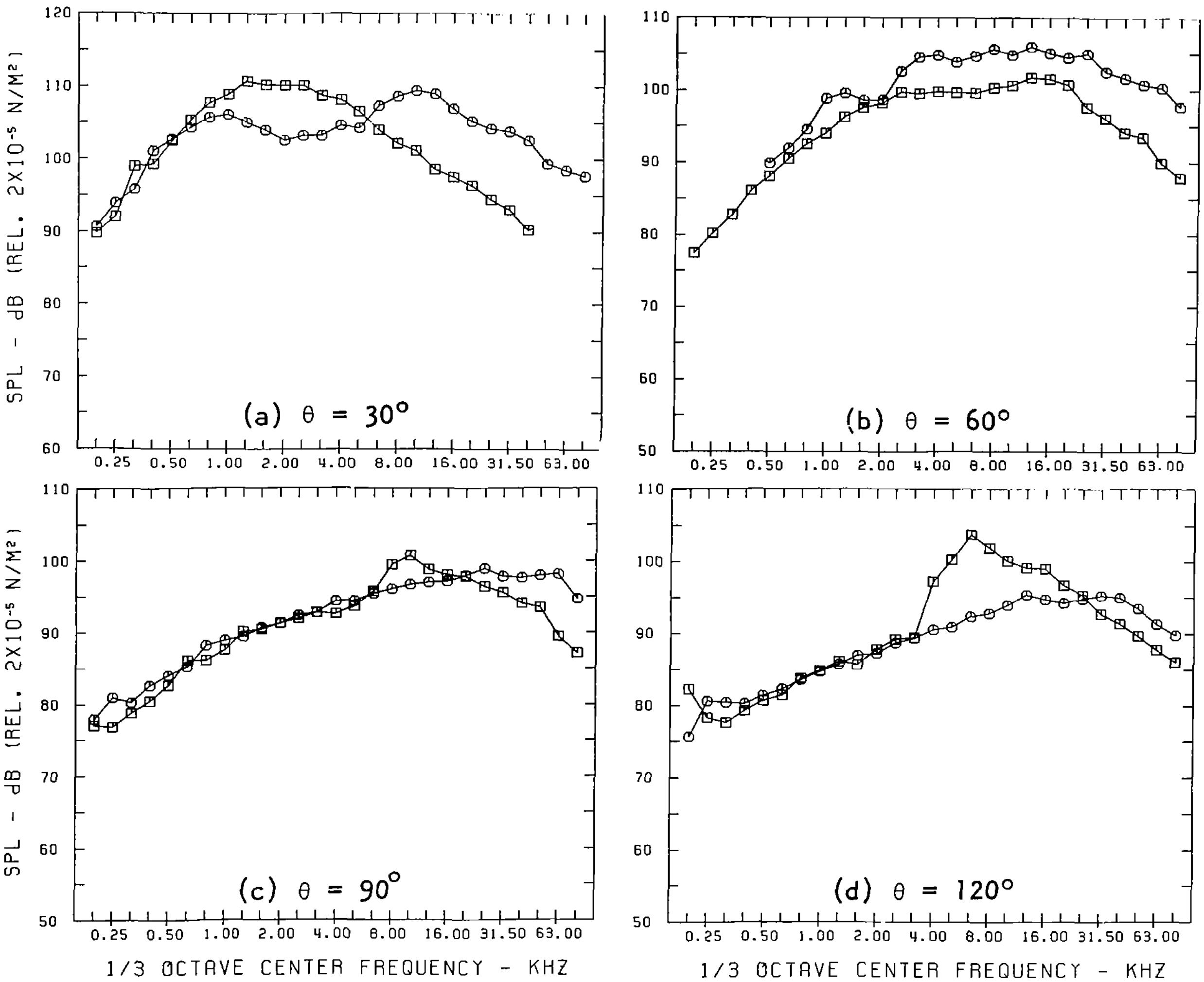

SPL - dB (REL. 2X10⁻⁵ N/M²)
(a) θ = 30°
(b) θ = 60°
(c) θ = 90°
(d) θ = 120°
0.25 0.50 1.00 2.00 4.00 8.00 16.00 31.50 63.00
1/3 OCTAVE CENTER FREQUENCY - KHZ


Figure A1.3

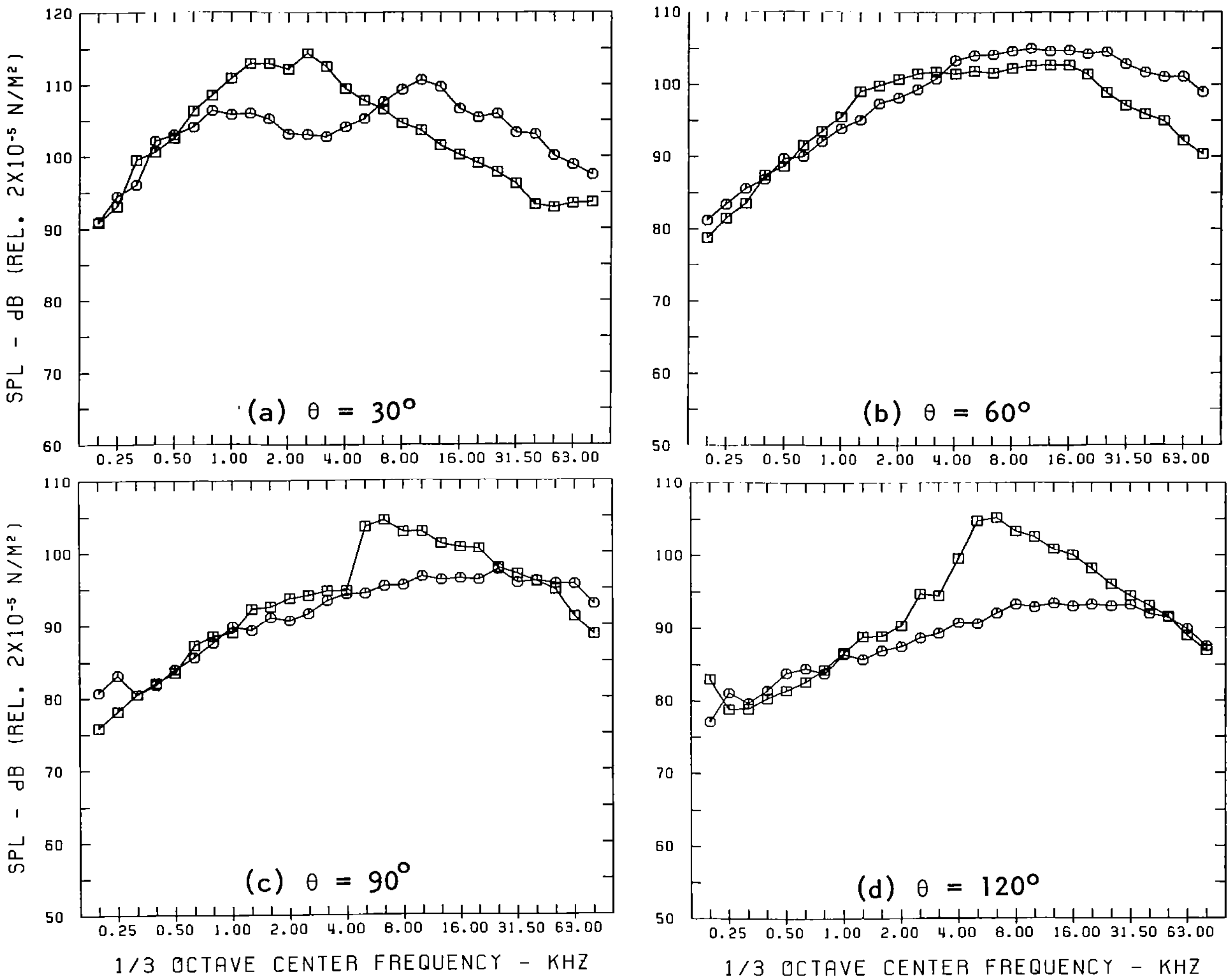

SPL - dB (REL. 2X10^-5 N/M²)
120
110
100
90
80
70
60
50
0.25 0.50 1.00 2.00 4.00 8.00 16.00 31.50 63.00
(a) θ = 30°
(b) θ = 60°
(c) θ = 90°
(d) θ = 120°
1/3 OCTAVE CENTER FREQUENCY - KHZ


Figure A1.4

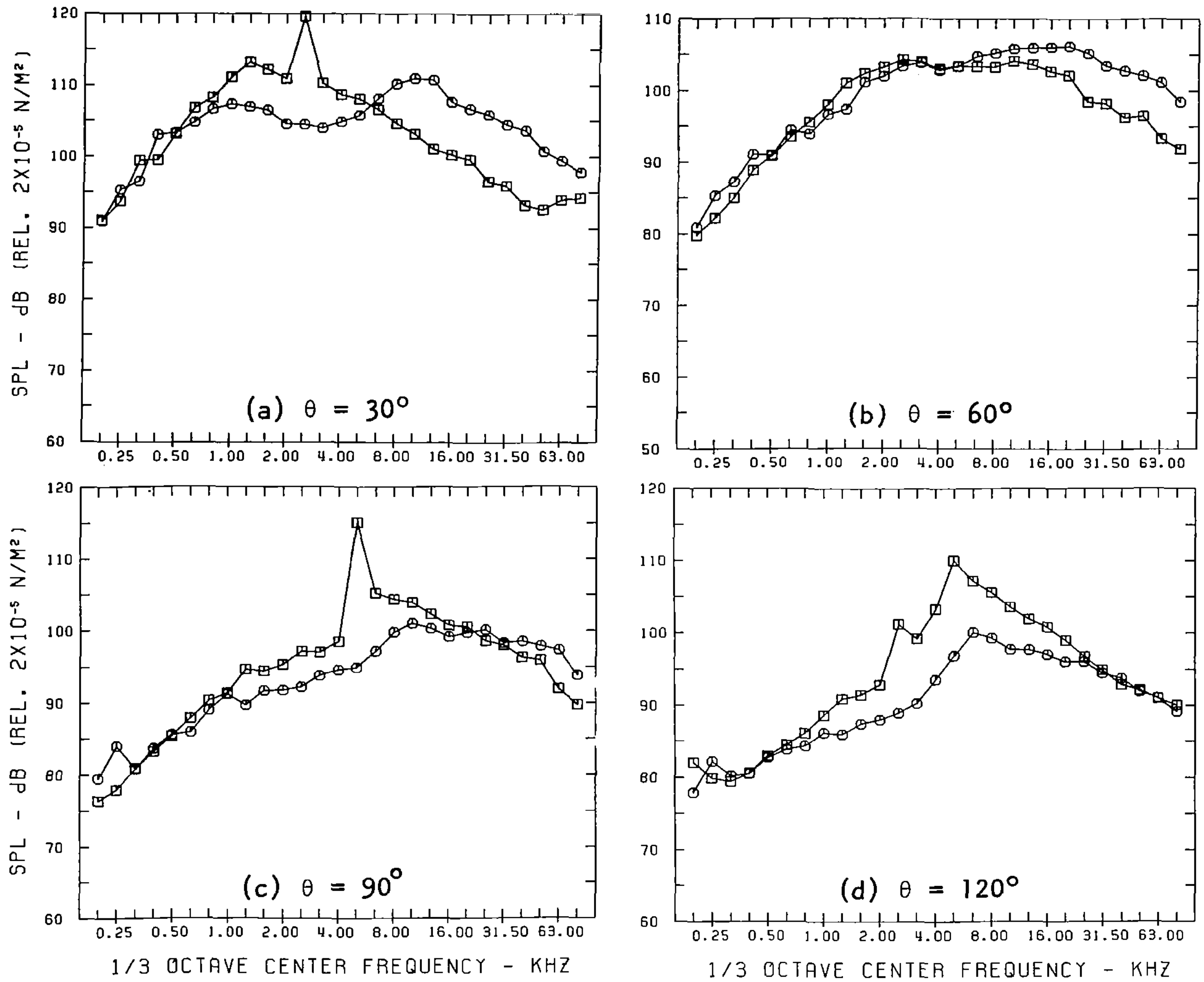
SPL - dB (REL. 2X10⁻⁵ N/M²)
(a) θ = 30°
(b) θ = 60°
(c) θ = 90°
(d) θ = 120°
0.25 0.50 1.00 2.00 4.00 8.00 16.00 31.50 63.00
1/3 OCTAVE CENTER FREQUENCY - KHZ
1/3 OCTAVE CENTER FREQUENCY - KHZ

Figure A1.5

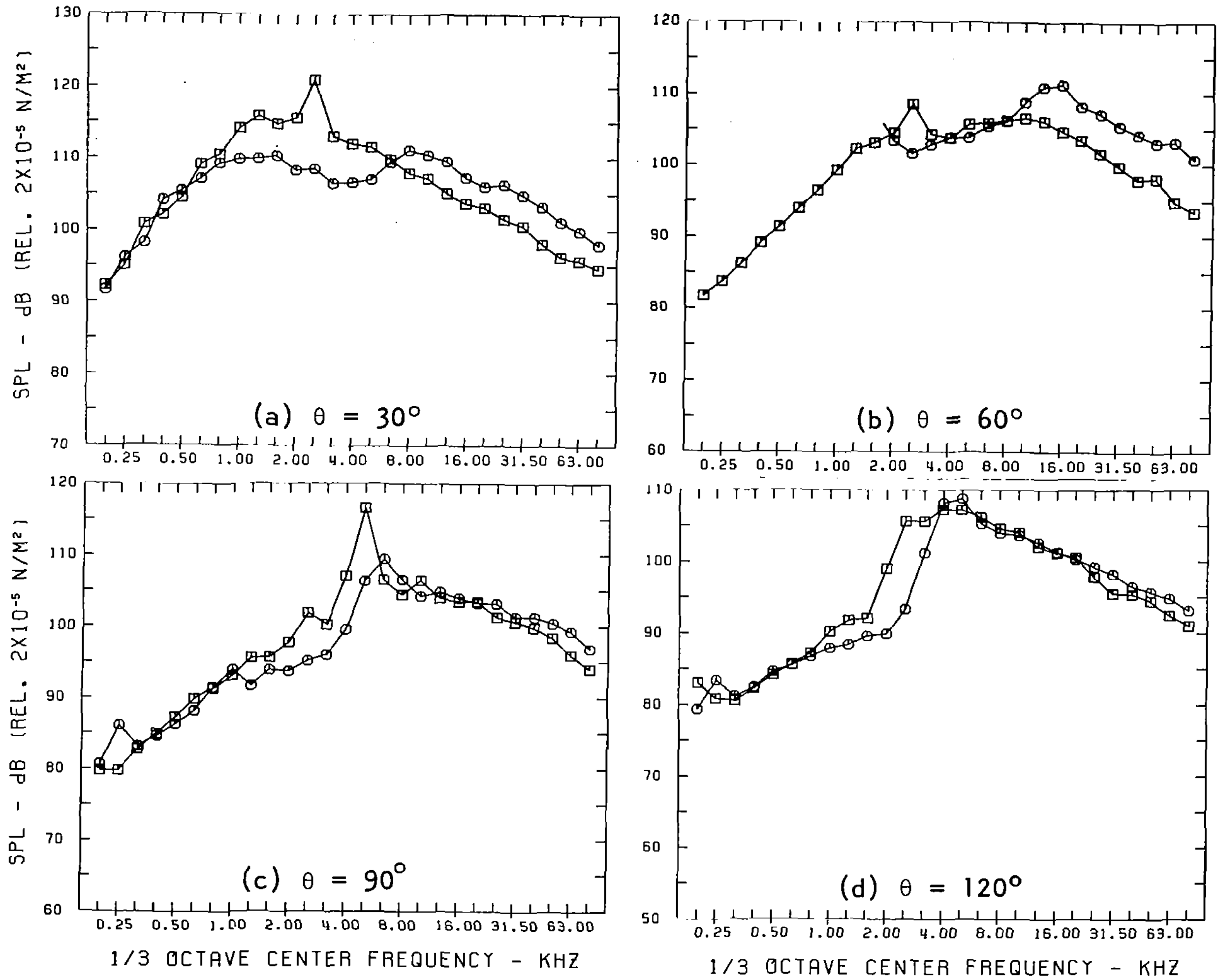
SPL - dB (REL. 2X10⁻⁵ N/M²)
(a) θ = 30°
(b) θ = 60°
(c) θ = 90°
(d) θ = 120°
0.25 0.50 1.00 2.00 4.00 8.00 16.00 31.50 63.00
1/3 OCTAVE CENTER FREQUENCY - KHZ

Figure A1.6

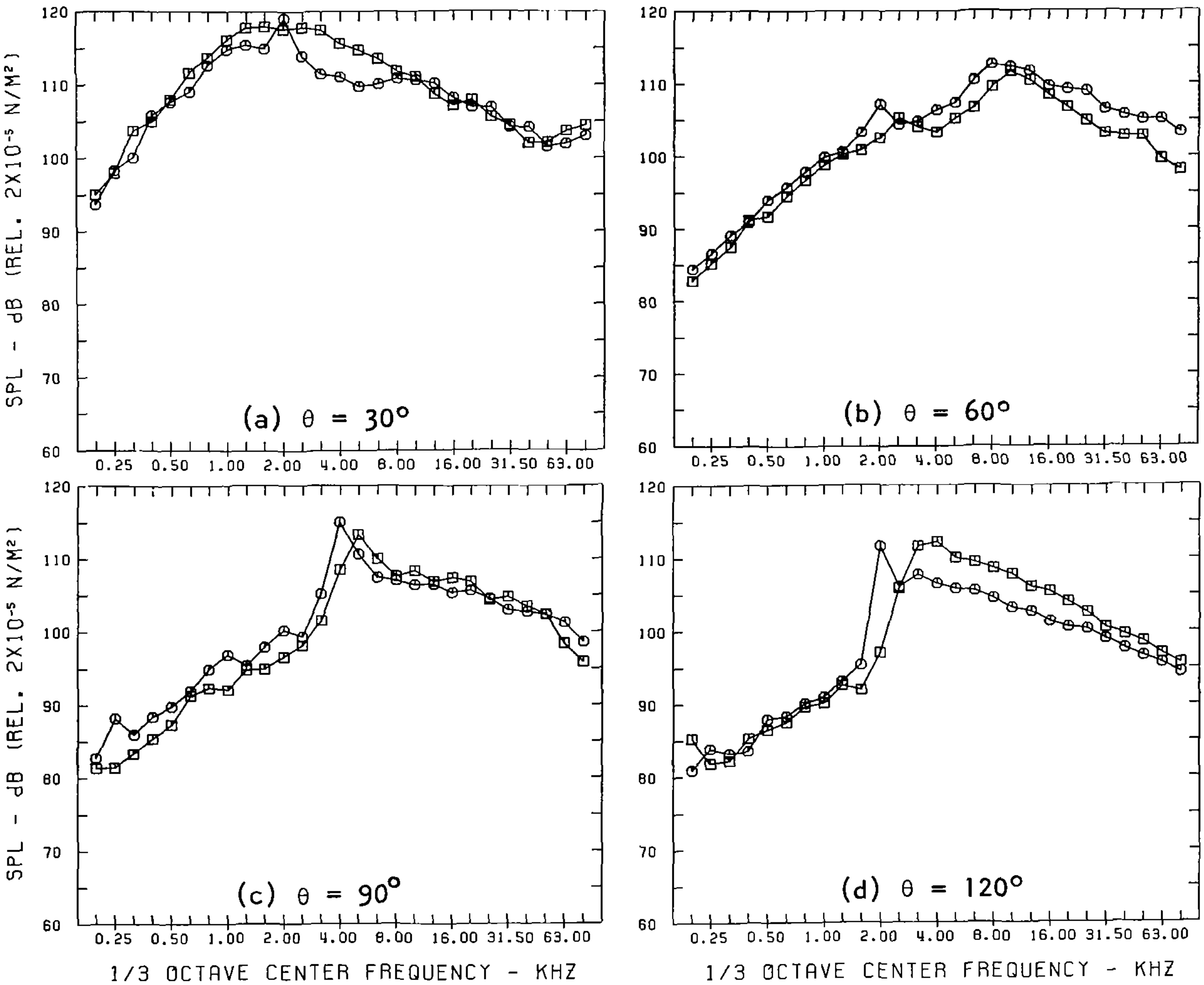

SPL - dB (REL. 2X10⁻⁵ N/M²)
(a) θ = 30°
(b) θ = 60°
(c) θ = 90°
(d) θ = 120°
0.25 0.50 1.00 2.00 4.00 8.00 16.00 31.50 63.00
1/3 OCTAVE CENTER FREQUENCY - KHZ


Figure A1.7

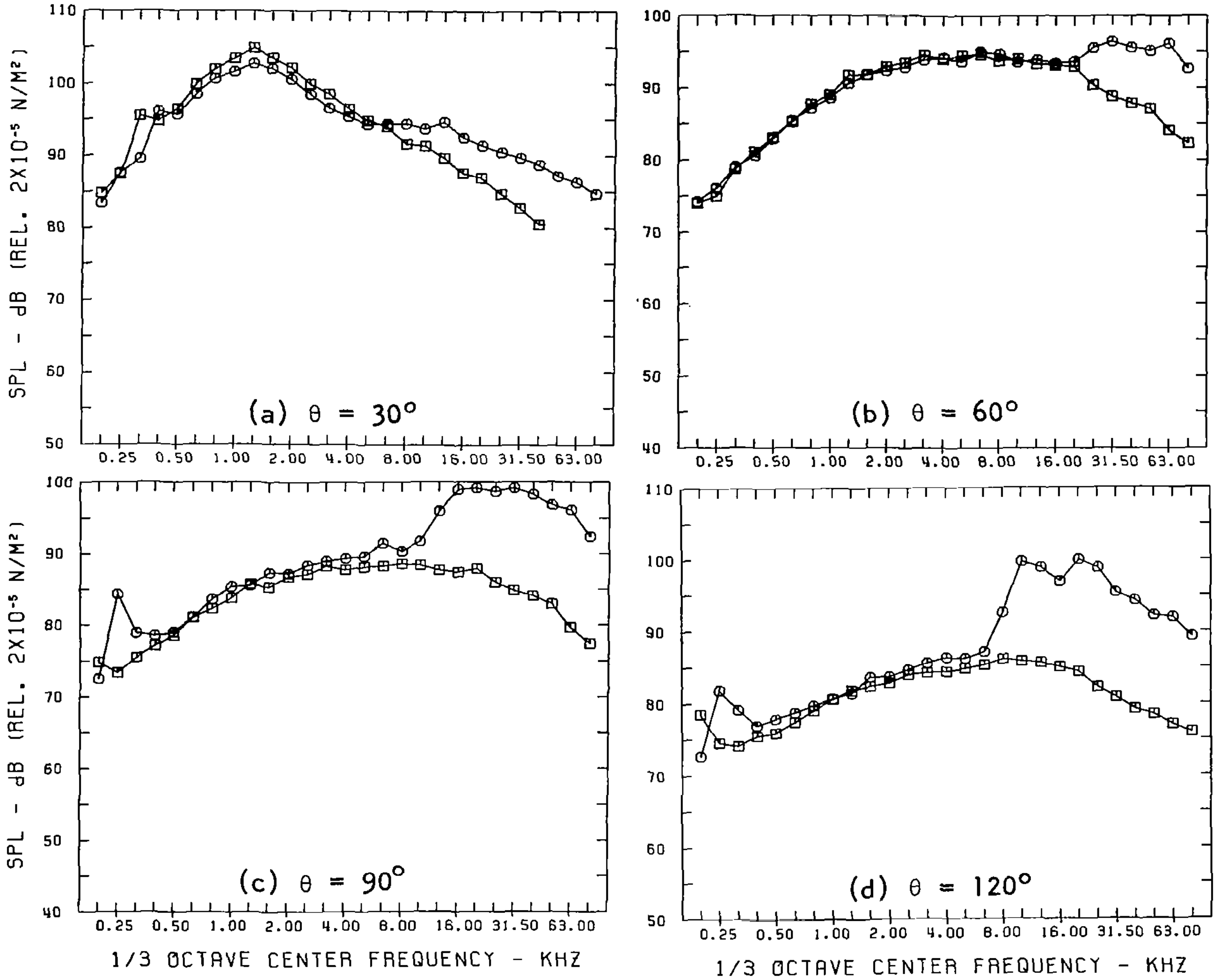

SPL - dB (REL. 2X10⁻⁵ N/M²)
(a) θ = 30°
(b) θ = 60°
(c) θ = 90°
(d) θ = 120°
0.25 0.50 1.00 2.00 4.00 8.00 16.00 31.50 63.00
1/3 OCTAVE CENTER FREQUENCY - KHZ


Figure A1.8

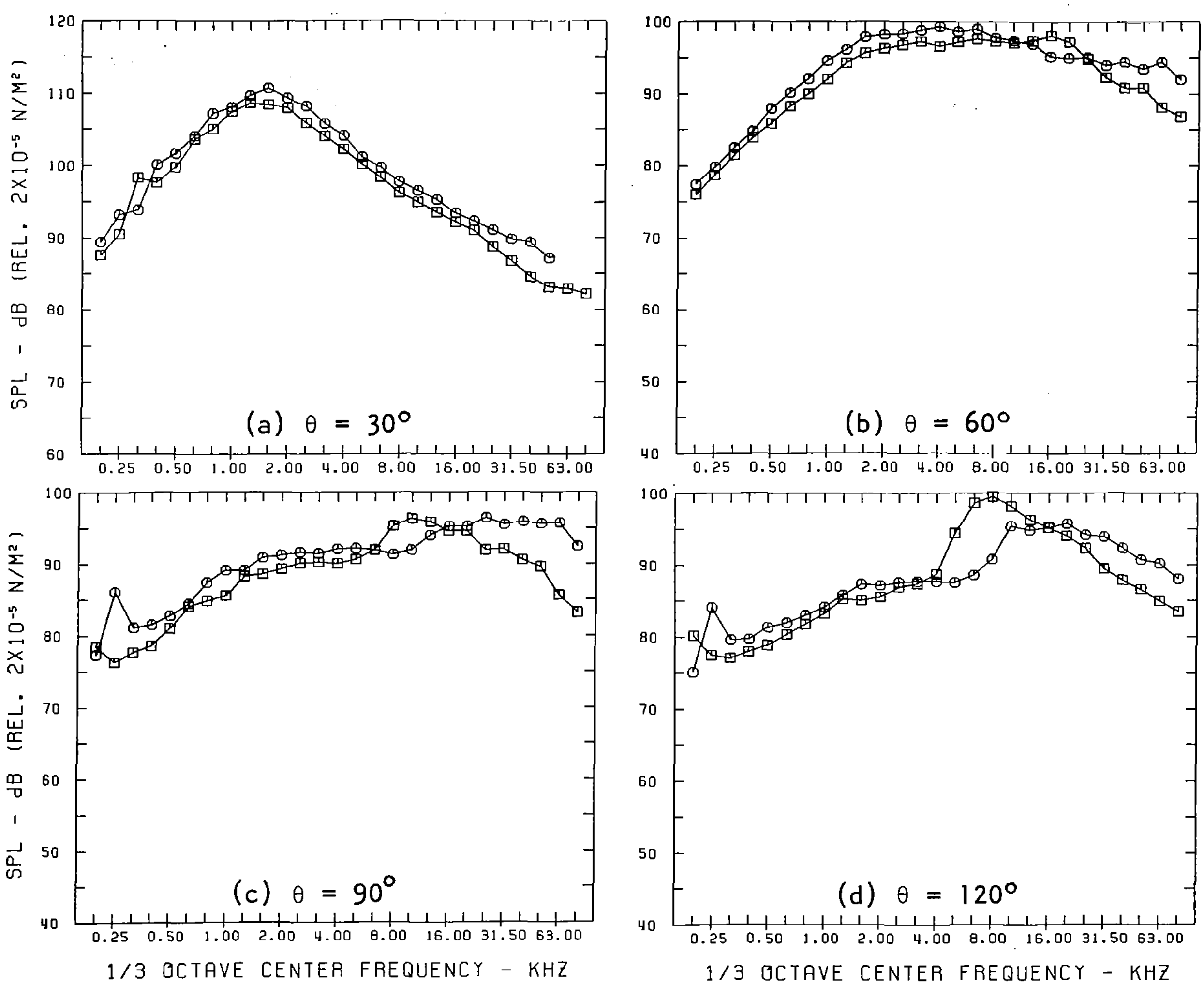

SPL - dB (REL. 2X10⁻⁵ N/M²)
(a) θ = 30°
(b) θ = 60°
(c) θ = 90°
(d) θ = 120°
0.25 0.50 1.00 2.00 4.00 8.00 16.00 31.50 63.00
1/3 OCTAVE CENTER FREQUENCY - KHZ


Figure A1.9

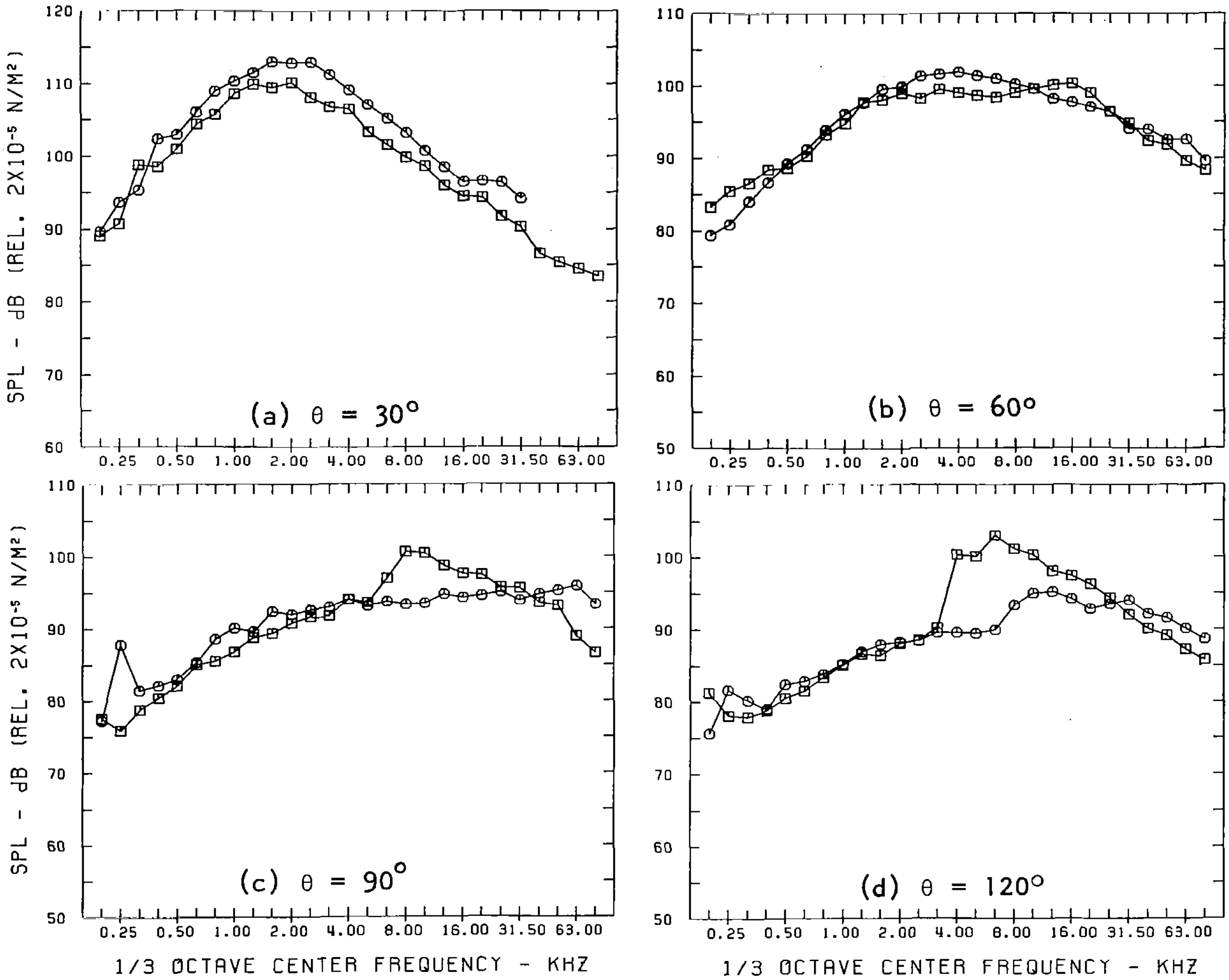

SPL - dB (REL. 2X10⁻⁵ N/M²)
(a) θ = 30°
(b) θ = 60°
(c) θ = 90°
(d) θ = 120°
0.25 0.50 1.00 2.00 4.00 8.00 16.00 31.50 63.00
1/3 OCTAVE CENTER FREQUENCY - KHZ


Figure A1.10

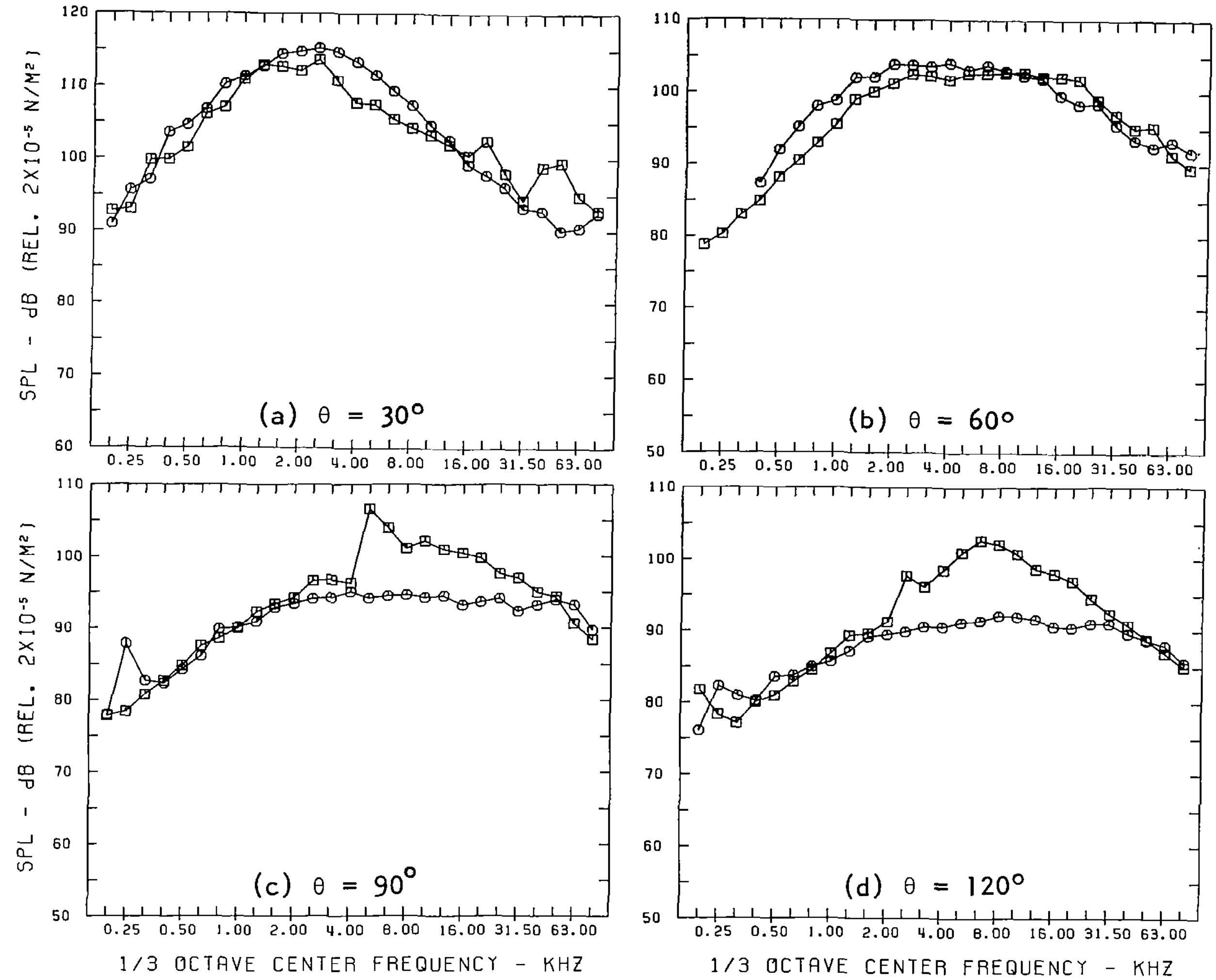

SPL - dB (REL. 2X10⁻⁵ N/M²)
(a) θ = 30°
(b) θ = 60°
(c) θ = 90°
(d) θ = 120°
0.25 0.50 1.00 2.00 4.00 8.00 16.00 31.50 63.00
1/3 OCTAVE CENTER FREQUENCY - KHZ


Figure A1.11

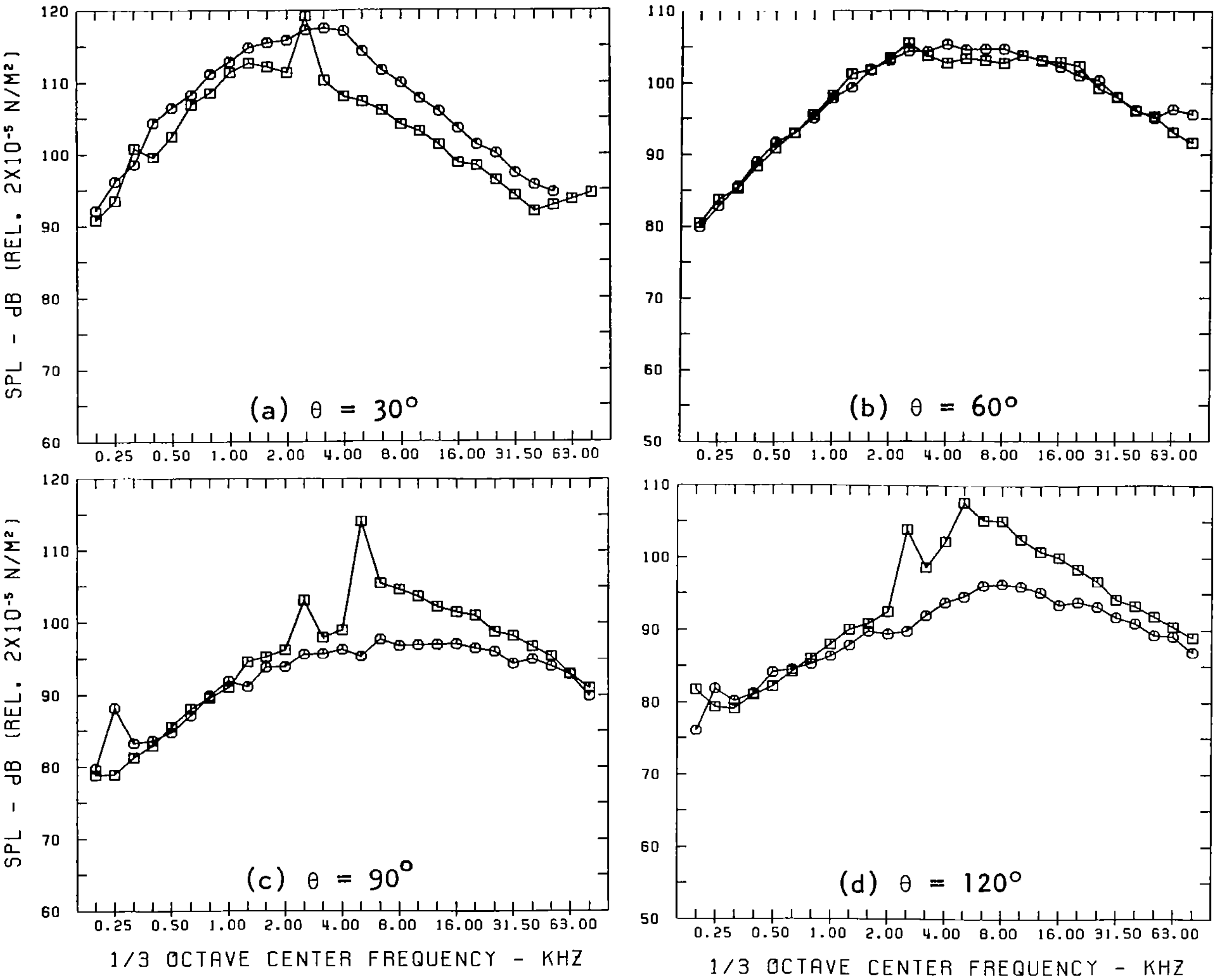

SPL - dB (REL. 2X10-5 N/M²)
(a) θ = 30°
(b) θ = 60°
(c) θ = 90°
(d) θ = 120°
0.25 0.50 1.00 2.00 4.00 8.00 16.00 31.50 63.00
1/3 OCTAVE CENTER FREQUENCY - KHZ


Figure A1.12

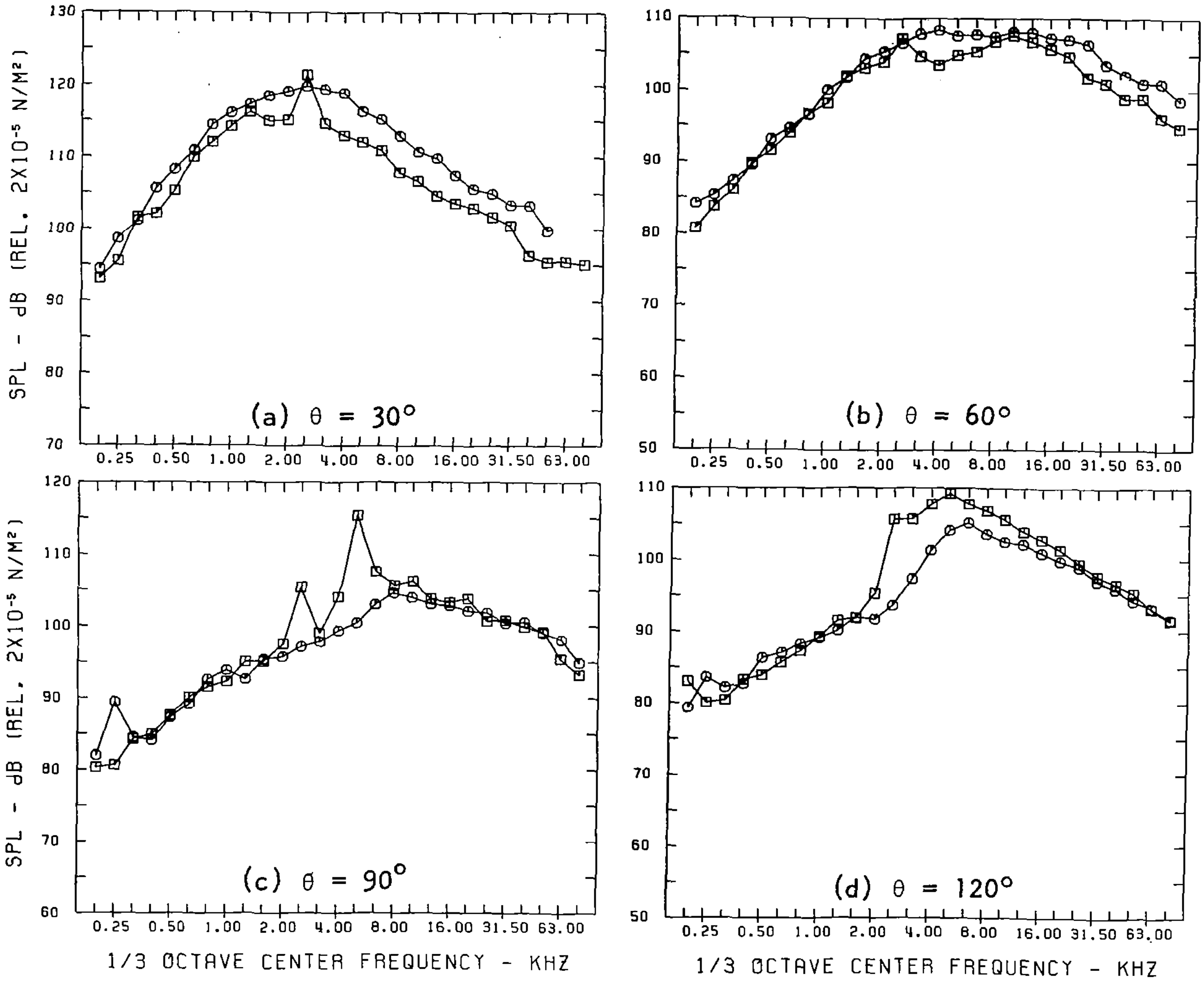
SPL - dB (REL. 2X10⁻⁵ N/M²)
(a) θ = 30°
(b) θ = 60°
(c) θ = 90°
(d) θ = 120°
0.25 0.50 1.00 2.00 4.00 8.00 16.00 31.50 63.00
1/3 OCTAVE CENTER FREQUENCY - KHZ

Figure A1.13

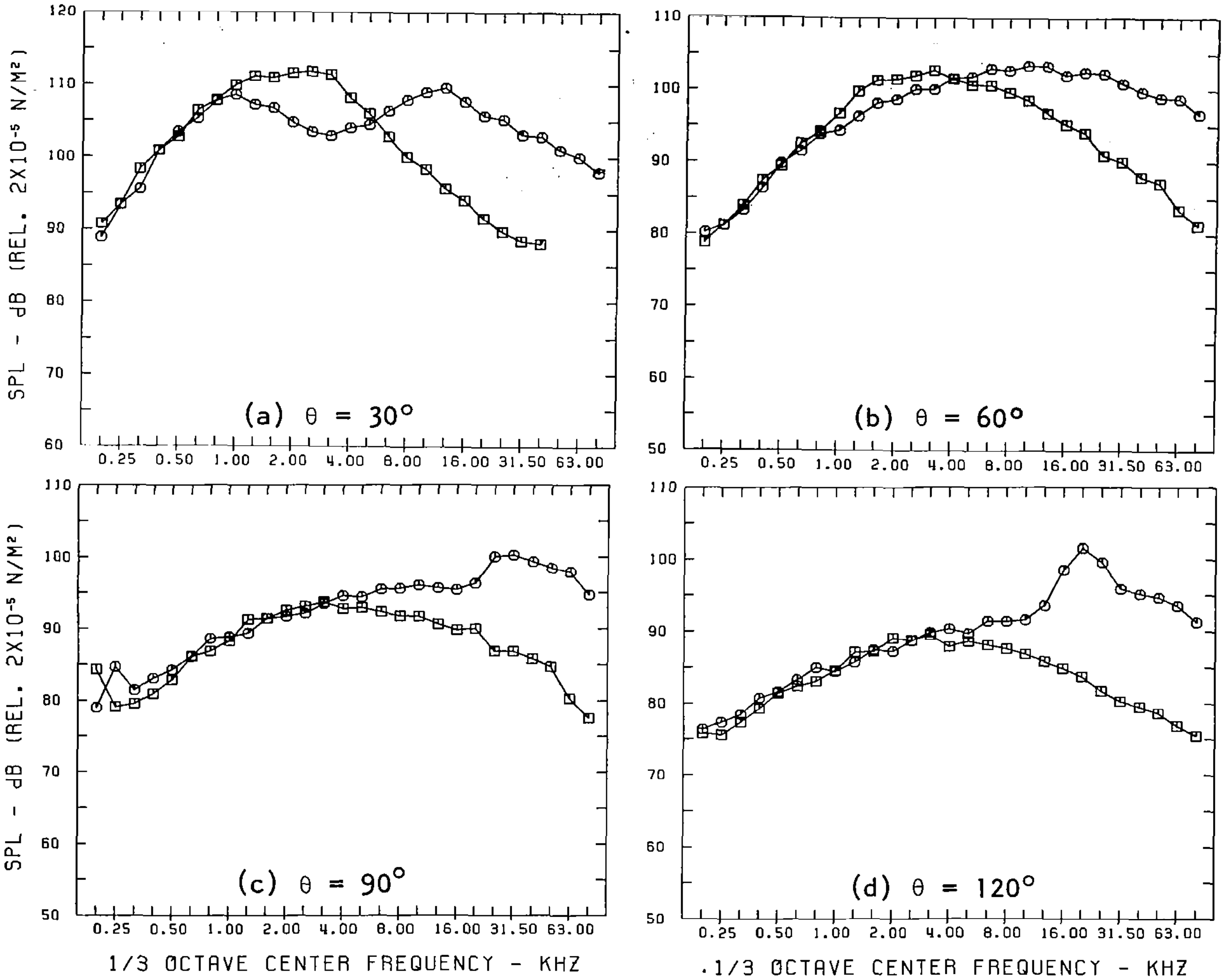
SPL - dB (REL. 2X10⁻⁵ N/M²)
(a) θ = 30°
(b) θ = 60°
(c) θ = 90°
(d) θ = 120°
0.25 0.50 1.00 2.00 4.00 8.00 16.00 31.50 63.00
1/3 OCTAVE CENTER FREQUENCY - KHZ

Figure A1.14

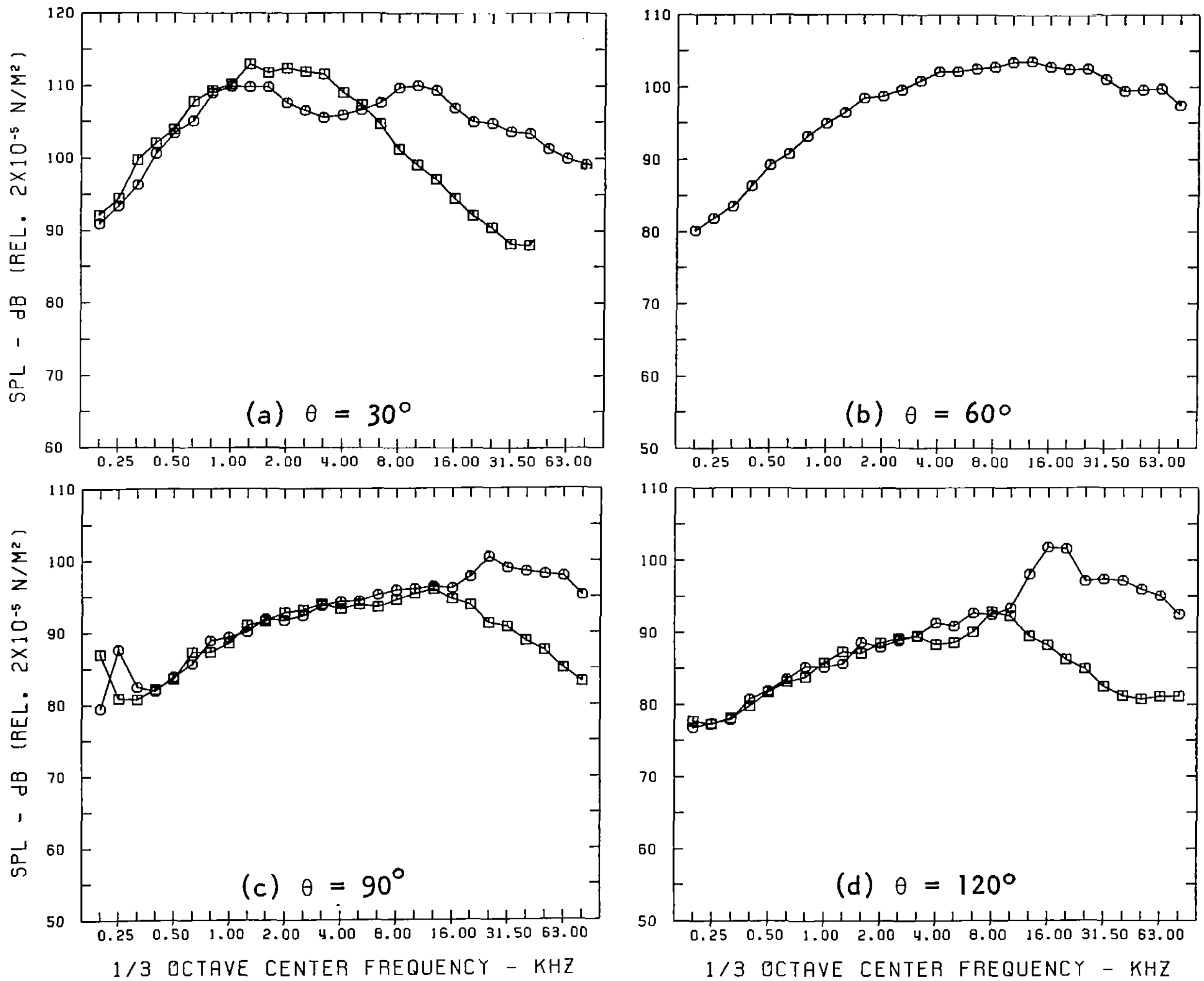
SPL - dB (REL. 2X10⁻⁵ N/M²)
(a) θ = 30°
(b) θ = 60°
(c) θ = 90°
(d) θ = 120°
0.25 0.50 1.00 2.00 4.00 8.00 16.00 31.50 63.00
1/3 OCTAVE CENTER FREQUENCY - KHZ

Figure A1.15

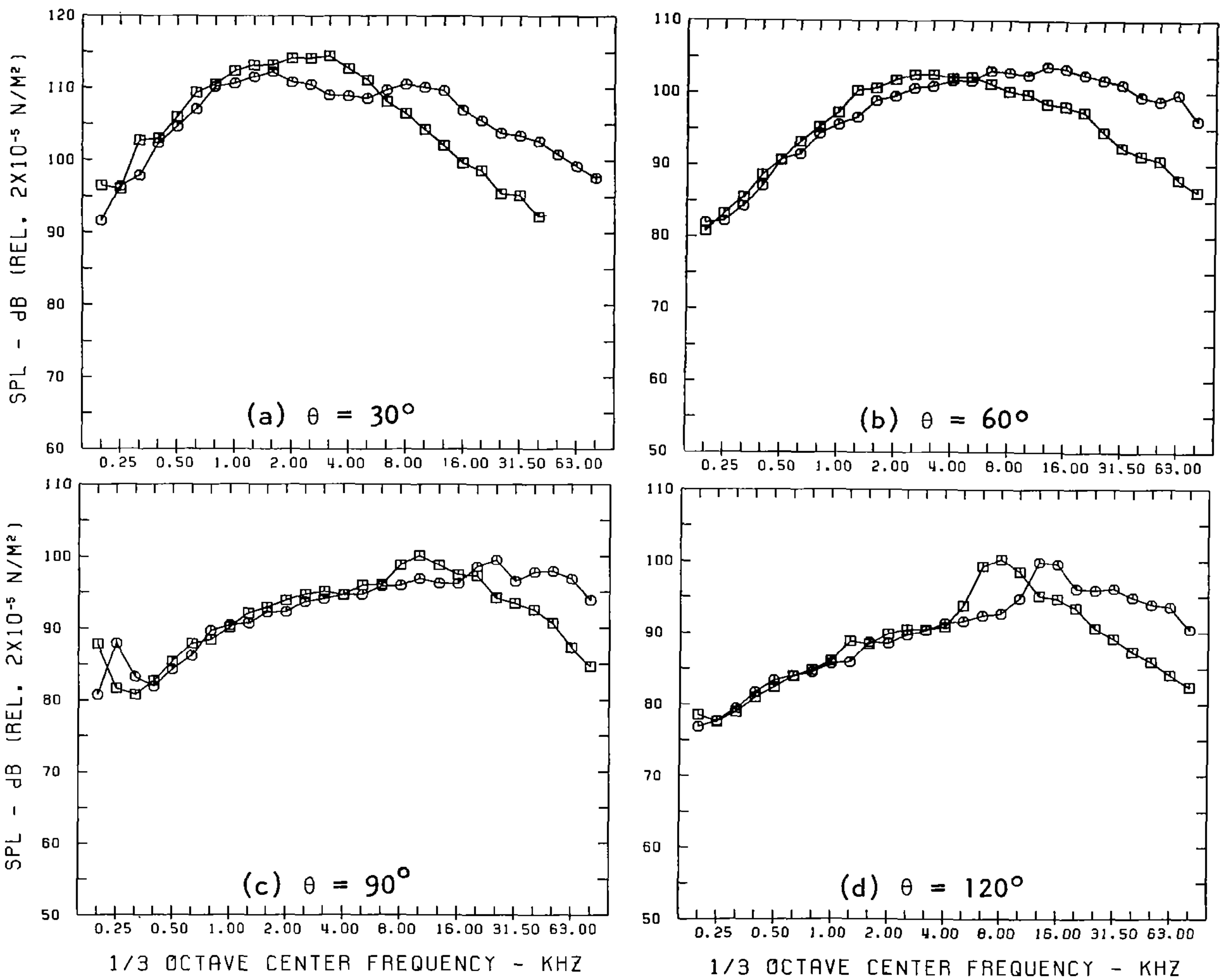
SPL - dB (REL. 2X10⁻⁵ N/M²)
(a) θ = 30°
(b) θ = 60°
(c) θ = 90°
(d) θ = 120°
0.25 0.50 1.00 2.00 4.00 8.00 16.00 31.50 63.00
1/3 OCTAVE CENTER FREQUENCY - KHZ

Figure A1.16

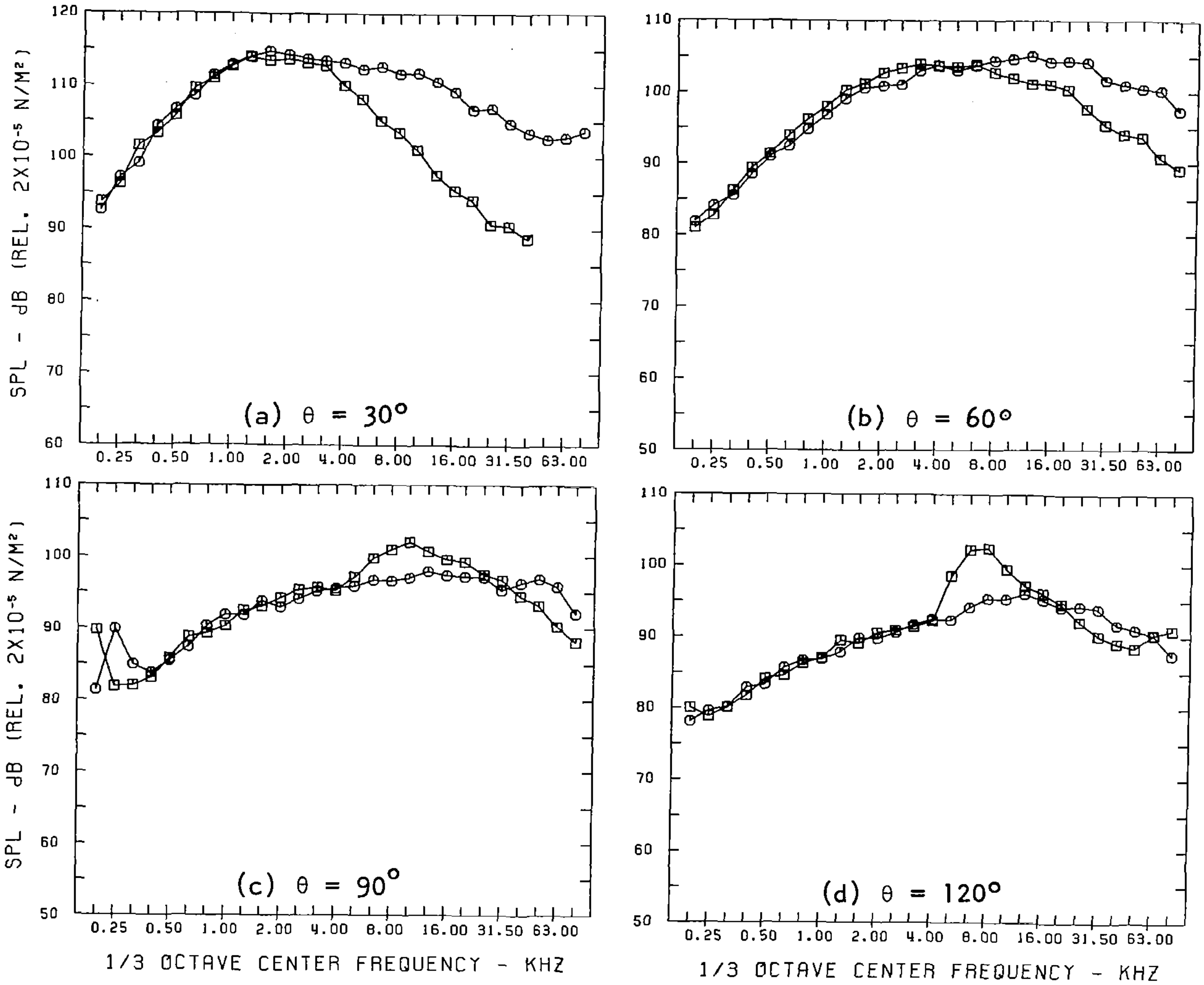

(a) θ = 30°
(b) θ = 60°
(c) θ = 90°
(d) θ = 120°
SPL - dB (REL. 2X10⁻⁵ N/M²)
1/3 OCTAVE CENTER FREQUENCY - KHZ
0.25 0.50 1.00 2.00 4.00 8.00 16.00 31.50 63.00


Figure A1.17

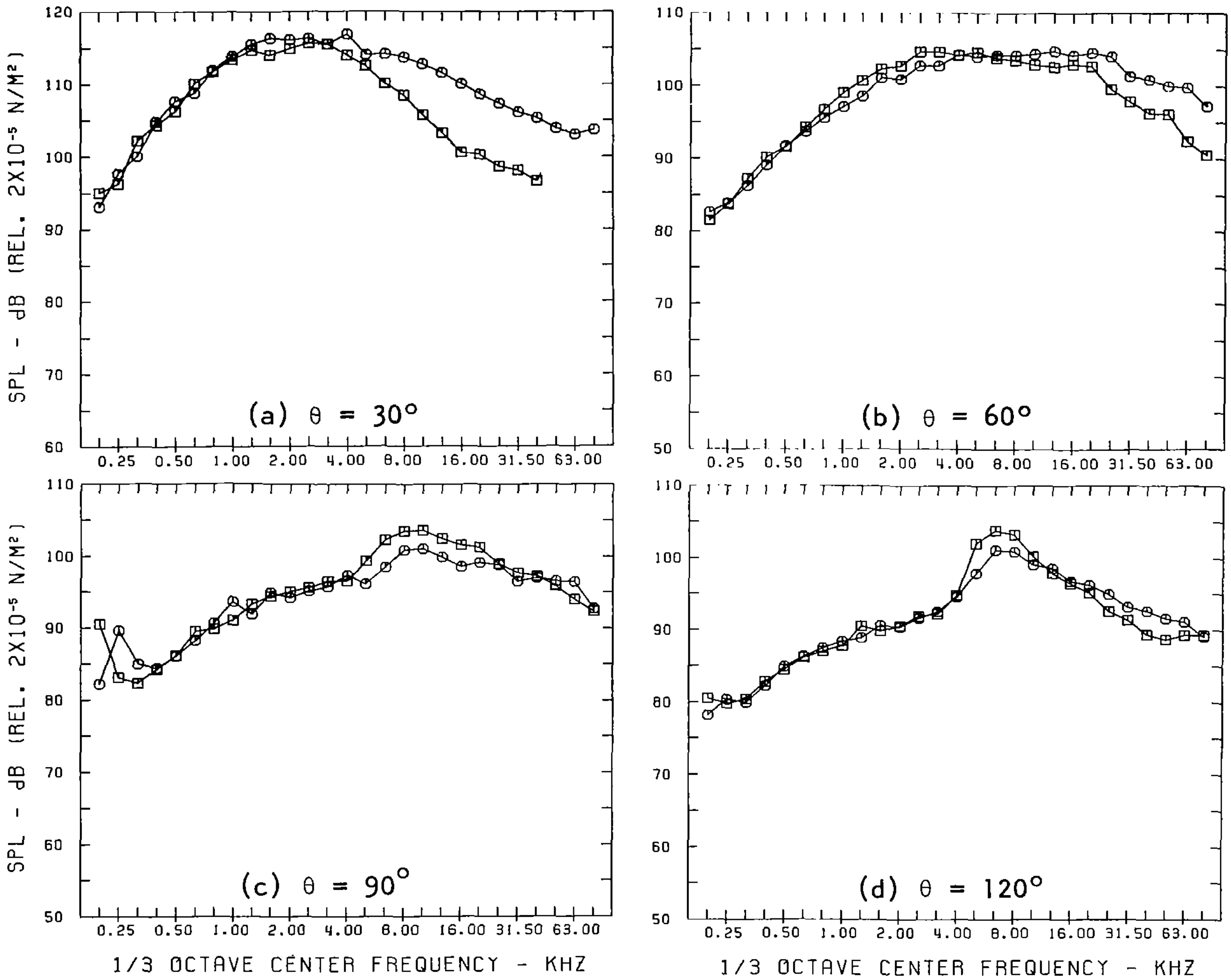
SPL - dB (REL. 2X10$^{-5}$ N/M$^2$)
(a) θ = 30°
(b) θ = 60°
(c) θ = 90°
(d) θ = 120°
0.25 0.50 1.00 2.00 4.00 8.00 16.00 31.50 63.00
1/3 OCTAVE CENTER FREQUENCY - KHZ

Figure A1.18

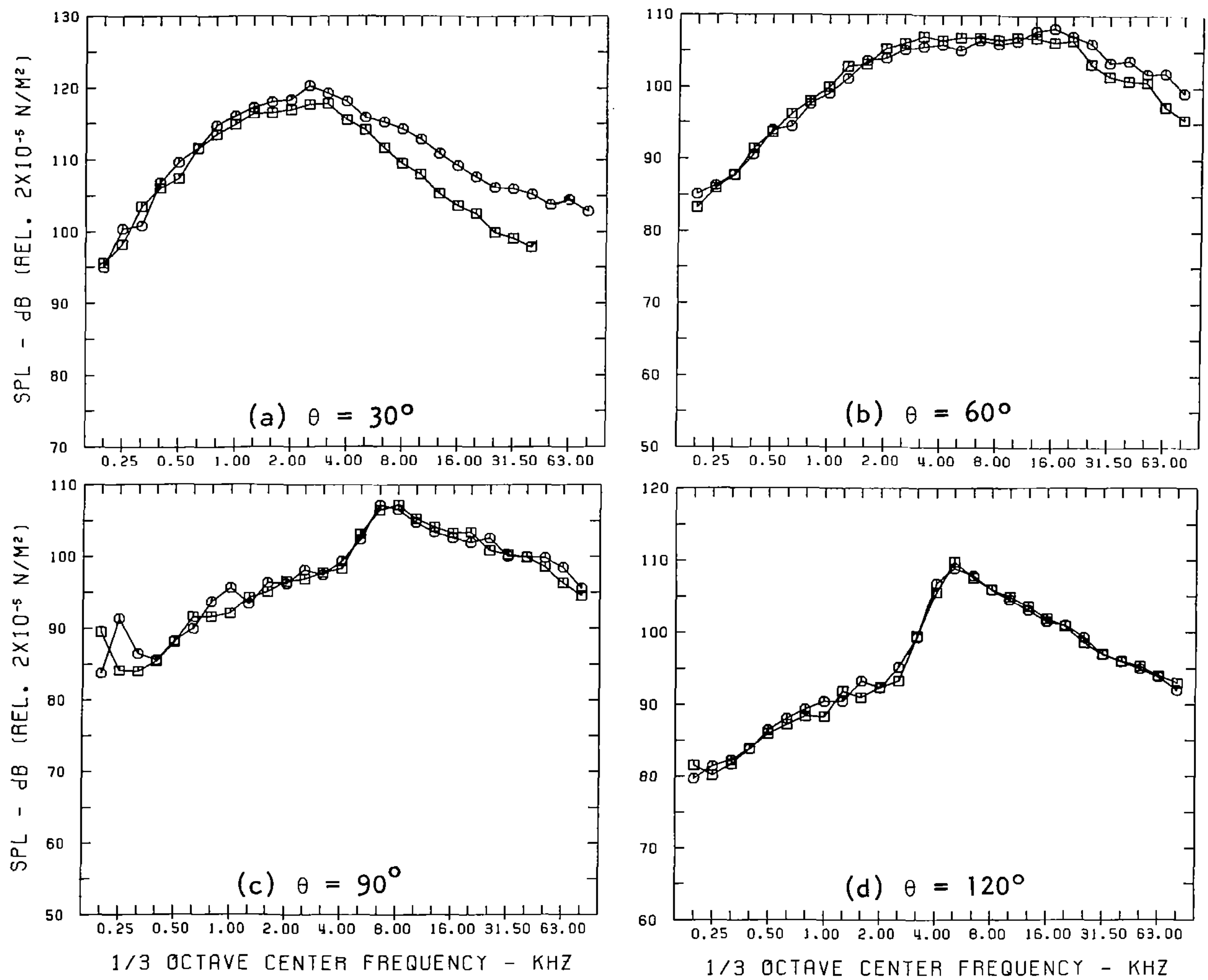

SPL - dB (REL. 2X10⁻⁵ N/M²)
(a) θ = 30°
(b) θ = 60°
(c) θ = 90°
(d) θ = 120°
0.25 0.50 1.00 2.00 4.00 8.00 16.00 31.50 63.00
1/3 OCTAVE CENTER FREQUENCY - KHZ


Figure A1.19

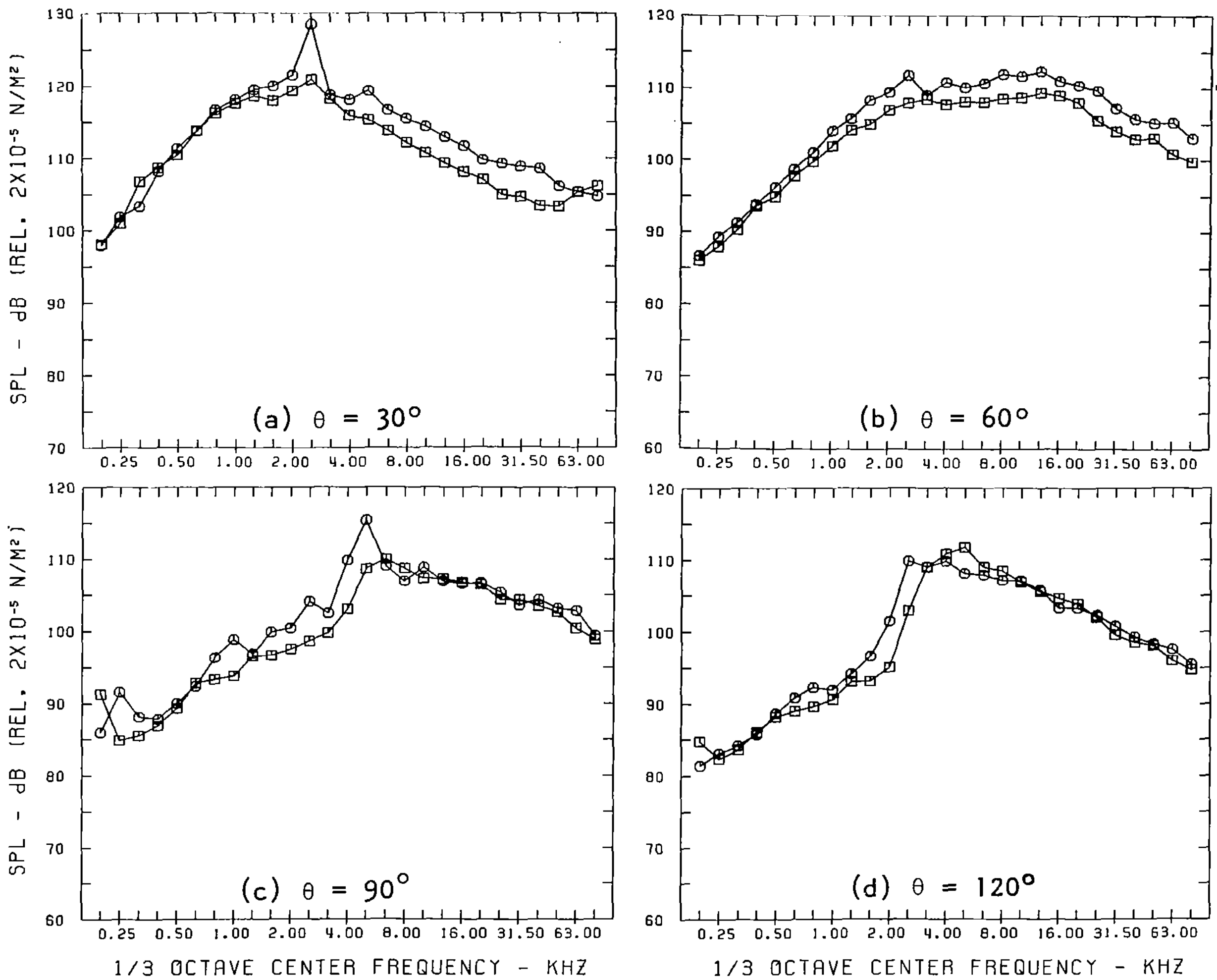

SPL - dB (REL. 2X10⁻⁵ N/M²)
1/3 OCTAVE CENTER FREQUENCY - KHZ
0.25 0.50 1.00 2.00 4.00 8.00 16.00 31.50 63.00
(a) θ = 30°
(b) θ = 60°
(c) θ = 90°
(d) θ = 120°


Figure A1.20

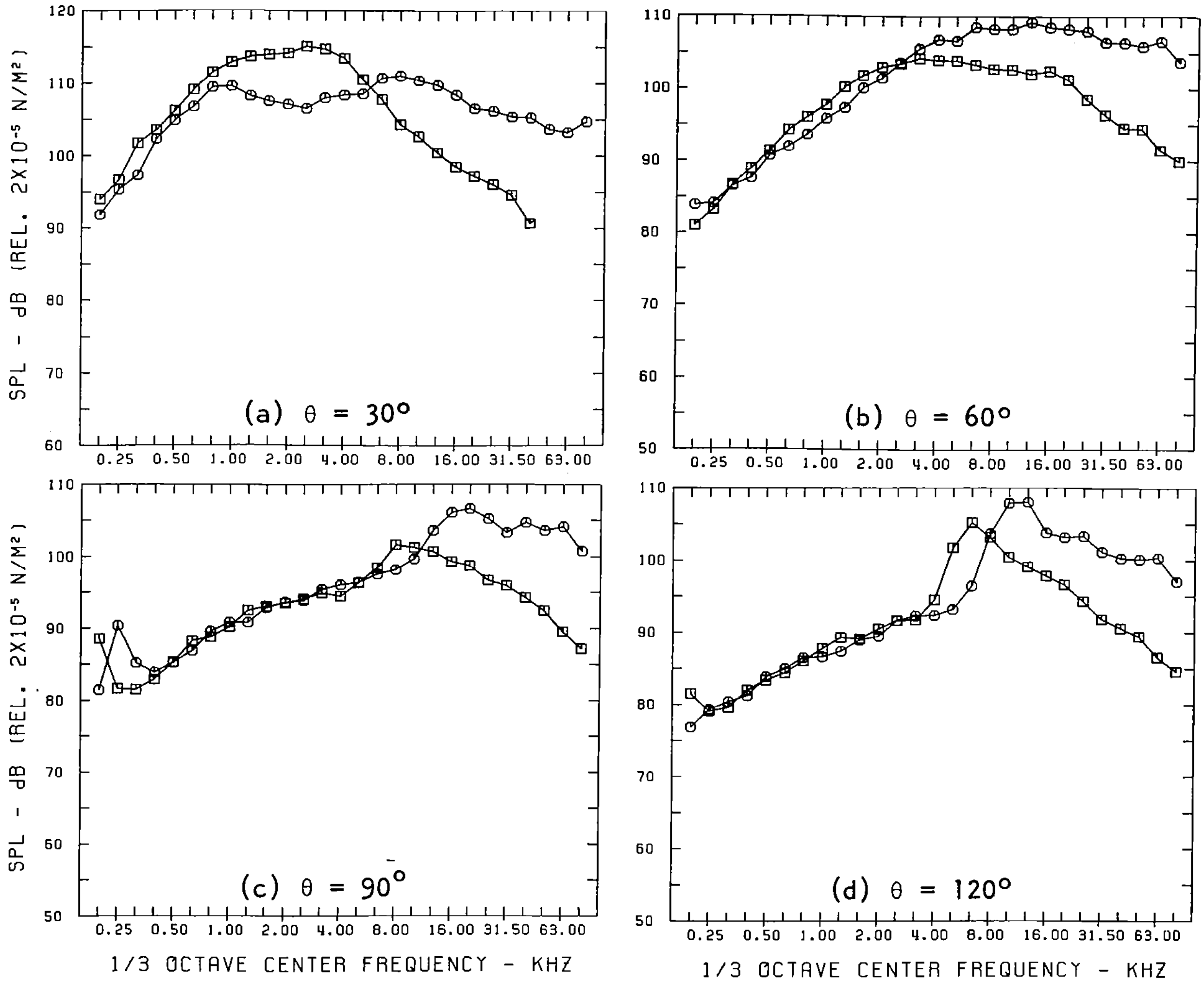
SPL - dB (REL. 2X10⁻⁵ N/M²)
(a) θ = 30°
(b) θ = 60°
(c) θ = 90°
(d) θ = 120°
0.25 0.50 1.00 2.00 4.00 8.00 16.00 31.50 63.00
1/3 OCTAVE CENTER FREQUENCY - KHZ

Figure A1.21

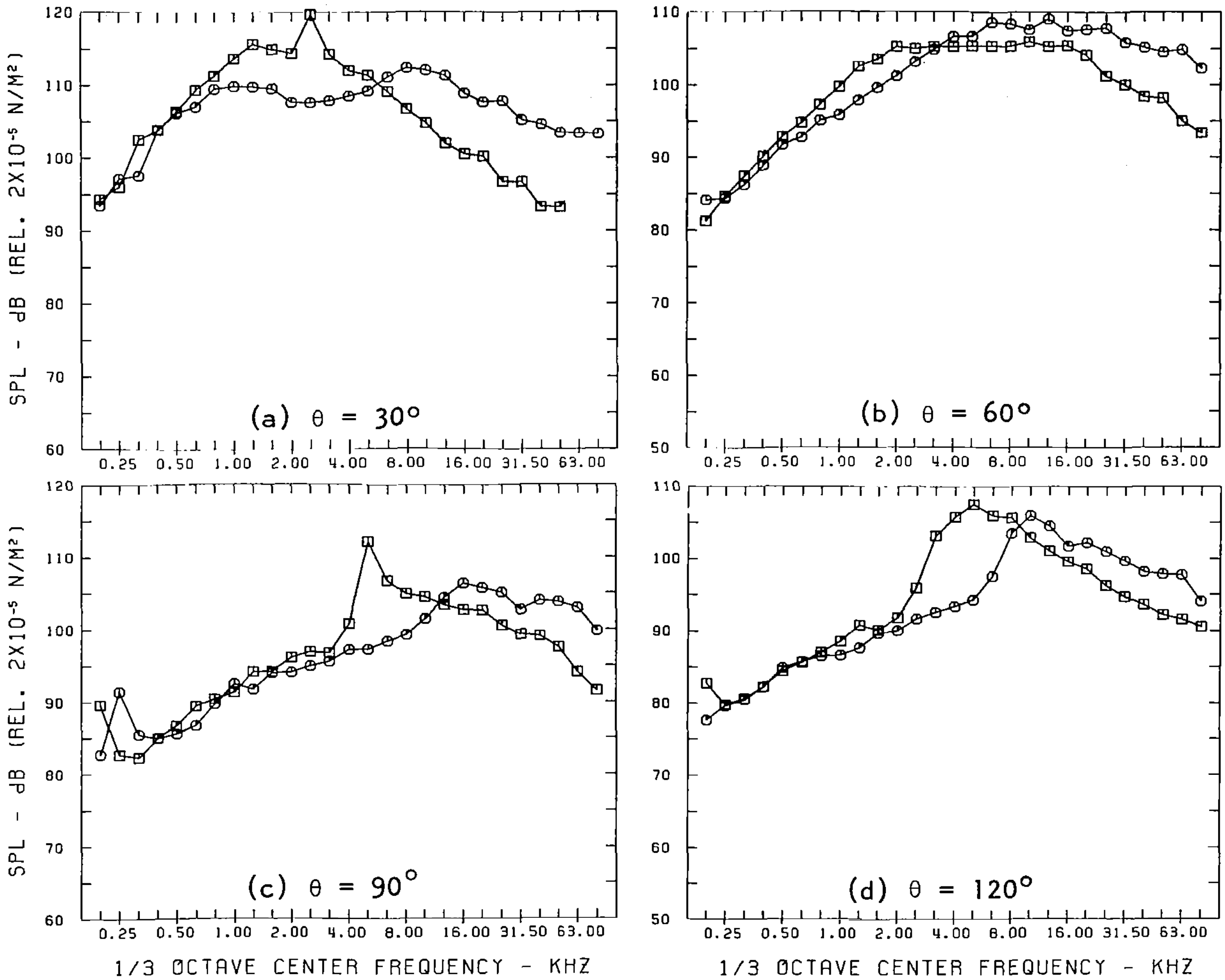
SPL - dB (REL. 2X10⁻⁵ N/M²)
(a) θ = 30°
(b) θ = 60°
(c) θ = 90°
(d) θ = 120°
0.25 0.50 1.00 2.00 4.00 8.00 16.00 31.50 63.00
1/3 OCTAVE CENTER FREQUENCY - KHZ

Figure A1.22

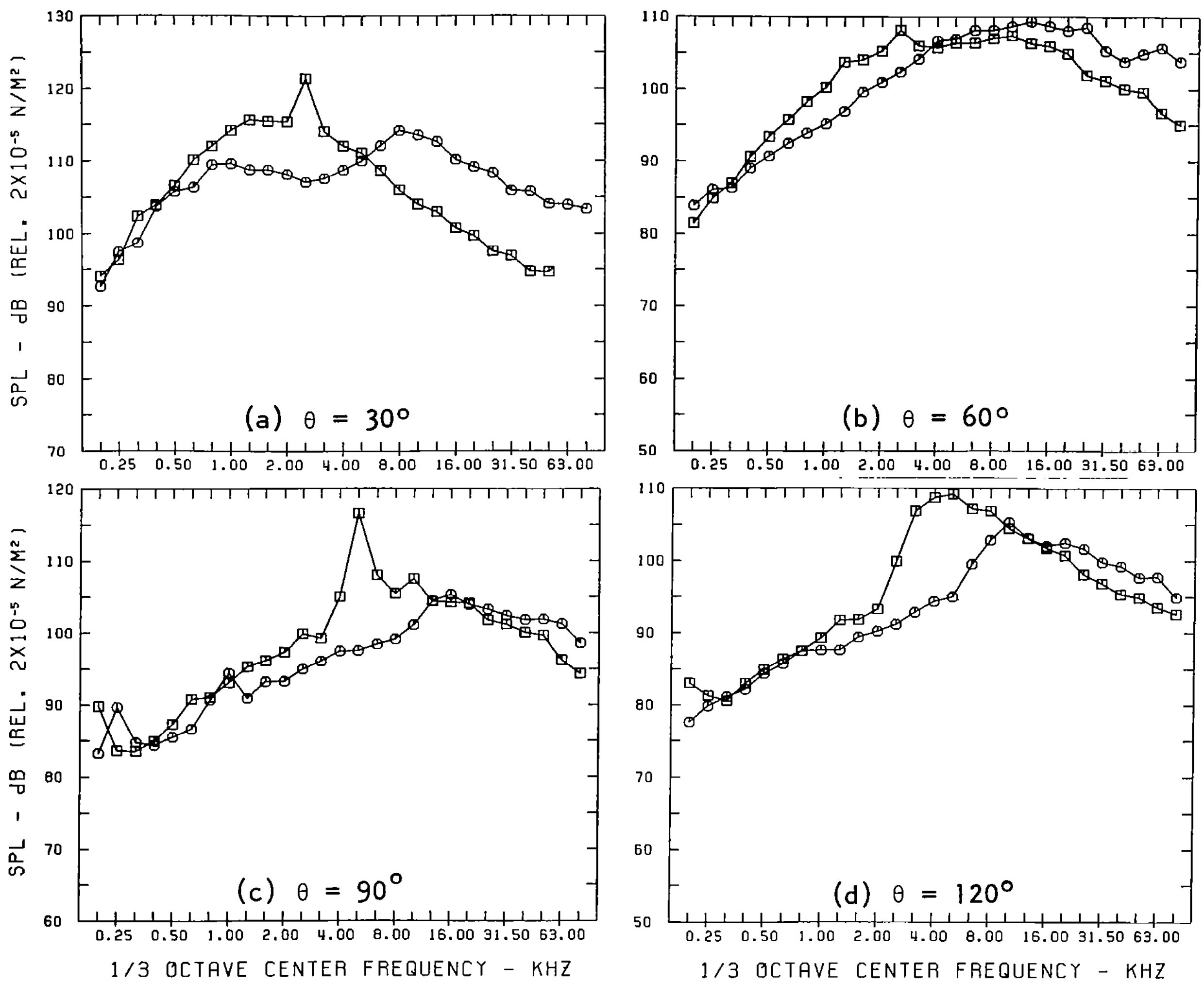
SPL - dB (REL. 2X10⁻⁵ N/M²)
(a) θ = 30°
(b) θ = 60°
(c) θ = 90°
(d) θ = 120°
0.25 0.50 1.00 2.00 4.00 8.00 16.00 31.50 63.00
1/3 OCTAVE CENTER FREQUENCY - KHZ

Figure A1.23

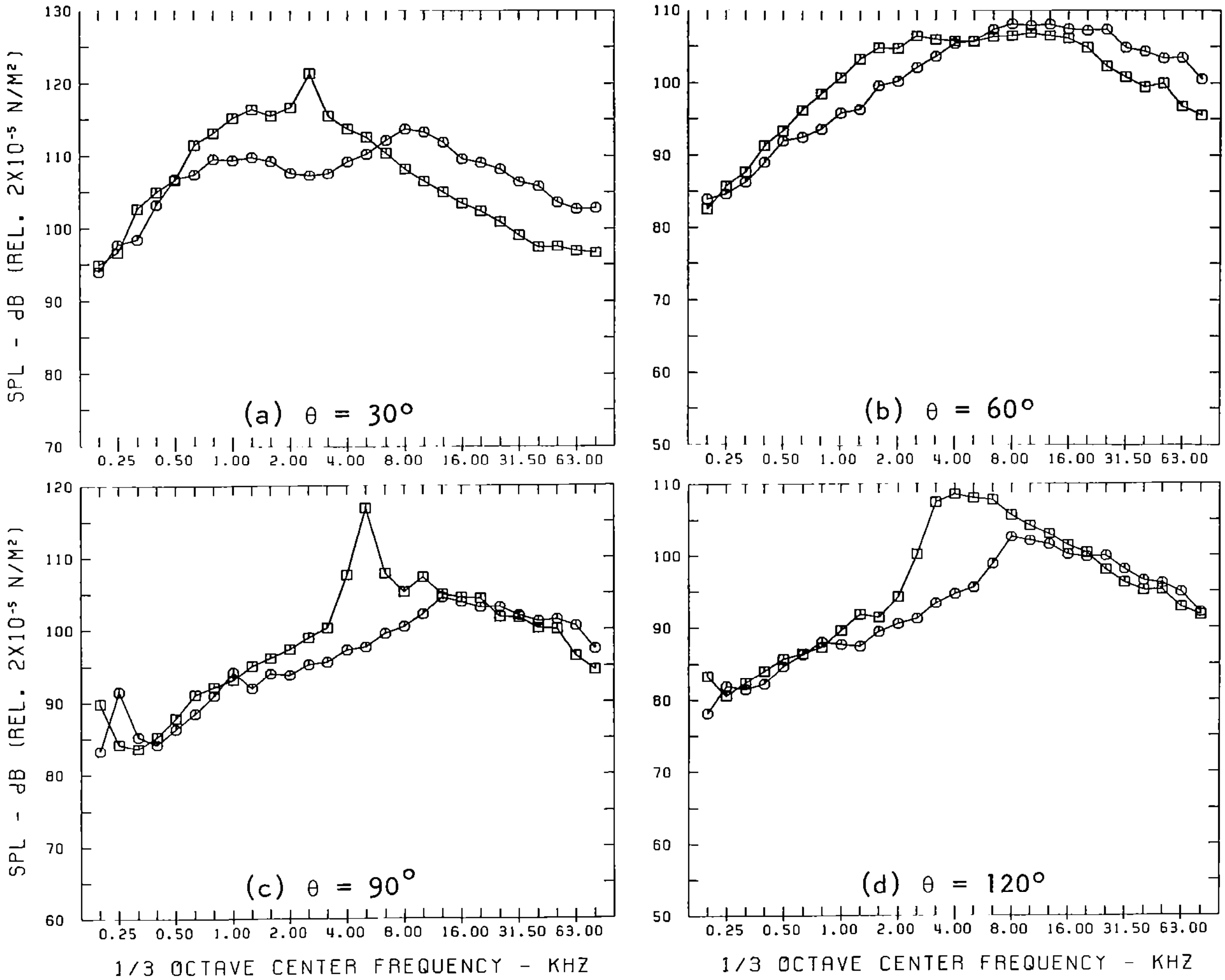

SPL - dB (REL. 2X10⁻⁵ N/M²)
(a) θ = 30°
(b) θ = 60°
(c) θ = 90°
(d) θ = 120°
0.25 0.50 1.00 2.00 4.00 8.00 16.00 31.50 63.00
1/3 OCTAVE CENTER FREQUENCY - KHZ
1/3 OCTAVE CENTER FREQUENCY - KHZ


Figure A1.24

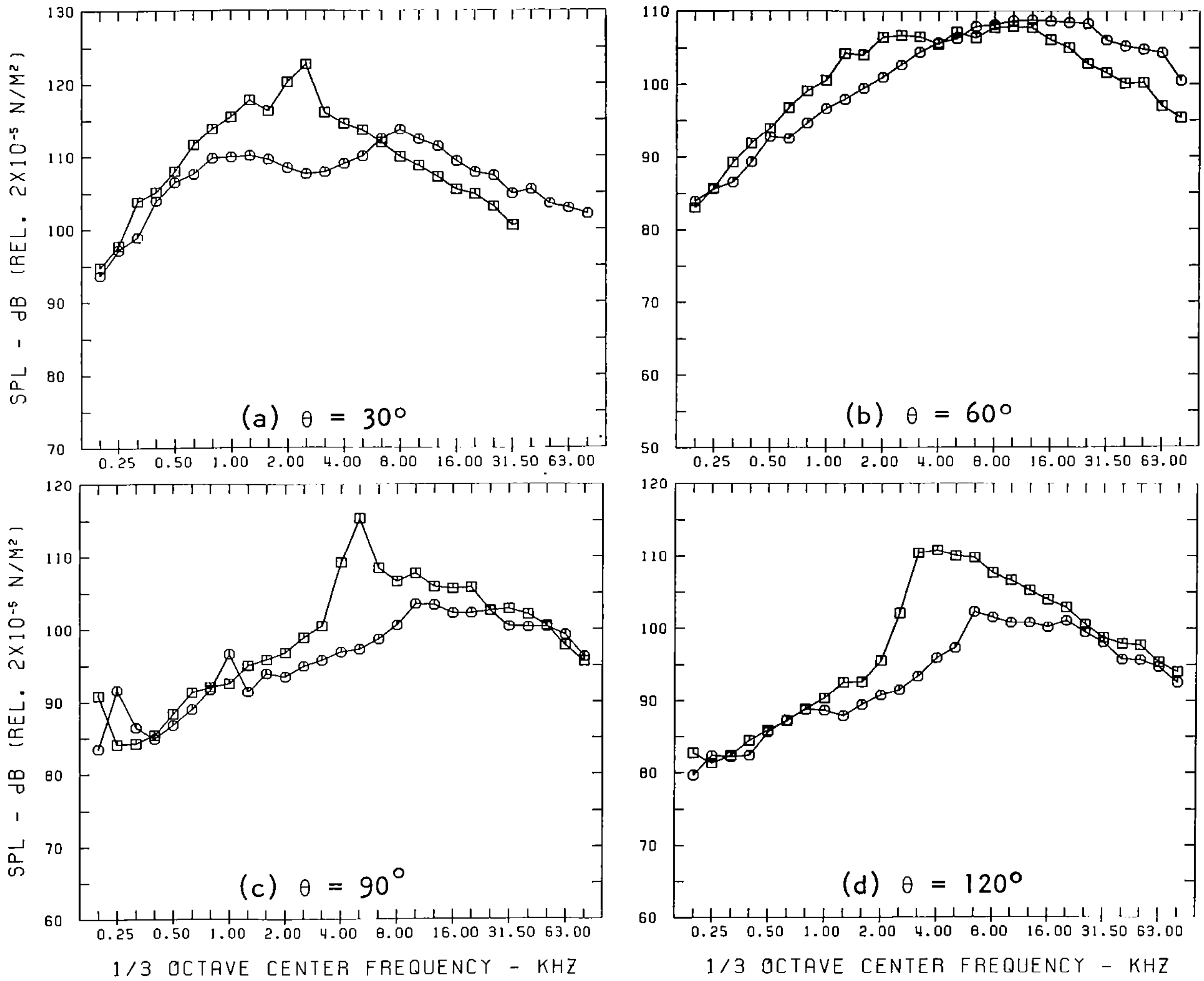
SPL - dB (REL. 2X10⁻⁵ N/M²)
(a) θ = 30°
(b) θ = 60°
(c) θ = 90°
(d) θ = 120°
0.25 0.50 1.00 2.00 4.00 8.00 16.00 31.50 63.00
1/3 OCTAVE CENTER FREQUENCY - KHZ

Figure A1.25

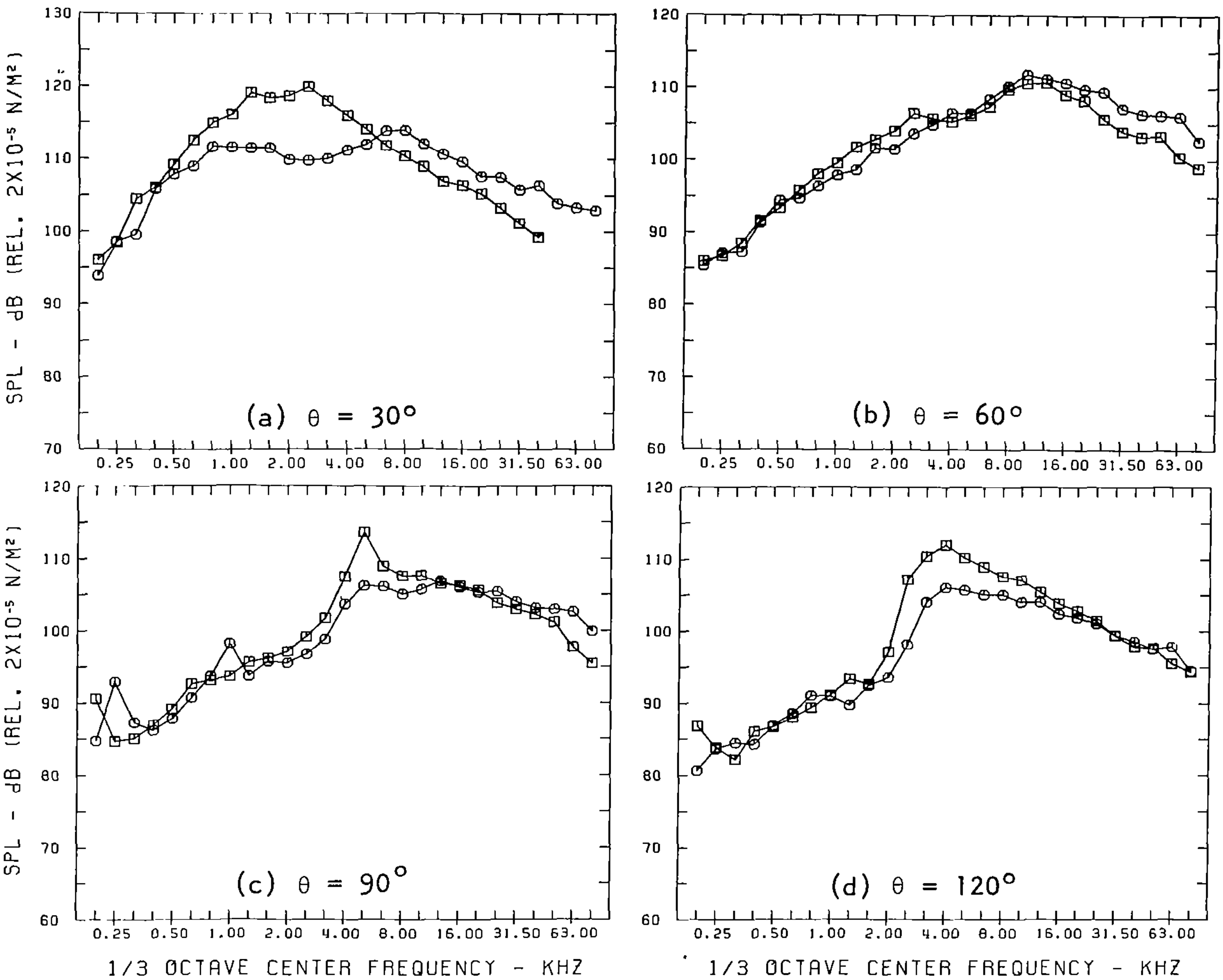

SPL - dB (REL. 2X10⁻⁵ N/M²)
130
120
110
100
90
80
70
60
(a) θ = 30°
(b) θ = 60°
(c) θ = 90°
(d) θ = 120°
0.25 0.50 1.00 2.00 4.00 8.00 16.00 31.50 63.00
1/3 OCTAVE CENTER FREQUENCY - KHZ


Figure A1.26

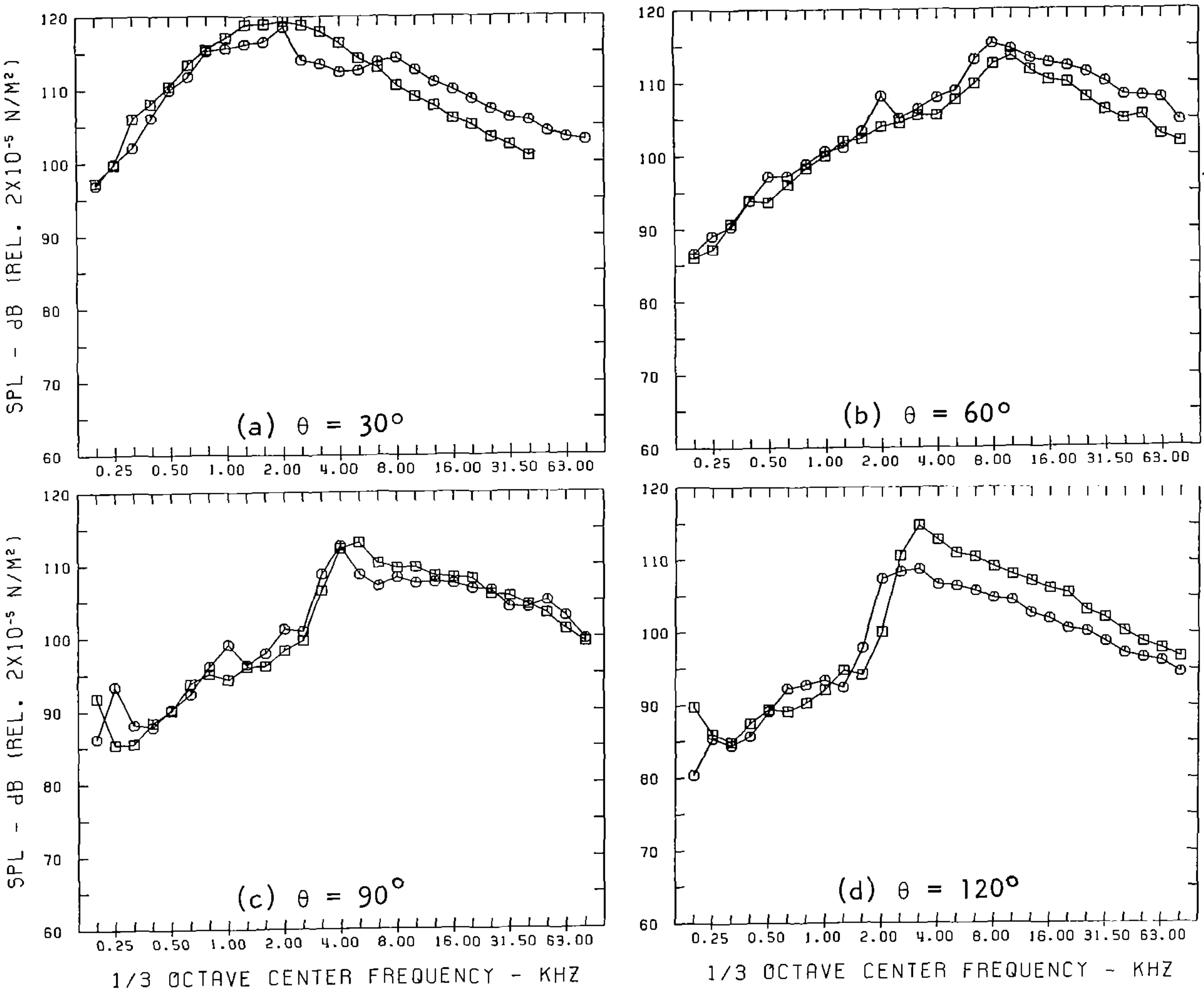

SPL - dB (REL. 2X10⁻⁵ N/M²)
120
110
100
90
80
70
60
(a) θ = 30°
(b) θ = 60°
(c) θ = 90°
(d) θ = 120°
0.25 0.50 1.00 2.00 4.00 8.00 16.00 31.50 63.00
1/3 OCTAVE CENTER FREQUENCY - KHZ


Figure A1.27

# APPENDIX 2

## ORTHOGONALITY CONDITION

Let $k_i$ be the $i^{th}$ eigenvalue and $(\hat{p}_{fi}, \hat{p}_{pi})$ be the $i^{th}$ eigenfunction of the eigenvalue problem defined by equations (5-12) to (5-17). It is straightforward to rewrite the differential equations and boundary conditions as follows:

$r \leq a$:

$$\frac{1}{r}\ \frac{d}{dr}\left(r\ \frac{d\hat{p}_{pi}}{dr}\right) + k_i^2\ (M_p^2 - 1)\ \hat{p}_{pi} = 0 \tag{A2-1}$$

$a \leq r \leq b$:

$$\frac{1}{r}\ \frac{d}{dr}\left(r\ \frac{d\hat{p}_{fi}}{dr}\right) + k_i^2\ (M_f^2 - 1)\ \hat{p}_{fi} = 0 \tag{A2-2}$$

$r \to 0$: $\qquad \hat{p}_{pi}$ is bounded $\hfill$ (A2-3)

$r = a$:

$$\hat{p}_{pi} = \hat{p}_{fi} \tag{A2-4}$$

$$\frac{1}{M_p^2}\ \frac{d\hat{p}_{pi}}{dr} = \frac{1}{M_f^2}\ \frac{d\hat{p}_{fi}}{dr} \tag{A2-5}$$

$r = b$: $\qquad \hat{p}_{fi} = 0 \hfill$ (A2-6)

Multiply (A2-1) by $\dfrac{\hat{p}_{pj}}{M_p^2}\ r$ and integrate over r from o to a, we find after performing one integration by parts to the first integral,

$$\frac{r}{M_p^2}\ \hat{p}_{pj}\ \frac{d\hat{p}_{pi}}{dr}\ \Bigg|_o^a - \int_o^a \frac{r}{M_p^2}\ \frac{d\hat{p}_{pi}}{dr}\ \frac{d\hat{p}_{pj}}{dr}\ dr + k_i^2\ \frac{(M_p^2 - 1)}{M_p^2} \int_o^a r\ \hat{p}_{pi}\ \ \hat{p}_{pj}\ dr$$

$$= 0 \tag{A2-7}$$

Multiply (A2-2) by $\dfrac{\hat{p}_{fj} r}{M_f^2}$ and integrate over r from r = a to r = b we obtain after one integration by parts,

$$\frac{r}{M_j^2}\,\hat{p}_{fj}\,\frac{d\hat{p}_{fi}}{dr}\Bigg|_a^b - \int_a^b \frac{r}{M_f^2}\,\frac{d\hat{p}_{fi}}{dr}\,\frac{d\hat{p}_{fj}}{dr}\,dr + k_i^2\,\frac{(M_f^2-1)}{M_f^2}\int_a^b r\,\hat{p}_{fi}\,\hat{p}_{fj}\;dr = 0 \qquad \text{(A2-8)}$$

Adding (A2-7) and (A2-8) and using boundary condition (A2-3) to (A2-6), we have,

$$-\int_o^a \frac{r}{M_p^2}\,\frac{d\hat{p}_{pi}}{dr}\,\frac{d\hat{p}_{pj}}{dr}\,dr - \int_a^b \frac{r}{M_f^2}\,\frac{d\hat{p}_{fi}}{dr}\,\frac{d\hat{p}_{fj}}{dr}\,dr$$

$$+\,k_i^2\left[\frac{M_p^2-1}{M_p^2}\int_o^a r\,\hat{p}_{pi}\,\hat{p}_{pj}\,dr + \frac{M_f^2-1}{M_f^2}\int_a^b r\,\hat{p}_{fi}\,\hat{p}_{fj}\,dr\right] = 0. \qquad \text{(A2-9)}$$

Equation (A2-9) holds for arbitrary i and j. Interchanging i and j in this equation, we find

$$-\int_o^a \frac{r}{M_p^2}\,\frac{d\hat{p}_{pj}}{dr}\,\frac{d\hat{p}_{pi}}{dr}\,dr - \int_a^b \frac{r}{M_f^2}\,\frac{d\hat{p}_{fj}}{dr}\,\frac{d\hat{p}_{fi}}{dr}\,dr$$

$$+\,k_j^2\left[\frac{M_p^2-1}{M_p^2}\int_o^a r\,\hat{p}_{pj}\,\hat{p}_{pi}\,dr + \frac{M_f^2-1}{M_f^2}\int_a^b r\,\hat{p}_{fj}\,\hat{p}_{fi}\;dr\right] = 0 \qquad \text{(A2-10)}$$

Subtract (A2-10) from (A2-9) and noting that $k_i \neq k_j$, the orthogonality condition

$$\frac{M_p^2-1}{M_p^2}\int_o^a r\,\hat{p}_{pi}\,\hat{p}_{pj}\,dr + \frac{M_f^2-1}{M_f^2}\int_a^b r\,\hat{p}_{fi}\,\hat{p}_{fj}\,dr = 0;\; i \neq j \qquad \text{(A2-11)}$$

is established.

# APPENDIX 3

## REAL AND IMAGINARY EIGENVALUES

To show that all the eigenvalues of eigenvalue problem (5-12) to (5-17) are real, we will make use of equation (A2-9) in Appendix 2. In this equation $(\hat{p}_{pi}, \hat{p}_{fi})$ can be any eigenfunction. We will now let $(\hat{p}^*_{pi}, \hat{p}^*_{fi})$ be $(\hat{p}_{pj}, \hat{p}_{fj})$, where * denotes the complex conjugate. Now (A2-9) can be written as

$$k_i^2 = \frac{\dfrac{1}{M_p^2}\displaystyle\int_o^a \left|\frac{d\hat{p}_{pi}}{dr}\right|^2 r\,dr + \dfrac{1}{M_f^2}\displaystyle\int_a^b \left|\frac{d\hat{p}_{fi}}{dr}\right|^2 r\,dr}{\dfrac{M_p^2 - 1}{M_p^2}\displaystyle\int_o^a r\left|\hat{p}_{pi}\right|^2 dr + \dfrac{M_f^2 - 1}{M_f^2}\displaystyle\int_a^b r\left|\hat{p}_{fi}\right|^2 dr} \, . \qquad \text{(A3-1)}$$

For $M_f^2 > 1$ and $M_p^2 > 1$, the right hand side is positive definite. Hence $k_i$ is real.

# APPENDIX 4

## THE SPECTRA OF DISCRETE REAL EIGENVALUES

In this appendix the spectra of the discrete real eigenvalues of equations (5-20) and (5-51) will be discussed. It will be shown that the set of real zeros of equation (5-51) which corresponds to subsonic primary stream Mach numbers is fundamentally different from the set of real zeros of equation (5-20) for supersonic primary Mach numbers.

In the eigenvalue problems that lead to equations (5-20) and (5-51), the eigenvalue k appears as $k^2$ so that if $k_j>0$ is an eigenvalue, $-k_j$ will also be an eigenvalue. It is, therefore, sufficient to restrict our attention to $k\geq 0$ alone. The right hand sides of equations (5-20) and (5-51) are identical. For a given set of parameters the graph of this quantity as a function of k has many branches as shown in Figure A4.1. For large values of k the zero crossings and vertical asymptotes are given by,

$$k_n \simeq \frac{n\pi}{\sqrt{M_f^2 - 1}\,(b-a)} \qquad \text{(zero crossings)}$$

and

$$k_n \simeq \frac{(n + \frac{1}{2})\,\pi}{\sqrt{M_f^2 - 1}\,(b-a)} \qquad \text{(vertical asymptotes)}$$

where n = integers. These formulae can be derived by using the asymptotic forms of the Bessel functions with large argument. As a function of k, the left hand side of equation (5-51) consists of a single curve with a vertical asymptote at $k = 0$ and a horizontal asymptote of negative one as $k \to \infty$. This is shown by the dotted curve in Figure A4.2. The real eigenvalues are given by the intersection points of this curve and the multi-branch graph of Figure A4.1. This is shown in Figure A4.2.

The graph of the left hand side of equation (5-20) as a function of k has infinitely many branches as illustrated by the dotted curves of Figure A4.3. These different branches are separated by vertical asymptotes at

$$k_n = \frac{S_n}{\sqrt{M_p^2 - 1}\,a}, \qquad n = 1, 2, 3, \ldots$$

where $S_n$ are the $n^{th}$ zero of $J_1(S)$. In Figure A4.3 the graph of the right hand side of equation (5-10) is also shown. The roots of this equation are given by the intersection points of these graphs. It is now obvious by comparing Figures A4.2 and A4.3 that the structure and arrangement of the eigenvalues for $M_p > 1$ are fundamentally different from those for $M_p < 1$. The numerical values as well as the number of eigenvalues within each branch of the graph is strongly influenced by the ratio of inner to outer jet radii and the jet flow Mach numbers. In contrast to this, when $M_p$ is subsonic there is always one eigenvalue in each branch of the graph of Figure A4.1. The physical implication is that the periodic shock structure which exists in the fan stream when the primary flow is subsonic will terminate when the primary stream Mach number is increased to unity. For $M_p > 1$, a new system of shocks will form in the flow. This new shock system usually would have a very different internal structure.

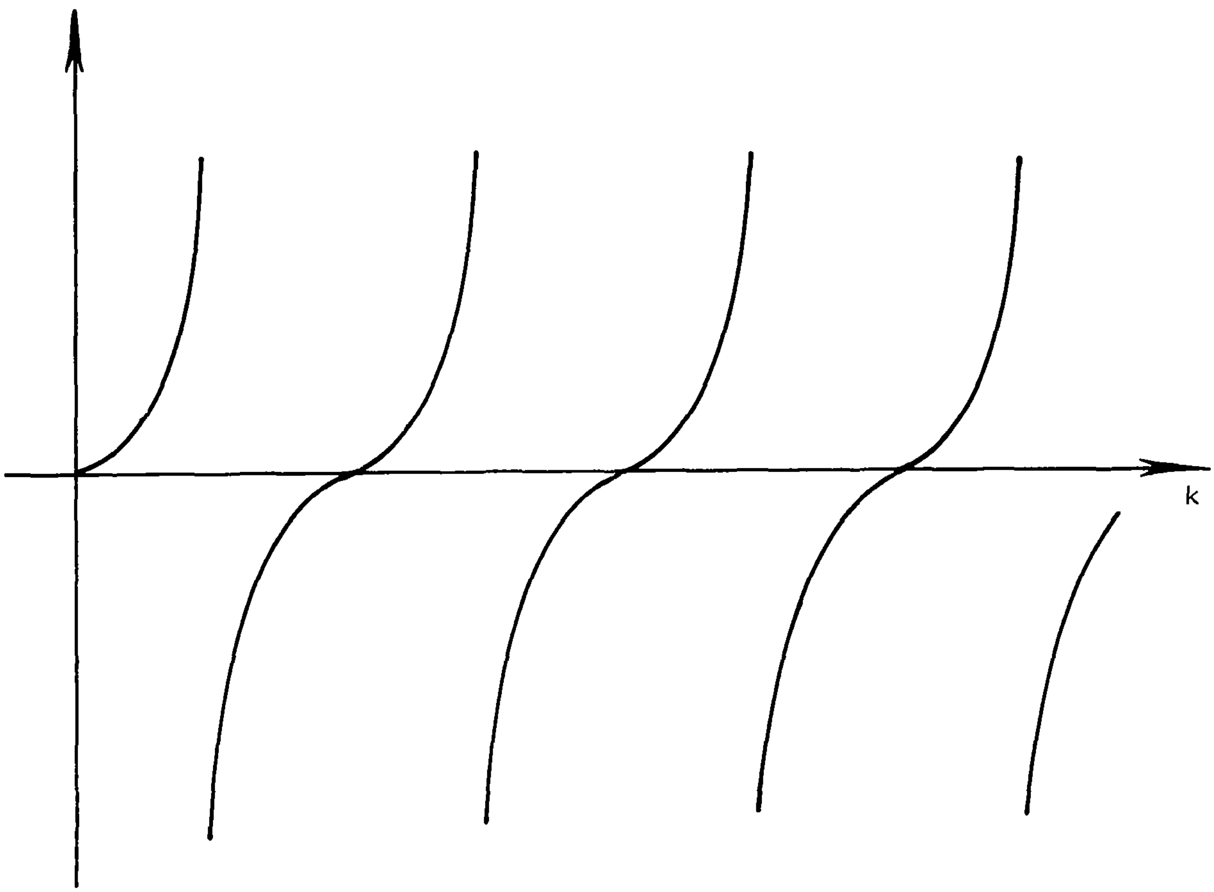


Figure A4.1 Graph of the right hand side of equations (5-20) and (5-51) as a function of k.

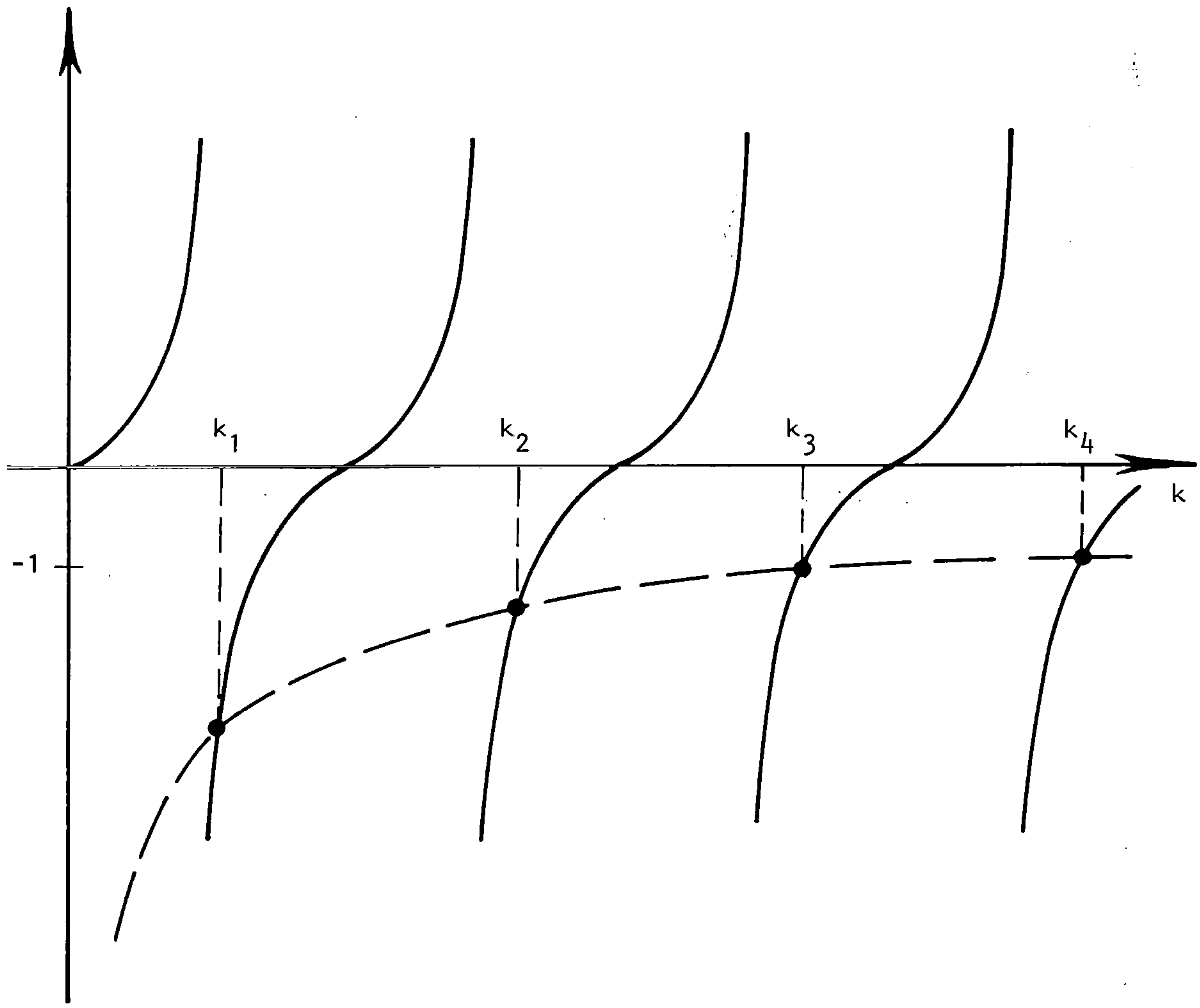


Figure A4.2 The spectrum of discrete real eigenvalues of equation (5-51).

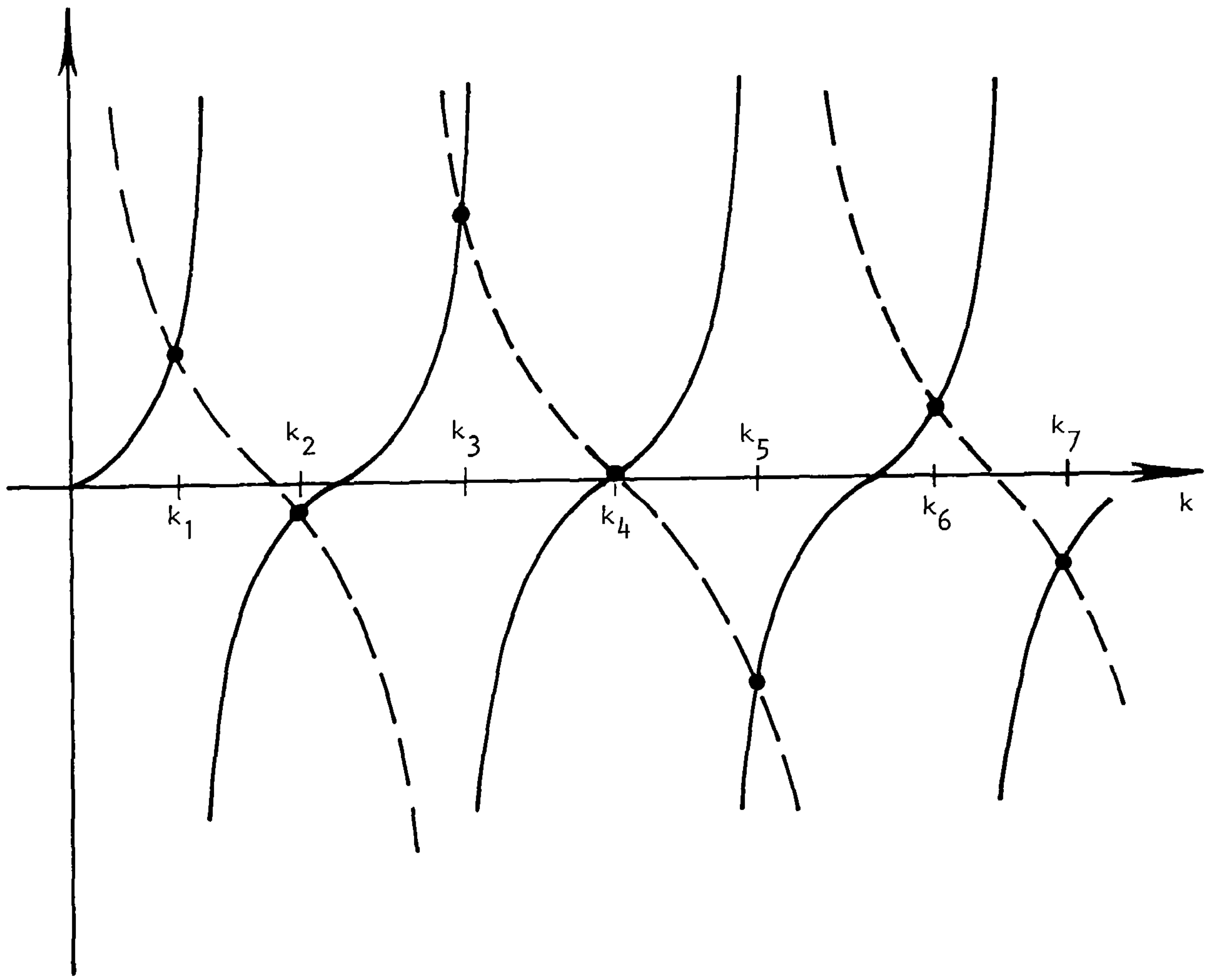


Figure A4.3 The spectrum of discrete eigenvalues of equation (5-20).

# APPENDIX 5

## LIST OF SYMBOLS

| | |
|---|---|
| $a, b$ | inner and outer radii of coannular jet |
| $a_p$, $a_f$ | speed of sound in primary, fan stream |
| $A$, $B$, $D$ | arbitrary constants |
| $A_p$, $A_f$ | exit area of primary, fan stream |
| $c_a$ | ambient speed of sound |
| $d$ | fan stream annulus width |
| $D_{eq}$ | diameter of equivalent single jet nozzle |
| $D_p$, $D_f$ | diameter of primary, fan nozzle exit |
| $e$ | denotes expansion fan |
| $f_p$ | peak frequency of shock associated noise |
| $I$ | acoustic intensity |
| Im | denotes imaginary part of |
| $I_o$, $I_1$ | modified Bessel function of zeroth-order, first-order |
| $J_o$, $J_1$ | Bessel function of zeroth-order, first-order |
| $L$ | shock cell length |
| $M_c$ | $= u_c/c_a$ |
| $M_d$ | design Mach number of convergent-divergent nozzle |
| $M_p$, $M_f$ | Mach number of primary, fan stream |
| $p$ | pressure |
| $p_a$ | ambient pressure |
| $p_{tp}$, $p_{tf}$ | total pressure of primary, fan nozzle |
| $r$ | radial coordinate |
| $r_p$, $r_f$ | radius of primary, fan nozzle exit |

| | |
|---|---|
| $R$ | distance from nozzle exit to microphone |
| Re | denotes real part of |
| s | denotes shock |
| TP | test point |
| $T_a$ | ambient temperature |
| $T_{tp}$, $T_{tf}$ | total temperature of primary, fan flow |
| $u$, $v$ | velocity components associated with periodic shock cell solutions |
| $u_c$ | convection velocity of large scale turbulence structures |
| $u_p$, $u_f$ | primary, fan stream velocity |
| $V_{eq}$ | fully-expanded exit velocity of equivalent single jet |
| $V_p$, $V_f$ | fully-expanded exit velocity of primary, fan stream |
| $x$, $y$ | coordinates |
| $Y_o$, $Y_1$ | Neumann function of zeroth-order, first-order |
| $\beta$ | $= (M_p{}^2 - 1)^{\frac{1}{2}}$ |
| $\Delta p$ | pressure difference at nozzle exit |
| $\theta$ | microphone or observer angle relative to jet exhaust axis |
| $\xi_p$, $\xi_f$ | pressure ratio of primary, fan nozzle |
| $\rho$ | density |
| $\rho_p$, $\rho_f$ | density of primary, fan stream |

# REFERENCES


1. Kozlowski, H.; and Packman, A. B.: Aerodynamic and acoustic tests of duct-burning turbofan exhaust nozzles. NASA CR-2628, 1976.

2. Knott, P. R.; Stringas, E. J.; Brausch, J. F.; Staid, P. S.; Heck, P. H.; and Latham, D.: Acoustic tests of duct-burning turbofan jet noise simulation. NASA CR-2966, 1978.

3. Pao, S.P.: A correlation of mixing noise from coannular jets with inverted flow profiles. NASA TP 1301, 1979.

4. Tanna, H. K.; Tester, B. J.; and Lau, J. C.: The noise and flow characteristics of inverted-profile coannular jets. NASA CR-158995, 1979.

5. Burrin, R. H.; and Tanna, H. K.: The Lockheed-Georgia coannular jet research facility. Lockheed-Georgia Company Report No. LG77ER0243, 1977.

6. Tanna, H. K.: Coannular jets -- are they really quiet and why? *Journal of Sound and Vibration*, Vol. 72, 97-118, 1980.

7. Harper-Bourne, M.; and Fisher, M. J.: The noise from shock waves in supersonic jets. Proceedings (No. 131) of the AGARD Conference on Noise Mechanisms, Brussels, Belgium, 1973.

8. Tanna, H. K.: An experimental study of jet noise. Part II: Shock associated noise. *Journal of Sound and Vibration*, Vol. 50, 429-444, 1977.

9. Tam, C. K. W.; and Tanna, H. K.: Shock associated noise of supersonic jets from convergent-divergent nozzles. *Journal of Sound and Vibration*, To appear in 1981.

10. Dosanjh, D. S.; Yu, J. C.; and Abdelhamid, A. N.: Reduction of noise from supersonic jet flows. *AIAA Journal*, Vol. 9, 2346-2353, 1971.

11. Dosanjh, D. S.; Bhutiani, P. K.; and Ahuja, K. K.: Jet noise suppression by coaxial multi-nozzle cold/heated jet flows. Grant DOT OS-20094, Mechanical and Aerospace Engineering Department Report, Syracuse University, 1977.

12. Dosanjh, D. S.; Bhutiani, P. K.; and Ahuja, K. K.: Supersonic jet noise suppression by coaxial cold/heated jet flows. *AIAA Journal*, Vol. 16, 268-270, 1978.

13. Bassiouni, M. R.; and Dosanjh, D. S.: Acoustic and flow characteristics of cold high-speed coaxial jets. *AIAA Journal*, Vol. 17, 153-159, 1979.

14. Prandtl, L.: *Phys. Zeits.*, Vol. 5, 599-601, 1904.

15. Pack, D. C.: A note on Prandtl's formula for the wave length of a supersonic gas jet. *Quart. J. Mech. Appl. Math.*, Vol. 3, 173-181, 1950.

16. Morse, P. M.; and Feshbach, H.: *Methods of Theoretical Physics*, Vol. I and II. McGraw-Hill Company, New York, 1953.

| 1. Report No. | 2. Government Accession No. | 3. Recipient's Catalog No. |
|---|---|---|
| NASA CR-3454 | | |
| 4. Title and Subtitle<br>SHOCK ASSOCIATED NOISE REDUCTION FROM INVERTED-VELOCITY-PROFILE COANNULAR JETS | | 5. Report Date<br>August 1981<br>6. Performing Organization Code |
| 7. Author(s)<br>H. K. Tanna, C. K. W. Tam and W. H. Brown | | 8. Performing Organization Report No.<br>LG81ER0162<br>10. Work Unit No. |
| 9. Performing Organization Name and Address<br>Lockheed-Georgia Company<br>86 South Cobb Drive<br>Marietta, Georgia 30063 | | 11. Contract or Grant No.<br>NAS1-15971 |
| 12. Sponsoring Agency Name and Address<br>National Aeronautics and Space Administration<br>Washington, D. C. 20546 | | 13. Type of Report and Period Covered<br>Contractor Report<br>14. Sponsoring Agency Code |

15. Supplementary Notes

Langley Technical Monitor: John M. Seiner
Lockheed Program Manager: H. K. Tanna
Final Report

16. Abstract

The work described in this report is conducted to quantify and obtain a physical understanding of the noise reduction mechanisms in supersonic inverted-velocity-profile coannular jets, with emphasis on the shock associated noise reduction. The acoustic measurements show that the shock noise from the outer stream is virtually eliminated when the inner stream is operated at a Mach number just above unity, regardless of all the other jet operating conditions. At this optimum condition, the coannular jet provides the maximum noise reduction relative to the equivalent single jet. Furthermore, the shock noise reduction can be achieved at inverted- as well as normal-velocity-profile conditions, provided the coannular jet is operated with the inner stream just slightly supersonic. To understand the acoustic results, simple analytical models for the shock structure and shock noise are developed. The model indicates that a drastic change in the outer stream shock cell structure occurs when the inner stream increases its velocity from subsonic to supersonic. At this point, the almost periodic shock cell structure of the outer stream nearly completely disappears, and hence, the noise radiated is minimum. Finally, the theoretically derived formulae for the peak frequencies and intensity scaling of shock associated noise are compared with the measured results, and good agreement is found for both subsonic and supersonic inner jet flows.

| 17. Key Words (Suggested by Author(s)) | 18. Distribution Statement |
|---|---|
| Coannular Jets, Coaxial Jets, Shock Structure, Shock Associated Noise, Aircraft Noise Reduction, Inverted Velocity Profiles, Supersonic Jets | Unclassified - Unlimited<br>Subject Category 71 |

| 19. Security Classif. (of this report) | 20. Security Classif. (of this page) | 21. No. of Pages | 22. Price |
|---|---|---|---|
| Unclassified | Unclassified | 159 | A08 |

For sale by the National Technical Information Service, Springfield, Virginia 22161

NASA-Langley, 1981